Advances in ^{1}H-Detected Solid-State NMR Spectroscopy

by

Jacqueline Tognetti

Thesis

Submitted to the University of Warwick

for the degree of

Doctor of Philosophy

Department of Chemistry and Physics

March 2022

THE UNIVERSITY OF WARWICK

Contents

List of Figures

Acknowledgments

I would like to thank my supervisors Steven and Józef for their guidance in these years. I would like to do a particular appreciation to Trent and Angelo from whom I learnt a lot. I would like to thank all the people in the NMR group for their continued support. A particular thank to my friend Alessandra, who was there for me. However, this thesis is dedicated to my parents, without them nothing of this would have been possible.

Declarations

The work presented in this thesis is my own, except where stated otherwise in the statement of contributions at page 33. The research was conducted under the supervision of Prof. Steven P. Brown and Józef R. Lewandowski at the University of Warwick. This thesis is submitted to the University of Warwick in support of my application for the degree of Doctor of Philosophy. It has been composed by myself and has not been submitted in any previous application for any degree. This is a thesis with inclusion of published work as outlined at https://warwick.ac.uk/fac/sci/mas/internal/phdportal/submitting. Parts of this thesis have been published or submitted for publication by the author:

Jacqueline Tognetti, W. Trent Franks, Józef R. Lewandowski, Steven P. Brown, ^{15}N-^{1}H through-bond heteronuclear correlation solid-state NMR spectroscopy with ^{1}H homonuclear decoupling at 60 kHz MAS. (Submitted for publication)

Jacqueline Tognetti, W. Trent Franks, Angelo Gallo, Józef R. Lewandowski, Accelerating ^{15}N and ^{13}C R_1 and $R_{1\rho}$ relaxation measurements by multiple pathway solid-state NMR experiments. Journal of Magnetic Resonance,331, 107049(2021)

W. Trent Franks‡, Jacqueline Tognetti‡, Józef R. Lewandowski, Slice and Dice: Nested Spin-lattice Relaxation Measurements. ‡These authors contributed equally to this work. (Submitted for publication)

Abstract

The overall aim of this thesis is to develop experimental methods to improve the acquisition of proton detected solid-state NMR experiments at fast ($\geq$ 60 kHz) magic angle spinning (MAS). ^{1}H-detection at fast MAS is often used to enhance the signal of natural abundance rare and low gamma nuclei. However, strong ^{1}H-^{1}H homonuclear dipolar couplings negatively impact the quality of the spectra and even 60-100 kHz MAS is not sufficient to average them out completely. Consequently, even in that spinning regime it is worthwhile to improve the proton resolution and coherence lifetimes by combining with ^{1}H homonuclear decoupling. In the first part of the thesis, supercycled Phase Modulated Lee-Goldburg (PMLG) homonuclear decoupling was evaluated in its windowed and windowless form at 60 kHz MAS, for nutation frequencies $\leq$ 100 kHz. The optimized decoupling scheme was then employed on the proton channel during the INEPT transfer for detecting the first natural abundance 2D ^{15}N-^{1}H CP-Refocused INEPT correlation experiment at 60 kHz MAS.

In the second part of the thesis, two methods for improving relaxation measurements via ^{1}H detected experiments at 100 kHz MAS are presented. Relaxation rates are important probes of molecular motions, but their measurements are typically time consuming. To partially alleviate this problem, we have developed approaches to obtain multiple measurements of relaxation rates in a single experiment. In the first of the presented methods ^{13}CO and ^{15}N relaxation rates are measured in a single experiment, sharing the same recycle delay, and, in the case of spin-lattice relaxation, also the relaxation delays. In the second approach, instead, relaxation delays on multiple nuclei of the protein backbone (^{15}N, ^{13}CO and ^{13}C$^{\alpha}$) can be fitted into the longest relaxation delays. This approach enables the measurement of multiple rates in the same nested experiment in a fraction of the time necessary for separate experiments.

Abbreviations

CP	Cross Polarization
CRAMPS	Combined Rotation And Multiple-Pulse Spectroscopy
DUMAS	DUal acquisition of Magic Angle Spinning
DUMBO	Decoupling Using Mind Boggling Optimization
EMF	Extended Model Free
FID	Free Induction Decay
FT	Fourier Transform
FWHM	Full Width Half Maximum
INEPT	Insensitive Nuclei Enhanced by Polarization Transfer
MAS	Magic Angle Spinning
NMR	Nuclear Magnetic Resonance
PAS	Principal Axis System
PMLG	Phase Modulated Lee-Goldburg
SIM-CP	Simultaneous Cross Polarization
SLIDE	SimultaneousLy Increasing and DEcreasing
SMF	Simple Model Free
SNR	Signal to Noise Ratio

Chapter 1

Introduction

Over the last years, nuclear magnetic resonance (NMR) has become an important analytical technique providing information about structure[1–3] and dynamics[4–6] for a wide range of molecules in the solid state. The first NMR experiments in the bulk phase were reported in 1946.[7,8] Because overall tumbling in solution averages out strong anisotropic interactions giving rise to well resolved spectra, solution NMR has become an important routine technique for characterising samples ranging from small molecules to proteins. In contrast, the challenge of removing the broadening due to presence of anisotropic interactions in the solid state has slowed the wide adoption of solid-state NMR. For solid-state NMR to reach "the masses" a number of instrumental and methodological challenges need to be addressed. Consequently, while solution NMR is generally well established and to a large extent standardised, solid-state NMR is still in active development motivated by various factors. Besides the obvious fact that many important substances are solids there are also several more subtle reasons to continue progressing solid-state NMR. For example, for large macromolecules the slow tumbling leads to increased linewidths in solution, introducing an intrinsic limitation for the size of systems. The lack of broadening associated with overall rotational diffusion means that there is no such intrinsic limit in the solid state. Thus, solid-state NMR holds promise to provide access to structural and dynamic information for systems beyond the reach of its solution counterpart. One of the promising aspects of solid-state NMR for probing molecular motions is that the window of time scales for motions that influence relaxation rates is much wider compared to solution, where mostly the motions up to the time scale of the overall tumbling can be detected.[9] One of the major challenges for solid-state NMR is that anisotropic interactions, such as dipolar couplings, lead to significant line broadening. For example, ^{1}H-^{1}H homonuclear dipolar couplings,[10–13] while being a potent tool to access structural features and enable magnetization transfer, can also result in generally broad spectra. This renders ^{1}H-detected experiments that are routine in solution, generally challenging in the solid state.

Before the 1990s, solid-state NMR avoided ^{1}H detection. The achievable magic angle spinning (MAS) frequencies were simply not sufficient to average the strong ^{1}H-^{1}H dipolar couplings. In some cases sophisticated homonuclear decoupling methods at slow spinning frequencies were exploited but in general, lower γ nuclei, such as ^{13}C, were preferred for acquisition because they yielded sufficient resolution to be able to extract structural information. Protons still played a huge role in enhancing the signal on rare and low γ isotopes, such as ^{13}C and ^{15}N, with the use of Cross-Polarization (CP)[14] and Insensitive Nuclei Enhancement by Polarization Transfer (INEPT),[15,16] taking advantage of the proton's high gyromagnetic ratio, natural abundance and short spin-lattice relaxations, which allows a faster repetition of the experiments. The development and applications of homonuclear decoupling that enabled ^{1}H-detected solid-state NMR before fast spinning became available have grown into a field of its own that has attracted some of the finest minds in the discipline. Different homonuclear decoupling rf schemes[12,13,17–25] have been developed for helping to average the ^{1}H homonuclear dipolar couplings and have been used, for example, to improve the resolution of the indirect dimension on ^{1}H-X 2D correlations.[26,27] To improve the resolution of ^{1}H spectra, in 1977 Combined Rotation and Multiple-Pulse Spectroscopy (CRAMPS) was introduced.[28] A stroboscopic acquisition of alternating pulsing and acquisition combined with magic angle spinning was able to grant good spectral resolution to enable more informative proton detected spectra.[29] However, these homonuclear decoupling schemes that have proven very useful for studies of small molecules have rarely been applied to biomolecules mostly due to the requirement for high ^{1}H nutation frequencies that can easily compromise fragile biomolecular samples. While the vast majority of studies of isotopically enriched biological samples[30,31] are conducted using traditional ^{13}C and ^{15}N detected experiments, partial deuteration has paved a way for ^{1}H detected experiments at moderate spinning frequencies.[32–36] However, while deuteration of samples combined with lower spinning frequencies addressed some of the issues for ^{1}H detected experiments on biological samples they introduced their own challenges and did not address problems, such as, removing unwanted coherent effects as spin diffusion.[37–42]

The advent of fast spinning probes has resulted in a step change for solid state NMR capabilities. Starting with breaking the 30 kHz spinning barrier in late 1990s,[43,44] reaching 60-110 kHz and beyond[45–49] has a major impact on quantitative structural and dynamics studies. The overall price for this progress was decrease of rotor sizes and consequently the available sample volumes. While for proteins, the need for less sample can be advantageous because the production of a protein often yields only a very small amount at elevated costs,[50] lower sample quantity leads to lower sensitivity. Consequently, the detection of rare and low γ nuclei, especially in small molecules and pharmaceuticals, where the nuclei are not usually isotopically labelled[51,52] becomes less practical under fast spinning conditions. Fortunately, in many cases proton detection can compensate for the losses of sensitivity associated with smaller sample sizes.[32,44,53–59] However, spinning frequencies on the order of 50-60 kHz MAS are still not sufficient to completely average out ^{1}H dipolar couplings[56,60,61] in rigid organic molecules and even at 100 kHz spinning there are still related effects that affect site-specificity of dynamics[42] and spectral resolution.[62–64] Since at 60 kHz the ^{1}H dipolar couplings are not sufficiently averaged, through-bond transfers, such as INEPT, are not favoured in both small molecules and more rigid biomolecules. Indeed, in addition to causing broadening and hence lowering sensitivity, the anisotropic interactions shorten the proton coherence lifetimes. Consequently, optimizing and using ^{1}H homonuclear decoupling even in this fast MAS regime seems fundamental to boost the quality of ^{1}H detected spectra.[56,65,66] However, the use of decoupling schemes at fast MAS (above 40 kHz) brings some challenges because while at low spinning frequencies (5 kHz- 15 kHz) the decoupling is governed by the 'quasi-static' condition, where the rotor period is long relative to the cycle time of the decoupling sequence, implying the use of high ^{1}H nutation frequencies, at faster MAS,[43,66–72] the decoupling uses cycle times comparable to the rotor period. Indeed, it is influenced by the relationship between the MAS frequency and the cycle time of the decoupling[73] and more recoupling conditions can be found. In this context, chapter 5 in this thesis explores, after an introduction of the decoupling scheme and derivation at fast MAS (in our case 60 kHz MAS), the challenges of the optimization of phase modulated Lee-Goldburg (PMLG) ^{1}H homonuclear decoupling at 60 kHz MAS for ^{1}H nutation frequencies of 100 kHz and less, applying the optimized decoupling for recording a 2D ^{15}N-^{1}H CP-Refocused INEPT correlation experiment of the dipeptide β-Asp-Ala and the pharmaceutical compound cimetidine.

Another area of solid-state NMR that has greatly benefited from the availability of fast spinning are relaxation measurements for quantification of molecular dynamics. Relaxation measurements[74,75] are widely used to investigate dynamics[4,76] for their ability to report on time-scale, amplitude and, in some cases, also direction of motions in a site-specific manner. In this thesis we explore the measurements of backbone ^{13}C and ^{15}N spin-lattice relaxation rates, R_1,[39,77,78] which report on ps-ns motions, and spin-lattice relaxation in the rotating frame relaxation rates, $R_{1\rho}$,[40,79–81] which sample motions on the order from ns to ms. While relaxation rates are powerful probes of dynamics, one of their downsides is that many relaxation measurements are typically necessary to build a reliable picture of molecular dynamics. Consequently, experiments often need to be acquired at different fields, temperatures and on different nuclei.[41,82,83]

Most of the experimental time in NMR is spent waiting for the spins to relax for the next acquisition. In addition, to achieve a good sensitivity in a challenging system, the experiment needs to be repeated many times. NMR relaxation measurements are particularly time-consuming, because they are characterized by long delays to allow the correct relaxation time sampling, for example T_1 delays on ^{13}C and ^{15}N can take up to tens of seconds. Different methods have been employed to speed up the experimental acquisition which involves protein manipulation and experimental design. For example, paramagnetic dopants can be added to the sample buffer to increase the rate of repetition of the experiments.[84–90] However, the contribution to relaxation from dynamics is usually masked from the dominant paramagnetic effect and it is not possible to have reliable sampling of relaxation in doped samples.[91]

Many methods have been developed to accelerate the acquisition of NMR experiments. For example, the initial polarization could be used more efficiently than the standard approaches, taking advantage of the orphaned polarization using a simultaneous cross-polarization (SIM-CP),[92] on two different nuclei, for example carbon and nitrogen using a single recycle delay for both the nuclei. This can be done in a time-shared experiment,[93,94] where the magnetization passes through different magnetization pathway to be recorded all together. To eliminate signal overlap that comes from the different experiments, a sequential acquisition was introduced with the DUal acquisition of Magic Angle Spinning (DUMAS) experiment,[92,95] to record the experiment on two nuclei on a different time, while the polarization on one of the nuclei is stored. In the original DUMAS experiment the acquisition is on the low γ channel(s), but it was developed to accommodate ^{1}H detection,[96] detection of orphaned polarization in mixed dimensionality,[97] as well as the use of multiple receivers.[98,99] In Chapter 6 and 7, we show how these techniques can be applied to speed up the acquisition of relaxation experiments at 100 kHz MAS, where the relaxation is quantified using sequential acquisition ^{1}H channel in a time-shared experiment, or nested acquisition to record relaxation measurements on multiple nuclei.

Chapter 2

NMR Theory

This chapter will provide a general review of the fundamentals of Nuclear Magnetic Resonance (NMR) spectroscopy, including basic quantum mechanics and Hamiltonian interactions. The chapter is based on the content of the following books: Spin dynamics: basics of nuclear magnetic resonance (M. H. Levitt),[100] Understanding NMR Spectroscopy (J. Keeler),[101] Introduction to Solid-State NMR Spectroscopy (M. J. Duer),[102] Protein NMR Spectroscopy, principles and practice,(J. Cavanagh, W. J. Fairbrother, A. G. Palmer III, N. J. Skelton),[103] Solid State NMR Studies of Biopolymer (McDermott, A. E.; T. Polenova).[104]

2.1 NMR Fundamentals

2.1.1 Spin Angular Momentum and the Zeeman Interaction

The nuclear magnetic resonance phenomenon originates from spin, which is an intrinsic property of the nuclei alongside with others such as mass and charge. Nuclear isotopes are distinguished by the spin quantum number, I. If a nucleus has $I \geq 1/2$, then the nucleus possesses an intrinsic magnetic moment, μ, which renders it inherently magnetic. μ is defined as:

$$\hat{\mu} = \gamma \hat{\mathbf{I}}, \tag{2.1}$$

where γ is the gyromagnetic ratio of the nucleus of interest, which is a unique constant for each isotope and $\hat{\mathbf{I}}$ is the spin angular momentum operator. In the presence of an external magnetic field B_0, the energy of a nuclear spin can be described by the Zeeman interaction:

$$\hat{H}_z = -\hat{\mu} \cdot \mathbf{B}, \tag{2.2}$$

where $\hat{\mu}$ is the nuclear magnetic moment operator. By convention, B_0 is assumed to be aligned with the z-axis such that $\mathbf{B} = (0,\, 0,\, B_0)$, and therefore termed longitudinal. In this way the Zeeman Hamiltonian is given by:

$$\hat{H}_z = -\mu_{\mathrm{z}} B_0 = -\gamma B_0 \hat{I}_z = \omega_0 \hat{I}_z. \tag{2.3}$$

The Larmor precession is the frequency of precession of the spins around the primary axis of the external magnetic field B_0 and the frequency of this precession is the Larmor frequency defined by

$$\omega_0 = -\gamma B_0. \tag{2.4}$$

$\hat{I}_z$ is the z-component (along an arbitrary z-axis) of the nuclear spin quantum operator $\hat{\mathbf{I}}$. The total magnitude of the spin-angular momentum operator squared is given by:

$$\hat{I}^2 = \hat{I}_x^2 + \hat{I}_y^2 + \hat{I}_z^2. \tag{2.5}$$

For spin 1/2, the matrix form of each of the x, y and z-components is:

$$\hat{I}_x = \begin{pmatrix} 0 & \frac{1}{2} \\ \frac{1}{2} & 0 \end{pmatrix}, \quad \hat{I}_y = \begin{pmatrix} 0 & -\frac{1}{2}i \\ \frac{1}{2}i & 0 \end{pmatrix}, \quad \hat{I}_z = \begin{pmatrix} \frac{1}{2} & 0 \\ 0 & -\frac{1}{2} \end{pmatrix}. \tag{2.6}$$

The magnitude of the projection of the spin angular momentum along the z axis, I_{z}, is quantised as follow

$$I_{\mathrm{z}} = m\hbar, \tag{2.7}$$

where m, the azimuthal quantum number, assumes values as I, $I-1$, ... $-I$ and $\hbar$ is the reduced Planck constant ($\hbar = h/2\pi$). Substituting equation 2.3, the corresponding energies of the eigenstates of the Zeeman Hamiltonian are equal to $-m\gamma\hbar B_0$. The number of eigenvalues for $\hat{I}_z$ depends on the spin quantum number of the nucleus, with there being $2I+1$ eigenfunctions. For an isotope with $I = 1/2$, $m = \pm\frac{1}{2}$, so I_{z} becomes equal to $\pm\ \hbar/2$. If substituted into the Zeeman interaction

$$E = \pm\frac{\hbar\gamma B_z}{2}. \tag{2.8}$$

The difference in energy, ΔE, between the two energy levels corresponding to an allowed transition, $\Delta m = 1$ is then equal to

$$\Delta E = -\hbar\gamma B_{\mathrm{z}}. \tag{2.9}$$

The energy difference ΔE is therefore connected to the angular frequency by

$$\Delta E = \hbar\omega_0, \tag{2.10}$$

where it is seen that the Larmor frequency ω_0 (in rad s^{-1}) represents the splitting between the energy state adjusted by the reduced Planck constant. In case of a spin $I = 1/2$ nucleus, the two eigenstates of the $\hat{I}_z$ operator are termed $|\alpha\rangle$ and $|\beta\rangle$ for $m = +1/2$ and $m = -1/2$ respectively:

$$\begin{array}{ll} |\alpha\rangle & \hat{I}_z |\alpha\rangle = \frac{1}{2} |\alpha\rangle \\ |\beta\rangle & \hat{I}_z |\beta\rangle = -\frac{1}{2} |\beta\rangle \end{array}, \tag{2.11}$$

$|\alpha\rangle$ is referred to as spin-up and $|\beta\rangle$ as spin-down. Considering the Zeeman interaction Hamiltonian in equation 2.3, so the two eigenstates of the Zeeman interaction can be written as

$$\begin{array}{l} \hat{H}_z |\alpha\rangle = \frac{1}{2}\omega_0 |\alpha\rangle \\ \hat{H}_z |\beta\rangle = -\frac{1}{2}\omega_0 |\beta\rangle \end{array}, \tag{2.12}$$

where the eigenvalues $\pm\frac{1}{2}\omega_0$ are the energies of the states. The energy difference between the two states in the magnetic field, known as Zeeman splitting, is equal to the Larmor frequency ω_0, as described in equation 2.10. The factor $\hbar$ has been omitted in order to shift the Hamiltonian from energy to angular frequency units (rad s^{-1}). At equilibrium in an applied magnetic field, the different energy states are unequally populated, as the lower energy orientation of the spins are more probable. The relative population states are given by the Boltzmann distribution:

$$\frac{p_\alpha}{p_\beta} = e^{\frac{\omega_0}{k_b T}}, \tag{2.13}$$

where k_b is the Boltzmann constant, and T is the temperature. Quantum mechanics describes the probability of the spins being in one of the two eigenstates. To have a complete description of the system, a wavefunction Ψ can be used to describe the linear superposition of the eigenfunction of the Zeeman operator for a spin $I = 1/2$ nucleus:

$$|\psi\rangle = c_\alpha |\alpha\rangle + c_\beta |\beta\rangle, \tag{2.14}$$

where c_α and c_β are complex numbers, termed superposition coefficients. $|c_\alpha|^2$and $|c_\beta|^2$are the probabilities for the spin to collapse to the spin-up and spin-down states respectively when measured.($|c_\alpha|^2$+$|c_\beta|^2$= 1). The complex conjugate is equal to

$$\langle\psi| = c_\alpha^* \langle\alpha| + c_\beta^* \langle\beta|. \tag{2.15}$$

The wavefunctions of equation 2.14 and 2.15 can be represented as a vector

$$\begin{aligned} |\psi\rangle &= \begin{pmatrix} c_\alpha \\ c_\beta \end{pmatrix} \\ \langle\psi| &= \begin{pmatrix} c_\alpha^* & c_\beta^* \end{pmatrix}. \end{aligned} \tag{2.16}$$

In quantum mechanics the average value of an observable, $\left\langle \hat{Q} \right\rangle$, is known as expectation value

$$\left\langle \hat{Q} \right\rangle = \left\langle \psi | \hat{Q} | \psi \right\rangle, \tag{2.17}$$

where for this two-level system, the matrix representation of $\hat{Q}$ is:

$$\mathbf{Q} = \begin{pmatrix} Q_{\alpha\alpha} & Q_{\alpha\beta} \\ Q_{\beta\alpha} & Q_{\beta\beta} \end{pmatrix}. \tag{2.18}$$

2.1.2 The Density Operator

The state of a spin system can be described by density operator theory. It is particularly useful because the evolution of the bulk magnetization can be followed directly from the density operator. As the expectation value of an operator depends on the products of its coefficients, it is convenient to define a density operator:

$$\hat{\rho} = |\psi\rangle \langle\psi|. \tag{2.19}$$

For a spin-1/2 system the matrix representation of the density operator, using equation 2.16, becomes equal to

$$\hat{\rho} = \begin{pmatrix} c_\alpha c_\alpha^* & c_\alpha c_\beta^* \\ c_\beta c_\alpha^* & c_\beta c_\beta^* \end{pmatrix}. \tag{2.20}$$

The diagonal elements of the density matrix represent the population states, *i.e.*, the probability of the spins existing in one of the eigenstates, while the off-diagonal elements correspond to coherences, which exist if there is a phase coherence between the spins. Coherence is generated by the application of radio-frequency pulses and will be discussed in Section 2.2.1. For any observable, it can be shown that the expectation value of its corresponding operator is equal to

$$\left\langle \hat{Q} \right\rangle = Tr\left(\hat{\rho}\hat{Q} \right). \tag{2.21}$$

To describe the spin system during an NMR experiment, it is necessary to describe the evolution of the density operator over time. The Liouville-von-Neumann equation, which follows from the time-dependent Schrödinger equation, determines the evolution

$$\frac{d\hat{\rho}(t)}{dt} = -i\left[\hat{\mathbf{H}}, \hat{\rho}(t)\right], \tag{2.22}$$

where the solution is

$$\hat{\rho}(t) = e^{-i\hat{\mathbf{H}}t}\hat{\rho}(0)e^{i\hat{\mathbf{H}}t}. \tag{2.23}$$

The $e^{-i\hat{\mathbf{H}}t}$ and $e^{i\hat{\mathbf{H}}t}$ terms are defined as propagator and $\hat{\mathbf{H}}$ represents the total Hamiltonian, which is the sum of the interactions that the spins experience; this will be discussed in the next section.

2.2 Hamiltonian Interactions in Solid-State NMR

The spins can experience electric and magnetic fields generated by the sample itself and by the external apparatus. The latter, namely the strong B_0 magnetic field, generates stronger interactions with the nuclear spins as compared to the internal interactions. In general, the total Hamiltonian, $\hat{H}_{total}$, used to describe an NMR experiment includes external and internal interaction:

$$\hat{H}_{total} = \hat{H}_Z + \hat{H}_{rf} + \hat{H}_\sigma + \hat{H}_D + \hat{H}_J + \hat{H}_Q. \tag{2.24}$$

The external interactions are described by the Zeeman interaction,$\hat{H}_Z$, and the radio-frequency interaction, $\hat{H}_{rf}$. The other four Hamiltonians represent the internal interactions: $\hat{H}_\sigma$, the magnetic shielding, $\hat{H}_D$ the dipole-dipole coupling, $\hat{H}_J$ the J-coupling and $\hat{H}_Q$ the quadrupolar interaction. The quadrupolar interaction is present only in nuclei with $I \geq 1/2$, and therefore will not be taken into consideration in this thesis.

2.2.1 External Interaction

The external interactions arise from the NMR spectrometer which supplies two or more magnetic fields: B_0 which is the strong, homogenous and static magnetic field supplied by the main “superconducting” solenoid and $B_1(t)$ which is generated by the R.F. probe coil. $B_1(t)$ is a weak, oscillating magnetic field. As described in section 2.1.1, the Zeeman interaction, $\hat{H}_Z = \omega_0\hat{I}_z$, is the interaction between the nuclear spins and the external magnetic field, B_0. At the thermal equilibrium the population state is aligned with B_z, however to observe an NMR signal transverse magnetisation is required corresponding to a first order coherence (see Section 3.1). The transverse magnetization is generated by the application of a weak oscillating on-resonance magnetic field B_1, where the magnetization nutates about B_1 at the nutation frequency ω_1

$$\omega_1 = \gamma B_1. \tag{2.25}$$

Following nutation into the transverse plane, the spins precess about the z-axis at ω_0, producing a changing magnetic field, which generates a current in the coil through the Faraday's law of electromagnetic induction, which give rise to the NMR signal. The weak oscillating on-resonance magnetic field $B_1(t)$

$$\mathbf{B_1}(t) = 2\left|B_1\right|\cos\left(\omega_{rf}t + \phi\right)\mathbf{e_x} = \left|B_1\right|\left(e^{i(\omega_{rf}t+\phi)} + e^{-i(\omega_{rf}t+\phi)}\right)\mathbf{e_x}, \tag{2.26}$$

is characterized by the magnitude B_1, radio-frequency ω_{rf} and ϕ is the initial phase. $B_1(t)$ has two counter-rotating fields with distinct frequencies $+\omega_{rf}$ and $-\omega_{rf}$. The frequency with the opposite sign to the Larmor frequency can be neglected. Therefore, as for equation 2.26, the Hamiltonian can be shown as

$$\hat{H}_{rf} = -\gamma B_1\left[\hat{I}_x\cos\left(\omega_{rf}t + \phi\right) + \hat{I}_y\sin\left(\omega_{rf}t + \phi\right)\right]. \tag{2.27}$$

A rotating frame of reference, rotating at frequency ω_{rf}, is employed to make the interpretation of the evolution of the system time-independent, and the difference between the Larmor frequency and rotating frame is the resonance offset, Ω (see next section). At the rotating frame, then, the field appears stationary and time-independent:

$$\hat{H}^{rot}_{rf} = -\gamma B_1\left[\hat{I}_x\cos\phi + \hat{I}_y\sin\phi\right], \tag{2.28}$$

The Hamiltonian for a *rf* pulse about the x-axis is:

$$\hat{H}_{rf} = \omega_1\hat{I}_x, \tag{2.29}$$

where ω_1 is the nutation frequency, the frequency at which the pulse rotates the magnetization about the x-axis. The evolution of the time dependent density matrix describing the effect of applying an on-resonance oscillating field to a spin-1/2 nucleus (starting at thermal equilibrium) is given by the solution to the Liouville von Neumann equation:

$$\hat{\rho}(t) = e^{-i\omega_1 t\hat{I}_x}\hat{\rho}(0)e^{i\omega_1 t\hat{I}_x} = \frac{1}{2}\begin{pmatrix}\cos(\omega_1 t) & i\sin(\omega_1 t)\\ -i\sin(\omega_1 t) & -\cos(\omega_1 t)\end{pmatrix}. \tag{2.30}$$

From the above equation, the *rf* pulse has generated off-diagonal terms which correspond to coherence between the spin eigenstates, in addition to population states (diagonal).

2.2.2 The Resonance Offset

To visualize the interaction without the angular rotation it is possible to describe the interaction from a rotating reference frame at frequency ω_{rf}, The difference between the Larmor frequency and the rotating frame frequency is the resonance offset:

$$\Omega = \omega_0 - \omega_{rf}. \tag{2.31}$$

In this rotating frame, the Zeeman Hamiltonian becomes:

$$\hat{H}_Z^{rot} = \Omega \hat{I}_z. \tag{2.32}$$

This means that, in the rotating frame, precession occurs under a residual field determined by Ω. To see the effect of the free evolution Hamiltonian on the density operator we recall the solution of the Liouville-von-Neumann equation. The propagator of the density matrix starting at $\hat{\rho} = \hat{I}_x$ is

$$\hat{\rho}(t) = \begin{pmatrix} 0 & \frac{1}{2}e^{-i\Omega t} \\ \frac{1}{2}e^{i\Omega t} & 0 \end{pmatrix}. \tag{2.33}$$

The NMR signal, which arises from the induced current in the coil through Faraday's law. The signal is acquired through quadrature detection ($p = -1$ coherence), which is described by the raising operator, $\hat{I}_+$. The raising operator corresponds to two components that are 90° out of phase with respect to each other which form the real and imaginary components of the Free Induction Decay (FID):

$$\hat{I}_+ = \hat{I}_x + i\hat{I}_y = \begin{pmatrix} 0 & 1 \\ 0 & 0 \end{pmatrix}. \tag{2.34}$$

The detected NMR signal in the rotating frame under resonance offset is then given using equation 2.33 and 2.34 by:

$$S(t) = Tr\,(\hat{\rho}\hat{I}_+) = \frac{1}{2}\left(\cos(\Omega t) + i\sin(\Omega t)\right) = \frac{1}{2}e^{+i\Omega t}, \tag{2.35}$$

This corresponds to the precession of the real and imaginary components of magnetisation in the transverse plane. As described above, this rotating magnetization, with a 90° separation in phase between the two components, induces a current in the coil, producing the NMR signal. The FID will be then Fourier transformed. The time domain signal, as recorded, is sensitive to the sign of Ω. The detection of the two components of the NMR signal through a process called quadrature detection (see Section 3.1), permits the sign discrimination of the frequency spectrum following Fourier transform (FT) of the recorded FID.

2.2.3 Internal Spin Interaction

The nuclei experience magnetic and electric fields originating from the sample itself. These can be described through the Internal Spin Hamiltonian which, for spin $I = 1/2$ in diamagnetic samples, involves chemical shielding,direct dipole-dipole couplings, and J-couplings. Each Hamiltonian spin interaction can be described in the Principal Axis System, PAS, in the general form of

$$\hat{H}_{\mathrm{A}}^{P} = \hat{\mathbf{I}} \cdot \tilde{\mathbf{A}} \cdot \hat{\mathbf{S}} = \begin{pmatrix} I_x & I_y & I_z \end{pmatrix} \begin{pmatrix} A_{XX} & 0 & 0 \\ 0 & A_{YY} & 0 \\ 0 & 0 & A_{ZZ} \end{pmatrix} \begin{pmatrix} S_x \\ S_y \\ S_z \end{pmatrix}, \tag{2.36}$$

where $\tilde{\mathbf{A}}$ is the rank two tensor of the interaction A, $\hat{\mathbf{I}}$ is the spin operator for one spin and $\hat{\mathbf{S}}$ is the second nuclear spin involved in the interaction or the external field, depending on the interaction. However, the PAS is different for each interaction, and it is to be remembered that the most important interaction remains the Zeeman interaction of the external magnetic field which is described by the laboratory frame. So, to monitor the interaction it is necessary convert from the PAS to the laboratory frame by rotation. The rotation between two different frames is best described by spherical tensors, rather than Cartesian tensors, whereby the Hamiltonian is expressed as:

$$\hat{H} = \sum_{j=0}^{2} \sum_{m=-j}^{+j} (-1)^m A_{j,m} \hat{T}_{j,-m}, \tag{2.37}$$

where A is the spatial component of the Hamiltonian and represents the magnitude and direction of the interaction (the irreducible spherical tensor component) and $\hat{T}$ is the spin operator. Changes in the reference frame under spatial rotation only affect the spatial components. The Hamiltonian components are denoted by j, which is the rank of the tensor, and m, the order of the tensor component, which can take $2j+1$ values. The rotation from a reference frame to a different axes system can be easily described by using the Euler angles, in which the rotation in the three dimensions is described by three angles (α, β, γ). By convention, in the first step, the rotation is applied on the z-axis around an angle α, secondly about the rotated y-axis by an angle β, and finally with a rotation about the z-axis of γ. Using spherical tensors brings a lot of advantages because under rotation, the rank of a spherical tensor operator is invariant. The rotation matrix is defined as

$$D^j_{kl}(\alpha\beta\gamma) = \exp(-ik\alpha)\, d^j_{kl}(\beta) \exp(-il\gamma), \tag{2.38}$$

where $d^j_{kl}(\beta)$ are the reduced Wigner matrices represented by trigonometric functions. Specifically changing the reference frame from PAS (P) to the LAB (L) frame, the spherical tensor component A is given by the summation

$$A^L_{jm'} = \sum_m A^P_{jm} D^j_{mm'} \left(\alpha_{PL}\beta_{PL}\gamma_{PL}\right). \tag{2.39}$$

The Euler angles $(\alpha_{PL}, \beta_{PL}, \gamma_{PL})$ describe the relative orientation between the PAS and the LAB frame. As noted above in section 2.2.1 the transformation from the PAS to the LAB frame is under a rotating frame, in which the xy frame rotates at the rf frequency ω_{rf}. The internal interactions are much smaller than the Zeeman interaction, for this reason the internal interaction (for spins $I = 1/2$) can be considered as a first order perturbation of the Zeeman Hamiltonian. In this case it is possible to apply the secular approximation and only the spin terms which commute with the Zeeman interaction are retained. Specifically, in the laboratory frame, only the A^L_{j0} terms are retained because only when $m = 0$ is the commutator equal to zero. In the laboratory frame, the Hamiltonian can then be described with the remaining terms:

$$\hat{H}^L_A = A^L_{00}\hat{T}_{00} + A^L_{20}\hat{T}_{20}. \tag{2.40}$$

The first is a zero-rank, *i.e.* orientation independent isotropic component, while in the anisotropic second-rank component the magnitude depends on its orientation. In solution-state, the overall tumbling makes the molecule assume all possible orientations, averaging the anisotropic contributions on a short time scale.

2.2.4 Chemical Shielding Interaction

The chemical shielding is generated by the external magnetic field B_0, which induces a current in the electron density of the molecule, leading to the circulating electronic currents generating a magnetic field B_{ind}. The spins experience both the external and the induced magnetic fields generating a local magnetic field:

$$\mathbf{B}^{\mathbf{I}}_{\mathbf{loc}} = \mathbf{B_0} + \mathbf{B}^{\mathbf{I}}_{\mathbf{ind}}, \tag{2.41}$$

where B_{ind} is usually on the order of 10^{-4} with respect to B_0 and it is linearly dependent on B_0:

$$\mathbf{B^{I}_{ind}} = \tilde{\sigma}\mathbf{B_0}, \tag{2.42}$$

where $\tilde{\sigma}$ is the chemical shielding tensor. The use of a 3x3 matrix for the second-rank $\tilde{\sigma}$ tensor takes into the account that B_{ind} has different direction with respect to the applied B_0. The chemical shielding Hamiltonian can be described in the Cartesian form by:

$$\hat{H}_{\sigma}^{PAS} = \gamma\hat{\mathbf{I}}\tilde{\sigma}\mathbf{B_0}. \tag{2.43}$$

The magnitude and direction of B_{ind} at a given nuclear site depends on both orientation of the molecule with respect to the external field and the location of the nuclear spins within the molecule. The chemical shielding tensor can be decomposed into anisotropic and isotropic components, where the isotropic component is invariant under rotation. The isotropic component can be written as the mean of the diagonal terms of the chemical shielding tensor in the PAS frame:

$$\sigma_{iso} = \frac{1}{3}\left(\sigma^{P}_{XX} + \sigma^{P}_{YY} + \sigma^{P}_{ZZ}\right), \tag{2.44}$$

while the anisotropic chemical shielding Δ_{aniso} describes the largest deviation in chemical shielding from the isotropic value:

$$\Delta_{aniso} = \sigma^{P}_{ZZ} - \sigma_{iso}. \tag{2.45}$$

The difference between the other two principal values, is described by the asymmetry term η:

$$\eta = \frac{\sigma^{P}_{XX} - \sigma^{P}_{YY}}{\Delta}, \tag{2.46}$$

which can take values between 0 and 1. Since the chemical shielding is directly proportional to the external magnetic field, to compare the chemical shielding at different fields, they are first compared to a specific resonance in a reference compound. The so-called chemical shift is given in parts per millions (ppm), and is field-independent:

$$\delta_{iso} = \frac{\omega_0^{sample} - \omega_0^{ref}}{\omega_0^{ref}} \times 10^6 = \frac{\sigma^{ref} - \sigma^{sample}}{1 - \sigma^{ref}} \times 10^6. \tag{2.47}$$

Parts per million is used because the magnitude of the chemical shift interaction is relatively small compared to the Larmor frequency, *i.e.*, Hz – kHz compared to MHz, respectively, at typically used B_0 magnetic field strength. Upon rotation of the PAS Hamiltonian, the chemical shielding Hamiltonian in the laboratory frame is equal to:

$$\hat{H}_\sigma = -\omega_0 \left[\sigma_{iso} + \frac{\Delta_{aniso}}{2} \left(3\cos^2\beta_{PL} - 1 + \eta \sin^2\beta_{PL} \cos 2\alpha_{PL} \right) \hat{I}_z \right], \tag{2.48}$$

where α_{PL} and β_{PL} for the Euler angles for the transformation from the PAS to the LAB frame. The angular dependence of the anisotropic terms can be averaged by the magic angle spinning.

2.2.5 Dipolar Coupling Interaction

The interaction of the magnetic fields generated by two different nuclei gives rise to the direct dipole-dipole interaction. It is a through-space interaction characterized both by intramolecular and intermolecular contacts and it is independent from B_0. In Cartesian coordinates, the dipolar coupling spin Hamiltonian is given by:

$$\hat{H}_D = -2\hat{\mathbf{I}}\tilde{\mathbf{D}}\hat{\mathbf{S}}, \tag{2.49}$$

where $\tilde{D}$ is the dipolar coupling tensor and it contains the principal values, $-\frac{d}{2}$, $-\frac{d}{2}$ and $+d$. d is the dipolar coupling constant (in Hz,) and it describes the magnitude of the interaction. In rad s^{-1} the dipolar coupling constant b ($b = 2\pi d$) is equal to:

$$b_{IS} = -\frac{\mu_0}{4\pi} \frac{\gamma_I \gamma_S \hbar}{r_{IS}^3}. \tag{2.50}$$

The dipolar coupling constant scales by the inverse cubed distance between the two nuclei I and S, ${r_{IS}}^3$, while it scales linearly with the gyromagnetic ratio of the two spins, γ_I and γ_S. To describe the interaction, the reference frame needs to be converted from the unit vector between the two nuclei, which represents the PAS, to the laboratory frame. As described in section 2.2.3 the Hamiltonian for the dipolar coupling between two nuclei in PAS shall be stated in spherical tensor form to facilitate the conversion and it is given by

$$\hat{H}_D^P = A_{20}^P \, \hat{T}_{20}, \tag{2.51}$$

where $A_{20}^P = \sqrt{6}\, b_{IS}$. Only an anisotropic part is present and there is no rank 0 term because the dipolar tensor is traceless ($A_{xx} + A_{yy} + A_{zz} = 0$). There are no $\hat{T}_{2,\pm 2}$ terms, since the dipolar interaction is axially symmetric. From equation 2.37, the spatial term in the laboratory frame, and for the secular approximation, is given by

$$A_{20}^{L} = A_{20}^{P}\, D_{00}^{2}\left(\alpha_{PL}\beta_{PL}\gamma_{PL}\right). \tag{2.52}$$

From equation 2.39 only the reduced Wigner matrix term is retained. Hence the spatial term for the dipolar coupling in the LAB frame is equal to

$$A_{20}^{L} = \sqrt{6}\, b_{IS}\frac{1}{2}\left(3\cos^{2}\beta - 1\right). \tag{2.53}$$

with the spin part given by

$$\hat{T}_{20} = \frac{1}{\sqrt{6}}\left(3\hat{I}_z\hat{S}_z - \hat{\mathbf{I}}\cdot\hat{\mathbf{S}}\right). \tag{2.54}$$

Therefore, the secular homonuclear dipolar coupling spin Hamiltonian is equal to

$$\hat{H}_{D,\mathrm{hom}\,o}^{L} = b_{IS}\frac{1}{2}\left(3\cos^{2}\beta - 1\right)\left(3\hat{I}_z\hat{S}_z - \hat{\mathbf{I}}\cdot\hat{\mathbf{S}}\right), \tag{2.55}$$

when the two coupled nuclei are from the same species, the $\hat{I}_x\hat{S}_x + \hat{I}_y\hat{S}_y$ term are present because the two spins, since they precess at similar frequencies, can induce spin transition and so the eigenfunctions of the spin system are linear combination of the degenerate Zeeman levels $|\alpha\beta\rangle$ and $|\beta\alpha\rangle$ states in a two spin system. For the heteronuclear dipolar couplings, when the two coupled nuclei are from two different species the term $\hat{I}_x\hat{S}_x + \hat{I}_y\hat{S}_y$ is zero:

$$\hat{H}_{D,het}^{L} = b_{IS}\frac{1}{2}\left(3\cos^{2}\beta - 1\right)\left(2\hat{I}_z\hat{S}_z\right). \tag{2.56}$$

The presence of the $\hat{I}_x\hat{S}_x + \hat{I}_y\hat{S}_y$ term leads to a range of transition frequencies that results in the broadening of the observed lineshapes. This implies that the Hamiltonian does not necessarily commute with itself at different points in time, and for this reason the magic angle spinning results in being less effective at decoupling in the homonuclear case with respect to the heteronuclear case. This is of particular importance in the case of ^{1}H solid-state NMR, where the narrow chemical shift range together with large numbers of homonuclear coupled spins leads to substantial broadening. Techniques to try and further decouple the homonuclear interaction are developed in Chapter 4.

2.2.6 J-coupling Interaction

The J-coupling interaction is the indirect interaction of the nuclei through electrons. The full Hamiltonian for the J-coupling is described as

$$\hat{H}_J = 2\pi \hat{\mathbf{I}} \tilde{\mathbf{J}}_{\mathbf{IS}} \hat{\mathbf{S}}, \tag{2.57}$$

where $\tilde{\mathrm{J}}_{IS}$ is the J-coupling tensor described by a 3x3 matrix. $\tilde{\mathrm{J}}_{IS}$ contains both isotropic and anisotropic term, however for light elements, such as ^{1}H, ^{13}C and ^{15}N the magnitude of the anisotropic term is usually small compared to dipolar couplings and therefore ignored. For this reason, the J-coupling tensor is normally termed as the scalar coupling, which is independent from the orientation and is given by the average of the diagonal terms of the J-coupling tensor matrix:

$$J_{IS} = \frac{1}{3}\left(J_{xx} + J_{yy} + J_{zz}\right). \tag{2.58}$$

The J-coupling, like dipolar coupling, is independent of the external magnetic field. J-couplings can be used to determined molecular structures, but normally the small magnitude (which is on the order of 100 of Hz) compared to other more dominant interaction in the solid-state, such as dipolar couplings, makes its observation difficult. However, J-coupling can be used in favourable biological samples where the molecular motion renders the line width narrow, or under averaging of the dominant interactions, as will be described later in the INEPT experiment.

2.2.7 Interaction under Magic-Angle-Spinning

The interaction under magic angle spinning implies a further frame transformation. In this case the PAS will be rotated to the rotor frame (R) and from the R frame to the LAB frame (Fig. 2.1).

The conversion from the PAS frame to the LAB (and again considering the secular approximation) considers the intermediate step of the rotor frame using two sets of Euler angles Ω_{PR} and Ω_{RL} and can be then expressed as

$$A_{20}^{L} = A_{20}^{P} \sum_{m'=-2}^{m'=+2} D_{m'0}^{2}(\Omega_{RL}) D_{0m'}^{2}(\Omega_{PR}). \tag{2.59}$$

The Wigner rotation matrix for the rotation from the rotor frame to the laboratory frame is:

$$D_{m0}^{2}(\Omega_{RL}) = e^{im\omega_r t} d_{m0}^{2}(\beta_{RL}). \tag{2.60}$$

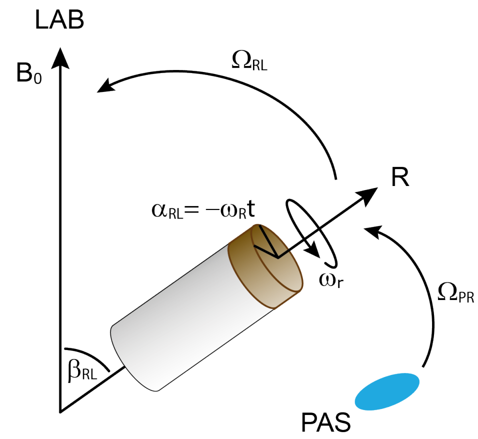

Figure 2.1: Schematic representation of the axis systems and frame transformations used in MAS NMR from the interaction in the principal axis system (PAS), to the rotor frame (R), until the laboratory frame (LAB). The MAS rotor is rotated through the time-dependent angle α_{RL} at frequency ω_r about an axis aligned at an angle of β_{RL} with respect to the external field.

For one rotor period, $2\pi/\omega_r$,

$$\int_0^{2\pi/\omega_r} e^{im\omega_r t} dt, \tag{2.61}$$

if m is a non-zero positive or negative integer, the spatial term averages to 0 after one complete rotor period, while if $m = 0$,

$$A^L_{20} = A^P_{20} D^2_{00}(\Omega_{RL}) D^2_{00}(\Omega_{PR}) = A^P_{20} d^2_{00}(\beta_{RL}) d^2_{00}(\beta_{PR}), \tag{2.62}$$

The orientation is now dependent on the Euler angle β_{RL}, which is the reduced Wigner rotation matrix and is equal to

$$d^2_{00}(\beta_{RL}) = \frac{1}{2}\left(3\cos^2\beta_{RL} - 1\right). \tag{2.63}$$

Setting the rotation of the rotor at an angle $\beta_{RL} = 54.74°$, *i.e.* the magic angle in the Magic Angle Spinning experiments, the spatial term becomes equal to 0. If the NMR signal is not acquired in a rotor synchronised manner, $m \neq 0$ must also be considered, and the spatial tensor in the LAB frame under magic angle spinning becomes equal to

$$A^L_{20} = A^P_{20}\left[\frac{1}{2}\sin^2\beta_{PR}\cos\left(2\gamma_{PR} - 2\omega_r t\right) - \frac{1}{\sqrt{2}}\sin 2\beta_{PR}\cos\left(\gamma_{PR} - \omega_r t\right)\right]\omega_r. \tag{2.64}$$

The consequence of the time-dependence at periodic intervals is the rise of "spinning side bands", which are lineshapes arising at multiple integers of the spinning frequency in Hz. The sidebands decrease in intensity as the spinning frequency increases. Given also the dependence of the spatial tensor on the rotor phase, γ_{PR}, integration over the powder average (from 0 to 2π) gives rise to in-phase spinning sidebands.[105]

2.3 Introduction to NMR Relaxation

In this section, I give a brief overview of NMR relaxation to provide some context for the relaxation measurements. Rather than presenting a comprehensive outline of relaxation theory I only highlight a number of concepts necessary to follow the manuscripts constituting the body of this thesis. For a more systematic treatment I refer the reader to numerous excellent reviews on the matter.[4,74] In an NMR experiment after rf pulses perturb the equilibrium magnetisation, the spins will not remain in the non-equilibrium state indefinitely, but rather they will eventually return to their original state. The process by which the spins return to the equilibrium state governed by the Boltzmann distribution is called relaxation. Relaxation occurs due to fluctuating magnetic fields which drive transitions between the spin energy levels restoring their populations to their equilibrium values. In NMR, the fluctuating magnetic fields driving the transitions between the energy levels arise from changes in orientation of molecules or parts of molecules due to molecular motions that modulate orientation dependent anisotropic interactions. For spin-1/2 nuclei, the main anisotropic interactions that contribute to relaxation are the dipolar coupling and chemical shift anysotropy, CSA. The process of return towards the thermal equilibrium for the longitudinal component of the magnetisation is governed by so called spin-lattice (or longitudinal) relaxation with a characteristic time T_1. The process of return towards the thermal equilibrium for the transverse component of the magnetisation is governed by so called spin-spin (or transverse) relaxation with a characteristic time T_2. The relaxation rates are simply given by the inverses of the appropriate relaxation times

$$R_x = \frac{1}{T_x} \tag{2.65}$$

where x is the index associated with the different relaxation types. In semi-classical theory, in order to quantify the effect of stochastic modulation of anisotropic interactions by molecular motions, the concept of a correlation function is used. The correlation function describes fluctuation of a magnetic field as function of time. It describes how the interaction of interest is correlated with itself as a function of the time separation between the sampling points, τ:

$$c(\tau) = c(t_1 - t_2) = \overline{B(t_1)B(t_2)} \tag{2.66}$$

where the overbar indicates ensemble average. A Fourier transform of a correlation function yields spectral density, which describes the fluctuations as a function of frequency that can be linked to the specific transitions between the spin energy levels and hence the relaxation rates.

Relaxation rates are linked to the probabilities of transitions between relevant energy levels for NMR spin system.

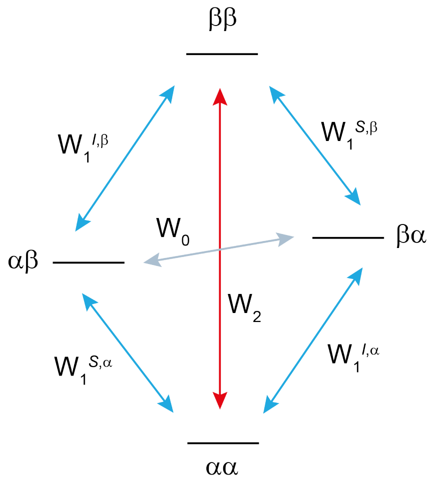

Figure 2.2: Energy level diagram for a two-spin system; the energy levels are labelled with the spin I as the first spin and S the second spin. The arrows show the possible relaxation induced transitions: four single-quantum transitions (light blue), a double-quantum transition (red), and a zero-quantum transition (grey).

For example, for two spins, I and S, coupled via dipolar coupling there are a total of six possible transition between spin states: zero quantum, W_0; single quantum, W_1; and double quantum transitions, W_2 (Fig. 2.2). In the case of longitudinal relaxation, T_1, via dipolar coupling involving two spins I and S, the rate of change of the population of the state $\alpha\alpha$, where the change of the population from its equilibrium value $(p_{xx} - p^0_{xx})$, is equal to

$$\begin{aligned}\frac{dp_{\alpha\alpha}}{dt} = -W_1^{I,\alpha}\left(p_{\alpha\alpha} - p^0_{\alpha\alpha}\right) - W_1^{S,\alpha}\left(p_{\alpha\alpha} - p^0_{\alpha\alpha}\right) - W_2\left(p_{\alpha\alpha} - p^0_{\alpha\alpha}\right) + \\ + W_1^{I,\alpha}\left(p_{\beta\alpha} - p^0_{\beta\alpha}\right) + W_1^{S,\alpha}\left(p_{\alpha\beta} - p^0_{\alpha\beta}\right) + W_2\left(p_{\beta\beta} - p^0_{\beta\beta}\right)\end{aligned} \tag{2.67}$$

Similar equations can be written for the changes in the other population states. The transition probabilities for spin I and S are grouped together and redefined to link them to the relaxation rates in Solomon equations.

$$R^I_{auto} = W_1^{I,\alpha} + W_1^{I,\beta} + W_2 + W_0 \tag{2.68}$$

$$R^S_{auto} = W_1^{S,\alpha} + W_1^{S,\beta} + W_2 + W_0 \tag{2.69}$$

The full set of equations can be rewritten in term of z-magnetization (I_{z} and S_{z}) instead of population states, and combinations of various transition probabilities redefined by relaxation rates

$$\frac{dI_z}{dt} = -R^I_{auto}(I_z - I_z^0) - \sigma_{IS}(S_z - S_z^0) \tag{2.70}$$

$$\frac{dS_z}{dt} = -R^S_{auto}(S_z - S_z^0) - \sigma_{IS}(I_z - I_z^0) \tag{2.71}$$

where the magnetisation on spin I_{z} will be affected by the transitions where I_{z} changes between α and β, *i.e.*, $\alpha\alpha$-$\beta\alpha$ and $\alpha\beta$-$\beta\beta$:

$$I_z = (p_{\alpha\alpha} - p_{\beta\alpha}) + (p_{\alpha\beta} - p_{\beta\beta}) \tag{2.72}$$

The same concept is applied to the spin S_{z}, for transitions $\alpha\alpha$-$\alpha\beta$ and $\beta\alpha$-$\beta\beta$:

$$S_z = (p_{\alpha\alpha} - p_{\alpha\beta}) + (p_{\beta\alpha} - p_{\beta\beta}) \tag{2.73}$$

and to their equilibrium values ${I_{\mathrm{z}}}^0$ and ${S_{\mathrm{z}}}^0$:

$$I_z = (p^0_{\alpha\alpha} - p^0_{\beta\alpha}) + (p^0_{\alpha\beta} - p^0_{\beta\beta}) \tag{2.74}$$

$$S_z = (p^0_{\alpha\alpha} - p^0_{\alpha\beta}) + (p^0_{\beta\alpha} - p^0_{\beta\beta}) \tag{2.75}$$

R^{auto} is the auto relaxation rate for the spins I and S and describes the rate which the magnetization returns to its equilibrium by dissipating polarization to the environment. σ_{IS} is the cross-relaxation and described the magnetization transfer from spin I and S and vice versa. Cross-relaxation will not be treated in this thesis. The relaxation rate constants, R^{auto} and σ_{IS}, introduced in the previous section in terms of transition probabilities, may be written in terms of the spectral density function. The transition probabilities, W_0, W_1 and W_2 are related to the spectral density sampled at their respective transition frequencies, through the equation:

$$W_0 = \frac{1}{10}b^2 J(\omega_{0,I} - \omega_{0,S}), \quad W_1 = \frac{3}{20}b^2 J(\omega_{0,I}), \quad W_2 = \frac{3}{5}b^2 J(\omega_{0,I} + \omega_{0,S}) \tag{2.76}$$

where b is the dipolar coupling constant (equation 2.50). Combining all of the above, the longitudinal relaxation rate due to fluctuation of dipolar relaxation, $R_{1,DD}$, could be written as:

$$R_{1,DD} = \frac{1}{10} b^2 \left\{ 3J\left(\omega_{0,I}\right) + 6J\left(\omega_{0,I} + \omega_{0,S}\right) + J\left(\omega_{0,I} - \omega_{0,S}\right) \right\} \tag{2.77}$$

. Analogously, following similar process for the chemical shift anisotropy, its contribution to the longitudinal relaxation rate could be written as:

$$R_{1,CSA} = \frac{2}{15} {\omega_0}^2 \left(\sigma_{11}^2 + \sigma_{22}^2 + \sigma_{33}^2 - \sigma_{11}\sigma_{22} - \sigma_{11}\sigma_{33} - \sigma_{22}\sigma_{33} \right) J\left(\omega_0\right), \tag{2.78}$$

where σ_{xx} are the components of the chemical shielding tensor. Because longitudinal relaxation rates are related to the probabilities of transitions at Larmor frequency and combination of Larmor frequencies, these rates probe motions on timescale of ps-ns. However, other relaxation rates sensitive to motions at other time scales can be defined. For example, $R_{1\rho}$ is spin-lattice relaxation in the rotating frame that is sensitive to slower motions with correlation times of nanoseconds to milliseconds. $R_{1\rho}$ is measured under the application of a variable length spinlock pulse. In solid-state $R_{1\rho}$ is often the choice of relaxation rate to probe slow motions because decay of transverse magnetisation is typically dominated by coherent effects, which are not related to molecular motions. In general, separation of incoherent effects related to the molecular motions and coherent effects not related to the molecular motions is one of the major challenges for quantification of molecular motions based on relaxation rates measurements. However, discussion of this is beyond the scope of this thesis. In specific case of $R_{1\rho}$, the coherent effects might be sufficiently supressed by combination of fast spinning, application of rf or/and appropriate sample preparation. For example, in ^{15}N $R_{1\rho}$ measurements the coherent contributions can be sufficiently suppressed by a $>$ 10 kHz spinlock pulse and $>$ 45 kHz MAS even in fully protonated proteins.[76] Derivation of expressions for $R_{1\rho}$ are a little bit more involved than those for R_1, especially because spinning frequency, ω_r, and spinlock frequency, ω_1, need to be included in the treatment. For illustration purposes the dipolar contribution to $R_{1\rho}$ can be expressed as:

$$\begin{aligned} R_{1\rho,DD} = \frac{1}{20} b^2 \{ & \frac{2}{3} J\left(\omega_1 + 2\omega_r\right) + \frac{2}{3} J\left(\omega_1 - 2\omega_r\right) + \frac{4}{3} J\left(\omega_1 + \omega_r\right) + \frac{4}{3} J\left(\omega_1 - \omega_r\right) + \\ & + 4J\left(\omega_1\right) + 3J\left(\omega_{0,S}\right) + J\left(\omega_{0,I} - \omega_{0,S}\right) + 6J\left(\omega_{0,I}\right) + 6J\left(\omega_{0,I} + \omega_{0,S}\right) \} \end{aligned} \tag{2.79}$$

and CSA contribution can be expressed as:

$$R_{1\rho,CSA} = \frac{1}{45} {\omega_{0,I}}^2 \left(\sigma_{11}^2 + \sigma_{22}^2 + \sigma_{33}^2 - \sigma_{11}\sigma_{22} - \sigma_{11}\sigma_{33} - \sigma_{22}\sigma_{33} \right) \left\{ 4J\left(\omega_1\right) + 3J\left(\omega_{0,I}\right) \right\} \tag{2.80}$$

In all the cases discussed so far, in order to evaluate relaxation rates, one needs to evaluate spectral densities at specific frequencies. In most cases, because the explicit form of correlation function is not known, explicit expressions for spectral density are not known. To overcome this problem and in order to quantify relaxation rates in terms of parameters of motion including correlation time and amplitude, there are a number of motional models to approximate the correlation function and spectral density. One such popular models is the so called Simple Model Free (SMF) approach developed by Lipari and Szabo.[106] In this approach, the correlation function in the presence of single time scale motion is expressed as

$$c_{SMF}(t) = S^2 + (1 - S^2)e^{-\frac{t}{\tau_c}}, \tag{2.81}$$

where S^2 is order parameter describing amplitude of motion and τ_c is the correlation time. S^2 goes from 0 to 1 where 0 represents completely unrestricted motions and 1 the completely rigid case. The corresponding spectral density function $J(\omega)$, calculated as the Fourier transform of the correlation function, is given as

$$J(\omega) = (1 - S^2)\frac{\tau_c}{1 + (\omega\tau_c)^2}, \tag{2.82}$$

where the two parameters are as discussed previously. It has been shown that in solid-state NMR, motions occurring on two or more time scales are required to adequately model the dynamics.[41] Therefore, typically, a more appropriate is application of an extension of the SMF: Extended Model Free (EMF) approach, where the contributions of motions occurring on two (or more) distinct time scales are considered.[107,108] The EMF spectral density is expressed as:

$$J(\omega) = (1 - {S_f}^2)\frac{\tau_f}{1 + (\omega\tau_f)^2} + (1 - {S_s}^2)\frac{\tau_s}{1 + (\omega\tau_s)^2} \tag{2.83}$$

where S_f^2 and S_s^2 are the order parameters related to fast and slow motion, respectively, and τ_f and τ_s are the correspective correlation times. The model can become even more complicated,[5,109] and involve more parameters. Probing motions over a large number of frequencies is necessary to have a complete overview of dynamics. Obtaining sufficient relaxation rate measurements can be very time-consuming. In order to make quantification of dynamics using relaxation rates more practical in this thesis, I present two approaches to accelerate acquisition of relaxation rates.

Chapter 3

NMR Experimental Methods

This chapter describes the experimental techniques used in this work. Firstly, the chapter will introduce signal detection by quadrature detection, as well as coherence selection by phase cycling and one- and multi-dimensional experiments. Then the discussion will break down the newly developed methods described in this thesis into separate components that can be found in the literature. Fully stylised pulse programs relating to papers arising from this thesis will be detailed in each section.

3.1 Signal detection

Only single quantum coherence of the order $p = 1$ can be directly observed in NMR, and the x- and y-components of the magnetization are detected. The signal is acquired with a real and imaginary part in a complex function:

$$S(t) = S_x + iS_y, \tag{3.1}$$

which is equal to

$$S(t) = S_0 \cos \Omega t \, e^{\frac{-t}{T_2}} + iS_0 \sin \Omega t \, e^{\frac{-t}{T_2}} = S_0 \, e^{i\Omega t} e^{\frac{-t}{T_2}}, \tag{3.2}$$

where, S_0 is the maximum signal and Ω is the resonance offset. T_2 is the spin-spin relaxation, which describes the loss of coherence in the transverse plane. The signal in the time-domain is converted into the frequency domain by Fourier transform:

$$S(\omega) = \int_0^{+\infty} S(t) \, e^{(-i\omega t)} dt = \frac{1/T_2}{(1/T_2)^2 + (\omega - \Omega)^2} - i \frac{\omega - \Omega}{(1/T_2)^2 + (\omega - \Omega)^2}. \tag{3.3}$$

The real part of the signal is an absorptive Lorentzian lineshape, while the imaginary part is a dispersive Lorentzian lineshape (see Fig. 3.1). It is not possible to cancel out one of the two, but it is possible to phase the spectrum such that absorptive lineshapes are shown, which are preferable for obtaining the smaller linewidth, i.e. peaks in the resulting spectrum are better resolved.

The method to achieve frequency discrimination in signal detection is called quadrature detection. Practically speaking, to detect both the x- and y- components of the magnetization, the signal from the coil is mixed down with two different reference frequencies (sin and cos) to obtain the two orthogonal components of the precessing magnetization. The two outputs are digitalized separately becoming the real and imaginary part of the signal.

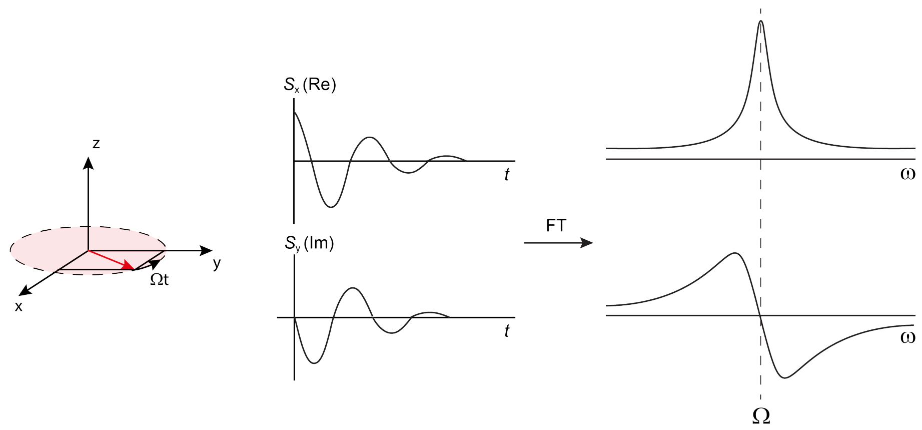

Figure 3.1: Schematic illustration of the real (Re) and imaginary (Im) components of the net magnetisation vector, the complex FID, and the absorptive (top) and dispersive (bottom) Lorentzian lineshapes obtained by Fourier transform.

3.2 Multidimensional NMR

A multidimensional NMR experiment can be simply described in four steps: preparation, evolution t_1, mixing and detection. Firstly, during the preparation step, coherence is generated by a single $\pi/2$ pulse and the magnetization can be transferred to the nuclei of interest via cross-polarization (if the nuclei of interest have low γ). During the evolution period t_1, the system is let free to evolve under a resonance offset and the mixing pulse is used to reconvert the n-order coherence into a detectable coherence, which is acquired during t_2. The second dimension is built by varying the length of t_1 by finite steps Δt_1, while repeating the experiment, obtaining a 2D map of frequency. In the direct dimension the frequency is detected during t_2, while in the indirect dimension during t_1. In the case of 3 (or more) dimensions, the simple block formed by the four parts will be repeated. The third frequency dimension is represented by a second evolution t_2. Second and third dimension can measure same or different interactions on different nuclei or different interactions the same nucleus. In this thesis, the two indirect dimension will be named t_1 and t_1', and they detect the chemical shift evolution on two different nuclei (see Fig. 3.2). To optimize the experimental time, it is possible to let the chemical shift evolve simultaneously on both the nuclei in a t_1 shared evolution. Further, I will present how the excitation of coherence for the third nucleus can be exploited by re-excitation of nested magnetization or from a separated excitation, in the first case, the initial excitation is done by a simultaneous excitation of both the nuclei through simultaneous cross-polarization, SIM-CP. The detections t_2 and t_2' can be achieved with a sequential acquisition on ^{1}H.

3.3 Phase cycling

Phase cycling is used to select the coherence pathway of an experiment. The phase cycling is based on the principle that if a pulse causes a change in coherence order from p_1 to p_2 ($\Delta p = p_1 - p_2$), then shifting the phase of the pulse by $\Delta\phi$ results in the coherence acquiring a phase shift of $\Delta p \cdot \Delta\phi$. This means that different Δp changes will have a different phase shift and in this way it would be possible to differentiate among pathways. Practically this means that the experiment will be repeated with different $\Delta\phi$, and then combining the results and depending on the phase set on the receiver, they will add up (desired coherence selection) while the un-desired coherences will cancel out.

3.4 Spectral Sensitivity and Experimental Time

NMR is an inherently insensitive technique, and the signal is proportional to the cube of the gyromagnetic ratio of the nuclei and B_0. Further, it depends on the relative natural abundance of the isotopes. For example, ^{1}H are characterized by high natural abundance ($\approx$ 99.97%) and gyromagnetic ratio, while nuclei such as ^{13}C and ^{15}N have a low natural abundance, 1.10% and 0.4%, respectively, and low γ, $\approx\gamma^1$H/4 for ^{13}C and $\approx\gamma^1$H/10 for ^{15}N. Even though ^{12}C is the most abundant isotope for carbon, it cannot be employed in NMR because it is not inherently magnetic, $I = 0$. On the other hand, ^{14}N, even though magnetic, has a spin quantum number $I = 1$, which introduces quadrupolar broadening and quadrupolar induced shift

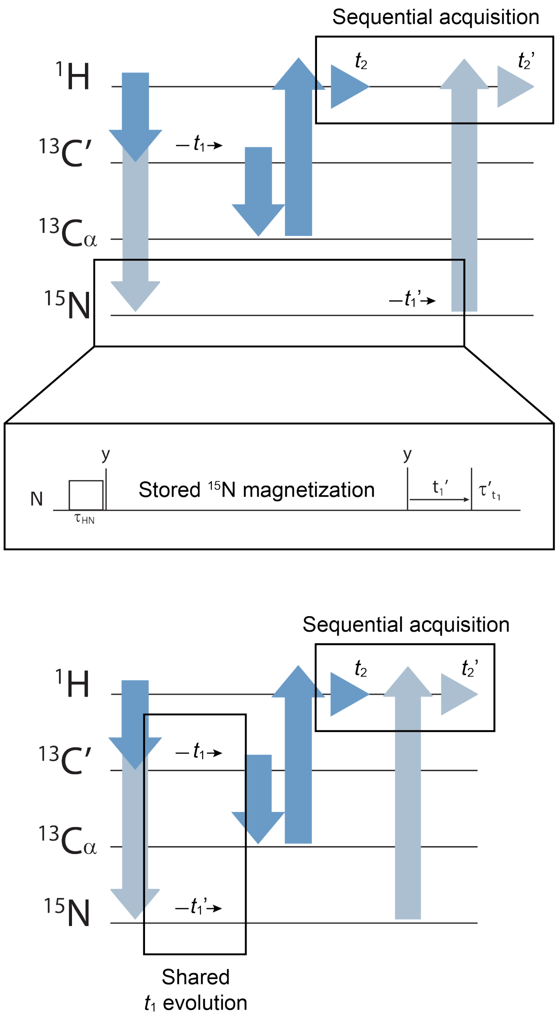

Figure 3.2: Schematic illustration of elements presented in section 3.2. After the simultaneous magnetization transfer on ^{13}C and ^{15}N, the t_1 evolution can be exploited with a shared-time or the magnetization stored and retrieved later, detecting with a sequential acquisition on ^{1}H.

associated with quadrupolar interaction, rendering it not suitable for site specific detection. To enhance the sensitivity, the experiment is repeated and the resulting transients co-added, n times, to increase the Signal to Noise Ratio (SNR), which grows proportionally to $\sqrt{n}$. The use of coadded transients is, as well, linked to coherence selection by phase cycling. The experiment is repeated only after the nuclei spins are back to the equilibrium and this waiting time is called the recycle delay. For a 1D experiment, the experimental time is given by the length of the experiment and the recycle delay multiplied by the number of coadded transients. For a 2D measurement, the experiment is repeated by building the t_1, therefore the experimental time scales up with the number of Δt_1, and it depends on the spectral width, which is normally chosen on the basis of the frequency range of interest. The same happens for a 3D experiment where the experimental time needs to take into account the second t_1' and its building blocks. The recycle delay is normally equal to 5 times the spin-lattice relaxation, T_1, to have a better balance of coadded transients and experimental time, the recycle delay can be equal to 1.3 * T_1. However, in the case of relaxation measurement, to obtain a reliable report on the relaxation, and so motions, it must be ensured that the spins are completely relaxed. T_1 can vary from a few ms to minutes and hours, depending on the motions of the sample, so the recycle delay could take a long period of time. For this reason, various methods can be used to reduce the waiting time. A method presented in this thesis involves the use nested experiments on two different nuclei, ^{13}C and ^{15}N, to share only one recycle delay between them, reducing the experimental time.

3.5 Proton Detection and Heteronuclear Correlation

As discussed above, the sensitivity depends on different factors, such as isotope natural abundance and gyromagnetic ratio. At fast spinning, sample quantities are limited, which means that direct acquisition on rare or low γ nuclei becomes more challenging. ^{1}H detection then can become a huge asset owing to the fact that at fast spinning, linewidths are narrower, such that direct acquisition is possible. For small rigid molecules, 60 kHz MAS is not enough to average out ^{1}H-^{1}H dipolar couplings and different schemes can be applied to narrow the linewidth. Biomolecules, which are more mobile, have a better resolution, in general. However, acquiring ^{13}C-^{1}H correlation experiments still requires extensive deuteration. Protons are used for the initial magnetization enhancement of low γ nuclei. Furthermore, ^{13}C and ^{15}N typically have longer longitudinal relaxation times, and so acquiring direct excitation experiments (for example one-pulse experiments) would be time consuming. Protons, instead, have shorter spin-lattice relaxation, allowing a more rapid repeat of the experiments. Generally, for spin-1/2 nuclei, two different ways are used to transfer polarization in both directions ($^1\text{H} \rightarrow X$ and back $X \rightarrow {}^1\text{H}$ transfer), which depend on the mobility of the molecules: Cross Polarization (CP)[14] and Insensitive Nuclei Enhanced by Polarization Transfer (INEPT).[15,16,110] The first is based on through-space interactions and relies on dipolar couplings, so it is more efficient for magnetization transfer in samples where the dipolar couplings are not completely averaged by molecular motion, so rigid or ordered ones. The second is a through-bond coherence transfer method based on J-couplings which is used in solution NMR and mobile samples. J-coupling based methods can be used in rigid solids, but in that case, the dominant interaction is the dipolar coupling, which leads to rapid coherence dephasing unless homonuclear decoupling is applied. During CP both the ^{1}H and X channels are irradiated, and the amplitude of the rf pulses has to match the Hartmann-Hahn conditions[14] to allow the magnetization transfer. Considering that the nutation frequency

$$\omega_1 = -\gamma B_1, \tag{3.4}$$

in a static experiment, the Hartmann-Hahn conditions are satisfied if:

$$\gamma_I B_1^I = \gamma_S B_1^S, \tag{3.5}$$

where I and S are the nuclei of interest with their respective gyromagnetic ratios. While under magic-angle spinning:

$$\gamma_I B_1^I \pm \gamma_S B_1^S = n\omega_r, \tag{3.6}$$

where n is a positive integer number 1, 2... and ω_r is the MAS rate in rad s^{-1}. Owing to RF inhomogeneities, it is not always possible to achieve this match condition across the whole sample, so typically a ramp[111] is used on one of the two channels. The amplitude of the ramp pulse is changed within a certain percentage (for example 70- 100%) and the average frequency is the match condition. As said above the CP transfer is based on the dipolar coupling between the two nuclei, so the resulting signal will depend on that, meaning that this method is not quantitative. The length of CP pulses, the contact time, depends on the inverse of the dipolar couplings between the two nuclei of interest and so it is also proportional to the distance in space. For example in the back X $\rightarrow$^{1}H transfer it is possible to choose the contact time to have a specific one-bond transfer (e.g.^{13}Cα $\rightarrow$^{1}Hα $\tau \approx 150\mu$s). In the case of irradiation of multiple magnetization pathways, the magnetization transfer can be done simultaneously with a SIM-CP, or separately by nesting experiments.

For describing the INEPT experiments based on scalar couplings, it is useful to introduce the product operator formalism.[101] The approach is useful for coupled spin systems, where the matrix representation can become complicated, and it works well with weak coupling ,i.e., J-couplings. For an isolated spin-1/2, four operators are required to described the NMR experiment: $1/2E$, I_x, I_y, I_z. where E is the identity operator, and I_x, I_y, I_z describes the magnetization along the respective axes in the rotating frame. The effect of a single rf pulse and evolution of coherence under resonance offset Ω can be described with trigonometry rules. Specifically, the INEPT experiment for spin I and S can be described as followed. At the beginning of the refocused INEPT element, the in-phase magnetization $\hat{I}_x$ is along the transverse plane after a $\pi/2$ pulse. During the first echo period, τ_1, the J-coupling is evolving under resonance offset and the in-phase magnetization is converted into anti-phase $\hat{I}_y \hat{S}_z$:

$$\hat{I}_x \xrightarrow{\tau_1-\pi-\tau_1} \cos\left(2\pi J_{IS}\tau_1\right) \hat{I}_x + \sin\left(2\pi J_{IS}\tau_1\right) \hat{I}_y \hat{S}_z \ , \tag{3.7}$$

where J_{IS} represents the J-coupling between $\hat{I}$ and $\hat{S}$. The anti-phase coherence is transferred from S to I with the $\pi/2$ pulses applied on both channels, which separates the two spin-echo evolution periods:

$$\sin\left(2\pi J_{IS}\tau_1\right) \hat{I}_y \hat{S}_z \xrightarrow{(\pi/2)\hat{I}_x} \xrightarrow{(\pi/2)\hat{S}_x} \sin\left(2\pi J_{IS}\tau_1\right) \hat{I}_z \hat{S}_y \ . \tag{3.8}$$

Following τ_1, in the second echo period , τ_2, the antiphase ^{1}H coherence is converted into in-phase $\hat{S}_x$ that is then detected during t_2.

$$\sin\left(2\pi J_{IS}\tau_1\right) \hat{I}_z \hat{S}_y \xrightarrow{\tau_2-\pi-\tau_2} \sin\left(2\pi J_{IS}\tau_2\right) \sin\left(2\pi J_{IS}\tau_1\right) \hat{S}_x \ . \tag{3.9}$$

The product-operator analysis predicts the maximum transfer, for $sin(\pi/2)$,i.e.,τ $= 1/\left(4J_{IS}\right)$. In an ideal situation, the signal build-up only depends on J-coupling, however during the echo period the spins are subjected to loss of coherence defined as the spin-echo dephasing time T_2' which determines a faster signal decay. To increase the possibility to observe a through-bond transfer in solids even at fast spinning, the dipolar coupling can be averaged by the application of ^{1}H homonuclear dipolar decoupling on the ^{1}H channel. The use of both CP and INEPT, with associated pulse sequences, will be illustrated in the following chapters.

3.6 CRAMPS

Combined Rotation and Multiple-Pulse Spectroscopy (CRAMPS) is a technique used to enhance the resolution and sensitivity of a spectrum. CRAMPS can be carried out as a 1D or 2D experiment and the acquisition is built with alternate periods of acquisition windows and pulses (see Fig. 3.3). During the pulsing period, ^{1}H homonuclear decoupling is applied to average the ^{1}H-^{1}H dipolar couplings, improving sensitivity and resolution of the spectrum. During the acquisition, the chemical shift evolves and can be directly detected, so the resulting spectrum under ^{1}H homonuclear decoupling will be scaled. Generally speaking, during the acquisition window, the amplifier is off and the receiver is open, and, for each acquisition windows, a constant number of complex data points is acquired. The dwell time and so the spectral width, is set by the actual acquisition time, determined by the sum of the acquisition windows. When the points are acquired, the receiver is closed, and the amplifier is turned on. Between these two, a ringdown/dead time is allowed for the spectrometer to physically enable the operation, avoiding pulsing while the receiver is still open (Fig. 3.3). A drawback of the experiment is that generally, ^{1}H homonuclear decoupling must be applied with high nutation frequencies to average the strong ^{1}H-^{1}H dipolar couplings, which can be detrimental for the apparatus. The total acquisition time is limited, and the sum of the acquisition windows is shorter than a normal acquisition, which can lower the sensitivity. Furthermore, the high nutation frequency required make the employment of this method difficult in biological NMR, where the high temperature generated by the *rf* can degrade the sample. The use of CRAMPS will be shown in Chapter 5.

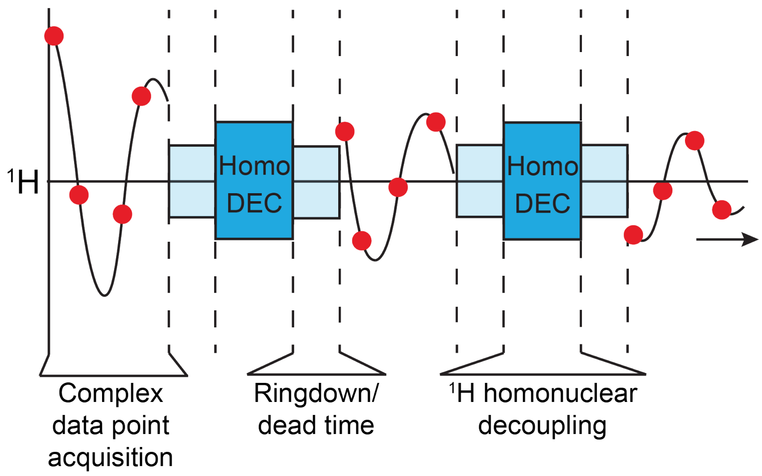

Figure 3.3: Schematic illustration of the CRAMPS experiment in acquisition, red dots indicate the number of complex data points, constant for each acquisition window.

3.7 Relaxation Experiments

In this thesis, two relaxation measurements are taken into consideration: R_1 and $R_{1\rho}$ for nuclei present in the peptide plane, such as ^{13}C and ^{15}N. In the case of relaxation experiments, we often refer to them as pseudo-XD experiments.[112] In the case of a pseudo-3D experiment, a second dimension is dedicated to the t_1 chemical shift evolution, and a third pseudo-dimension contains a list of increasing relaxation delays (T_1) or spinlock ($T_{1\rho}$) times. Every 2D spectrum of the 3rd dimension will be recorded with a specific time point of the list. Having a pseudo-3rd dimension allows the relaxation to be monitored in a residue-specific manner. To measure relaxation on sparse low gamma nuclei it is necessary to use cross polarization, to enhance the sensitivity on these nuclei. An additional benefit of this procedure, as explained in section 3.4, is that the repetition of the experiment will be linked to ^{1}H T_1, and not the X nucleus. In the R_1 experiment after CP, it is not possible to take advantage of inversion recovery or saturation recovery as it is typical for ^{1}H. Instead, the "Torchia" method[113] is used, where a two-step phase cycle cancels out the direct X-spin Boltzmann magnetization, enabling the enhanced magnetization to be monitored. A variable delay list is applied, and the enhanced X magnetization is allowed to relax to the equilibrium.

Typically, the integral of the non-overlapping peaks is recorded and the data at different t delay time list will be fitted to the following mono-exponential equation

$$M_t = M_0 e^{-\frac{t}{T_1}}. \tag{3.10}$$

While relaxation is multi-exponential, the mono-exponential fit is a good approximation if we take in consideration the first part of the relaxation slope until 60% of the decay.[80] The $R_{1\rho}$ measurement is carried out with variable spinlock pulse lengths, with nutation frequencies that can span from few Hz until tens of kHz, and the decay of magnetization treated in same way as described by Equation 3.10.

Chapter 4

Statement of contribution

Chapter 5, Page 34. ^{15}N-^{1}H through-bond heteronuclear correlation solid-state NMR spectroscopy with ^{1}H homonuclear decoupling at 60 kHz MAS. All work by thesis author under supervision, paper writing by thesis author and others.

Chapter 6, Page 71. Accelerating ^{15}N and ^{13}C R_1 and $R_{1\rho}$ relaxation measurements by multiple pathway solid-state NMR experiments.Pulse sequence development by thesis author and others. Acquisition of experiments and data analysis by thesis author. Paper writing by thesis author and others.

Chapter 7, Page 90. Slice and Dice: Nested Spin-lattice Relaxation Measurements. Pulse sequence development and python code by others. Section of pulse program output in the python program by thesis author. Acquisition of experiments and data analysis by thesis author. Paper writing by thesis author and others.

Chapter 5

^{15}N-^{1}H Through-Bond Heteronuclear Correlation Solid-State NMR Spectroscopy with ^{1}H Homonuclear Decoupling at 60 kHz MAS

^{15}N-^{1}H through-bond heteronuclear correlation solid-state NMR spectroscopy with ^{1}H homonuclear decoupling at 60 kHz MAS*

Jacqueline Tognetti[1,2], W. Trent Franks[1,2], Józef R. Lewandowski[1], Steven P. Brown[2#]

1. *Department of Chemistry, University of Warwick, Coventry CV4 7AL, United Kingdom*
2. *Department of Physics, University of Warwick, Coventry CV4 7AL, United Kingdom*
   # email: S.P.Brown@warwick.ac.uk

** Dedicated to Shimon Vega (1943-2021)*

Abstract

Phase modulated Lee-Goldburg (PMLG) homonuclear decoupling in solid-state nuclear magnetic resonance at 60 kHz magic-angle spinning (MAS) is implemented in ^{1}H-detected ^{15}N-^{1}H heteronuclear correlation NMR experiments. Through-bond refocused INEPT experiments are considered, where the initial ^{15}N transverse magnetisation is generated by ^{1}H-^{15}N cross polarisation (CP). Two PMLG-block types, $PMLG5_{mm}^{\bar{x}x}$ and $PMLG9_{mm}^{\bar{x}x}$, were tested for a moderate ^{1}H nutation frequency of ~100 kHz or less utilizing Combined Rotation And Multiple Pulse Sequence (CRAMPS) and spin-echo ^{1}H experiments. A protocol for the optimisation of ^{1}H homonuclear decoupling with respect to ^{1}H nutation frequency, resonance offset, and the cycle time is presented, observing the effect on the scaling factor λ_{CS}, ^{1}H coherence spin-echo lifetime, and the coherence transfer efficiency of the Refocused INEPT pulse sequence. Optimum performance is observed with the application of windowed PMLG, $PMLG5_{mm}^{\bar{x}x}$, during the spin-echoes, corresponding to a high scaling factor (λ_{CS}) of 0.82, where the ratio of the rotor period to the decoupling cycle time, $\Psi = \tau_r / \tau_c$, is 0.57. With these parameters, it is possible to acquire a 2D natural abundance ^{15}N-^{1}H correlation spectrum on the dipeptide β-AspAla, and the pharmaceutical cimetidine at 60 kHz MAS based on the through-bond (J-coupling) ^{15}N → ^{1}H transfer.

1. Introduction

Direct ^{1}H detection is increasingly important for solid-state NMR study of pharmaceuticals[1-4] and biological molecules.[5-8] The availability of ever faster Magic Angle Spinning (MAS) frequencies reduces line broadening due to ^{1}H homonuclear dipolar couplings.[9-14] In particular, ^{1}H detection is advantageous for the identification of specific correlations to nuclei with low gyromagnetic ratio, γ, such as the two natural-abundant isotopes of nitrogen, ^{14}N and ^{15}N. Our focus here is on the spin I = 1/2 ^{15}N, though it is to be noted that there is increasing application of ^{14}N-^{1}H experiments for the much higher natural abundance (99.6%) spin I = 1 nucleus.[15-22] The low sensitivity of ^{15}N, associated with its low natural abundance and gyromagnetic ratio, can be overcome by the use of ^{15}N-^{1}H correlation experiments with proton acquisition, thanks to the high natural abundance and γ that characterise protons, provided that fast MAS can achieve sufficient ^{1}H line narrowing.[23-26] We note that an ^{15}N-detected MAS-*J*-HMQC ^{1}H-^{15}N two-dimensional spectrum has also been recorded at natural abundance and 12.5 kHz MAS using Frequency Switched Lee-Goldburg (FSLG) ^{1}H homonuclear decoupling.[27] ^{1}H-detected heteronuclear ^{15}N-^{1}H correlation experiments can be achieved by inverse polarization, CP, as applied to small molecules[23,25,26,28-30] and ^{15}N-labelled proteins as a hNH experiment.[31-33] An alternative to CP-based dipolar-mediated through-space transfer is a *J*-coupling mediated through-bond refocused INEPT solid-state NMR experiment.[34-37] Specifically, we consider the CP-Refocused INEPT correlation experiment,[38,39] whereby J-coupling mediated ^{15}N-^{1}H back-transfer ensures only the observation of peaks due to through-bond transfer in a ^{15}N-^{1}H spectrum.[26] However, fast dephasing due to strong ^{1}H homonuclear dipolar couplings shortens ^{1}H coherence lifetimes, reducing sensitivity, making *J*-coupling based experiments challenging. Even 60 kHz MAS is not sufficient to completely average out ^{1}H homonuclear dipolar couplings.[40] The application of ^{1}H homonuclear decoupling[41-44] under fast MAS during the ^{15}N-^{1}H coherence transfer improves sensitivity sufficiently for refocused INEPT transfer.[26,39]

While a large number of ^{1}H homonuclear decoupling schemes have been optimised under static conditions for operation at low (5-10 kHz) and moderate (~15 kHz) MAS frequencies;[41-54] there have only been a few papers presenting ^{1}H homonuclear decoupling at faster MAS frequencies of (35+ kHz)[55,56] and (60+ kHz).[57-62] ^{1}H homonuclear decoupling is clearly not being applied under quasi-static conditions under such fast MAS and the performance is dependent upon the ratio between the rotor period, τ_r, and the cycle time of the ^{1}H homonuclear decoupling, τ_c. Lee-Goldburg[45,46,49,59] and DUMBO[50,62] based decoupling are characterized by short cycle times which makes them compatible with faster MAS implementations. Nevertheless, a short cycle time means high ^{1}H nutation frequencies, ν_1, for the scheme which can be demanding on the instrumentation. In this work, we employ phase modulated Lee-Goldburg (PMLG)[49] in a 1D ^{1}H Combined Rotation and Multiple-Pulse Sequence (CRAMPS)[63] experiment at 60 kHz MAS using relatively low nutation frequencies. The performance of PMLG depends on multiple factors such as the type of PMLG-block, frequency offset, and ^{1}H nutation frequency.[41,42,53,54] ^{1}H homonuclear decoupling sequences are usually evaluated through three principal parameters: the chemical shift scaling factor (λ_{CS}),[57,58,64] and linewidth improvement reflected in sensitivity and resolution determined through observation of the the chemical shift evolution,[62] and extended coherence lifetimes as observed through echo expeiments.[57] A bimodal Floquet theory analysis shows that ^{1}H homonuclear decoupling requires a fine optimization at MAS above 40 kHz owing to the considerable number of zero- and first-order degeneracies.[65] The two types of degeneracy arise when $n\nu_{\mathrm{r}} + k\nu_{\mathrm{c}} = 0$, where ν_r is MAS spinning frequency and ν_c is the cycle frequency of the decoupling block, and *n* and *k* are integers. When these conditions are met, degeneracies occur within the diagonal block of the Floquet Hamiltonian and the effective Hamiltonian[66] leading to dipolar line-broadening.

Here, we systematically investigate the ^{1}H homonuclear decoupling parameters that affect sensitivity in the ^{15}N-^{1}H CP-Refocused INEPT experiment under ^{1}H homonuclear decoupling and fast MAS. 1D CRAMPS was extensively used to optimise the ^{1}H homonuclear decoupling at various Larmor frequency, showing enhanced resolution at low to moderate ^{1}H nutation frequency. It is shown that optimized decoupling enables the recording of two-dimensional through-bond ^{15}N-^{1}H MAS NMR correlation spectra for moderately sized organic molecules such as the dipeptide β-AspAla and the pharmaceutical cimetidine.

2. Experimental

^{15}N-labelled glycine, and natural abundance (NA) glycine, β-AspAla and cimetidine were purchased from Sigma Aldrich or Bachem (β-AspAla) and packed as received into 1.3 mm zirconia rotors. ^{15}N-Glycine was packed into a restricted volume in the centre of the rotor using silicone spacers. ^{15}N-labelled glycine was used to optimise ^{1}H homonuclear decoupling in 1D and 2D correlation experiments and the 2D ^{15}N-^{1}H CP-refocused INEPT experiment. Glycine NA and β-AspAla NA were used to test the ^{15}N-^{1}H natural abundance CP-refocused INEPT correlation experiment.

The experiments were performed on a Bruker Avance III (500 MHz) or Avance NEO (600 MHz, 1 GHz) spectrometer operating at a ^{1}H Larmor frequency ν_{0H} = 500.13 MHz (11.7 T), 599.45 MHz (14.1 T), 1000.40 MHz (23.5 T) and sample spinning using a Bruker 1.3 mm HXY probe at 60 kHz. The 90˚ pulse duration of 2.5 µs (ν_1 = 100 kHz) for ^{1}H and 4 µs (ν_1 = 62.5 kHz) or 3.5 µs (ν_1 = 71.4 kHz, cimetidine) for ^{15}N was calibrated using a one-pulse experiment and a CP followed by a 90° pulse experiment, respectively. A recycle delay of 3 s or 5 s (cimetidine) was used.

^{1}H chemical shifts are referenced with respect to tetramethylsilane (TMS) via L-alanine at natural abundance as a secondary reference (1.1 ppm for the CH_3 ^{1}H resonance) corresponding to adamantane at 1.85 ppm.[67,68] ^{15}N chemical shifts are referenced relative to liquid CH_3NO_2 at 0 ppm,[69] using the NH_3^+ peak of glycine natural abundance at −347.4 ppm as secondary reference. To convert to the chemical shift scale frequently used in protein NMR, where the alternative IUPAC reference (see Appendix 1 of ref. [70]) is liquid ammonia at −50 ˚C, it is necessary to add 379.5 to the given values.[71] ^{1}H and ^{15}N chemical shifts can be experimentally determined to an accuracy of ±0.2 and ±0.1 ppm, respectively. The ^{15}N RF transmitter frequency was centred at −304.5 ppm (or −291.5 ppm cimetidine). Where the ^{1}H resonance offset is referred to, 0 kHz refers to on-resonance with the NH_3^+ peak of glycine at 8.4 ppm, with a positive resonance offset referring to a move of the RF transmitter frequency to higher ppm.

1D CRAMPS. The acquisition window was optimized to acquire 40 complex data points, each corresponding to 0.1 µs, with a ringdown delay of 1 µs and a deadtime optimized to be 2.2 µs, corresponding to a total acquisition window, τ_w, of 7.2 µs. The total acquisition time is 15 ms. Both $PMLG5_{mm}^{\bar{x}x}$ and $PMLG9_{mm}^{\bar{x}x}$ ^{1}H homonuclear decoupling schemes were optimized over a ^{1}H nutation frequency ($\nu_{1\,^{1}H}$) range from ~10 to ~120 kHz.

2D ^{15}N-^{1}H CP-Refocused INEPT. Cross polarization (CP) from ^{1}H to ^{15}N was used for the initial excitation of ^{15}N transverse magnetisation, where the ^{1}H nutation frequency was ~80 kHz (or ~95 kHz for cimetidine) using a zero-quantum (ZQ) match condition;[72 73] and a ^{15}N nutation frequency of ~20 kHz (or ~25 kHz for cimetidine) with a linear ramp[74] (70%-100%) on the ^{15}N channel (glycine and β-AspAla) or ^{1}H (cimetidine). A CP contact time of 2 ms (or 4 ms for cimetidine) was used. The MISSISSIPPI suppression scheme[75] was applied with a spinlock nutation frequency of ~30 kHz for four intervals of 2 ms (or 5 ms for cimetidine) to remove residual ^{1}H transverse magnetisation. Low-power[76] heteronuclear ^{1}H and ^{15}N decoupling was applied during t_1 evolution and ^{1}H acquisition, respectively, using WALTZ64[77,78] at a nutation frequency of ~10 kHz. The pulse sequence used corresponds to a modified version of that presented by Althaus et al (**Fig. 1b**).[26]

Each ^{1}H-detected FID was acquired for 30 ms with a spectral width of 80 ppm (or 40 ppm for cimetidine). The ^{15}N dimension was acquired with 96 (glycine NA and β-AspAla NA) or 64 (cimetidine) t_1 FIDs with a dwell time of 300 µs (glycine NA) or 142 µs (β-AspAla NA) or 160 µs (cimetidine), corresponding to a ^{15}N spectral width of 66 ppm (glycine NA) or 138 ppm (β-AspAla NA) or 102 ppm (cimetidine) and a maximum t_1 of 15 ms (glycine NA), 6.9 ms (β-AspAla NA), or 5.1 ms (cimetidine). The States-TPPI method was employed to achieve sign discrimination in the indirect dimension.

The pulse sequences, datasets, lists, compound pulse lists, and pulse shapes can be found online at the Warwick online repository, (WRAP *Link*, to be deposited upon acceptance of article).

3. Results and Discussion

3.1 ^{15}N-^{1}H CP- refocused INEPT – pulse sequence and product operator analysis

Our implementation of the ^{15}N-^{1}H CP- refocused INEPT experiment at 60 kHz MAS is shown in **Fig. 1a**. Note that the pulse sequence in **Fig. 1a** corresponds to a modified version of that used by Althaus et al. at ν_r = 40 kHz.[26] The pulse sequence begins with an initial ^{1}H to ^{15}N CP transfer to provide the largest pool of polarization possible for the low-γ and natural abundance ^{15}N nucleus. The ^{15}N transverse magnetisation is allowed to evolve during t_1. The desired magnetisation is stored during a *z*-filter period, which is used with ^{1}H magnetisation suppression using the MISSISSIPPI sequence[75] to remove the background proton signals. A ^{15}N-^{1}H refocused INEPT element is used to transfer the magnetization back to proton for acquisition. INEPT utilizes the ^{1}H-^{15}N *J*-couplings to restrict the signals observed to those with direct one-bond H-N connections. Each spin-echo duration should be an integer number of rotor periods to ensure that the chemical shift anisotropy is completely averaged by MAS. Homonuclear ^{1}H decoupling, here PMLG,[49] is applied during the two spin-echoes of the refocused INEPT element. Under fast MAS, at a spinning frequency of 60 kHz in this work, low power heteronuclear decoupling,[76] specifically WALTZ-64[78] decoupling, is applied on ^{1}H and ^{15}N during t_1 and t_2, respectively. The resulting spectrum is a 2D ^{15}N-^{1}H through-bond correlation spectrum, as illustrated in **Fig. 1b** for natural abundance glycine.

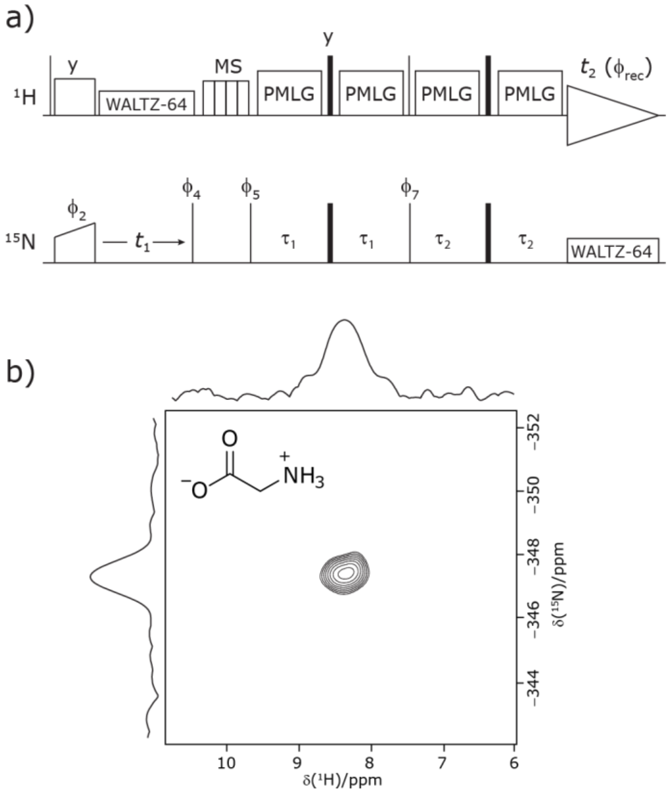

Figure 1. a) Pulse sequence for the ^{15}N-^{1}H CP-refocused INEPT experiment utilised in this paper. Narrow lines and filled black rectangles represent $\pi/2$ and π pulses, respectively. Where not stated, the phase of a pulse is x. The following phase cycle is applied: ϕ_2 = {x*2, $-x$*2}, ϕ_4 = {$-y$*4, y*4}, ϕ_5 = {y*8, $-y$*8}, ϕ_7 = {x, $-x$} and acquisition ϕ_{rec} = {x, $-x$, $-x$, x, $-x$, x, x, $-x$, $-x$, x, x, $-x$, x, $-x$, $-x$, x}. States-TPPI is implemented on ϕ_4. b) A ^{15}N-^{1}H (ν_0 = 500 MHz) 2D CP (contact time = 2 ms)-refocused INEPT MAS (ν_r = 60 kHz) NMR correlation spectrum with skyline projections of natural abundance glycine and its molecular structure. $PMLG9_{mm}^{\bar{x}x}$ was applied at a ^{1}H nutation frequency of 106 kHz (τ_{LG} = 2.92 µs) during both τ_1 = 2.091 ms (179 τ_c) and τ_2 = 0.993 ms (85 τ_c) at a ^{1}H transmitter offset of −2.6 kHz, with zero-offset corresponding to being on resonance with the NH_3^+ peak. 192 transients were coadded for each of 96 t_1 FIDs, corresponding to a total experimental time of 16 hours. The base contour is at 40 % of the maximum intensity.

It is helpful to first review a product operator analysis of the refocused INEPT pulse sequence element. At the beginning of the refocused INEPT element, the in-phase magnetization $\hat{S}_x$ is along the transverse plane for ^{15}N. During the first echo period (τ_1) the in-phase magnetization is converted into anti-phase $\hat{S}_y\hat{I}_z$:

$$\hat{S}_x \xrightarrow{\tau_1-\pi-\tau_1} \cos\left(2\pi J_{IS}\tau_1\right)\hat{S}_x + \sin\left(2\pi J_{IS}\tau_1\right)\hat{S}_y\hat{I}_z \ , \quad (1)$$

where $\hat{I}$ represents the ^{1}H spins. The anti-phase coherence is transferred from S to I with the 90° pulses applied on both channels, which separates the two spin-echo evolution periods:

$$\sin(2\pi J_{IS}\tau_1)\hat{S}_y\hat{I}_z \xrightarrow{(\pi/2)\hat{I}_x} \xrightarrow{(\pi/2)\hat{S}_x} \sin(2\pi J_{IS}\tau_1)\hat{S}_z\hat{I}_y \ . \quad (2)$$

Following τ_1, in the second echo period (τ_2), the antiphase ^{1}H coherence is converted into in-phase $\hat{I}_x$ that is then detected during acquisition (t_2).

$$\sin(2\pi J_{IS}\tau_1)\hat{S}_z\hat{I}_y \xrightarrow{\tau_2-\pi-\tau_2} \sin(2\pi J_{IS}\tau_2)\sin(2\pi J_{IS}\tau_1)\hat{I}_x \ . \quad (3)$$

The product-operator operator analysis predicts maximum transfer, for sin(π/2), i.e., $\tau = 1/(4J_{IS})$, i.e., 2.7 ms, for a one-bond ^{15}N-^{1}H scalar coupling (90 Hz) for fast MAS alone. When the proton magnetization is along the transverse plane, for example as $\hat{I}_y\hat{S}_z$ during τ_2, the ^{1}H-^{1}H dipolar couplings shorten the coherence lifetime compared to when the ^{1}H magnetization is longitudinal, as during τ_1.[39] As expanded upon below, the different influence of the interactions is evident in the optimum length of the τ_1 and τ_2 periods: the spectrum in **Fig. 1b** was recorded with τ_2 (1.0 ms) shorter than τ_1 (2.1 ms) , as discussed further below, note that ^{1}H homonuclear decoupling scales the *J*-coupling.[79-81]

3.2 ^{1}H PMLG homonuclear decoupling under fast MAS

As noted in the above discussion of **Fig. 1a**, PMLG ^{1}H homonuclear decoupling is employed during the two spin-echo durations of the refocused INEPT pulse sequence element that transfers magnetisation from ^{15}N to ^{1}H. Lee-Goldburg decoupling[45] can be considered to be analogous to MAS where the sample is rotated around an axis inclined at the magic angle, θ_m, equal to $\tan^{-1}(\sqrt{2})$, to the external magnetic field in that the ratio of the nutation frequency, ν_1, to the resonance offset, $\Delta\nu_{LG}$, is also set equal to $\tan^{-1}(\sqrt{2})$. This leads to an effective field, ν_{eff_LG}, that is given by Pythagoras' theorem, as:

$$\nu_{\mathrm{eff\_LG}} = \sqrt{\nu_1^2 + \Delta\nu_{\mathrm{LG}}^2} \ . \quad (4)$$

For fixed ν_1, the Lee-Goldburg condition is satisfied as:

$$\tan(\theta_{\mathrm{m}}) = \frac{\nu_1}{\Delta\nu_{\mathrm{LG}}} = \sqrt{2}\,, \tag{5}$$

i.e., $\Delta\nu_{\mathrm{LG}} = \frac{\nu_1}{\sqrt{2}}$ and $\nu_{\mathrm{eff\_LG}} = \sqrt{\frac{3}{2}}\nu_1$. In the PMLG implementation[49] of the LG condition, rf irradiation is applied on resonance for a duration, τ_{LG}, that is the inverse of $\nu_{\mathrm{eff\_LG}}$

$$\tau_{\mathrm{LG}} = \frac{1}{\nu_{\mathrm{eff\_LG}}} = \sqrt{\frac{2}{3}}\frac{1}{\nu_1}\,, \tag{6}$$

but with an equivalent sweep (in discrete jumps) of the rf phase from 0° to $\phi_{\mathrm{last}}{}^{\circ}$ over the duration, τ_{LG}, whereby ϕ_{last} depends on $\Delta\nu_{\mathrm{LG}}$ according to:

$$\phi_{\mathrm{last}} = 360° \cdot \Delta\nu_{\mathrm{LG}} \cdot \tau_{\mathrm{LG}} = 360° \cdot \frac{\nu_1}{\sqrt{2}} \cdot \sqrt{\frac{2}{3}}\frac{1}{\nu_1} = \frac{360°}{\sqrt{3}} = 207.8°\,. \tag{7}$$

An overall rotation, ξ_{LG}, of 360° around the effective field is achieved:

$$\xi_{\mathrm{LG}} = 360° \cdot \nu_{\mathrm{eff\_LG}} \cdot \tau_{\mathrm{LG}} = 360°\,. \tag{8}$$

In the experimental implementation of PMLG under MAS, the duration over which the phase is swept (as discrete steps) from 0° to the ideal ϕ_{last} value of 207.8°, $\tau_{\mathrm{LG\_expt}}$, can vary from the ideal value, τ_{LG}. In this way, the equivalent resonance offset, $\Delta\nu_{\mathrm{expt}}$, changes from the ideal value, $\Delta\nu_{\mathrm{LG}}$, to satisfy: $\phi_{\mathrm{last}} = \frac{360°}{\sqrt{3}} = 360° \cdot \Delta\nu_{\mathrm{LG\_expt}} \cdot \tau_{\mathrm{LG\_expt}}$, so that $\Delta\nu_{\mathrm{LG\_expt}} = \frac{1}{\sqrt{3}\tau_{\mathrm{LG\_expt}}}$.

Nishiyama et al.[57] have shown that this deviation from the ideal condition can be expressed in terms of how the angle, θ, deviates from the magic angle, θ_{m}:

$$\theta = \tan^{-1}\left(\frac{\nu_1}{\Delta\nu_{\mathrm{LG\_expt}}}\right) = \tan^{-1}\left(\nu_1 \cdot \tau_{\mathrm{LG\_expt}} \cdot \sqrt{3}\right). \tag{9}$$

The actual effective field, $\nu_{\mathrm{eff\_LG\_expt}}$, that is calculated by Pythagoras' theorem as $\sqrt{(\nu_1^2 + \Delta\nu_{\mathrm{LG\_expt}}^2)}$ is not equal to $1 / \tau_{\mathrm{LG\_expt}}$ and also deviates from the ideal value, $\nu_{\mathrm{eff\_LG}}$. As a consequence, the overall rotation about the actual effective field, $\xi_{\mathrm{LG\_expt}}$, also deviates from $\xi_{\mathrm{LG}} = 360^{\circ}$ according to:

$$\xi_{\mathrm{LG\_expt}} = 360° \cdot \nu_{\mathrm{eff\_LG\_expt}} \cdot \tau_{\mathrm{LG\_expt}} = 360° \cdot \sqrt{\nu_1^2 + \frac{1}{3\tau_{\mathrm{LG\_expt}}^2}} \cdot \tau_{\mathrm{LG\_expt}}\,. \tag{10}$$

Note that Nishiyama et al. refer to this rotation angle as ψ, but this symbol is used in this paper to denote the ratio of the rotor period to the cycle time (see later discussion), according to Leskes et al.[65]

Following the notation of Leskes et al.[82] a PMLG block is specified as $PMLGn_{\mathrm{R}}^{\phi}$, where: first, *n* is the number of finite pulses for each LG cycle, with *n* equal to 5 or 9 investigated here; second, *R* is the sense of the initial rotation for the phase steps, *m* for clockwise and *p* for counter-clockwise; and third, the initial phase, ϕ, is usually *x* or –x (denoted $\overline{x}$). As stated above (see eq. 7) and as shown in **Fig.2a** and **2b**, τ_{LG} is the time to sweep the phase over *n* discrete steps, i.e., as *n* finite pulses, from 0° to 207.8°. A single PMLG block, $PMLGn_{\mathrm{R}}^{\phi}$, is of duration $2\tau_{\mathrm{LG}}$ with a 180° jump after *n* finite pulses in the first τ_{LG} followed by *n* finite pulses in the second τ_{LG}, whereby the phase steps are in the opposite direction. This corresponds to changing the sign of the equivalent resonance offset, as in the frequency-switched (FS) LG experiment, where rf irradiation is alternated between $+\Delta\nu_{\mathrm{LG}}$ and $-\Delta\nu_{\mathrm{LG}}$.[46,83,84] As further shown by Leskes et al.[82] supercycling can be achieved as $PMLGn_{\mathrm{RR}}^{\phi\phi}$. Specifically, in this work, we use the $PMLG5_{mm}^{\overline{x}x}$ and $PMLG9_{mm}^{\overline{x}x}$ implementations.

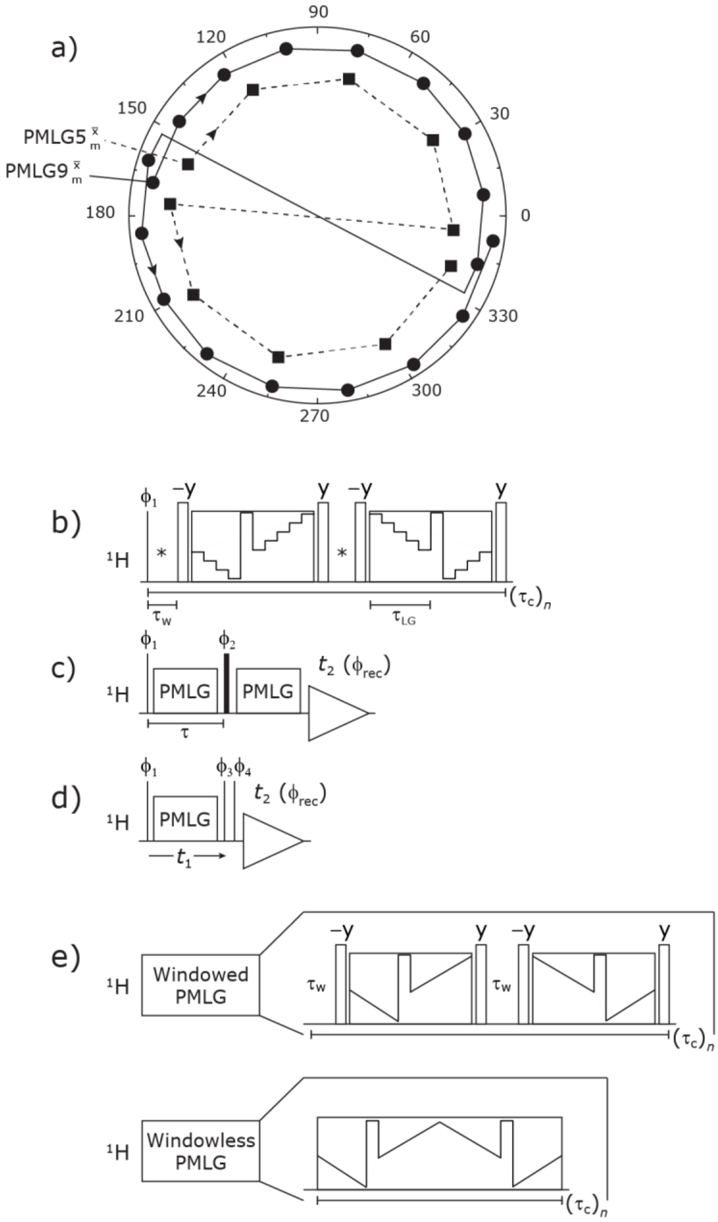

Figure 2. a) Representation of the phase rotation for $PMLG5_m^{\bar{x}}$ and $PMLG9_m^{\bar{x}}$. The phase increments are calculated according to 207.8˚ divided by the number of steps. The starting point for both is –*x*. Pulse sequence for b) a ^{1}H 1D CRAMPS experiment with supercycled $PMLG5_{mm}^{\bar{x}x}$, where the asterix represents an acquisition window, τ_w, c) a ^{1}H spin-echo and d) a 2D ^{1}H-^{1}H correlation experiment. Thin lines and filled rectangles represent 90^o and 180^o pulses, respectively, while open rectangles denote tilt pulses. In c) and d), the block named PMLG can accommodate either a e) windowed, where τ_w is an equivalent period of free evolution, or a windowless sequence, whereby there is continuous rf irradiation during $PMLGn_{\mathrm{R}}^{\phi}$ blocks, i.e., there are no tilt pulses and τ_w = 0. The following phase cycle is applied for b) 1D CRAMPS: ϕ_1 = {*x*, –*x*, –*x*, *x*}, ϕ_{PMLG} = {*x*, –*x*, –*x*, *x*} and acquisition ϕ_{rec} = {*x*, –*x*, –*x*, *x*}; c) ^{1}H spin-echo: ϕ_1 = {*x*, –*x*}, ϕ_2 = {*y**2, *x**2}, ϕ_{PMLG} = {*x*, –*x*} and acquisition ϕ_{rec} = {*x*, –*x*, –*x*, *x*}; d) ^{1}H-^{1}H homonuclear correlation: ϕ_1 = {*x*, –*x*}, ϕ_3 = {–*x**2, *x**2}, ϕ_4 = {*x**4, *y**4}, ϕ_{PMLG} = {*x*, –*x*} and acquisition ϕ_{rec} = {*x*, –*x*, –*x*, *x*, *y*, –*y*, –*y*, *y*}.

In the windowed implementation of PMLG[85] acquisition windows of duration τ_W are placed between the $PMLGn_{\mathrm{R}}^{\phi}$ blocks (see **Fig. 2b**). In addition, tilt pulses of duration τ_{tilt} can be used.[53,86-89] The cycle time for a complete $PMLG5_{mm}^{\bar{x}x}$ or $PMLG9_{mm}^{\bar{x}x}$ supercycle, τ_c, is:

$$\tau_{\mathrm{c}} = 2\tau_{\mathrm{w}} + 4\tau_{\mathrm{LG\_expt}} + 4\tau_{\mathrm{tilt}} . \quad (11)$$

3.3 Optimisation of CH_2 and NH_3 signal intensity in a 1D CRAMPS experiment of ^{15}N-glycine

The optimization of the ^{1}H nutation frequency and $\tau_{\mathrm{LG\_expt}}$ was exploited differently for windowless and windowed sequences. For windowless sequences, a broad optimization was performed with a ^{1}H spin-echo experiment (**Fig. 2c**) to find good candidate parameters which yield long ^{1}H coherence lifetime. As noted below, the ^{1}H-^{1}H correlation experiment (**Fig.2d**) was used to determine the λ_{CS} of the candidate sequences, but can only be used sparingly as the experimental time is relatively long (~20 minutes for 4 co-added transients and 96 t_1 FIDs for each combination of $\tau_{\mathrm{LG\_expt}}$ and ν_1). The windowed sequences were optimized with the faster 1D CRAMPS experiment which gives both λ_{CS} and the ^{1}H linewidth in a few seconds for a particular combination of parameters. Specifically for windowed $PMLG5_{mm}^{\bar{x}x}$ and $PMLG9_{mm}^{\bar{x}x}$, a two variable optimization was performed over a range of ^{1}H nutation frequencies between 0 and 110-120 kHz and $\tau_{\mathrm{LG\_expt}}$ between 3.5 and 7.5 μs for ^{15}N labelled glycine (**Fig. 3a** for $PMLG5_{mm}^{\bar{x}x}$ and **Fig. S1** with slices extracted at different peak intensities, hence with different resolution).

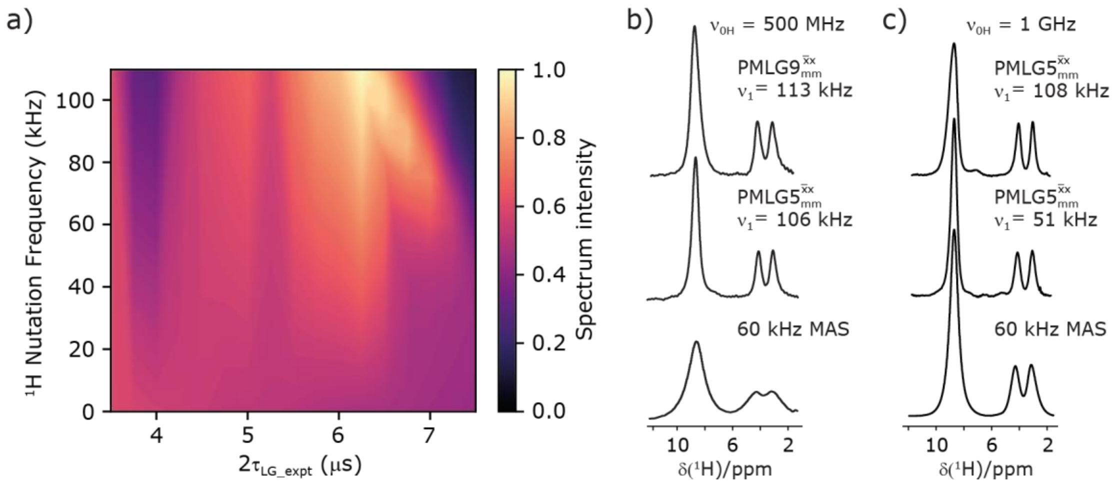

Figure 3. ^{1}H MAS (ν_r = 60 kHz) NMR of ^{15}N-labelled glycine. a) $PMLG5_{mm}^{\bar{x}x}$ 1D CRAMPS (see **Fig. 2b**, τ_{tilt} = 0.54 μs, Ω = –0.6 kHz) two-variable optimization (ν_0 = 500 MHz) of both $\tau_{\mathrm{LG\_expt}}$ (in steps of 0.25 μs) and the ^{1}H nutation frequency, ν_1 (0 kHz – 110 kHz) for the NH_3^+ peak intensity. b) Comparison between ^{1}H (ν_0 = 500 MHz) 1D CRAMPS MAS NMR spectra acquired with windowed $PMLG9_{mm}^{\bar{x}x}$ (ν_1 = 113 kHz, $\tau_{\mathrm{LG\_expt}}$ = 2.92 μs, τ_{tilt} = 0.82 μs, Ω = –0.6 kHz), windowed $PMLG5_{mm}^{\bar{x}x}$ (ν_1 = 106 kHz, $\tau_{\mathrm{LG\_expt}}$ = 3.1 μs, τ_{tilt} = 0.54 μs, Ω = –0.6 kHz), and a one-pulse MAS-alone experiment. c)

Comparison between ^1H (ν_0 = 1 GHz) 1D CRAMPS MAS NMR spectra acquired with windowed $PMLG5_{mm}^{\bar{x}x}$ (ν_1 = 108 kHz, τ_{LG_expt} = 3.10 µs, τ_{tilt} = 0.18 µs, Ω = –7.0 kHz), windowed $PMLG5_{mm}^{\bar{x}x}$ (ν_1 = 52 kHz, τ_{LG_expt} = 3.63 µs, τ_{tilt} = 0.70 µs, Ω = –8.6 kHz), and a one-pulse MAS-alone experiment. 8 (a) or 32 (b and c) co-added transients were added for a recycle delay of 3 s. For all experiments, τ_w = 7.20 µs.

Figure 3a reports on the NH_3^+ ^1H resonance, noting its relevance in this paper for the ^1H-^{15}N refocused INEPT experiment. Figure S2 shows that optimum performance for the NH_3^+ ^1H resonance (**Fig. S2b**) is closely matched by that for the CH_2 ^1H resonances (**Fig. S2a**). 1D CRAMPS ^1H NMR spectra of ^{15}N-glycine for our best implementations of supercycled windowed $PMLG5_{mm}^{\bar{x}x}$ and $PMLG9_{mm}^{\bar{x}x}$ at ν_0 = 500 MHz (**Fig. 3b**) are shown in **Fig. 3b**, where enhanced resolution compared to MAS alone is evident. Moreover, both $PMLG5_{mm}^{\bar{x}x}$ and $PMLG9_{mm}^{\bar{x}x}$ implemented at ν_0 = 500 MHz (**Fig. 3b**) show better resolution than 60 kHz MAS alone at ν_0 = 1 GHz (**Fig. 3c**). At ν_0 = 1 GHz, optimised 1D CRAMPS ^1H NMR spectra of ^{15}N-glycine for windowed $PMLG5_{mm}^{\bar{x}x}$ at a ^1H nutation frequency of 108 and 51 kHz are presented in Fig. 3c that show enhanced resolution compared to MAS alone.

Table 1 compares the experimentally optimised τ_{LG_expt} to the ideal τ_{LG} values: at ν_0 = 500 MHz, the experimental values are less than half the ideal values, i.e., τ_{LG_expt} = 3.10 µs and 2.92 µs compared to 7.23 µs and 7.70 µs, respectively. As **Table 1** further shows, with the corresponding changes in $\Delta\nu_{LG\_expt}$ and ν_{eff_expt}, the angle θ is 29.7° and 29.6°, respectively. While a very high nutation frequency of over 200 kHz has been used in the first experimental implementations of PMLG at 65 kHz MAS frequency[59,65] resulting in a θ value of 61° for the spectrum presented by Leskes et al,[59] a similar value (of 31.2°) far from the magic angle has been reported by Nishiyama et al. for the implementation of windowed $PMLG5_{mm}^{\bar{x}x}$ at an MAS frequency of 80 kHz and a ^1H nutation frequency of 125 kHz.[57] Moreover, the actual rotation, ξ_{LG_expt}, reported by Nishiyama et al. of 243° is similar to that of 239° for our implementation of both windowed $PMLG5_{mm}^{\bar{x}x}$ and $PMLG9_{mm}^{\bar{x}x}$ at a MAS frequency of 60 kHz (see **Table 1**). **Table 1** also lists the implementations of $PMLG5_{mm}^{\bar{x}x}$ by Leskes et al. at 10 kHz MAS[82] and Mao & Pruski at 12.5, 19.5, 25.0 and 41.7 kHz MAS:[90] the angle θ is seen to vary between 45° and 64°. It is observed that an angle θ below and above the magic angle corresponds to an actual rotation, ξ_{LG_expt}, less than and more than the ideal 360°, respectively. Fig. 3c also shows the good decoupling performance observed at ν_0 = 1 GHz with windowed $PMLG5_{mm}^{\bar{x}x}$ for a ^1H nutation frequency of only 51 kHz, where the angle θ is only 17.6°.

Table 1. Implementation of $PMLG5_{mm}^{\bar{x}x}$ and $PMLG9_{mm}^{\bar{x}x}$ ^1H homonuclear decoupling: variation from the ideal Lee-Goldburg condition for this work and previous publications

Decoupling	ν_r (kHz)	ν_1 (kHz)	τ_{LG} (μs)	τ_{LG_expt} (μs)	θ_m (deg)	θ (deg)	$\Delta\nu_{LG}$ (kHz)	$\Delta\nu_{LG\_expt}$ (kHz)	ν_{eff_LG} (kHz)	$\nu_{eff\_LG\_expt}$ (kHz)	ξ_{LG} (deg)	ξ_{LG_expt} (deg)
Windowed $PMLG5_{mm}^{\bar{x}x}$ [a] (500 MHz)	60.0	106	7.70	3.10		29.7	75.0	186.2	129.8	214.3		239.2
Windowless $PMLG5_{mm}^{\bar{x}x}$ [b] (500 MHz)	60.0	106	7.70	3.10		29.7	75.0	186.2	129.8	214.3		239.2
Windowed $PMLG9_{mm}^{\bar{x}x}$ [a] (500 MHz)	60.0	113	7.23	2.92		29.7	79.9	197.7	138.4	227.7		239.4
Windowless $PMLG9_{mm}^{\bar{x}x}$ [b] (500 MHz)	60.0	113	7.23	2.92	54.7	29.7	79.9	197.7	138.4	227.7	360.0	239.4
Windowed $PMLG5_{mm}^{\bar{x}x}$ [c] (1 GHz, ν_1 = 108 kHz)	60.0	108	7.56	3.10		30.1	76.4	186.2	132.3	215.3		240.3
Windowed $PMLG5_{mm}^{\bar{x}x}$ [c] (1 GHz, ν_1 = 51 kHz)	60.0	51	16.01	3.63		17.6	36.1	159.3	62.4	167.2		218.2
Literature parameters												
$PMLG5_{pp}^{\bar{x}x}$ [d]	80.0	125	6.53	2.80		31.2	88.4	206.2	153.1	241.1		243.1
$PMLG5_{mm}^{\bar{x}x}$ [e]	65.0	216	3.78	4.80		60.9	152.7	120.3	264.5	247.2		427.2
$PMLG5_{mm}^{\bar{x}x}$ [f]	41.7	155	5.27	3.75		45.2	109.6	154.0	189.8	218.5		294.9
$PMLG5_{mm}^{\bar{x}x}$ [f]	41.7	155	5.27	7.75		64.3	109.6	74.5	189.8	172.0		479.8
$PMLG5_{mm}^{\bar{x}x}$ [g]	12.5	78	10.47	12.50	54.7	59.4	55.2	46.2	95.5	90.6	360.0	407.9
$PMLG5_{mm}^{\bar{x}x}$ [g]	19.5	126	6.48	8.00		60.2	89.1	72.2	154.3	145.2		418.2
$PMLG5_{mm}^{\bar{x}x}$ [g]	25.0	162	5.04	6.25		60.3	114.6	92.4	198.4	186.5		419.6
$PMLG5_{mm}^{\bar{x}x}$ [h]	10.0	95	8.59	7.25		50.0	67.2	79.6	116.4	124.0		323.5
$PMLG5_{mm}^{\bar{x}x}$ [i]	65.0	250	3.27	5.00		65.2	176.8	115.5	306.2	275.4		495.7

Parameters from this work for a) **Fig. 3b** and **Table 3**, b) **Fig. S3** and c) **Fig. 3c** and **Table 3**
Values extracted from d) Nishiyama et al. Fig. 2 and 3,[57] e) Leskes et al. Table 1,[59] f) and g) Mao et al.,[90] Fig. 3 and Fig. 2, respectively; h) Leskes et al. Fig. 2;[82] i) simulated values extracted from Leskes et al. Fig. 2[65]

Table 2 states the τ_c values, as calculated from τ_{LG_expt}, τ_w and τ_{tilt}, for the implementations of $PMLG5_{mm}^{\bar{x}x}$ and $PMLG9_{mm}^{\bar{x}x}$ in this work, as well as that reported in the literature. An important parameter for predicting decoupling performance is the ratio, ψ, of the MAS rotor period, τ_r, to the decoupling cycle time, τ_c, and vice versa, the ratio of the corresponding frequency, $\nu_c = 1/\tau_c$, to the MAS frequency, ν_r:[65]

$$\Psi = \frac{\tau_r}{\tau_c} = \frac{\nu_c}{\nu_r}. \tag{12}$$

For low to moderate MAS frequencies, small integer values of ψ are to be avoided since these values correspond to recoupling rather than decoupling conditions.[53,88,91-93] For fast MAS (of at least 40 kHz), there are more values of ψ that need to be avoided.[62,65,90] Specifically, by employing bimodal Floquet theory, Leskes et al. have identified values of *n* and *k* that result in deteriorated decoupling due to zero-order and first-order recoupling conditions, according to:

$$n\nu_r + k\nu_c = 0\,, \tag{13}$$

where *n* takes values 1, 2, 3, 4 while $-15 \le k \le -1$.[65] While there is a dense set of degeneracies for values of ψ below 1.50, there are windows of good decoupling performance that can be found. The ψ value of both the windowless sequences, $PMLG5_{mm}^{\bar{x}x}$ (ψ = 1.34) and $PMLG9_{mm}^{\bar{x}x}$ (ψ = 1.43), are in line with the value of 1.40 – 1.60 reported by Mao et al. for spectra acquired among a range of different spinning frequencies (12.5 kHz to 41.7 kHz) and ^{1}H nutation frequencies (78 kHz – 162 kHz) as indicated in **Table 1** and **2**.[90] For windowed sequences, the ψ value is usually lower. For the 1D CRAMPS spectra presented in **Fig. 3b**, **Table 2** shows that ψ equals 0.58 and 0.57 for windowed $PMLG5_{mm}^{\bar{x}x}$ and windowed $PMLG9_{mm}^{\bar{x}x}$, respectively, at ν_0 = 500 MHz, and 0.61 and 0.53 at ν_0 = 1 GHz for a ^{1}H nutation frequency of 108 and 51 kHz, respectively. These ψ values are similar to the values of 0.60 and 0.63 for the experimental implementation of windowed $PMLG5_{mm}^{\bar{x}x}$ by Nishiyama et al. at an MAS frequency of 80 kHz and a ^{1}H nutation frequency of 125 kHz[57] and by Leskes et al. at an MAS frequency of 65 kHz and a ^{1}H nutation frequency of 216 kHz.[59]

Table 2. Implementation of $PMLG5_{mm}^{\bar{x}x}$ and $PMLG9_{mm}^{\bar{x}x}$ ^{1}H homonuclear decoupling: scaling factors and comparison of rotor period to cycle time for this work and previous publications

	τ_{LG_expt} (μs)	τ_W (μs)	τ_{tilt} (μs)	τ_c (μs)	τ_r (μs)	ψ^l	λ_{CS_calc}	λ_{CS_expt}
Windowed $PMLG5_{mm}^{\bar{x}x}$ [a] (500 MHz)	3.10	7.20	0.54	28.96	16.67	0.58	0.76[k]	0.82
Windowless $PMLG5_{mm}^{\bar{x}x}$ [b] (500 MHz)	3.10	-	-	12.40	16.67	1.34	0.76[j]	0.66
Windowed $PMLG9_{mm}^{\bar{x}x}$ [a] (500 MHz)	2.92	7.20	0.82	29.36	16.67	0.57	0.77[k]	0.76
Windowless $PMLG9_{mm}^{\bar{x}x}$ [b] (500 MHz)	2.92	-	-	11.68	16.67	1.43	0.78[j]	0.60
Windowed $PMLG5_{mm}^{\bar{x}x}$ [c] (1 GHz)	3.10	7.20	0.18	27.52	16.67	0.61	0.74[k]	0.82
Windowed $PMLG5_{mm}^{\bar{x}x}$ [c] (1 GHz)	3.63	7.20	0.70	31.70	16.67	0.53	0.90[k]	0.92
Literature parameters								
$PMLG5_{pp}^{\bar{x}x}$ [d]	2.80	4.84	-	20.88	12.50	0.60	0.86[j]	0.82
$PMLG5_{mm}^{\bar{x}x}$ [e]	4.80	2.70	-	24.60	15.38	0.63	0.40[j]	0.48
$PMLG5_{mm}^{\bar{x}x}$ [f]	3.75	-	-	15.00	24.00	1.60	0.50[j]	0.36

$PMLG5_{mm}^{\bar{x}x}$ f	7.75	-	-	31.00	24.00	0.77	0.19[j]	0.21
$PMLG5_{mm}^{\bar{x}x}$ g	12.50	-	-	50.00	80.00	1.60	0.26[j]	-
$PMLG5_{mm}^{\bar{x}x}$ g	8.00	-	-	32.00	51.20	1.60	0.25[j]	-
$PMLG5_{mm}^{\bar{x}x}$ g	6.25	-	-	25.00	40.00	1.60	0.25[j]	-
$PMLG5_{mm}^{\bar{x}x}$ h	7.25	4.35	-	37.70	100.00	2.65	0.55[j]	0.47
$PMLG5_{mm}^{\bar{x}x}$ i	5.00	-	-	20.00	15.38	0.77	0.18[j]	-

Parameters from this work for a) **Fig. 3b** and **Table 3**, b) **Fig. S5** and c) **Fig. 3c** and **Table 3**
Values extracted from d) Nishiyama et al. Fig. 2 and 3,[57] e) Leskes et al. Table 1,[59] f) and g) Mao et al.,[90] Fig. 3 and Fig. 2, respectively; h) Leskes et al. Fig. 2;[82] i) simulated values extracted from Leskes et al. Fig. 2[65]
λ_{CS} is calculated with j) eq. 16 and k) eq. 17 as stated in this paper, following from Nishiyama et al.[57]
l) ψ is calculated with eq. 12, following from Leskes et al.[65]

3.4 Windowed and windowless PMLG ^{1}H decoupling, ^{1}H spin-echo dephasing and scaling factors

It is well established that the application of rf ^{1}H homonuclear decoupling leads to a chemical shift scaling: for a static sample, the chemical shift scaling factor, λ_{CS}, for perfect decoupling cannot exceed $\cos^{-1}(\theta_m) = 1/\sqrt{3} = 0.577$.[64,93,94] The 1D ^{1}H CRAMPS spectra presented in **Fig. 3b** and **Fig. 3c** have chemical shift axes that have been corrected for this scaling, i.e., a scaling is applied so as to ensure that the chemical shift separation between the NH_3^+ peak and the lower ppm CH_2 peak corresponds to the MAS-only ^{1}H chemical shifts, i.e., 8.4 – 3.0 = 5.4 ppm. The full width at half maximum, (FWHM), of the three ^{1}H resonances before and after scaling for the spectra presented in **Fig. 3b** and **Fig. 3c** are presented in **Table 3**. **Table 3** also states that λ_{CS} equals 0.82 and 0.76 for windowed $PMLG5_{mm}^{\bar{x}x}$ and windowed $PMLG9_{mm}^{\bar{x}x}$, respectively, at ν_0 = 500 MHz, and 0.82 and 0.92 at ν_0 = 1 GHz for a ^{1}H nutation frequency of 108 and 51 kHz, respectively. **Table 3** also reports, as a measure of decoupling efficiency, K, given by

$$\mathrm{K} = \frac{\mathrm{FWHM}_{\mathrm{MAS}} - \mathrm{FWHM}_{\mathrm{scaled}}}{\mathrm{FWHM}_{\mathrm{MAS}}} = \frac{\mathrm{FWHM}_{\mathrm{MAS}} - \left(\mathrm{FWHM}_{\mathrm{PMLG}} / \lambda_{\mathrm{cs}}\right)}{\mathrm{FWHM}_{\mathrm{MAS}}}, \tag{14}$$

where a K closer to 1 corresponds to better decoupling performance. FWHM_{MAS} is obtained under MAS alone, FWHM_{PMLG} is the linewidth recorded using PMLG, and FWHM after scaling, FWHM_{scaled}, is equal to $\mathrm{FWHM}_{PMLG} / \lambda_{CS}$. High scaling factors that are significantly above 0.577, like those stated in **Table 3**, have been reported for 60 kHz MAS by Salager et al. for an experimental optimisation protocol based on a quality factor considering the intensity of the two most intense resonances, CH_3 and NH_3, in β-AspAla as well as their peak separation in Hz.[58] Specifically, λ_{CS} equals 0.73 and 0.84 for the eDUMBO-PLUS-1 and eDUMBO-PLUS-large sequences, respectively, for 60 kHz MAS and a ^{1}H nutation frequency of 170 kHz, with optimum resolution observed for eDUMBO-PLUS-1. Salager et al. have further presented a scaling factor theorem for homonuclear decoupling, derived for a static system of homonuclear I = 1/2 spins coupled by a dipolar interaction that are subject to cyclic rf irradiation:

$$|\lambda_{\mathrm{CS}}|^2 \leq \frac{1}{3}\left(2|\lambda_{\mathrm{D}}|+1\right), \tag{15}$$

where λ_D is the dipolar scaling factor, i.e., zero corresponds to perfect decoupling, showing that λ_{CS} cannot exceed 1 / √3, when $\lambda_D = 0$[64].

For $PMLG5_{mm}^{\bar{x}x}$, Nishiyama et al. report a λ_{CS} of 0.82 at 80 kHz MAS and a ^{1}H nutation frequency of 125 kHz. Nishiyama et al. further state equations for calculating λ_{CS} for $PMLG5_{mm}^{\bar{x}x}$ decoupling without and with tilt pulses:

$$\lambda_{\mathrm{CS\_calc\_no\_tilt\_pulses}} = \frac{2\tau_{\mathrm{LG\_expt}}\cos^2\theta + \tau_w}{2\tau_{LG\_\mathrm{expt}} + 2\tau_{tilt} + \tau_w}, \tag{16}$$

$$\lambda_{\mathrm{CS\_calc\_with\_tilt\_pulses}} = \frac{\frac{2\tau_{tilt}\sin\theta}{\theta} + 2\tau_{LG\_\mathrm{expt}}\cos\theta\cos 2\theta + \tau_w}{2\tau_{LG\_\mathrm{expt}} + 2\tau_{tilt} + \tau_w}. \tag{17}$$

These calculated λ_{CS} values are presented in **Table 2** for the experimental implementations of $PMLG5_{mm}^{\bar{x}x}$ in the literature, as well as $PMLG5_{mm}^{\bar{x}x}$ and $PMLG9_{mm}^{\bar{x}x}$ in this work. Deviation of the experimental scaling factor compared to theoretical behaviour can arise from phase transients that cause phase propagation delays[88,95].

Table 3. Analysis of windowed $PMLG5_{mm}^{\bar{x}x}$ and $PMLG9_{mm}^{\bar{x}x}$ ^{1}H homonuclear decoupling efficiency for ^{1}H (ν_0 = 500 MHz and 1 GHz) CRAMPS NMR at ν_r = 60 kHz of ^{15}N-glycine[a]

	δ (ppm)	$FWHM_{MAS}$ (Hz)	$FWHM_{MAS}$ (ppm)	$FWHM_{PMLG}$ (Hz)	$FWHM_{PMLG}$ (ppm)	$FWHM_{scaled}$ (Hz)	$FWHM_{scaled}$ (ppm)	Scaling factor, λ_{CS}	K[b]	$FWHM_{PMLG}$ (Hz)	$FWHM_{PMLG}$ (ppm)	$FWHM_{scaled}$ (Hz)	$FWHM_{scaled}$ (ppm)	Scaling factor, λ_{CS}	K[b]
ν_0 = 500 MHz				$PMLG5_{mm}^{\bar{x}x}$						$PMLG9_{mm}^{\bar{x}x}$					
NH_3^+	8.4	664	1.33	230	0.46	280	0.56		0.58	273	0.55	359	0.72		0.46
CH_2	4.2	800[c]	1.60	217	0.43	264	0.53	0.82	0.67	213	0.43	280	0.56	0.76	0.65
CH_2	3.0	800[c]	1.60	224	0.45	273	0.55		0.66	232	0.46	305	0.61		0.62
ν_0 = 1 GHz				$PMLG5_{mm}^{\bar{x}x}$ (ν_1 = 108 kHz)						$PMLG5_{mm}^{\bar{x}x}$ (ν_1 = 51 kHz)					
NH_3^+	8.4	700	0.70	583	0.58	711	0.71		−0.02	475	0.48	516	0.52		0.26
CH_2	4.2	740	0.74	346	0.35	422	0.42	0.82	0.43	448	0.45	487	0.49	0.92	0.34
CH_2	3.0	740	0.74	311	0.31	379	0.38		0.49	440	0.44	478	0.48		0.35

[a] See spectra in **Fig. 3b** (ν_0 = 500 MHz) and **Fig. 3c** (ν_0 = 1 GHz), for the pulse sequence in **Fig. 2b** and experimental parameters in **Table 2**
[b] calculated with **eq. 14**
[c] FWHM extracted from the indirect dimension of a 2D ^{1}H-^{1}H correlation experiment with MAS alone, see **Fig. S3**

As well as scaling the chemical shifts, ^1H homonuclear decoupling also scales evolution under a heteronuclear *J*-coupling by the same factor.[37,57,79] For magnetisation transfer from ^{15}N to ^1H during the spin echoes of the refocused INEPT pulse sequence element, the efficiency depends upon this scaling of the ^{15}N - ^1H *J*-couplings, but also the spin-echo dephasing time, T_2'.[90,96,97]

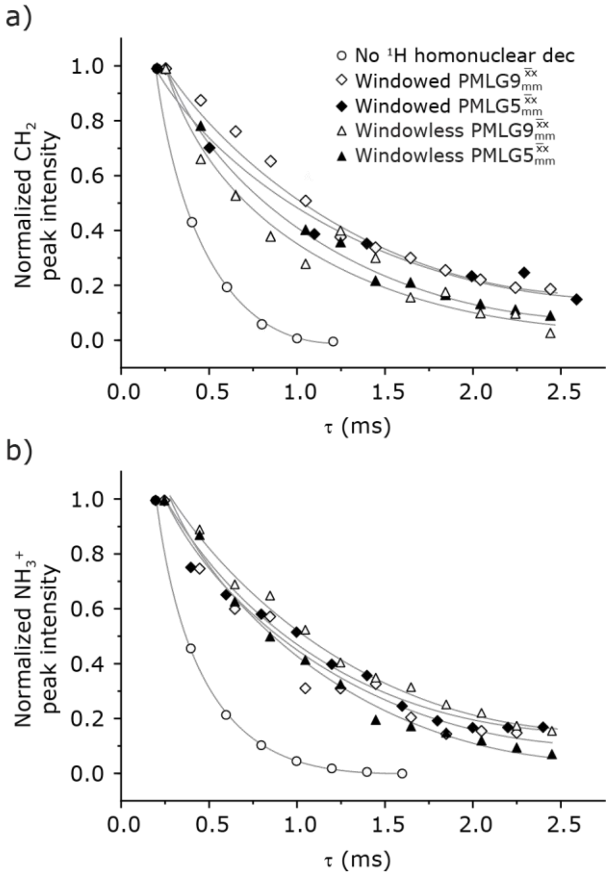

Figure 4. Dephasing of the ^{15}N-glycine a) CH_2 (the higher ppm ^1H resonance is considered) and b) NH_3^+ proton resonances as a function of the spin-echo (see **Fig. 2c**) duration, τ, with no ^1H homonuclear decoupling (empty circles), windowed $PMLG9_{mm}^{\bar{x}x}$ (empty diamonds), windowed $PMLG5_{mm}^{\bar{x}x}$ (full diamonds), windowless $PMLG9_{mm}^{\bar{x}x}$ (empty triangles), and windowless $PMLG5_{mm}^{\bar{x}x}$ (full triangles) for nutation frequencies and resonance offsets as stated in **Table 4**. Fits to an exponential decay function are shown, with the spin-echo dephasing times, T_2', as listed in **Table 4**. 16 transients were co-added for a recycle delay of 3 s. For all experiments with windowed ^1H homonuclear decoupling, τ_w = 7.20 µs.

Fig. 4 compares spin-echo dephasing curves (see pulse sequence in **Fig. 2c**) for MAS alone to those for windowed and windowless $PMLG5_{mm}^{\bar{x}x}$ and $PMLG9_{mm}^{\bar{x}x}$, with the values for experimental parameters and extracted T_2' presented in **Table 4**. (Note that $PMLG9_{mm}^{\bar{x}x}$ homonuclear decoupling was implemented with a slightly changed nutation frequency of ν_1 = 109 kHz, as compared to ν_1 = 113 kHz for the 1D CRAMPS spectrum in **Fig. 3b**). In windowless PMLG decoupling, there is continuous *rf* irradiation, i.e., there are no tilt pulses and τ_w = 0, while, in the windowed version, τ_w is replaced by a delay (**Fig. 2e**). Indeed, this corresponds to the first implementation of windowed PMLG in the indirect dimension of a two-dimensional ^{1}H-^{1}H experiment where there is evolution under MAS alone in the direct dimension.[49] Such a 2D experiment (see **Fig. 2d**) is used to measure λ_{CS} for our implementation of windowless $PMLG5_{mm}^{\bar{x}x}$ and $PMLG9_{mm}^{\bar{x}x}$, as reported in **Tables 2** and **4** (spectra are presented in **Fig. S3**).

Table 4 ^{1}H dephasing time, T_2', and T_2' scaled by the experimental λ_{CS}, λ_{CS} T_2', as determined by a ^{1}H spin-echo MAS NMR experiment[a] for ^{15}N-glycine with optimised *rf* carrier offset and ν_1

	Offset (kHz)	ν_1 (kHz)	λ_{CS}	NH_3^+ T_2' (ms)	NH_3^+ λ_{CS} T_2' (ms)	CH_2 T_2'[b] (ms)	CH_2 λ_{CS} T_2' (ms)
No decoupling	2	-	1	0.25	0.25	0.22	0.22
Windowed $PMLG5_{mm}^{\bar{x}x}$	1	106	0.82	1.04	0.85	1.14	0.93
Windowed $PMLG9_{mm}^{\bar{x}x}$	0.75	109	0.76	0.91	0.69	1.10	0.84
Windowless $PMLG5_{mm}^{\bar{x}x}$	1	106	0.66	0.86	0.57	0.80	0.53
Windowless $PMLG9_{mm}^{\bar{x}x}$	–0.25	109	0.60	1.15	0.69	0.78	0.47

[a] As implemented at ν_0 = 500 MHz and ν_r = 60 kHz, see **Fig. 4a** for the CH_2 resonance and **Fig. 4b** for the NH_3^+ peak. The τ_{tilt} is equal to 0.54 μs for windowed $PMLG5_{mm}^{\bar{x}x}$ and 0.82 μs for windowed $PMLG9_{mm}^{\bar{x}x}$

[b] For the CH_2 group, the T_2' of the higher-ppm ^{1}H resonance is stated

Considering **Fig. 4** and **Table 4**, the ^{1}H dephasing times, T_2', for the CH_2 (the higher ppm resonance is considered) and NH_3^+ peaks are 0.20 ms and 0.25 ms for 60 kHz MAS alone. With ^{1}H homonuclear decoupling the ^{1}H dephasing time for both groups increases. The longest CH_2 dephasing time is observed for windowed $PMLG5_{mm}^{\bar{x}x}$, T_2' = 1.14 ms, slightly longer than for windowed $PMLG9_{mm}^{\bar{x}x}$, where T_2' is equal to 1.10 ms. However, the scaling by λ_{CS} needs to be considered and **Table 4** reports the product of λ_{CS} and T_2' in each case. After this scaling (**Table 4**), windowed $PMLG5_{mm}^{\bar{x}x}$ achieves an over 4 fold improvement with respect of MAS alone, compared to the slightly under 4 fold improvement of windowed $PMLG9_{mm}^{\bar{x}x}$. A similar comparison can be made for the NH_3^+ peak, where windowless $PMLG9_{mm}^{\bar{x}x}$ shows the longest T_2' equal to 1.15 ms. The longest value of the product, λ_{CS} T_2', is observed for windowed $PMLG5_{mm}^{\bar{x}x}$ at 0.85 ms, thanks again to the large λ_{CS}; this corresponds to an over 3.5 fold improvement with respect to MAS alone.

3.5 Optimisation of tilt pulses via the NH_3^+ signal intensity in a 1D CRAMPS experiment of ^{15}N-glycine

The duration of the tilt pulses, τ_{tilt}, was optimised in a two-variable optimization with τ_{LG_expt}, for the intensity of the NH_3^+ resonance in a 1D CRAMPS spectrum of ^{15}N-glycine at 60 kHz MAS as presented in **Fig. 5a** with windowed $PMLG5_{mm}^{\bar{x}x}$. It is evident from **Fig. 5** that the optimum values for the two parameters, τ_{LG_expt} and τ_{tilt}, are linked, i.e., when one becomes longer the other shortens, maintaining the same combined length of ~7.1 µs (considering two sandwich pulses per $PMLGn_{R}^{\phi}$ block – see **Fig. 2b**) to maintain the same cycle time, τ_c (see eq. 11), and hence ensure a constant optimum ψ (see eq. 12). The couples with best NH_3^+ signal intensity were 6.75 & 0.15 µs, 6.5 & 0.30 µs and 6.25 & 0.45 µs for 2 τ_{LG} and τ_{tilt}, respectively, with a preference for a longer τ_{LG_expt} and shorter τ_{tilt} (see **Fig. 5b**). A fine optimisation with 16 co-added transients was employed to identify the optimum parameters as used in **Fig. 3c** (and repeated in **Fig. 5c**, left-hand spectrum).

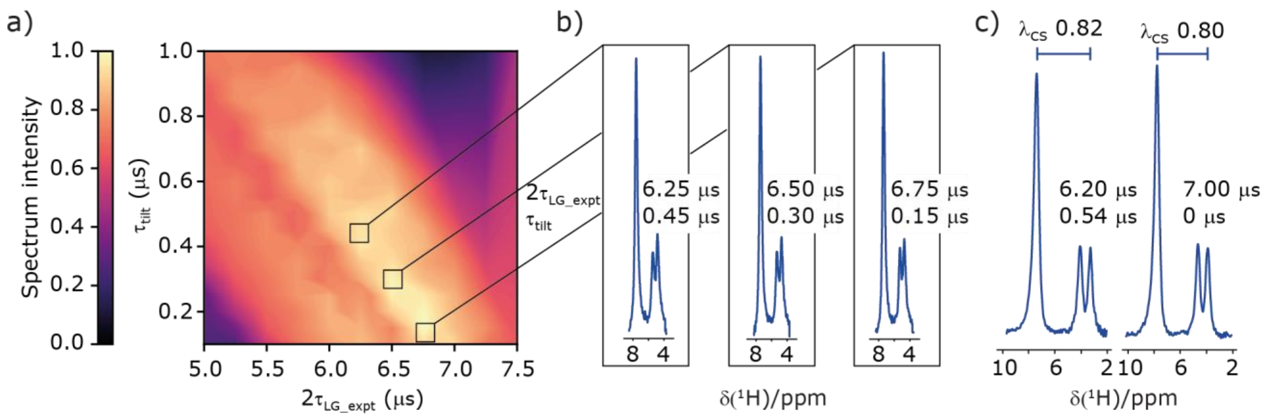

Figure 5. a) Two-variable optimization of 2 τ_{LG_expt} (0.25 µs step) and τ_{tilt} (0.05 µs step) for the NH_3^+ peak intensity in a 1D ^{1}H-CRAMPS (ν_0 = 500 MHz) MAS (ν_r = 60 kHz) spectrum of ^{15}N-labelled glycine. Windowed $PMLG5_{mm}^{\bar{x}x}$ was applied with ν_1 = 106 kHz and a ^{1}H transmitter offset of –0.6 kHz. 4 co-added transients were collected for each optimization point. b) Slices extracted from the contour plot show the best spectrum intensities obtained with the indicated 2 τ_{LG_expt} and τ_{tilt}. c) 1D ^{1}H CRAMPS ^{15}N-labelled glycine spectra acquired with windowed $PMLG5_{mm}^{\bar{x}x}$ using 2 τ_{LG_expt} = 6.20 µs and τ_{tilt} = 0.54 µs (left) and windowed $PMLG5_{mm}^{\bar{x}x}$ without τ_{tilt} (right). 32 co-added transients were added. For all experiments with windowed ^{1}H homonuclear decoupling, τ_w = 7.20 µs.

The ^{1}H CRAMPS spectrum on the right in **Figure 5c** was acquired with the same nutation frequency and offset, but with no tilt pulses and 2 τ_{LG_expt} was chosen to be 7 µs such that the cycle time and hence ψ are the same. The intensity of the NH_3^+ peak obtained with windowed $PMLG5_{mm}^{\bar{x}x}$ at τ_{LG_expt} = 6.20 µs and τ_{tilt} = 0.54 µs is within 5% of that obtained without tilt pulses. Note, however, that the peak widths for $PMLG5_{mm}^{\bar{x}x}$ without tilt pulses are 235 Hz for the NH_3^+ peak, and 224 Hz and 231 Hz for the CH_2 peaks. After scaling (λ_{CS} = 0.80), the FWHM become 294 Hz, 280 Hz and 289 Hz, respectively, which is ~15 Hz larger than those stated in **Table 3** for windowed $PMLG5_{mm}^{\bar{x}x}$ with τ_{LG_expt} = 6.20 µs and τ_{tilt} = 0.54 µs.

3.6 Optimisation of the ^{15}N-glycine NH_3^+ signal intensity in a 1D-filtered CP-refocused INEPT NMR spectrum for PMLG ^{1}H decoupling at 60 kHz MAS

Under a ^{1}H homonuclear decoupling sequence such as PMLG, the proton offset frequency influences the performance;[53,89] this is linked to the overall z-rotation that the spins need under decoupling to avoid artifacts and RF imperfections.[82] As shown by Leskes et al.,[86] the non-supercycled *m*-block is particularly beneficial in narrowing lines of strong coupled spins, as for the CH_2 groups of ^{15}N-glycine, close to the on-resonance position. With the implementation of supercycled PMLG schemes,[87] the sign of the offset is no longer a determining factor as the supercycle brings the effective rotation of the spins closer to the z-axis.[98] However, the choice of the optimum offset still plays a significant role for achieving good decoupling performance, therefore it is necessary to investigate both positive and negative offsets. Here the optimization was performed directly on the ^{15}N-^{1}H CP-Refocused INEPT experiment, where windowed $PMLG5_{mm}^{\bar{x}x}$ was applied over a wide range of offset values from ~+10 kHz to –12 kHz, whereby on-resonance corresponds to the NH_3^+ peak. **Figure 6** shows that the best offsets in term of sensitivity are at +1 kHz and –3.5 kHz, highlighted by dashed vertical lines. Between the two best performing offsets, the sensitivity experiences a fluctuation (**Fig. 6**) corresponding to the on-resonance position (solid line), dropping to zero for a small negative offset of –0.5 kHz. It is then important to optimize the offset avoiding the on-resonance position. The need for a fine optimization of this parameter is emphasized by the considerable change in sensitivity that is observed for a small variation of the offset.[53,54,93] For example, the relative sensitivity of the NH_3^+ peak falls from 0.9 to 0.5 when switching the offset from ~–3.5 to –-2.5 kHz. In general, in **Figure 6** the offsets close to the on-resonance position yield better sensitivity symmetrically in a range between ±4 kHz, in agreement with the rotation improvement brought by the supercycled ^{1}H homonuclear decoupling.[86]

The same offset optimization was carried out on the different PMLG- block types, and similar trends were shown with a better sensitivity in the proximity of the on-resonance position. The offsets which gave the maximum sensitivity were 0.75 kHz for windowed $PMLG9_{mm}^{\bar{x}x}$, –0.25 kHz for $PMLG9_{mm}^{\bar{x}x}$ and +1 kHz for $PMLG5_{mm}^{\bar{x}x}$ (the same as windowed $PMLG5_{mm}^{\bar{x}x}$) (See **Fig. S4**).

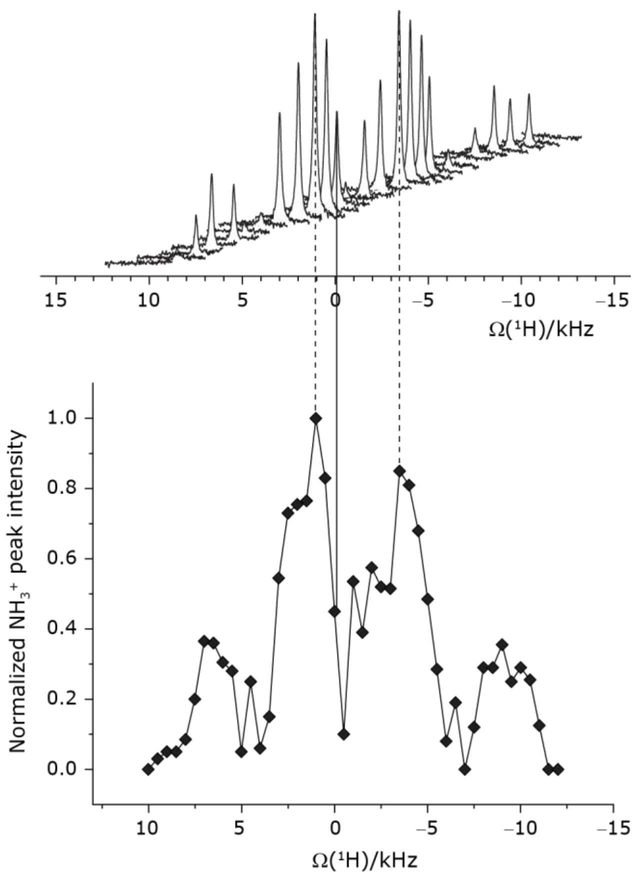

Figure 6. ^{1}H RF carrier optimization for a 1D-filtered (t_1 = 0) ^{15}N-^{1}H (ν_0 = 500 MHz) CP (contact time = 2 ms)-Refocused INEPT MAS (ν_r = 60 kHz) NMR experiment for ^{15}N-labelled glycine, whereby windowed $PMLG5_{mm}^{\bar{x}x}$ ^{1}H homonuclear decoupling was applied with τ_{LG_expt} = 3.1 µs, τ_{tilt} = 0.54 µs and a ^{1}H nutation frequency, ν_1, of 106 kHz during τ_1 (1.999 ms, 69 τ_c) and 104 kHz during τ_2 (1.391 ms ,48 τ_c). 16 transients were coadded. For all experiments with windowed ^{1}H homonuclear decoupling, τ_w = 7.20 µs. The zero-offset is set with the carrier being on resonance with the NH_3^+ peak, corresponding to the solid vertical line. Dashed vertical lines indicate the two highest signal intensities at +1 kHz and –3.5 kHz.

The implementation of the ^{1}H decoupling scheme into the heteronuclear correlation experiment required the further optimisation of the spin-echo durations during the Refocused INEPT transfer. This was carried out separately for τ_1 and τ_2 (see pulse sequence in **Fig. 1a**) because, as stated in section 3.1, for the two spin echoes, different spins are along the transverse plane, ^{15}N for the first and ^{1}H for the second spin echo. To ensure the best conditions, a double-optimisation of ^{1}H homonuclear decoupling nutation frequency vs τ_1 and τ_2 was carried out. Specifically, the two-variable optimisation was performed for ^{15}N-labelled glycine for windowed or windowless $PMLG5_{mm}^{\bar{x}x}$ and $PMLG9_{mm}^{\bar{x}x}$ for the best offset (see **Table 5**) and the results are reported in **Table 5**. The dependence with respect to the second spin-echo duration, τ_2, is presented in **Figure 7**.

Table 5 Optimised *rf* carrier offset, spin-echo duration and nutation frequencies for four implementations of PMLG ^{1}H homonuclear decoupling and MAS-alone for a ^{15}N-^{1}H CP-refocused INEPT MAS NMR experiment for ^{15}N-glycine[a]

^{1}H homonuclear decoupling	Offset (kHz)[b]	λ_{CS}	τ_1 (ms)[c]	$\lambda_{CS}\ \tau_1$ (ms)	ν_1 (kHz) for τ_1	τ_2 (ms)[c]	$\lambda_{CS}\ \tau_2$ (ms)	ν_1 (kHz) for τ_2	Relative intensity[d]
No decoupling	2.00	1.00	1.600	1.600	-	0.300	0.300	-	0.08
Windowed $PMLG5_{mm}^{\bar{x}x}$	1.00	0.82	1.999 (69 τ_c)	1.639	106	1.391 (48 τ_c)	1.140	106	1.00
Windowed $PMLG9_{mm}^{\bar{x}x}$	0.75	0.76	2.085 (71 τ_c)	1.585	104	1.498 (51 τ_c)	1.138	106	0.80
Windowless $PMLG5_{mm}^{\bar{x}x}$	1.00	0.66	2.096 (169 τ_c)	1.383	102	0.496 (40 τ_c)	0.327	102	0.52
Windowless $PMLG9_{mm}^{\bar{x}x}$	–0.25	0.60	2.091 (179 τ_c)	1.254	104	1.192 (102 τ_c)	0.715	102	0.48

[a] As implemented on at ν_0 = 500 MHz and ν_r = 60 kHz. τ_{tilt} is equal to 0.54 µs for windowed $PMLG5_{mm}^{\bar{x}x}$ and 0.82 µs for windowed $PMLG9_{mm}^{\bar{x}x}$. See **Fig. 7**
[b] relative to the NH_3^+ ^{1}H resonance
[c] $\tau_1 = n\ \tau_c$, $\tau_2 = m\ \tau_c$,where *n* and *m* are positive integers
[d] See **Fig. 8**

Considering **Table 5**, the ^{1}H nutation frequencies are in the range of 102-106 kHz for all the PMLG-block types, with a maximum of 2 kHz difference between that applied in τ_1 and τ_2 for the same PMLG block. For τ_1, the optimum values for PMLG decoupling are 2.0 or 2.1 ms, as compared to 1.6 ms from MAS alone. However, as discussed in section 3.4, it is the product $\lambda_{CS} \cdot \tau$, that needs to be considered, in which case similar values are obtained as compared to MAS alone. By comparison, a clear difference is observed for τ_2, where the evolution of ^{1}H coherence is markedly affected by the ^{1}H-^{1}H dipolar couplings. Indeed, the coherence transfer increases from 0.3 ms for MAS alone to 1.5 ms for windowed $PMLG9_{mm}^{\bar{x}x}$ and 1.4 ms for windowed $PMLG5_{mm}^{\bar{x}x}$. After scaling, the product $\lambda_{CS}\ \tau_2$, 1.14 ms for both windowed $PMLG9_{mm}^{\bar{x}x}$ and $PMLG5_{mm}^{\bar{x}x}$, are still ~4 times longer than the optimum τ_2 for MAS alone. We note a discrepancy for τ_2 under windowless $PMLG5_{mm}^{\bar{x}x}$, which is considerably shorter (0.3 ms after scaling) with respect to the other ^{1}H homonuclear implementations.

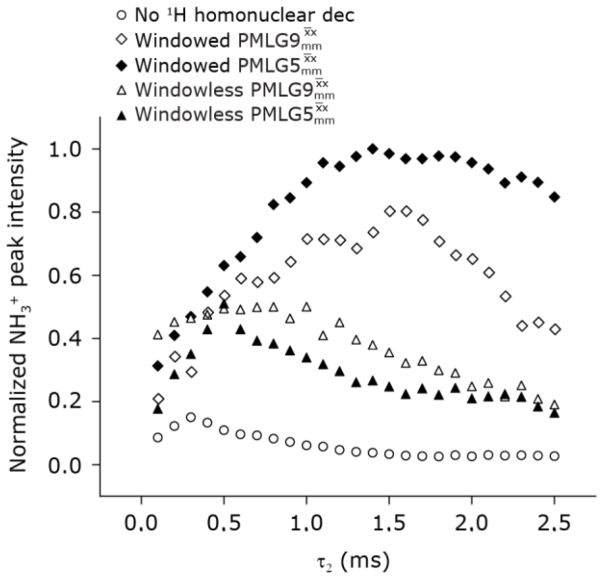

Figure 7. Dependence upon the second spin-echo duration, τ_2, for ^{15}N-labelled glycine of the NH_3^+ peak in a 1D-filtered (t_1 = 0) ^{15}N-^{1}H (ν_0 = 500 MHz) CP(contact time = 2 ms)-Refocused INEPT MAS (ν_r = 60 kHz) NMR spectrum for: windowed $PMLG5_{mm}^{\bar{x}x}$ (τ_{LG_expt} = 3.1 µs, τ_{tilt} = 0.54 µs, ν_1 = 106 kHz for τ_1 and 106 kHz for τ_2 full diamonds), windowless $PMLG5_{mm}^{\bar{x}x}$ same conditions but with no tilt pulses, full triangles, with ν_1 = 102 kHz for τ_1 and 102 kHz for τ_2), windowed $PMLG9_{mm}^{\bar{x}x}$ (τ_{LG_expt} = 2.92 µs, τ_{tilt} = 0.82 µs, ν_1 = 104 kHz for τ_1 and 106 kHz for τ_2 empty diamonds), windowless $PMLG9_{mm}^{\bar{x}x}$ same conditions but with no tilt pulses, empty triangles, with ν_1 = 104 kHz for τ_1 and 102 kHz for τ_2), MAS alone (empty circles). 8 transients were coadded. For all experiments with windowed PMLG, τ_w = 7.20 µs.

In **Figure 8**, we compare the different peak intensities for the NH_3^+ peak of ^{15}N-labelled glycine for the windowless and windowed implementation of $PMLG5_{mm}^{\bar{x}x}$ and $PMLG9_{mm}^{\bar{x}x}$ in a ^{15}N-^{1}H CP-refocused INEPT 1D filtered (t_1 = 0) spectrum. The best performance is for our optimum implementation of windowed $PMLG5_{mm}^{\bar{x}x}$ with a 12.5 times better relative sensitivity compared to MAS alone.

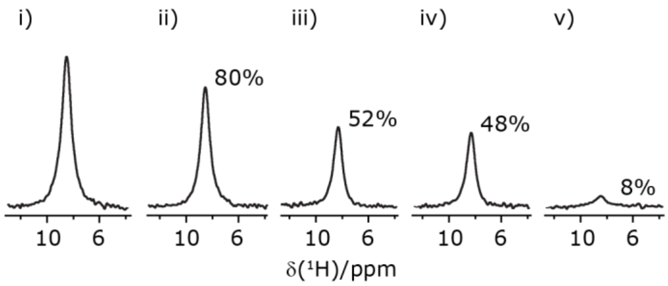

Figure 8. Comparison of the sensitivity of 1D-filtered (t_1 = 0) ^{15}N-^{1}H (ν_0 = 500 MHz) CP (contact time = 2 ms)-Refocused INEPT MAS (ν_r = 60 kHz) NMR spectra of ^{15}N-glycine recorded with the application of different optimised PMLG ^{1}H decoupling conditions, i) to iv) compared to MAS alone, v): i) windowed $PMLG5_{mm}^{\bar{x}x}$ (τ_{LG_expt} = 3.1 µs, τ_{tilt} = 0.54 µs, τ_1 = 1.999 ms (69 τ_c) with ν_1 = 106 kHz; τ_2 = 1.391 ms (48 τ_c) with ν_1 = 106 kHz), ii) windowed $PMLG9_{mm}^{\bar{x}x}$ (τ_{LG_expt} = 2.92 µs, τ_{tilt} = 0.82 µs, τ_1 = 2.085 ms (71 τ_c) with ν_1 = 104 kHz; τ_2 = 1.498 ms (51 τ_c) with ν_1 = 106 kHz), iii) windowless $PMLG5_{mm}^{\bar{x}x}$ (τ_{LG_expt} = 3.1 µs, τ_1 = 2.096 ms (169 τ_c) with ν_1 = 102 kHz; τ_2 = 0.496 ms (40 τ_c) with ν_1 = 102 kHz), iv)

windowless $PMLG9_{mm}^{\bar{x}x}$ (τ_{LG_expt} = 2.92 µs, τ_1 = 2.090 ms (179 τ_c) with ν_1 = 104 kHz; τ_2 = 1.192 ms (102 τ_c) with ν_1 = 102 kHz), v) no decoupling τ_1 = 1.6 ms (96 τ_r) and τ_2 = 0.3 ms (18 τ_r). For all experiments with windowed ^{1}H homonuclear decoupling, τ_w = 7.20 µs. All the spectra were acquired with 16 coadded transients and the corresponding ^{1}H transmitter offset reported in **Table 5**.

3.7 2D ^{15}N-^{1}H CP-refocused INEPT NMR spectra with PMLG ^{1}H decoupling at 60 kHz MAS of a dipeptide and a pharmaceutical at natural abundance

Due to the better sensitivity of windowed $PMLG5_{mm}^{\bar{x}x}$ with respect to windowed $PMLG9_{mm}^{\bar{x}x}$ and the other PMLG-type (**Fig. 8**), it was selected as the ^{1}H homonuclear decoupling sequence for a ^{15}N-^{1}H correlation experiment recorded for the β-AspAla dipeptide at natural abundance, with the improvement of resolution achieved in the 1D ^{1}H CRAMPS compared here with a ^{1}H one-pulse recorded at Larmor frequency of 500 MHz and 1 GHz (**Fig. 9a**). Note that a ^{15}N CP MAS spectrum for the β-AspAla dipeptide has been presented in Tatton *et al.*[22] The ^{15}N-^{1}H CP-Refocused INEPT was implemented with the offset and coherence transfer delays optimised for ^{15}N-labelled glycine, as stated in **Table 5**, i.e., τ_{LG_expt} = 3.1 µs, τ_{tilt} = 0.54 µs, τ_1 = 2.0 ms with ν_1 = 106 kHz, ν_2 = 1.4 ms with ν_1 = 106 kHz, and an offset of +1 kHz. High-performance ^{1}H homonuclear decoupling achieved with a finely optimised implementation of windowed $PMLG5_{mm}^{\bar{x}x}$ enables the recording at natural abundance of a 2D ^{15}N-^{1}H correlation spectrum at 60 kHz MAS with a through-bond back transfer (**Fig. 9b**). The sensitivity of the windowed $PMLG5_{mm}^{\bar{x}x}$ implementation is compared to a ^{15}N-^{1}H CP- Refocused INEPT spectrum recorded with no decoupling at the optimum τ_1 = 1.6 ms and τ_2 = 0.3 ms values in **Table 5** for ^{15}N-labelled glycine, only noise is observed in **Fig. 9c**.

Furthermore, windowed $PMLG5_{mm}^{\bar{x}x}$ was employed to record a 2D ^{15}N-^{1}H CP-Refocused INEPT spectrum of the pharmaceutical cimetidine at natural abundance (**Fig. 9d**), for which ^{1}H, ^{15}N CPMAS and ^{14}N-^{1}H spectra have been presented in Refs. [99,100]. In this case, spin-echo curves were recorded, because as discussed above the coherence transfer times during the Refocused INEPT depends both on the *J*-coupling between the involved nuclei and the ^{1}H dephasing T_2', which determines the optimum τ_1 and τ_2. The ^{1}H coherence lifetime (see **Fig. S5** and **Table S1** in comparison to Table 4) for two of the protons directly bonded to the nitrogens, N3 and N10) is longer than the NH_3^+ T_2' of ^{15}N-glycine acquired with the same windowed $PMLG5_{mm}^{\bar{x}x}$ ^{1}H decoupling. For this reason, τ_1 and τ_2 were increased to 2.5 ms and 2.0 ms, respectively. Note that weaker intensity is observed for the proton directly bonded to N15, where the respective ^{1}H T_2' is ~0.5 ms after scaling (**Table S1**). Further investigation is required to understand the shorter T_2' for this proton and the very weak signal for the N15-H15 cross peak in the 2D CP-refocused INEPT spectrum in Fig. 9d.

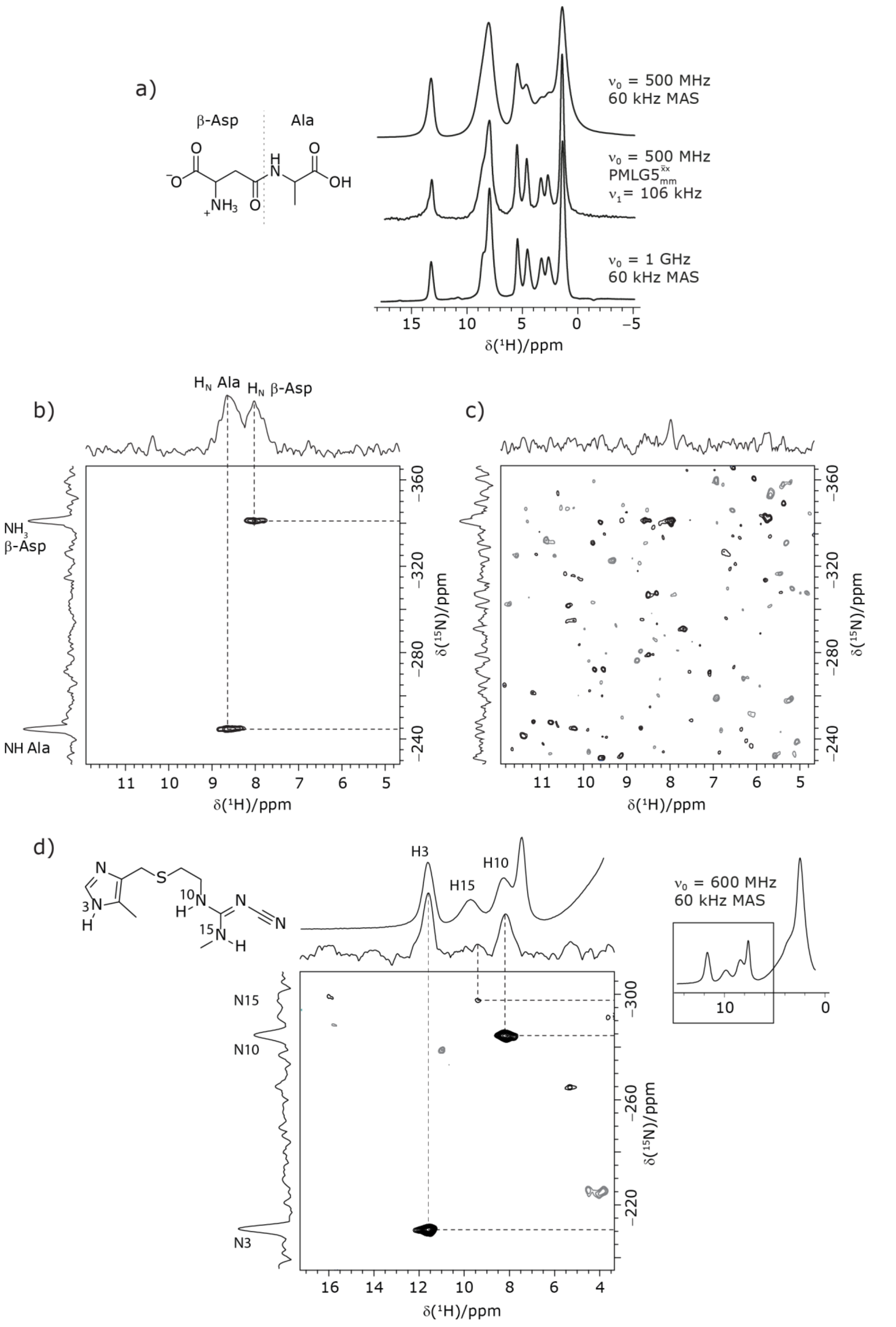
a)
β-Asp
Ala
ν0 = 500 MHz
60 kHz MAS
ν0 = 500 MHz
PMLG5
ν1 = 106 kHz
ν0 = 1 GHz
60 kHz MAS
δ(1H)/ppm
b)
HN Ala
HN β-Asp
NH3 β-Asp
NH Ala
δ(15N)/ppm
c)
d)
H3
H15
H10
N15
N10
N3
ν0 = 600 MHz
60 kHz MAS

Figure 9. MAS (ν_r = 60 kHz) NMR spectra of (a-c) the dipeptide β-AspAla and (d) the pharmaceutical cimetidine, in both cases at natural abundance, employing windowed $PMLG5_{mm}^{\bar{x}x}$ (τ_{LG_expt} = 3.1 μs, τ_{tilt} = 0.54 μs and τ_w = 7.20 μs). (a) Comparison of a ^{1}H 1D CRAMPS acquired with windowed $PMLG5_{mm}^{\bar{x}x}$ (at ν_0 = 500 MHz with ^{1}H one-pulse spectra recorded at ν_0 = 500 MHz and 1 GHz. (b, c) 2D ^{15}N-^{1}H (ν_0 = 500 MHz) CP (contact time = 2 ms)-Refocused INEPT MAS NMR spectra with (b) windowed $PMLG5_{mm}^{\bar{x}x}$ ^{1}H homonuclear decoupling during the spin-echo durations used for ^{15}N-^{1}H Refocused INEPT coherence transfer or (c) MAS alone. In (b), windowed $PMLG5_{mm}^{\bar{x}x}$ was implemented with ν_1(^{1}H) = 106 kHz during τ_1 (1.999 ms, 69 τ_c) and ν_1(^{1}H) = 106 kHz during τ_2 (1.391 ms, 48 τ_c), with the transmitter frequency centred at 10.3 ppm. For both b) and c), 224 transients were co-added for each of 96 t_1 FIDs, corresponding to a total experimental time of 23 h with a recycle delay of 3 s. The base contour is at 50 % of the respective maximum intensity in b) and c). d) A 2D ^{15}N-^{1}H (ν_0 = 600 MHz) CP (contact time = 4 ms)-Refocused INEPT MAS NMR spectrum with windowed $PMLG5_{mm}^{\bar{x}x}$ ^{1}H homonuclear decoupling (ν_1(^{1}H) = 106 kHz during τ_1 (2.491 ms, 86 τ_c) and ν_1(^{1}H) = 106 kHz during τ_2 (1.999 ms, 69 τ_c)), with the transmitter frequency centred at 11.0 ppm. 1024 transients were co-added for each of 64 t_1 FIDs, corresponding to a total experimental time of 92 h with a recycle of 5 s. The base contour is at 30 % of the maximum intensity.

4. Conclusions and Outlook

The establishing of 2D ^{15}N-^{1}H heteronuclear correlation for natural abundance solids using a ^{1}H detected CP-*J* coupling based Refocused INEPT MAS NMR experiment[26,38,39] has been demonstrated, for what we believe to be the first time, at an MAS frequency of 60 kHz. The application of ^{1}H homonuclear decoupling, specifically the $PMLG5_{mm}^{\bar{x}x}$ supercycle[26,39,57,82] results in a factor of nine sensitivity enhancement as compared to MAS alone. Notably, in our implementation at 500 MHz, a comparatively low ^{1}H nutation frequency, for a 1.3 mm rotor, of 100 kHz was used, with this being associated with a high chemical shift scaling factor of 0.82 and a large deviation from the ideal Lee-Goldburg condition. The CP-Refocused INEPT pulse sequence is complementary to dipolar coupling-based double CP or the use of symmetry-based decoupling to establish ^{15}N-^{1}H heteronuclear correlation under fast MAS.[26,29,30,101] Note that the use of symmetry-based recoupling is more prone to t_1 noise.[102-104] In future work, the extension of our approach to 100+ kHz MAS could be considered, noting an increasing number of applications to pharmaceuticals and other small and moderately sized organic molecules.[9,105-111]

Acknowledgements

JT thanks Bruker and EPSRC for a PhD studentship through the EPSRC Centre for Doctoral Training in Molecular Analytical Science, grant number EP/L015307/1. The UK High-Field Solid-State NMR Facility used in this research was funded by EPSRC and BBSRC (EP/T015063/1), as well as, for the 1 GHz instrument, EP/R029946/1. The renewal of the 600 MHz solid-state NMR console (Avance NEO) was funded by BBSRC (BB/T018119/1), EPSRC and University of Warwick.

References

1. P. C. Vioglio, M. R. Chierotti and R. Gobetto, *Adv. Drug Deliv. Rev.*, 2017, **117**, 86.
2. E. Pindelska, A. Sokal and W. Kolodziejski, *Adv. Drug Deliv. Rev.*, 2017, **117**, 111.
3. X. Lu, Y. Tsutsumi, C. Huang, W. Xu, S. R. Byrn, A. C. Templeton, A. V. Buevich, J.-P. Amoureux and Y. Su, *Phys. Chem. Chem. Phys.*, 2020, **22**, 13160.
4. M. Li, W. Xu and Y. Su, *Trac-Trends Anal. Chem.*, 2021, **135**, 116152.
5. J. R. Lewandowski, J.-N. Dumez, Ü. Akbey, S. Lange, L. Emsley and H. Oschkinat, *J. Phys. Chem. Lett.*, 2011, **2**, 2205.
6. D. Lacabanne, J. Boudet, A. A. Malär, P. Wu, R. Cadalbert, L. Salmon, F. H.-T. Allain, B. H. Meier and T. Wiegand, *J. Phys. Chem. B*, 2020, **124**, 11089.
7. V. Jirasko, A. Lends, N. A. Lakomek, M. L. Fogeron, M. E. Weber, A. A. Malär, S. Penzel, R. Bartenschlager, B. H. Meier and A. Böckmann, *Angew. Chem.*, 2021, **133**, 5399.
8. S. Bahri, R. Silvers, B. Michael, K. Jaudzems, D. Lalli, G. Casano, O. Ouari, A. Lesage, G. Pintacuda and S. Linse, *Proc. Natl. Acad. Sci.*, 2022, **119**, e2114413119.
9. U. Sternberg, R. Witter, I. Kuprov, J. M. Lamley, A. Oss, J. R. Lewandowski and A. Samoson, *J. Magn. Reson.*, 2018, **291**, 32.
10. Y. Nishiyama, *Solid State Nucl. Magn. Reson.*, 2016, **78**, 24.
11. A. A. Malär, S. Smith-Penzel, G.-M. Camenisch, T. Wiegand, A. Samoson, A. Böckmann, M. Ernst and B. H. Meier, *Phys. Chem. Chem. Phys.*, 2019, **21**, 18850.
12. M. Schledorn, A. A. Malär, A. Torosyan, S. Penzel, D. Klose, A. Oss, M. L. Org, S. Wang, L. Lecoq and R. Cadalbert, *Chembiochem*, 2020, **21**, 2540.
13. Z. Zhang, A. Oss, M.-L. Org, A. Samoson, M. Li, H. Tan, Y. Su and J. Yang, *J. Phys. Chem. Lett.*, 2020, **11**, 8077.
14. E. C.-Y. Yuan, S.-J. Huang, H.-C. Huang, J. Sinkkonen, A. Oss, M.-L. Org, A. Samoson, H.-C. Tai and J. C. C. Chan, *Chem. Commun.*, 2021, **57**, 4110.
15. Z. Gan, J. P. Amoureux and J. Trébosc, *Chem. Phys. Lett.*, 2007, **435**, 163.
16. S. Cavadini, S. Antonijevic, A. Lupulescu and G. Bodenhausen, *J. Magn. Reson.*, 2006, **182**, 168.
17. J. A. Jarvis, M. Concistre, I. M. Haies, R. W. Bounds, I. Kuprov, M. Carravetta and P. T. Williamson, *Phys. Chem. Chem. Phys.*, 2019, **21**, 5941.
18. M. Grüne, R. Luxenhofer, D. Iuga, S. P. Brown and A.-C. Pöppler, *J. Mater. Chem. B*, 2020, **8**, 6827.
19. K. Bártová, I. Císařová, A. Lyčka and M. Dračínský, *Dyes Pigment.*, 2020, **178**, 108342.
20. M. K. Pandey and Y. Nishiyama, *Phys. Chem. Chem. Phys.*, 2018, **20**, 25849.
21. A. Pugliese, M. Toresco, D. McNamara, D. Iuga, A. Abraham, M. Tobyn, L. E. Hawarden and F. Blanc, *Mol. Pharm.*, 2021, **18**, 3519.
22. A. S. Tatton, J. P. Bradley, D. Iuga and S. P. Brown, *Z. Phys. Chem.*, 2012, **226**, 1187.
23. Y. Ishii and R. Tycko, *J. Magn. Reson.*, 2000, 199.
24. Y. Ishii, J. P. Yesinowski and R. Tycko, *J. Am. Chem. Soc.*, 2001, **123**, 2921.
25. D. H. Zhou, G. Shah, C. Mullen, D. Sandoz and C. M. Rienstra, *Angew. Chem., Int. Ed. Engl.*, 2009, **48**, 1253.
26. S. M. Althaus, K. Mao, J. A. Stringer, T. Kobayashi and M. Pruski, *Solid State Nucl. Magn. Reson.*, 2014, **57-58**, 17.
27. A. Lesage, P. Charmont, S. Steuernagel and L. Emsley, *J. Am. Chem. Soc.*, 2000, **122**, 9739.
28. T. Kobayashi, K. Mao, P. Paluch, A. Nowak‐Król, J. Sniechowska, Y. Nishiyama, D. T. Gryko, M. J. Potrzebowski and M. Pruski, *Angew. Chem.*, 2013, **125**, 14358.
29. S. L. Veinberg, K. E. Johnston, M. J. Jaroszewicz, B. M. Kispal, C. R. Mireault, T. Kobayashi, M. Pruski and R. W. Schurko, *Phys. Chem. Chem. Phys.*, 2016, **18**, 17713.
30. C. Guzmán-Afonso, Y.-l. Hong, H. Colaux, H. Iijima, A. Saitow, T. Fukumura, Y. Aoyama, S. Motoki, T. Oikawa and T. Yamazaki, *Nat. Commun.*, 2019, **10**, 3537.
31. E. K. Paulson, C. R. Morcombe, V. Gaponenko, B. Dancheck, R. A. Byrd and K. W. Zilm, *J. Am. Chem. Soc.*, 2003, **125**, 15831.
32. V. Chevelkov, K. Rehbein, A. Diehl and B. Reif, *Angew. Chem., Int. Ed. Engl.*, 2006, **45**, 3878.

33. D. H. Zhou, G. Shah, M. Cormos, C. Mullen, D. Sandoz and C. M. Rienstra, *J. Am. Chem. Soc.*, 2007, **129**, 11791.
34. C. Fyfe, K. Wong-Moon, Y. Huang and H. Grondey, *J. Am. Chem. Soc.*, 1995, **117**, 10397.
35. O. Soubias, V. Réat, O. Saurel and A. Milon, *J. Magn. Reson.*, 2002, **158**, 143.
36. B. Alonso and D. Massiot, *J. Magn. Reson.*, 2003, **163**, 347.
37. B. Elena, A. Lesage, S. Steuernagel, A. Bockmann and L. Emsley, *J. Am. Chem. Soc.*, 2005, **127**, 17296.
38. K. Mao, J. W. Wiench, V. S.-Y. Lin and M. Pruski, *J. Magn. Reson.*, 2009, **196**, 92.
39. K. Mao and M. Pruski, *J. Magn. Reson.*, 2009, **201**, 165.
40. G. P. Holland, B. R. Cherry, J. E. Jenkins and J. L. Yarger, *J. Magn. Reson.*, 2010, **202**, 64.
41. P. K. Madhu, *Solid State Nucl. Magn. Reson.*, 2009, **35**, 2.
42. K. R. Mote, V. Agarwal and P. K. Madhu, *Prog. Nucl. Magn. Reson. Spectrosc.*, 2016, **97**, 1.
43. P. Hodgkinson, *Annu. Rep. NMR Spectrosc.*, 2011, **72**, 185.
44. E. Vinogradov, P. K. Madhu and S. Vega, *New Techniques in Solid-State NMR*, 2005, 33.
45. M. Lee and W. I. Goldburg, *Phys. Rev.*, 1965, **140**, A1261.
46. M. H. Levitt, A. C. Kolbert., A. Bielecki and D. J. Ruben, *Solid State Nucl. Magn. Reson.*, 1993, **2**, 151.
47. M. Hohwy and N. C. Nielsen, *J. Chem. Phys.*, 1997, **106**, 7571.
48. M. Hohwy, P. Bower, H. Jakobsen and N. Nielsen, *Chem. Phys. Lett.*, 1997, **273**, 297.
49. E. Vinogradov, P. K. Madhu and S. Vega, *Chem. Phys. Lett.*, 1999, **314**, 443.
50. D. Sakellariou, A. Lesage, P. Hodgkinson and L. Emsley, *Chem. Phys. Lett.*, 2000, 253.
51. P. Madhu, X. Zhao and M. H. Levitt, *Chem. Phys. Lett.*, 2001, **346**, 142.
52. M. E. Halse and L. Emsley, *Phys. Chem. Chem. Phys.*, 2012, **14**, 9121.
53. F. M. Paruzzo and L. Emsley, *J. Magn. Reson.*, 2019, **309**, 106598.
54. C. Coelho, J. Rocha, P. Madhu and L. Mafra, *J. Magn. Reson.*, 2008, **194**, 264.
55. I. Schnell, S. P. Brown, H. Y. Low, H. Ishida and H. W. Spiess, *J. Am. Chem. Soc.*, 1998, **120**, 11784.
56. J.-P. Amoureux, B. Hu, J. Trébosc, Q. Wang, O. Lafon and F. Deng, *Solid State Nucl. Magn. Reson.*, 2009, **35**, 19.
57. Y. Nishiyama, X. Lu, J. Trebosc, O. Lafon, Z. Gan, P. K. Madhu and J. P. Amoureux, *J. Magn. Reson.*, 2012, **214**, 151.
58. E. Salager, J.-N. Dumez, R. S. Stein, S. Steuernagel, A. Lesage, B. Elena-Herrmann and L. Emsley, *Chem. Phys. Lett.*, 2010, **498**, 214.
59. M. Leskes, S. Steuernagel, D. Schneider, P. K. Madhu and S. Vega, *Chem. Phys. Lett.*, 2008, **466**, 95.
60. J.-P. Amoureux, B. Hu and J. Trébosc, *J. Magn. Reson.*, 2008, **193**, 305.
61. Z. Gan, P. Madhu, J.-P. Amoureux, J. Trébosc and O. Lafon, *Chem. Phys. Lett.*, 2011, **503**, 167.
62. E. Salager, R. S. Stein, S. Steuernagel, A. Lesage, B. Elena and L. Emsley, *Chem. Phys. Lett.*, 2009, **469**, 336.
63. B. Gerstein, R. Pembleton, R. Wilson and L. Ryan, *J. Chem. Phys.*, 1977, **66**, 361.
64. E. Salager, J. N. Dumez, L. Emsley and M. H. Levitt, *J. Magn. Reson.*, 2011, **212**, 11.
65. M. Leskes, P. K. Madhu and S. Vega, *J. Magn. Reson.*, 2009, **199**, 208.
66. R. Ramesh and M. S. Krishnan, *J. Chem. Phys.*, 2001, **114**, 5967.
67. S. Hayashi and K. Hayamizu, *Bull. Chem. Soc. Jpn.*, 1991, **64**, 685.
68. E. K. Corlett, H. Blade, L. P. Hughes, P. J. Sidebottom, D. Walker, R. I. Walton and S. P. Brown, *Crystengcomm*, 2019, **21**, 3502.
69. S. Hayashi and K. Hayamizu, *Bull. Chem. Soc. Jpn.*, 1991, **64**, 688.
70. R. K. Harris, E. D. Becker, S. M. C. De Menezes, P. Granger, R. E. Hoffman and K. W. Zilm, *Pure Appl. Chem.*, 2008, **80**, 59.
71. G. E. Martin and C. E. Hadden, *J. Nat. Prod.*, 2000, **63**, 543.
72. B. Meier, *Chem. Phys. Lett.*, 1992, **188**, 201.
73. S. Laage, J. R. Sachleben, S. Steuernagel, R. Pierattelli, G. Pintacuda and L. Emsley, *J. Magn. Reson.*, 2009, **196**, 133.
74. G. Metz, X. Wu and S. O. Smith, *J. Magn. Reson.*, 1994, **110**, 219.
75. D. H. Zhou and C. M. Rienstra, *J. Magn. Reson.*, 2008, **192**, 167.

76. M. Ernst, M. A. Meier, T. Tuherm, A. Samoson and B. H. Meier, *J. Am. Chem. Soc.*, 2004, **126**, 4764.
77. A. Shaka, J. Keeler and R. Freeman, *J. Magn. Reson. (1969)*, 1983, **53**, 313.
78. Z. Zhou, R. Kummerle, X. Qiu, D. Redwine, R. Cong, A. Taha, D. Baugh and B. Winniford, *J. Magn. Reson.*, 2007, **187**, 225.
79. A. Lesage, S. Steuernagel and L. Emsley, *J. Am. Chem. Soc.*, 1998, **120**, 7095.
80. A. S. Tatton, I. Frantsuzov, S. P. Brown and P. Hodgkinson, *J. Chem. Phys.*, 2012, **136**, 084503.
81. A. Lesage, L. Emsley, M. Chabanas, C. Coperet and J.-M. Basset, *Angew. Chem.*, 2002, **114**, 4717.
82. M. Leskes, P. K. Madhu and S. Vega, *Chem. Phys. Lett.*, 2007, **447**, 370.
83. M. Mehring and J. Waugh, *Phys. Rev. B*, 1972, **5**, 3459.
84. A. Bielecki, A. C. Kolbert and M. H. Levitt, *Chem. Phys. Lett.*, 1989, **155**, 341.
85. E. Vinogradov, P. K. Madhu and S. Vega, *Chem. Phys. Lett.*, 2002, **354**, 193.
86. M. Leskes, P. K. Madhu and S. Vega, *J. Chem. Phys.*, 2006, **125**, 124506.
87. S. Paul, R. S. Thakur, M. Goswami, A. C. Sauerwein, S. Mamone, M. Concistre, H. Forster, M. H. Levitt and P. K. Madhu, *J. Magn. Reson.*, 2009, **197**, 14.
88. V. E. Zorin, M. Ernst, S. P. Brown and P. Hodgkinson, *J. Magn. Reson.*, 2008, **192**, 183.
89. C. Coelho, J. Rocha, P. K. Madhu and L. Mafra, *J. Magn. Reson.*, 2008, **194**, 264.
90. K. Mao and M. Pruski, *J. Magn. Reson.*, 2010, **203**, 144.
91. S. Hafner and H. W. Spiess, *J. Magn. Reson. Ser. A*, 1996, **121**, 160.
92. E. Vinogradov, P. Madhu and S. Vega, *Chem. Phys. Lett.*, 2000, **329**, 207.
93. A. Lesage, D. Sakellariou, S. Hediger, B. Eléna, P. Charmont, S. Steuernagel and L. Emsley, *J. Magn. Reson.*, 2003, **163**, 105.
94. J. S. Waugh, L. M. Huber and U. Haeberlen, *Phys. Rev. Lett.*, 1968, **20**, 180.
95. A. J. Vega, *J. Magn. Reson.*, 2004, **170**, 22.
96. A. Lesage, M. Bardet and L. Emsley, *J. Am. Chem. Soc.*, 1999, **121**, 10987.
97. V. E. Zorin, S. P. Brown and P. Hodgkinson, *J. Chem. Phys.*, 2006, **125**, 144508.
98. L. Bosman, P. K. Madhu, S. Vega and E. Vinogradov, *J. Magn. Reson.*, 2004, **169**, 39.
99. A. S. Tatton, T. N. Pham, F. G. Vogt, D. Iuga, A. J. Edwards and S. P. Brown, *Crystengcomm*, 2012, **14**, 2654.
100. K. Maruyoshi, D. Iuga, A. E. Watts, C. E. Hughes, K. D. Harris and S. P. Brown, *J. Pharm. Sci.*, 2017, **106**, 3372.
101. F. A. Perras, T. W. Goh, L.-L. Wang, W. Huang and M. Pruski, *Solid State Nucl. Magn. Reson.*, 2019, **98**, 12.
102. A. J. Robertson, M. K. Pandey, A. Marsh, Y. Nishiyama and S. P. Brown, *J. Magn. Reson.*, 2015, **260**, 89.
103. M. Shen, S. Wegner, J. Trébosc, B. Hu, O. Lafon and J.-P. Amoureux, *Solid State Nucl. Magn. Reson.*, 2017, **87**, 111.
104. A. Venkatesh, X. Luan, F. A. Perras, I. Hung, W. Huang and A. J. Rossini, *Phys. Chem. Chem. Phys.*, 2020, **22**, 20815.
105. Y. Nishiyama, M. Malon, Y. Ishii and A. Ramamoorthy, *J. Magn. Reson.*, 2014, **244**, 1.
106. Y. Nishiyama, T. Kobayashi, M. Malon, D. Singappuli-Arachchige, I. Slowing and M. Pruski, *Solid State Nucl. Magn. Reson.*, 2015, **66**, 56.
107. J. Struppe, C. M. Quinn, M. Lu, M. Wang, G. Hou, X. Lu, J. Kraus, L. B. Andreas, J. Stanek and D. Lalli, *Solid State Nucl. Magn. Reson.*, 2017, **87**, 117.
108. J. Struppe, C. M. Quinn, S. Sarkar, A. M. Gronenborn and T. Polenova, *Mol. Pharm.*, 2019, **17**, 674.
109. R. Zhang, Y.-l. Hong, T. Ravula, Y. Nishiyama and A. Ramamoorthy, *J. Magn. Reson.*, 2020, **313**, 106717.
110. P. Moutzouri, F. M. Paruzzo, B. Simoes de Almeida, G. Stevanato and L. Emsley, *Angew. Chem., Int. Ed. Engl.*, 2020, **59**, 6235.
111. P. Moutzouri, B. Simões de Almeida, D. Torodii and L. Emsley, *J. Am. Chem. Soc.*, 2021, **143**, 9834.

Table of Contents

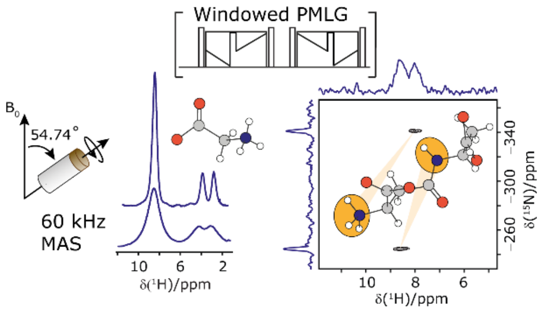

Application to a dipeptide and a pharmaceutical of ^{15}N-^{1}H heteronuclear NMR correlation at natural abundance in the solid state via *J* couplings is enabled by optimisation of phase-modulated Lee-Goldburg (PMLG) ^{1}H homonuclear decoupling, far from the ideal magic-angle condition, during the spin-echo durations.

5.1 Supporting Information

Electronic Supplementary Information (ESI)

^{15}N-^{1}H through-bond heteronuclear correlation solid-state NMR spectroscopy with ^{1}H homonuclear decoupling at 60 kHz MAS

Jacqueline Tognetti, W. Trent Franks, Józef R. Lewandowski, Steven P. Brown

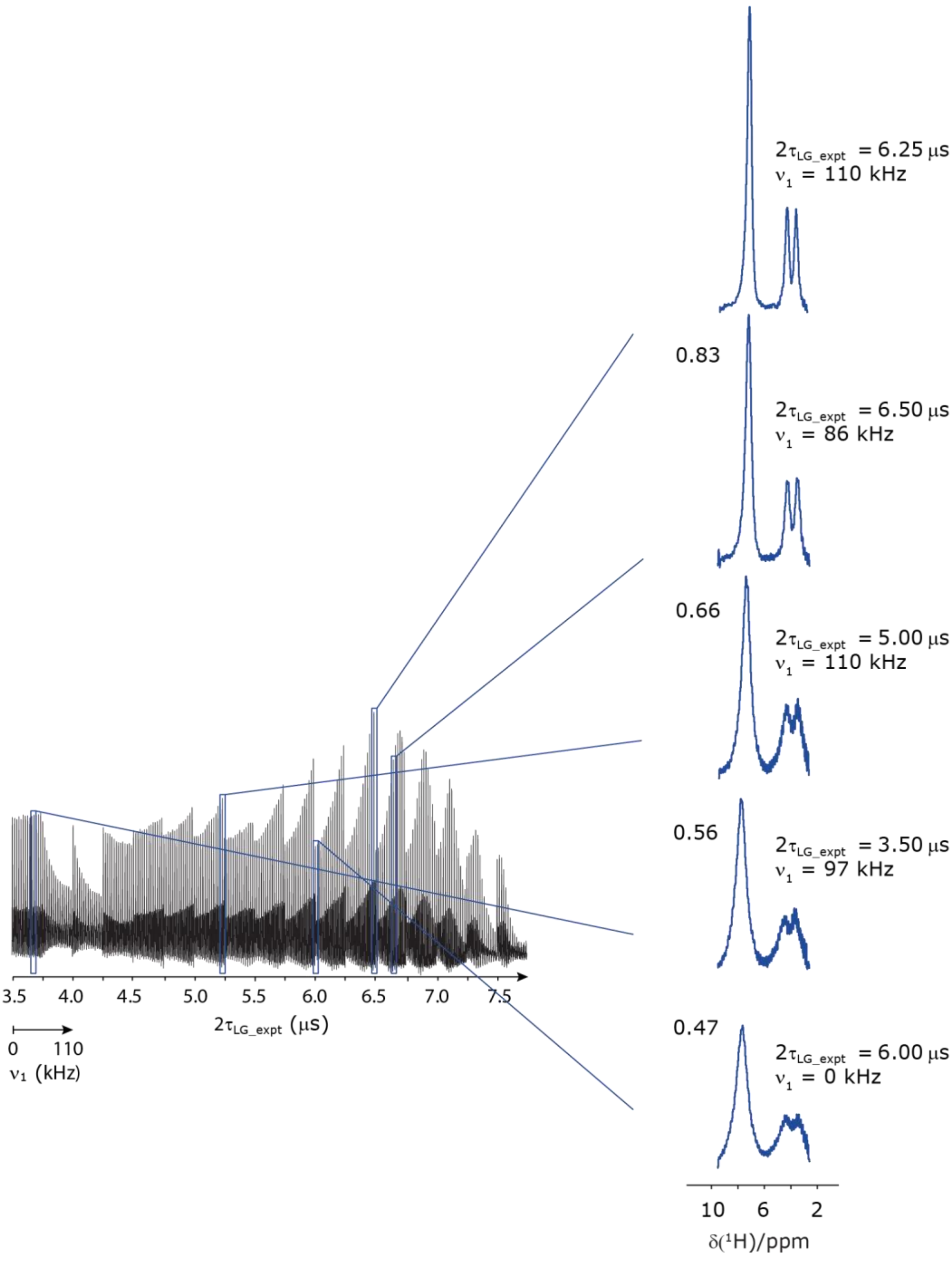

Figure S1. A stacked representation of a two-variable optimization (see **Fig. 3a**) of both τ_{LG_expt} (in steps of 0.25 µs) and ν_1 in a 1D ^{1}H-CRAMPS (ν_0 = 500 MHz) MAS (ν_r = 60 kHz) NMR experiment of ^{15}N-glycine, in which windowed $PMLG5_{mm}^{\bar{x}x}$ was applied with τ_{tilt} = 0.54 μs and a ^{1}H transmitter offset of –0.6 kHz, corresponding to the data shown in Figure 3a of the main text. 8 co-added transients were collected for each optimization point. On the right, slices from the optimization are shown with the associated τ_{LG_expt} and ν_1. The relative intesity of the NH_3^+ peak with respect to the best ^{1}H homonuclear decoupling performance at 2 τ_{LG_expt} = 6.25 μs and ν_1 = 110 kHz is stated.

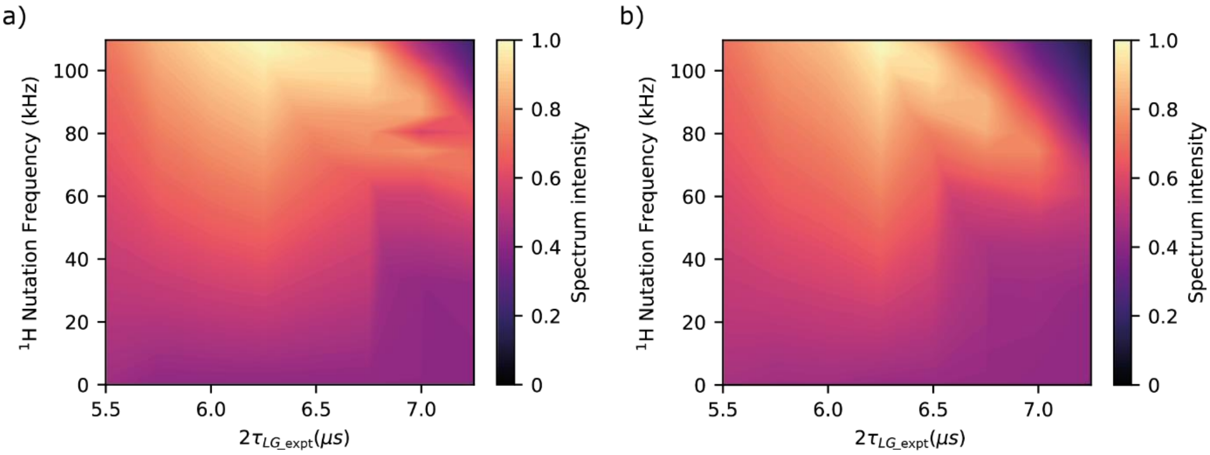

Figure S2. Zoom of the region between τ_{LG_expt} = 5.5 μs – 7.5 μs of the two-variable optimization of τ_{LG_expt} (in steps of 0.25 μs) and ν_1 in a 1D ^{1}H-CRAMPS (ν_0 = 500 MHz) MAS (ν_r = 60 kHz) NMR spectrum of the ^{15}N-glycine a) CH_2 and b) NH_3^+ peak intensity, corresponding to the data shown in Figure 3a of the main text. Windowed $PMLG5_{mm}^{\bar{x}x}$ was applied with τ_w = 7.20 μs, τ_{tilt} = 0.54 μs and a ^{1}H transmitter offset of –0.6 kHz. 8 co-added transients were collected for each optimization point for a recycle delay of 3 s.

2D ^{1}H-^{1}H correlation. Each ^{1}H-detected FID was acquired for 30 ms with a spectral width of 57 ppm. The ^{1}H indirect dimension was acquired with 96 t_1 FIDs with a dwell time of 29.16 µs (57 ppm spectral width - no ^{1}H homonuclear decoupling), 12.40 µs (134 ppm spectral width - windowless $PMLG5_{mm}^{\bar{x}x}$) and 11.68 µs (143 ppm – windowless $PMLG9_{mm}^{\bar{x}x}$). The maximum t_1 were 1.40 ms, 0.59 ms and 0.56 ms using no ^{1}H homonuclear decoupling, windowless $PMLG5_{mm}^{\bar{x}x}$ and windowless $PMLG9_{mm}^{\bar{x}x}$, respectively. The States-TPPI method was employed to achieve sign discrimination in the indirect dimension.

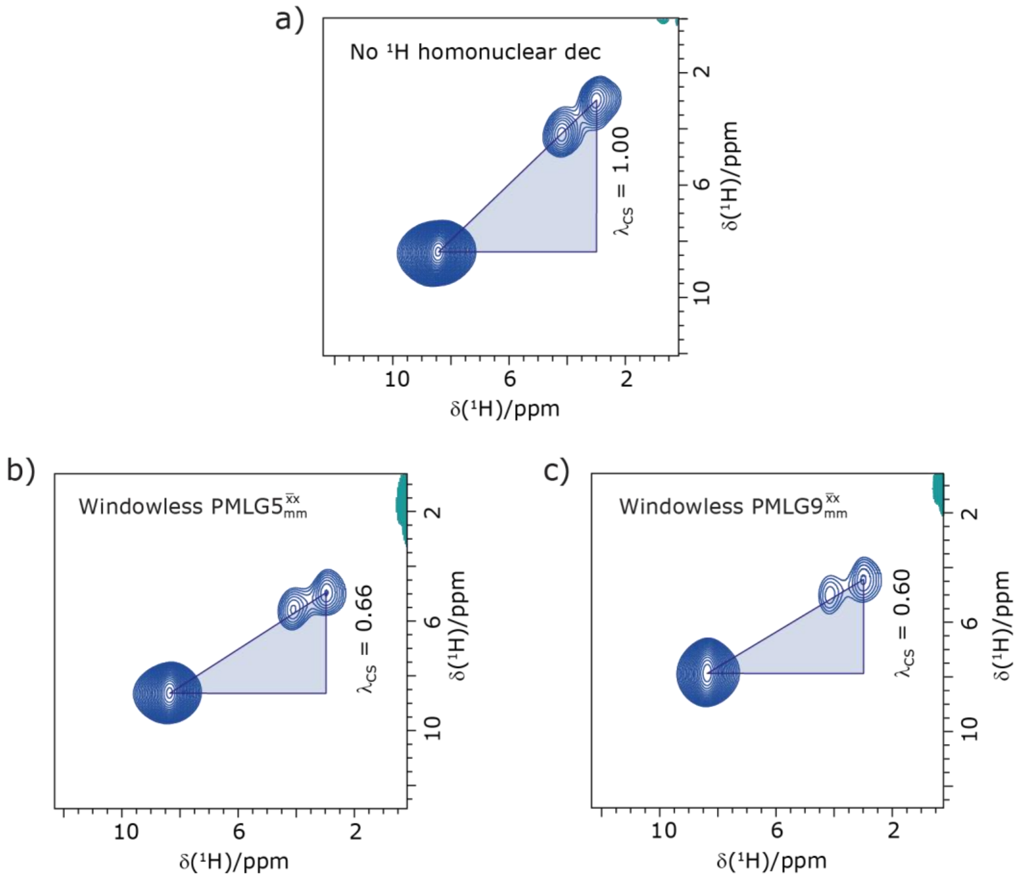

Figure S3. 2D ^{1}H-^{1}H (ν_0 = 600 MHz) correlation spectra of ^{15}N-Glycine acquired at ν_r = 60 kHz MAS with a) no ^{1}H homonuclear decoupling, b) windowless $PMLG5_{mm}^{\bar{x}x}$ (τ_{LG} = 3.10 µs, ν_1 = 104 kHz, Ω = 1 kHz) and c) b) windowless $PMLG9_{mm}^{\bar{x}x}$ (τ_{LG} = 2.92 µs, ν_1 = 104 kHz, Ω = –0.8 kHz). In all the experiments 4 transients were coadded for 96 t_1 FIDs for a recycle delay of 3 s. The zero-offset is set with the carrier being on resonance with the NH_3^+ peak in the indirect dimension.

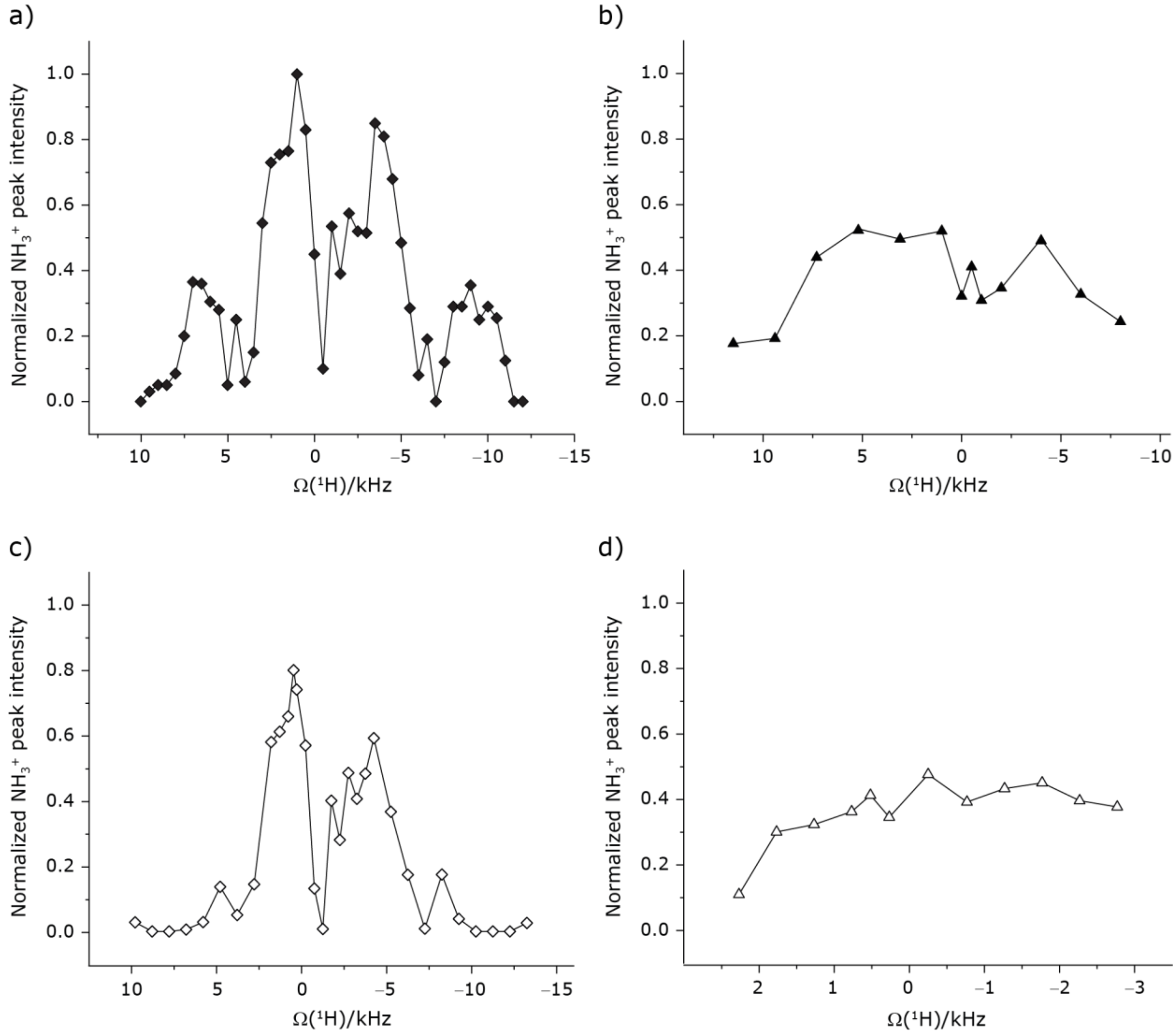

Figure S4. ^1H RF carrier optimization for a 1D-filtered (t_1 = 0) ^{15}N-^1H (ν_0 = 500 MHz) CP (contact time = 2 ms)-Refocused INEPT MAS (ν_r = 60 kHz) NMR experiment for ^{15}N-labelled glycine, whereby a) windowed $PMLG5_{mm}^{\bar{x}x}$ ^1H homonuclear decoupling (See **Fig. 6**) was applied with τ_{LG_expt} = 3.1 µs, τ_{tilt} = 0.54 µs and a ^1H nutation frequency, ν_1, of 106 kHz during τ_1 (1.999 ms, 69 τ_c) and 104 kHz during τ_2 (1.391 ms ,48 τ_c), b) windowless $PMLG5_{mm}^{\bar{x}x}$ ^1H homonuclear decoupling was applied with τ_{LG_expt} = 3.1 µs and a ^1H nutation frequency, ν_1, of 104 kHz during τ_1 (2.096 ms, 169 τ_c) and 102 kHz during τ_2 (0.496 ms, 40 τ_c), c) windowed $PMLG9_{mm}^{\bar{x}x}$ ^1H homonuclear decoupling was applied with τ_{LG_expt} = 2.92 µs, τ_{tilt} = 0.82 µs and a ^1H nutation frequency, ν_1, of 104 kHz during τ_1 (2.085 ms, 71 τ_c) and 106 kHz during τ_2 (1.498 ms, 51 τ_c) and d) windowless $PMLG9_{mm}^{\bar{x}x}$ ^1H homonuclear decoupling was applied with τ_{LG_expt} = 2.92 µs and a ^1H nutation frequency, ν_1, of 104 kHz during τ_1 (2.091 ms, 179 τ_c) and 102 kHz during τ_2 (1.192 ms, 102 τ_c). 16 transients were coadded. For all experiments with windowed decoupling τ_w was substituted with a delay of 7.20 µs. The zero-offset is set with the carrier being on resonance with the NH_3^+ peak.

Cimetidine

Here, the normalized intensity is related to the respective maximum intensity for each peak , i.e. the maximum intensity is equal to 1 for all the resonances. However, note that the NH15 proton signal intensity is ~30 % of that of NH3.

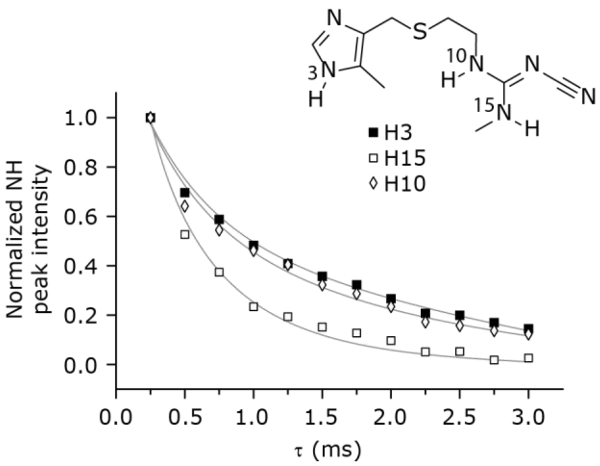

Figure S5. Dephasing of cimetidine NH proton (ν_0 = 600 MHz) resonances as a function of the spin-echo duration, τ, with windowed $PMLG5_{mm}^{\bar{x}x}$ (τ_{LG_expt} = 3.10 µs, τ_{tilt} = 0.54 µs and τ_w = 7.20 µs) for a nutation frequency of 106 kHz. Fits to an exponential decay function are shown, with the spin-echo dephasing times, T_2', as listed in **Table S1**. 8 transients were co-added for a recycle delay of 5 s.

Table S1. Cimetidine ^{1}H dephasing time, T_2', for the three NH resonances and T_2' scaled by the experimental λ_{CS},, λ_{CS} T_2', acquired on a ^{1}H spin-echo[a] experiment using windowed $PMLG5_{mm}^{\bar{x}x}$ [b]

	δ (ppm)	ν_1 (kHz)	λ_{CS}	T_2' (ms)	λ_{CS} T_2' (ms)
NH3	11.6			1.34	1.10
NH15	9.7	106	0.82	0.58	0.48
NH10	8.2			1.23	1.01

[a]Implemented at ν_0 = 600 MHz and ν_r = 60 kHz (see Fig. S5). Windowed $PMLG5_{mm}^{\bar{x}x}$ was implemented with τ_{LG} = 3.10 µs, τ_{tilt} = 0.54 µs and τ_w = 7.20 µs

[b] Ω_{rf} = – 0.8 kHz, where the zero-offset is set with the carrier being on resonance with the NH_3^+ peak of ^{15}N-glycine

Chapter 6

Accelerating ^{15}N and ^{13}C R_1 and $R_{1\rho}$ Relaxation Measurements by Multiple Pathway Solid-State NMR Experiments

Journal of Magnetic Resonance 331 (2021) 107049

Contents lists available at ScienceDirect

Journal of Magnetic Resonance

journal homepage: www.elsevier.com/locate/jmr

Accelerating ^{15}N and ^{13}C R_1 and $R_{1\rho}$ relaxation measurements by multiple pathway solid-state NMR experiments

Jacqueline Tognetti [a,b], W. Trent Franks [a,b], Angelo Gallo [b], Józef R. Lewandowski [b,*]

[a] Department of Physics, University of Warwick, Coventry CV4 7AL, United Kingdom
[b] Department of Chemistry, University of Warwick, Coventry CV4 7AL, United Kingdom

ARTICLE INFO

Article history:
Received 8 July 2021
Revised 9 August 2021
Accepted 11 August 2021
Available online 21 August 2021

Keywords:
Solid-state NMR
Magic angle spinning
NMR relaxation
Staggered acquisition

ABSTRACT

Magic angle spinning (MAS) Solid-state NMR is a powerful technique to probe dynamics of biological systems at atomic resolution. R_1 and $R_{1\rho}$ relaxation measurements can provide detailed insight on amplitudes and time scales of motions, especially when information from several different site-specific types of probes is combined. However, such experiments are time-consuming to perform. Shortening the time necessary to record relaxation data for different nuclei will greatly enhance practicality of such approaches. Here, we present staggered acquisition experiments to acquire multiple relaxation experiments from a single excitation to reduce the overall experimental time. Our strategy enables one to collect ^{15}N and ^{13}C relaxation data in a single experiment in a fraction of the time necessary for two separate experiments, with the same signal to noise ratio.

1. Introduction

Quantifying biomolecular motions plays a fundamental role towards the understanding of biophysical processes as modulated by protein dynamics. In solid-state NMR the range of time scales that can be detected by relaxation experiments is not limited by overall tumbling as in solution-state NMR. Molecular processes that are characteristic of protein functions like enzymatic catalysis, protein folding, and ligand binding are on the order of µs-ms which is the same as the timescale amenable for study by solid state NMR using relaxation techniques. NMR relaxation [1–4] experiments, however, are time-consuming considering the very long delays necessary to adequately sample relaxation times and the large number of scans often required to achieve appropriate signal to noise ratios for challenging systems [5–7]. In particular, ^{15}N R_1 can be < 0.02 s^{-1} requiring relaxation delays up to ~ 50 s (on top of the recycling delay). In addition, the description of protein motions spanning a wide range of time scales, often requires access to multiple independent probes in order to obtain a detailed view of dynamics, *e.g.* joint use of ^{15}N and ^{13}C' relaxation leads to an improved view of backbone dynamics [2]. Finally, some experiments require multiple measurements on the same probes under different conditions, *e.g.* relaxation dispersion where $R_{1\rho}$ is measured as a function of the applied field strength of the spin-locking pulses [6,8] or variable temperature measurements [9,10]. Overall, this means that quantification of protein dynamics may involve recording many time-consuming experiments, which limits the wide adoption of this powerful methodology. In order to make such studies more widespread, it will be thus useful to develop approaches which reduce the overall experimental time required.

Paramagnetic doping is a widely applicable approach to reduce the recycling times in solid-state NMR experiments [11–14]. However, the addition of paramagnetic dopants will also change the measured ^{15}N and ^{13}C relaxation rates [6], with the contribution related to the distance of the monitored site to the paramagnetic centre often dominating the contributions from the local dynamics [15]. Similarly to paramagnetic doping, for a number of reasons, selective excitation methods popular in solution NMR [16,17] are not yet appropriate for accelerating quantitative relaxation measurements in solids.

Solid-state NMR experiments could be devised to use the available initial polarization more efficiently than standard approaches, *e.g.* time-shared experiments and sequential acquisition experiments that exploit orphaned polarization. Time-shared experiments [18,19] pass the signal through multiple polarization pathways and collect all experiments at once. In the Dual Acquisition Magic Angle Spinning (DUMAS) [20] acquisition scheme, the acquisition of the nitrogen and carbon-based experiments are separated in time (with polarization from one source being stored) to eliminate signal overlap from the separate experiments. This

* Corresponding author.
E-mail address: J.R.Lewandowski@warwick.ac.uk (J.R. Lewandowski).

https://doi.org/10.1016/j.jmr.2021.107049
1090-7807/© 2021 The Authors. Published by Elsevier Inc.

multiple acquisition scheme has been also used for ^{1}H detection [21], for detection of orphaned polarization [22], for use with multiple receivers [21], and for mixed dimensionality multi-receiver experiments [23]. Sequential acquisition results in a small time-penalty for the second acquisition but the time loss is usually very short compared to the recovery time.

In this study, we present experiments to measure ^{15}N/^{13}C $R_{1\rho}$ [1,2,8,24,25] and R_1 [26,27], with staggered acquisition ^{1}H-detected experiments. We demonstrate that relaxation measurements on a model protein obtained with staggered and standard acquisition are the same within the experimental error. We quantify sensitivity of the multiple acquisition experiments and the overall experimental time gains with respect to the standard experiments.

2. Experimental

Uniformly [^{1}H,^{13}C,^{15}N] labelled GB1 was prepared as described previously [28] and doped with 4,4-dimethyl-4-silapentane-1-sul fonic acid (DSS) as an internal standard. ~ 0.5 mg of hydrated microcrystalline protein was centrifuged into a 0.7 mm solid-state NMR rotor using a device developed in-house [29].

All experiments were performed on a Bruker Avance III spectrometer, using a Bruker HCND Probe operating in triple resonance at 700.13 ^{1}H Larmor frequency and sample spinning rate of 100 kHz +/- 3 Hz. The experiments were carried out at a nominal temperature of 281.2 K (based on external calibration, calculated by the difference between the water and sodium 3-(trimethylsi lyl)propane-1-sulfonate (DSS) peaks) using a gas flow of 400 L/h [30,31]. The nutation frequencies for the 90° pulses were calibrated so that ^{1}H is at 2 μs (ν_1 = 125 kHz); ^{13}C, 2.5 μs (ν_1 = 100 kHz); and ^{15}N, 4.15 μs (ν_1 = 60.24 kHz). The ^{15}N carrier radiofrequency (RF) was centred at 120 ppm, while the ^{13}C was placed at 55 ppm and 175 ppm, for ^{13}C$^\alpha$ and ^{13}C' respectively. The carbon frequency was moved by changing the carrier frequency in the Bruker pulse code using pre-determined constants. The ^{1}H carrier was placed near the water frequency (~4.7 ppm) for the standard ^{15}N $R_{1\rho}$ relaxation experiment. Each ^{1}H free induction decay was acquired for 30 ms with a spectral width of 35 ppm with 16 coadded transients. Both the ^{15}N and ^{13}C' dimensions for the $R_{1\rho}$ experiments were acquired with 82 rows with a dwell of 300 μs, with a spectral width of 47 ppm (^{15}N) and 19 ppm (^{13}C'), for a total of 12.6 ms in the indirect dimensions. In the hcαC'cαHα + hNH$_N$ variant, both the ^{15}N and ^{13}C' dimensions were acquired with 72 rows with a dwell of 300 μs, maintaining the same spectral widths. The number of rows sampled in the indirect dimension of the two parts of the simultaneous experiment must be the same, but the spectral width is not restricted in this way. For the R_1 measurements ^{15}N and ^{13}C'dimensions were acquired with 64 rows with a dwell of 300 μs, with a spectral width of 47 ppm (^{15}N) and 19 ppm (^{13}C'), for a total of 9.6 ms in the indirect dimensions. The recovery delay was 2.5 s for all the $R_{1\rho}$ experiments and 1.5 s for the R_1 measurements. The States-TPPI method was employed for quadrature detection in the indirect dimensions [32]. Heteronuclear ^{1}H decoupling (~10 kHz WALTZ-64 [33]) was applied during t_1 evolution on ^{13}C, ^{15}N, and during the COSY-based transfers. Heteronuclear decoupling on the ^{13}C channel (~10 kHz WALTZ-64) was applied during both direct acquisitions, while ^{15}N heteronuclear decoupling (~10 kHz WALTZ-64) was only used for the HN acquisition. The MISSISSIPPI [34] solvent suppression scheme was applied with a spinlock field of ~ 50 kHz for four 20 ms intervals for the $R_{1\rho}$ and R_1 singleton experiments, and the R_1 staggered experiments. For the $R_{1\rho}$ staggered experiments the four MISSISSIPPI intervals were 20 ms for the first ^{13}C' pathway acquisition, and 7.5 ms for the subsequent ^{15}N pathway. All spinlock fields for the $R_{1\rho}$ experiments were calibrated to be ν_1 = 5 kHz by nutation; eleven points from 2 ms to 210 ms were collected. The spacing between points in the delay schedules for the R_1 measurements is based on the spacing of the Fibonacci sequence where appropriate beginning and ending times were chosen based on previous experience. The complete set of time-points used for both $R_{1\rho}$ and R_1 can be found in the supporting information.

Simultaneous cross-polarization (SIM-CP) [35] was used for the initial excitation of ^{13}C and ^{15}N, where the average ^{1}H field was ~ 130 kHz with a linear 15% ramp (85%-100%, from ~ 121.5 to 139.5 kHz) using a zero-quantum (ZQ) match condition transfer for both ^{13}C and ^{15}N, where both channels are irradiated at ~ 30 kHz, and the carrier is on resonance with the indicated resonance. The contact times for ^{13}C$^\alpha$, ^{13}C' and ^{15}N were optimized on both the single and staggered pathway correlation experiments. The contact time was 2.1 ms for ^{1}H–^{13}C' CP and 150 μs for the ^{1}H–^{13}C$^\alpha$ CP. For the ^{1}H–^{15}N CP, the contact times were 2 ms and 1.7 ms for individual and staggered $R_{1\rho}$ measurements respectively. The ^{1}H pulse duration is set to the longest contact time of the two nuclei for SIM-CP. Polarization is always stored on the low-gamma nuclei after CP, no matter which CP time is longer, to provide the most flexibility in CP times. Our pulse sequence naming convention indicates all transfer steps in the sequence by nucleus name. An upper-case nucleus indicates that the chemical shift is evolved. A lower-case name indicates that polarization is transferred through, but there is no chemical shift evolution (this is sometimes designated with parentheses). A pulse sequence name with square braces where nucleus names are separated by commas indicates separate polarization pathways in the same experiment. In the text, we refer to these experiments with a "+" between the independent experiments.

Gaussian Q3 cascade pulses were calibrated for selective ^{13}C inversion where a 320 μs pulse gives a bandwidth of 10.5 kHz (~60 ppm) and 760 μs produces a bandwidth of 5.3 kHz (~30 ppm) for ^{13}C' and ^{13}C$^\alpha$ respectively. For the selective ^{13}C$^\alpha$–^{13}C' coherence transfer, the J-coupling delay (τ) was 3.5 ms in the $R_{1\rho}$ measurements and 3 ms in the R_1 measurements for the period were the ^{13}C$^\alpha$ magnetization is transverse and 4.25 ms for the period where ^{13}C' is transverse. The pulse sequences, datasets, lists, compound pulse lists, and pulse shapes can be found online in the Mendeley Data: http://dx.https://doi.org/10.17632/x7kk4rkpj3.1.

All relaxation rates are reported at the 95% confidence level from 2000 steps of Monte Carlo error analysis [36].

3. Results and discussion

Quantification of protein dynamics based on relaxation rates relies on suppression of coherent effects that can obscure the information on the molecular motions encoded in the measured rates [4]. For example, in uniformly [^{1}H,^{13}C,^{15}N] labelled samples, spin diffusion [27,37,38] will lead to the averaging of the rates for nearby sites, compromising their site-specific nature. In addition, coherent effects can lead to additional decay of magnetisation compromising R_2 and $R_{1\rho}$ measurements [3,24]. However, the leftover anisotropic interactions, especially strong ^{1}H–^{1}H proton dipolar couplings, can be reduced by fast spinning and combined with deuteration and/or alternating labelling to effectively average out the interactions [27,38,39]. The exact conditions to attenuate the spin diffusion sufficiently so that it has a negligible effect on the site-specificity of the rates depends on the exact type of relaxation probes. For example, for ^{15}N nuclei spinning frequencies > 20 kHz are sufficient to obtain site-specific ^{15}N R_1 rates [38,40] and spinning rates > 60 kHz are sufficient to obtain site-specific ^{15}N $R_{1\rho}$ rates without the need for deuteration or any special labelling pattern [24]. For ^{13}C' nuclei spinning frequencies > 60 kHz are adequate for recording site-specific $R_1/R_{1\rho}$ rates [2,27] but for the aliphatic carbons more demanding conditions need to be met: for $^{13}C^{\alpha}$ either (1) a combination of alternate ^{13}C labelling, and extensive deuteration and 50–60 kHz spinning need to be employed for site specific R_1 measurements [39] or (2) a combination of alternate ^{13}C labelling and > 80 kHz spinning [29] or (3) > 100 kHz spinning for uniformly ^{13}C-labelled samples [29]. Alternate ^{13}C labelling is still required in fully protonated samples in order to collect site specific aliphatic ^{13}C $R_{1\rho}$ rates since many sidechain sites still show spin diffusion even at 100 kHz spinning in uniformly labelled samples [29].

Based on the above discussion recording ^{15}N and ^{13}C' R_1 and $R_{1\rho}$ relaxation rates in uniformly ^{15}N and ^{13}C labelled samples at 100 kHz spinning should result in measurements with negligible influence of coherent effects. In addition, under these conditions ^{1}H-detected spectroscopy in fully protonated samples is the most practical detection mode. Consequently, below we will explore a range of solutions for simultaneous measurements of ^{15}N and ^{13}C' relaxation rates using ^{1}H-detected experiments.

Constructing Multiple Acquisition Psuedo-3D experiments from 2D correlation experiments

To construct multiple pathway experiments, we will adapt 2D ^{1}H-detected correlation experiments into pseudo-3D experiments by adding relaxation periods at the appropriate places in the pulse sequence (Fig. 1**a,b and** Fig. 3**a,b**). For the ^{13}C' measurements, we found that a direct adaptation of the standard CP-based ^{1}H-detected ^{13}C–^{1}H correlation experiment was not sufficient. The final ^{13}C'–^{1}H transfer spreads the polarization to several nearby protons, causing reduction of the sensitivity and increasing the spectral overlap. The polarization can be transferred either to the $^{13}C^{\alpha}$ or to the ^{15}N to have a single "read-out" proton. We have chosen to transfer through the $^{13}C^{\alpha}$ to the $^{1}H^{\alpha}$ (Fig. 1**a, 3a**) to avoid disturbing any stored ^{15}N polarization, and because we have sufficient resolution in this sample at this spinning rate. This results in an hC'cαHα experiment, where the 2D correlation spectrum encodes the i^{th} residue ^{13}C' and $^{1}H^{\alpha}$ frequency. The transfer efficiency of the COSY [41] scheme used for ^{13}C–^{13}C polarization transfer is similar to, or better than, a ^{13}C–^{15}N transfer and is much easier to set up experimentally. While we chose COSY mixing for ease of use, any number of other homonuclear mixing schemes could be used.

To adapt the individual experiments into simultaneous experiments the initial excitation period is turned into a SIM-CP period so that both pathways are excited. We then must identify the longest-lived state and store this state after the SIM-CP excitation. The experiment is acquired on the short-lived state(s) first. Then, the stored polarization is re-excited, and an experiment is acquired on the long-lived state with a second, separate acquisition. This approach should mitigate losses from relaxation and simplifies the timings and polarization transfers that would be needed for a single acquisition of multiple pathways.

Simultaneous measurement of ^{13}C' and ^{15}N R_1

The ^{13}C' (hC'cαH) and ^{15}N (hNH) R_1 measurements (Fig. 1**a** and 1**b** respectively) can be combined relatively straightforwardly

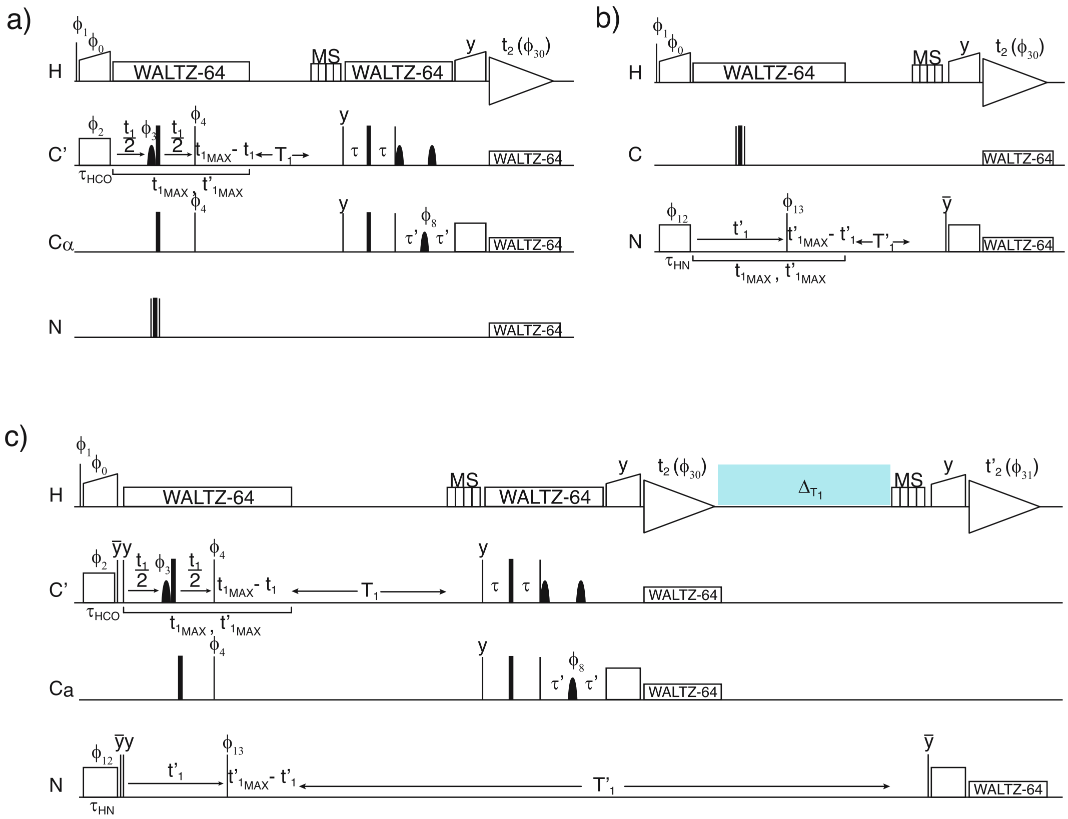

Fig. 1. Pulse sequence of individual a) hC′cαHα R_1 and b) hNH R_1 measurement, and c) combination in the staggered acquisition experiment. Narrow and broad black lines represent 90° and 180° hard pulses, respectively. Rounded pulses represent 180° selective shaped pulses. When not shown, the phase of the pulses is x. The phase cycling for both the experiments is as follow: φ_0= {y*8, -y*8}, φ_1= {x*2, -x*2}, φ_2= {x*16, -x*16}, φ_3= {y*4, x*4}, φ_4= {-y, y}, φ_8= {x*32, y*32} and acquisition φ_{30}= {y, -y, -y, y, -y, y, y, -y, -y, y, y, -y, y, -y, -y, y, -y, y, y, -y, y, -y, -y, y, y, -y, -y, y, -y, y, y, -y, -y, y, y, -y, y, -y, -y, y, y, -y, -y, y, -y, y, y, -y, y, -y, -y, y, -y, y, y, -y, -y, y, y, -y, y, -y, -y, y}for the hC'CαHα portion. φ_{12}= {x*2, -x*2}, φ_{13}= {y, -y}, φ_{16}= {x*4, -x*4} and acquisition φ_{31}= {-y, y, y, -y, y, -y, -y, y, y, -y, -y, y, -y, y, y, -y} for the hNH portion. States-TPPI is employed on φ_4 (**a**, **c**) and φ_{13} (**b**, **c**).

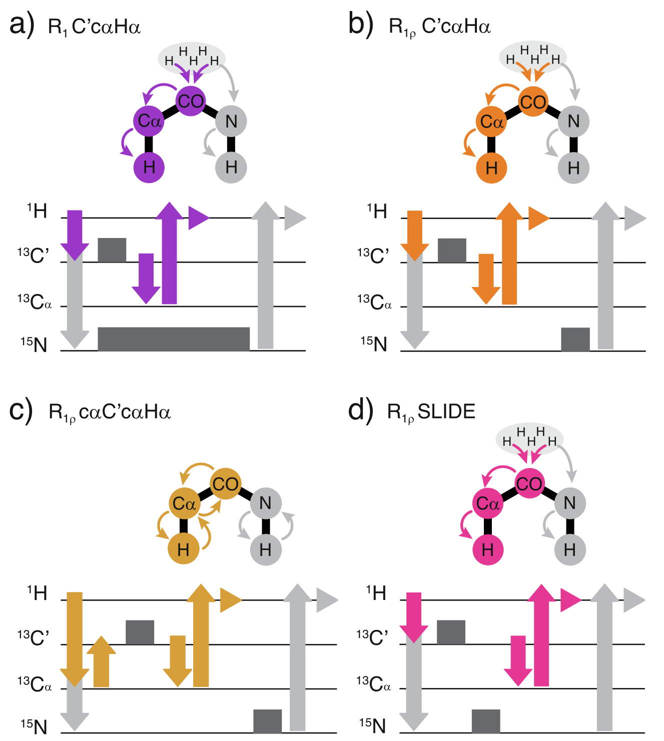

Fig. 2. Schematic representation of ^{13}C (colour specified in each implementation) and ^{15}N (light grey) magnetization pathway for the a) staggered R_1 hC'cαHα + hNH$_N$ (violet) implementation and staggered $R_{1\rho}$ measurements b) hC'cαHα + hNH$_N$ (orange), c) hcαC'cαHα + hNH$_N$ (gold) and d) SLIDE (pink) experiments. $R_{1\rho}$ and R_1 times are represented by dark grey blocks. (For interpretation of the references to colour in this figure legend, the reader is referred to the web version of this article.)

(Fig. 1**c**). A schematic representation of the magnetization pathways is found in Fig. 2**a**. The individual pseudo-3D alters the 2D correlation experiment by adding a relaxation delay after the chemical shift encoding and immediately before the water suppression (we choose simultaneous rather than sequential relaxation periods to avoid large increases in experimental times due to required long relaxation delays). It is not strictly necessary to encode the chemical shift before the relaxation period. Indeed, the resolution could be better for ^{13}C$^{\alpha}$ rather than ^{13}C', however ^{13}C' was labelled to prove the desired polarization pathway was achieved. Alternative schemes for the ^{13}C homonuclear transfer and chemical shift labelling may be more efficient than this implementation [42]. To combine the two experiments, the initial CP is converted to simultaneous cross-polarization (SIM-CP), and then the ^{15}N and ^{13}C' chemical shift is encoded simultaneously (time-shared). Once the longest of the chemical shift delays is finished, the clock for both T_1 delays starts. The delays required to sample the relaxation times of each nucleus are on the same order of magnitude, but the ^{13}C' relaxation time is approximately half of the ^{15}N relaxation time. The ^{13}C' experiment is thus finished relaxing well before the ^{15}N. Therefore, the ^{13}C' pathway is acquired while the ^{15}N is still relaxing. This has the consequence that the ^{15}N delay has to be sufficiently long to allow the ^{13}C' pathway experiment to finish, which includes the ^{13}C' relaxation delay time, homonuclear transfer, and the acquisition on ^{1}H$^{\alpha}$.

To ensure appropriate alignment of the two polarisation transfer pathways, the remainder of the ^{15}N delay (Δ_{T1}) is calculated as shown by equation (1.1).

$$\Delta_{T_1} = T_1' - (T_1 + MS + {}^{13}C^1H\,CP + COSY + t_2) \quad (1.1)$$

The duration of the solvent suppression (MS), COSY transfer, ^{13}C$^{\alpha}$–^{1}H$^{\alpha}$ CP and acquisition is on the scale of 100 ms, so the first point of the ^{15}N relaxation time must be longer than this time. A long initial time delay is only relevant when fast relaxing ^{15}Ns are present in the sample but is not much of a concern in general. For example, if the initial time point is 100 ms the signal would be lost for an ^{15}N with a T_1 < 30 ms, but typical backbone ^{15}N T_1s are on the order of dozens of seconds. ^{1}H–^{15}N/^{13}C' cross-correlation effects are thought to be negligible due to self-decoupling effects [43,44]. To ensure that cross-correlated relaxation effects are completely supressed a series of π-pulses on the ^{1}H channel could be applied [45] (and easily incorporated into our sequences) but in our hands such procedure made no difference for fully protonated GB1 at 100 kHz spinning [29]. Consequently, since there is no requirement for any complex irradiation schemes during the relaxation delay, there is no need for separate relaxation delays for the two types of nuclei. The ^{13}C' experiment is effectively collected during the ^{15}N experiment, which means that the overall pulse sequence duration is equal to the standard ^{15}N R_1 experiment. Thus, with the same overall experimental time of a ^{15}N R_1 experiment we also obtain a ^{13}C' R_1 measurement. The same concept can be applied for aliphatic carbons (^{13}C^{ali}) on the peptide side chain in an alternately ^{13}C-labelled sample (i.e. samples expressed using (1,3) or (2) ^{13}C glycerol, (1) or (2) ^{13}C glucose, or other such labelling schemes).

Fig. 3**a** and 3**b** show the 2D ^{1}H$^{\alpha}$–^{13}C' and ^{1}H–^{15}N 2D GB1 correlation spectra from the first slice of the staggered hC'cαHα + hNH$_N$ experiment. Fig. 3**b** is a typical 2D ^{1}H–^{15}N fingerprint GB1 spectrum, while Fig. 3**a** is the 2D hC'cαHα correlation with 60 observable peaks, considering two ^{1}H$^{\alpha}$ for each glycine. The latter spectrum is detected on ^{1}H$^{\alpha}$, which is possible due to the good spectral resolution at 100 kHz spinning frequency [46,47] and the efficient water suppression from the MISSISSIPPI scheme [34]. The sensitivity of the hC'cαHα spectrum is ~ 80% the hNH$_N$ spectrum principally due to signal lost during the C' to C$^{\alpha}$ COSY transfer. The signal derived from the ^{13}C' of glycine residues is transferred to both of the ^{1}H$^{\alpha}$ protons, resulting in a lower relative signal intensity. The individual relaxation rates extracted from one consistent ^{1}H$^{\alpha}$–^{13}C' glycine peak is fitted and reported.

The final point of concern is whether the application of pulses on the ^{13}C and ^{1}H channels during the ^{15}N R_1 relaxation delay interferes with the measurement itself. However, since the ^{13}C' and ^{15}N R_1 rates found using the single and combined experiments are the same within error (Fig. 3**c,d**) we conclude that any interference effects are here negligible.

Simultaneous measurement of ^{15}N and ^{13}C' $R_{1\rho}$

The individual ^{13}C' and ^{15}N $R_{1\rho}$ experiments are adapted for ^{1}H-detection by adding a spinlock into correlation experiments that were used in the previous section, as shown in Fig. 4**a,b**. Since ^{15}N is expected to have the greater $T_{1\rho}$, and there is only an inversion during the ^{13}C experiment, we perform the ^{13}C-based transient of the experiments first, and then do the ^{15}N-based transient (Fig. 4**c**). To be more specific, in the first multiple pathway variant (Fig. 2**b**) the magnetization is transferred from ^{1}H to ^{13}C' and ^{15}N, generating two polarization paths from the "bulk" ^{1}H polarization. SIM-CP for ^{13}C' and ^{15}N may draw from the same pool of polarization so the ^{13}C' might leech polarization from the ^{15}N, or vice versa. To prevent dilution of the initial polarization pool, a pathway (Fig. 2**c**) was devised where the polarization is transferred from the ^{1}H$^{\alpha}$ to the ^{13}C$^{\alpha}$, and from ^{1}H^{N} to ^{15}N using short duration, one-bond transfers, so specific ^{1}H polarization pools are utilized. An experiment was then constructed to chauffeur the polarization from ^{1}H$^{\alpha}$ to ^{13}C$^{\alpha}$ to ^{13}C', and then back (Fig. 4**d**). The source of the polarization should, thus, be different

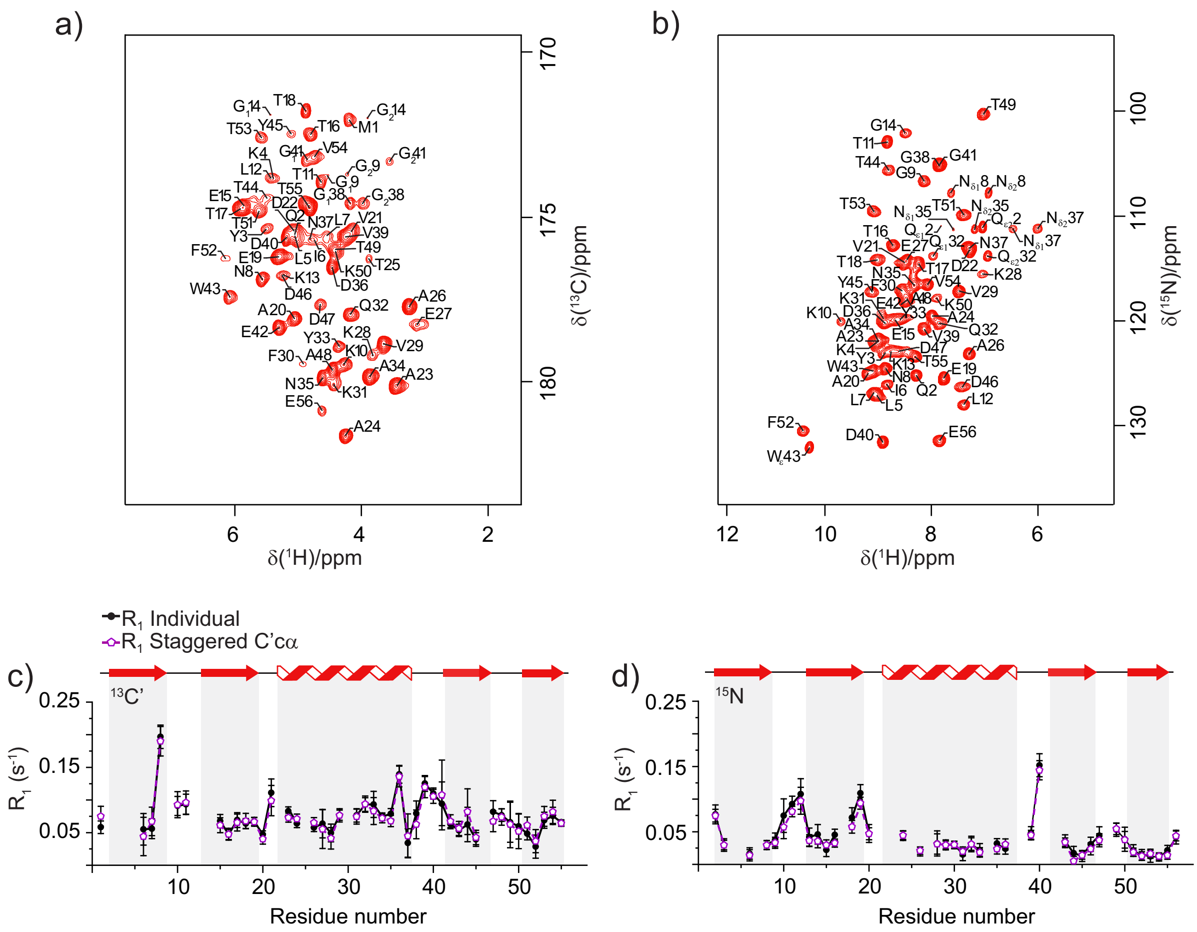

Fig. 3. 2D spectra for crystalline [U-^{13}C,^{15}N]GB1 obtained at 100 kHz spinning with assignments: a) hC′cαHα and b) N-H$_N$. Comparison of c) ^{13}C′ and d) ^{15}N R_1 rates per residue between the standard hC′cαHα and hNH$_N$ experiments (blue) and staggered acquisition (violet). Error bars represent two standard deviations within the correspondent rate. For the severely overlapping peaks, values were removed. (For interpretation of the references to colour in this figure legend, the reader is referred to the web version of this article.)

for ^{13}C′ and ^{15}N, which could improve the initial CP efficiency enough to compensate for the extra transfers. In both experiments, after the SIM-CP, the ^{15}N polarization is stored while the spin-gymnastics are happening on the ^{13}C channel. The experiments are the same after the COSY transfer to ^{13}C′. The $R_{1\rho}$ spinlock is applied on the ^{13}C′, followed by ^{13}C′ chemical shift evolution. The ^{13}C′ coherence is then transferred to ^{13}C$^{\alpha}$ through COSY transfer and the signal acquired on ^{1}H$^{\alpha}$ after ^{13}C$^{\alpha}$–^{1}H$^{\alpha}$ CP. A waiting period is inserted after the first detection period so the ^{15}N measurement starts at a constant time after excitation to avoid any T_1(^{15}N) contribution to the observed rate. The ^{15}N and ^{13}C′ spinlocking fields are implemented sequentially rather than simultaneously to avoid any potential interference or recoupling effects between ^{15}N and ^{13}C pulses. The ^{15}N magnetization is then re-excited to encode the ^{15}N $R_{1\rho}$ and ^{15}N chemical shift, and the signal is acquired on ^{1}H^{N} after ^{15}N–^{1}H CP. ^{15}N decoupling is turned off during the ^{1}H$^{\alpha}$ acquisition to preserve the stored polarization; its application has a negligible effect on the ^{1}H$^{\alpha}$ linewidth. ^{13}C decoupling is applied during all acquisition periods, even though there is little effect on the H^{N} resonance, because the ^{13}C polarization was detected previously, and thus it is not important to preserve. A soft-hard π-pulse pair is used during chemical shift evolution to ensure that the proper ^{13}C pathway is selected; the removal of the homonuclear scalar coupling is a secondary bonus of this approach.

The ^{15}N read-out portion is delayed by:

$$\Delta = T_{1\rho MAX} - T_{1\rho(n)} + 10ms \tag{1.2}$$

where $T_{1\rho\mathrm{MAX}}$ is the longest spinlocking pulse that will be used in the experiment, $T_{1\rho(n)}$ is the current spinlocking pulse time, and 10 ms is arbitrarily added to avoid negative times. If detuning or heating from the ^{13}C spinlocking pulse are a concern, the spinlock field could be turned on during this waiting period. In the context of presented here experiments, removing Δ altogether would reduce the experiment time by ~ 1 h compared to 10 h total time but might introduce variation from ^{15}N longitudinal relaxation.

Fig. 5**a-d** shows the comparison of the measured site-specific ^{13}C′ and ^{15}N $R_{1\rho}$ rates for the individual/singleton and the staggered hC′cαHα + hNH$_N$ and hcαC′cαHα + hNH$_N$ implementations of the experiment. The sensitivity of the hC′cαHα spectrum is ~ 60% of the HN spectrum principally due to signal lost during the ^{13}C′ to ^{13}C$^{\alpha}$ COSY transfer. The sensitivity of the hcαC′cαHα spectrum is ~ 40% of the HN spectrum, which indicates that selecting the polarization pool did not compensate for the polarization lost during the transfer; the direct ^{1}H–^{13}C′ CP version is more efficient. The measured rates for all comparable experiments are the same within the experimental error. This demonstrates that the measured ^{13}C′ and ^{15}N $R_{1\rho}$ relaxation rates are not affected by additional pulses used during the staggered experiments. The results are the same as the individual experiments, but more data is acquired for a given experimental time. The comparison of the relaxation curves measured using the standard experiments with

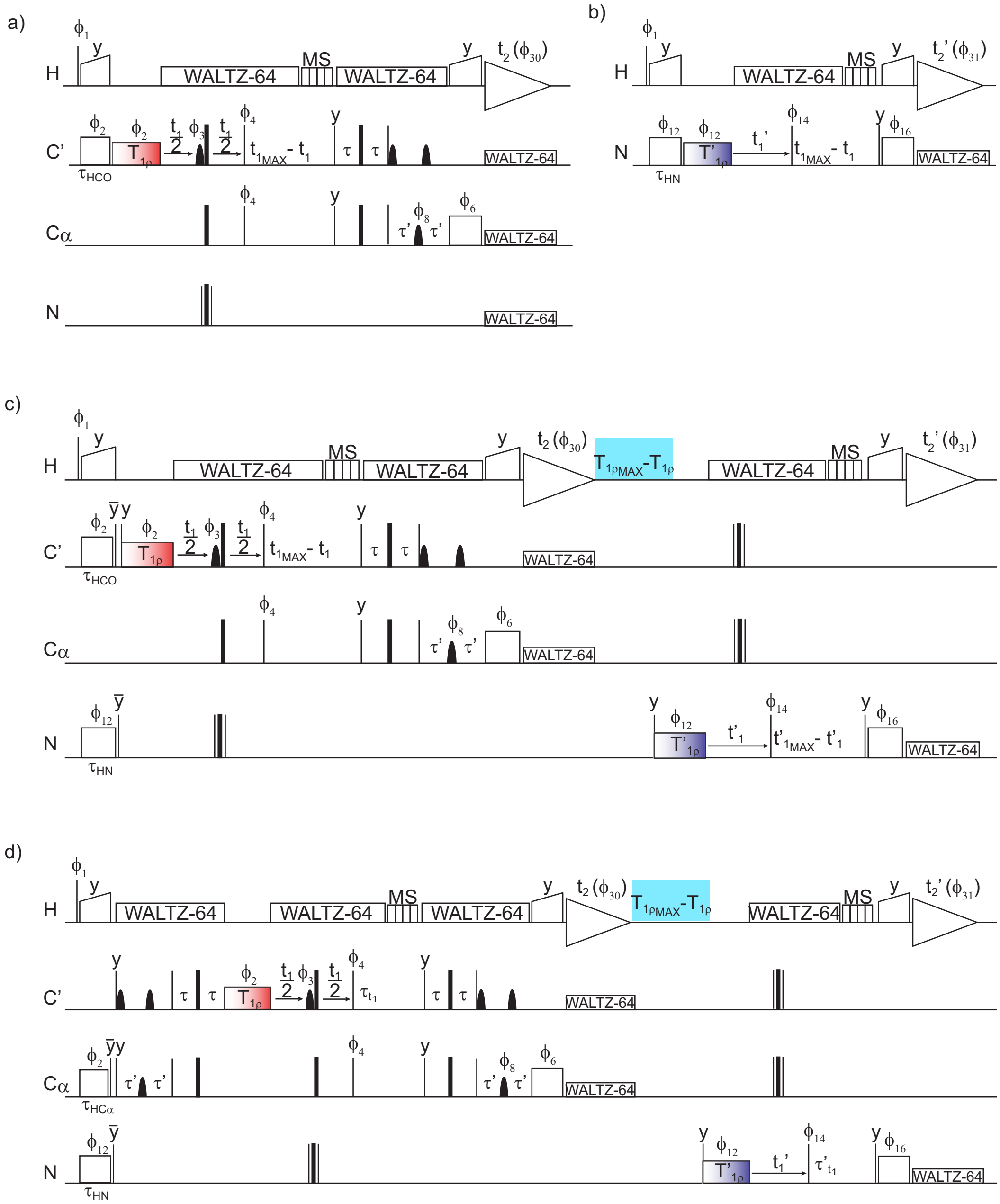

Fig. 4. Pulse sequence of individual a) hC′cαHα ^{13}C′ $R_{1\rho}$, b) hNH$_N$ ^{15}N $R_{1\rho}$ experiment, Staggered acquisition c) hC′cαHα + hNH$_N$ (C′+N) $R_{1\rho}$ and d) hcαC′cαHα + hNH$_N$ (C′+N) $R_{1\rho}$, where τ_{t1} = t_{1MAX}-$t_1$and τ'_{t1} = t'_{1MAX}-t'_1 Narrow and broad black lines represent 90° and 180° hard pulses, respectively. Rounded pulses represent 180° selective shaped pulses. When not shown, the phase of the pulses is x. The phase cycling for both the experiments is as follow: φ_1= {x*8, -x*8}, φ_2= {x*2, -x*2}, φ_3= {y*4, x*4}, φ_4= {-y, y}, φ_6= {x*16, -x*16}, φ_8= {x*32, y*32} and acquisition φ_{30}= {y, -y, -y, y, -y, y, y, -y, -y, y, y, -y, y, -y, -y, y, -y, y, y, -y, y, -y, -y, y, y, -y, -y, y, -y, y, y, -y, -y, y, y, -y, y, -y, -y, y, y, -y, -y, y, -y, y, y, -y, y, -y, -y, y, -y, y, y, -y, -y, y, y, -y, y, -y, -y, y}for the hC′cαHα portion. φ_{12}= {x*2, -x*2}, φ_{14}= {y, -y}, φ_{16}= {x*4, -x*4} and acquisition φ_{31}= {-y, y, y, -y, y, -y, -y, y, y, -y, -y, y, -y, y, y, -y} for the hNH$_N$ portion. States-TPPI is employed on φ_4 (**a**, **c**, **d**) and φ_{14} (**b**, **c**, **d**).

the multiple acquisition experiments presented here can be found in the Supporting Information.

To reduce the experiment time further, the chemical shift and spinlock periods can be optimized with time-sharing. The chemical shift is allowed to evolve on the two nuclei, ^{13}C' (t_1) and ^{15}N (t'_1) at the same time (Fig. 6**a**). The evolution time is implemented so that the polarization for both nuclei is stored for the longest of the two nested evolutions t_1 and t'_1. To avoid unintended magnetization transfers or any other interference during the spinlock, (*e.g.* CP), the spinlocks are never applied at the same time. The spinlock pulses are combined by **S**imultaneous**Ly** **I**ncreasing and **DE**creasing (SLIDE) the times, where the ^{13}C time increments but the ^{15}N decrements to fit the experiments in a constant time period (Fig. 6**b**). This SLIDE period is constructed by inserting the delay Δ_{SLIDE} between the two spinlock periods to limit the contribution from T_1 and to separate the spinlock pulses on the two nuclei. The delay Δ_{SLIDE}, is described by:

$$\Delta_{SLIDE} = T_{1\rho MAX} + T'_{1\rho MAX} - (T_{1\rho} + T'_{1\rho}) + 10ms \quad (1.3)$$

These modifications reduce the experiment time by 1 h from the staggered experiment, for a total of 9 h acquisition, a total savings of 40% with respect to the two individual experiments (15 h in total). If sample heating during the spinlock periods is a concern, compensatory pulses can be added either before the initial excitation or after the final acquisition.

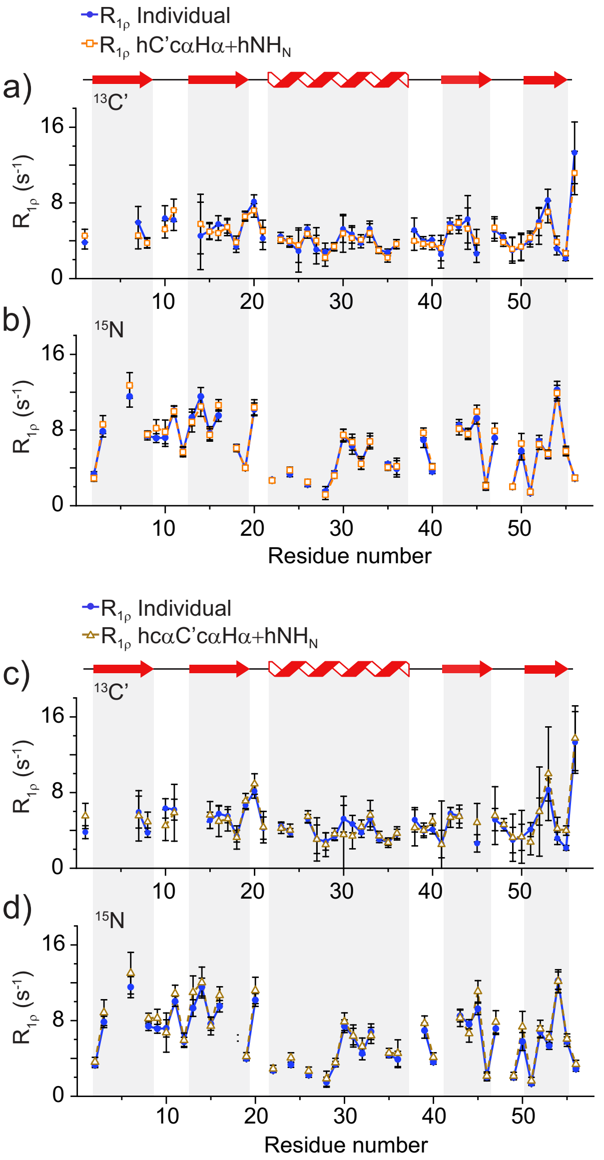

Fig. 5. A comparison of the $R_{1\rho}$ rates for a) ^{13}C' and b) ^{15}N between the separate single-acquisition experiments (blue) and staggered hC'cαHα + hNH$_N$ (orange-empty square) double acquisition experiments as a function of the residue number. Comparison of $R_{1\rho}$ rates of c) ^{13}C' and d) ^{15}N between the separate single-acquisition experiment (blue) and staggered hcαC'cαHα + hNH$_N$ (gold- empty triangle) double acquisition experiments. Error bars represent two standard deviations within the correspondent rate. For the severely overlapping peaks values are not included. (For interpretation of the references to colour in this figure legend, the reader is referred to the web version of this article.)

A concern with the SLIDE experiment is the introduction of changes in the peak intensity due to T_1 relaxation into the $T_{1\rho}$ data. For crystalline GB1 this is not a large concern since the $T_{1\rho}$ of ^{15}N and ^{13}C' are an order of magnitude shorter than T_1, and thus the differences in the intensity due to T_1 relaxation are smaller than the overall experimental error. If T_1s were shorter, the use of constant time periods throughout the experiment will negate any T_1 effects.

Since the ^{15}N pulse does not always start at the same time, the T_1 relaxation could have an effect on the measured $R_{1\rho}$ rates. However, in our case this is negligible because the longest time wait on ^{15}N, 210 ms (Δ + T_1(^{13}C'), for the last time-point delay) should result in the intensity changes < 2%. This is demonstrated in the comparison of the resulting $R_{1\rho}$ rates between SLIDE and the individual hC'cαHα and hNH$_N$ experiments, which are the same within error (Fig. 6**c,d**), and in the sensitivity of SIM-CP (see below).

As a comparison between SLIDE and the other staggered $R_{1\rho}$ variants, the delay Δ in the hC'cαHα + hNH$_N$ and hcαC'cαHα + h NH$_N$ experiments, an additional time waiting with respect to SLIDE, is not required and could be eliminated, since T_1 effects do not introduce a large error in the $R_{1\rho}$ rates measurements. This would save one hour in our reference experiment, calculated with the sum of Δ for each FID, making hC'cαHα + hNH$_N$ last as long as SLIDE. This statement is valid for GB1, which has long relaxation times, but for other bio-macromolecules, typically with shorter T_1s, Δ becomes fundamental to assure that the longitudinal relaxation does not compromise the ^{15}N $R_{1\rho}$ data, where the ^{15}N experiment always has the same starting point relative to the initial excitation.

Sensitivity and Time Savings

To get a better idea of time savings achievable with staggered experiments, we compare the staggered experiments time with the singleton experiments run sequentially. If there were no losses in sensitivity between standard and SIM-CP and there were no differences in relaxation delay schedules, staggered experiments could produce a maximum factor of 2 in time saving. However, SIM-CP is typically slightly less sensitive than standard CP (i.e. individual ^{1}H-^{15}N and ^{1}H–^{13}C) meaning that more transients need to be acquired to obtain the same signal-to-noise ratio (SNR) in the staggered experiments compared to equivalent singleton experiments. In the first instance, we have used SIM-CP settings obtained from optimisation of individual CPs. In this case, we observed that we lose 12% and 8% efficiency when employing SIM-CP in R_1 measurements rather than individual ^{1}H–^{13}C' and ^{1}H-^{15}N CP steps, respectively (see Fig. 7). For the $R_{1\rho}$ measurements with the favourable hC'cαHα + hNH$_N$ pathway the observed decreases in efficiency are 15 and 10% for the staggered ^{13}C' and ^{15}N relaxation measurements (see Fig. 8). This means that by accounting for the additional transients that need to be acquired to get the same SNR as in individual experiments the staggered experiments time saving factors would be reduced from the theoretical maximum of 2 to ~ 1.6 for R_1 and ~ 1.5 for $R_{1\rho}$.

We have investigated whether the SIM-CP losses can be minimised if the optimisation is performed directly on the SIM-CP experiment instead of transferring the settings from optimisations for individual CPs. Indeed, if SIM-CP is optimised directly on crystalline GB1 the losses compared to individual CPs can be reduced. Fig. 8 shows comparisons between first points for singleton and staggered $R_{1\rho}$ experiments where SIM-CP was optimised directly rather than using settings from individual CPs. We can see that for the preferential hC'cαHα + hNH$_N$ pathway the SIM-CP losses are reduced to 12 and 3% for ^{13}C' and ^{15}N relaxation measurements. This means that in theory we could get ~ 1.7 times saving from employing staggered $R_{1\rho}$ and, by extrapolation, up to ~ 1.76 times from staggered R_1 experiments.

For a completely fair comparison of time savings between singleton and staggered experiments we also have to: 1. take into account that one may choose different relaxation delay schedules for these experiments and 2. account for differences in pulse sequence duration in the case of sequential experiments.

For backbone R_1 measurements, relaxation delays much longer than the recycle delay are often required and a few experiments with the longest relaxation delays dominate the overall experimental time. In the case of singleton experiments, the relaxation delays can be tailored to individual relaxation probes with longer final delays for the nuclei with longer T_1s and shorter final delays for nuclei with shorter T_1s. In the case of staggered experiments, the longest relaxation delays will be dictated by the slower

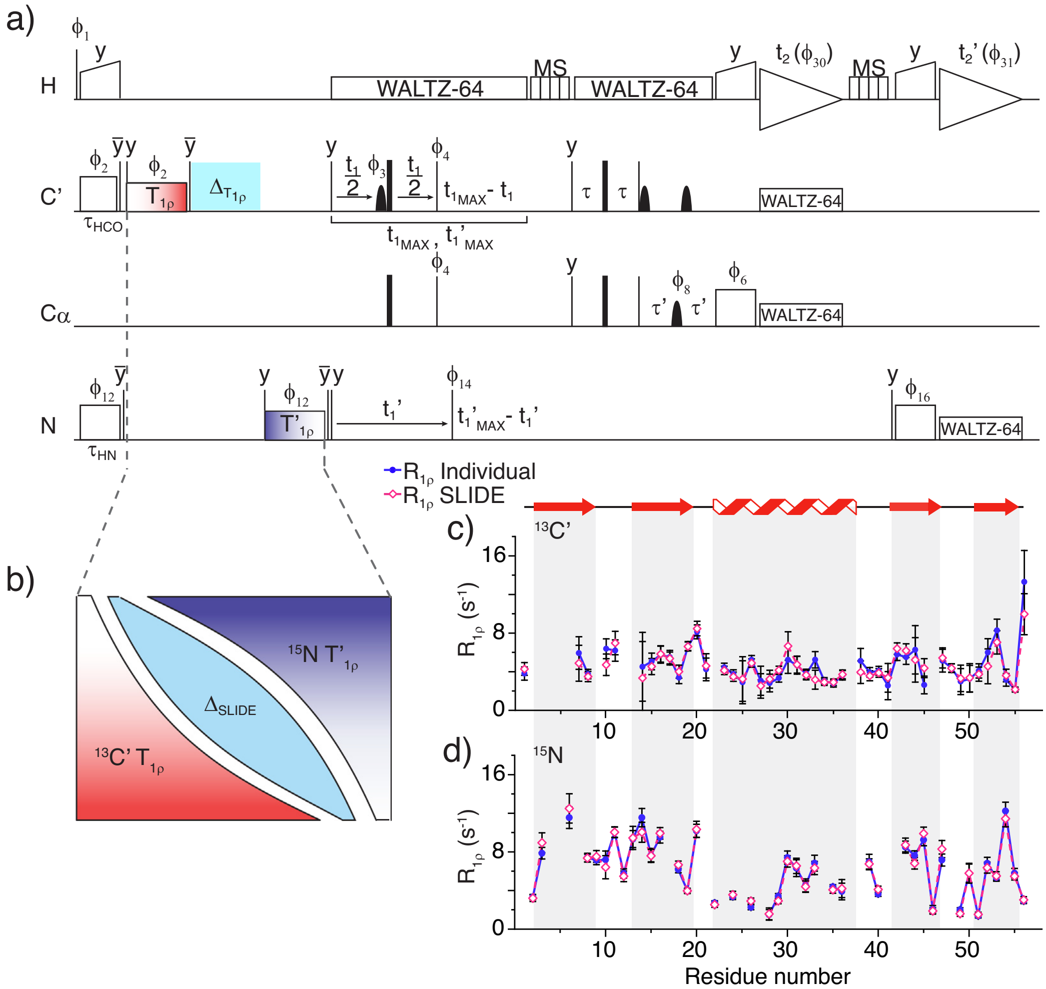

Fig. 6. Time share a) pulse sequence with b) zoom of the constant time defined by ^{13}C' incrementing, ^{15}N decrementing $T_{1\rho}$ lists and $\Delta_{T1\rho}$. Comparison of c) ^{13}C' and d) ^{15}N $R_{1\rho}$ rates per residue between the standard hC'cαHα and hNH$_N$ experiments (blue) and SLIDE (pink). Error bars represent two standard deviations within the correspondent rate. For the severely overlapping peaks, values were removed. Narrow and broad black lines represent 90° and 180° hard pulses, respectively. Rounded pulses represent 180° selective shaped pulses. When not shown, the phase of the pulses is x. The phase cycling for both the experiments is as follow: φ_1= {x*8, -x*8}, φ_2= {x*2, -x*2}, φ_3= {y*4, x*4}, φ_4= {-y, y}, φ_6= {x*16, -x*16}, φ_8= {x*32, y*32} and acquisition φ_{30}= {y, -y, -y, y, -y, y, y, -y, -y, y, y, -y, y, -y, -y, y, -y, y, y, -y, y, -y, -y, y, y, -y, -y, y, -y, y, y, -y, -y, y, y, -y, y, -y, -y, y, y, -y, -y, y, -y, y, y, -y, y, -y, -y, y, -y, y, y, -y, -y, y, y, -y, y, -y, -y, y} for the hC'cαHα portion. φ_{12}= {x*2, -x*2}, φ_{14}= {y, -y}, φ_{16}= {x*4, -x*4} and acquisition φ_{31}= {-y, y, y, -y, y, -y, -y, y, y, -y, -y, y, -y, y, y, -y} for the hNH$_N$ portion. States-TPPI is employed on φ_4 and φ_{14} in **a**. (For interpretation of the references to colour in this figure legend, the reader is referred to the web version of this article.)

relaxing nucleus: typically, ^{15}N. In $R_{1\rho}$ measurements where the relaxation times are typically shorter than the recycle delay, the choice of the longest delays has a less dramatic effect on the overall experimental time.

For the staggered acquisition R_1 measurements, the ^{13}C' sampling schedule is built into the ^{15}N schedule, so the staggered experiments have the same length as the ^{15}N individual experiments. In this context, the saved time from staggered implementation corresponds to the duration of the ^{13}C' experiments: ^{13}C' experiment takes place during the ^{15}N R_1 measurements and the relaxation delay is shared. However, if ^{13}C' T_1s are significantly shorter than ^{15}N T_1s the longest relaxation delays in singleton ^{13}C' experiments can be shorter than the relaxation delays dictated by ^{15}N T_1s in a staggered experiment.

Comparisons can get very quickly complicated depending on precise choice of sampling and experimental conditions. Consequently, below we discuss one illustrative example in order to highlight general considerations for running staggered vs. singleton experiments rather than provide absolute numbers.

At 700 MHz spectrometer in crystalline GB1 at room temperature the average ^{15}N and ^{13}C' T_1s are on the order of 25 and 12.5 s respectively. If we chose to sample the relaxation delays up to 1x T_1, this means that the longest delays would be 25 s for ^{15}N and 12.5 s for ^{13}C'. If we use seven logarithmically spaced sampling of relaxation delays from 0.2 to 25 s in case of ^{15}N and 0.2 to 12.5 s in case of ^{13}C', we get 0.20, 0.45, 1.00, 2.24, 5.00, 11.18, 25.00 sampling for ^{15}N and 0.20, 0.40, 0.79, 1.58, 3.1498, 6.27, 12.50 sampling schedule for ^{13}C'. Taking these sampling schedules and the experimental parameters we used on GB1, the individual ^{15}N R_1 measurement would take approximately 27 h and individual ^{13}C' R_1 measurement about 14.7 h. If we chose the ^{15}N schedule for the staggered R_1 measurement it would take ~ 27 h. This means that if there is no difference in sensitivity, the staggered experiment would take ~ 1.55 times shorter rather than 2 times shorter. Considering the decreases in sensitivity due to lower efficiency of SIM-CP we discussed above, the real time saving factor for running staggered R_1 measurement would be ~ 1.4 times.

It is important to point out that in the above comparison the main difference comes from the experiments with the longest relaxation delays. In the example discussed above the last 2D with relaxation delay of 25 s would take ~ 14.3 h, which is more than all the other six points in this experiment or almost as long as all 7

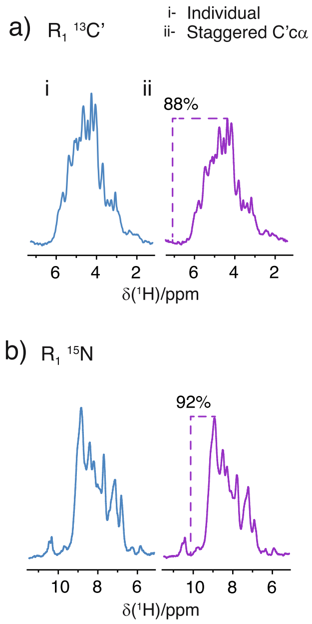

Fig. 7. Sensitivity comparison of ^{1}H 1D integrated spectrum intensity on a) ^{13}C' and b) ^{15}N for the R_1 individual experiments with initial ^{1}H-^{13}C and ^{1}H-^{15}N CP steps (i) and staggered acquisition experiment with initial ^{1}H-^{15}N/^{13}C CP step (ii). The ^{1}H 1D integrated spectrum intensity of the staggered acquisition is indicated as a percentage scaled to the individual experiment (100%). The experiments were acquired consecutively with 512 coadded transients. In this case SIM-CP settings were based on the settings optimised on individual ^{1}H-^{15}N and ^{1}H-^{13}C CP steps.

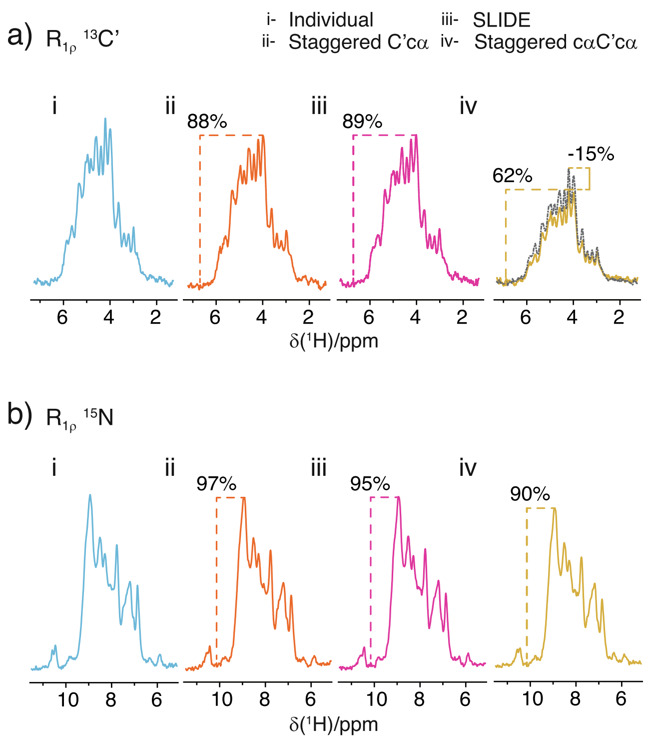

Fig. 8. Sensitivity comparison of ^{1}H 1D integrated spectrum intensity on a) ^{13}C' and b) ^{15}N for the $R_{1\rho}$ individual experiment (i, blue), staggered hC'cαHα + hNH$_N$ (ii, orange), SLIDE (iii, pink) and hcαC'cαHα + hNH$_N$ (iv, gold). The individual hcαC'cαHα intensity is shown in (a, iv) in dotted line on gold solid line and the SIM-CP is 15% lower than the individual experiment. The ^{1}H 1D integrated spectrum intensity of each staggered acquisitions is indicated as a percentage scaled to the individual experiment (100%). (For interpretation of the references to colour in this figure legend, the reader is referred to the web version of this article.)

points in the individual ^{13}C R_1 measurement (14.7 h). This highlights that the percentage time gain from using a staggered experiment will be better the closer to each other the maximum relaxation delays for ^{13}C and ^{15}N experiments are, and that for more dynamic samples with shorter relaxation times (i.e. more challenging samples) the percentage gains will improve as well. Notably for $R_{1\rho}$ measurements where relaxation delays are typically shorter than recycle delay, the impact of the different sampling schedules in the individual vs. staggered experiments will be much smaller than for R_1 measurements.

Overall, one could expect 1.3–1.6 times real saving in time by using staggered experiments for measuring ^{15}N and ^{13}C' R_1 and $R_{1\rho}$ relaxation. Even though these savings might not appear very large as percentage gain, because relaxation measurements can be really time consuming, real time savings may be very respectable in absolute terms when applied to challenging samples. For example, measurement of ^{15}N R_1 on GB1:IgG complex requires about two–three weeks of experimental time and most likely comparable amount of time for ^{13}C' R_1 measurements. In this particular case, staggered experiments would result in real time savings of about two weeks compared to individual experiments.

4. Conclusion

In summary, we propose approaches for simultaneous acquisition of ^{15}N and ^{13}C R_1 and $R_{1\rho}$ using ^{1}H-detected experiments at fast (100 kHz) spinning on fully protonated protein samples. We employ sequential ^{15}N and ^{13}C acquisition with concurrent relaxation delay periods for R_1 and sequential ^{15}N and ^{13}C spinlocking pulses for $R_{1\rho}$ measurements. The ^{15}N experiments are detected on amide ^{1}Hs and ^{13}C' experiments are detected on ^{1}H$^{\alpha}$s. For ^{13}C' experiments we find that hC'cαHα pathway yields higher SNR compared to hcαC'cαHα pathway. We propose various solutions to further minimise the overall experimental time through, *e.g.* time-shared evolution or SLIDE for time-optimised sampling of ^{15}N and ^{13}C spinlocking pulses (all pulse sequences in Bruker format are available for download from: http://dx.https://doi.org/10.17632/x7kk4rkpj3.1.). The relaxation rates obtained from simultaneous experiments are within experimental error the same as the relaxation rates obtained from the individual experiments. In crystalline GB1, the real time gains for simultaneous ^{15}N and ^{13}C' relaxation measurements are about 1.2–1.4 times for R_1 and 1.3–1.5 times for $R_{1\rho}$ compared to running individual experiments. Calculation of the real time gains takes into account SNR losses due to application of SIM-CP compared to conventional CP and additional delays, as well as pulse sequence duration increases due to sequential acquisition. These gains should improve further for dynamic proteins with shorter relaxation times and thus shorter required relaxation delays. The approaches demonstrated here improve the practicality of powerful but time-consuming relaxation measurements for quantifying protein dynamics in the solid-state.

This approach may be less effective with other typical sample preparation protocols, for example triply labelled and back exchanged samples. In triply labelled samples the amide protons are the only available source of polarization, so the efficiency of SIM-CP is expected to be reduced. Both experiments lose sensitivity due to sharing one polarization source, with additional loss for ^{13}C' due to the long ^{13}C'-^{1}H CP contact time that increases the number of correlations (where the ^{13}C'-^{13}C$^{\alpha}$ transfer would be removed). While the application of these experiments to samples with one polarization source does not seem promising that does not preclude its application to all deuterated samples. Our approach might be worthwhile to improve the measurement rate of sidechain relaxation in samples with high degree of deuterium labelling. In the case of the R_1 experiments only, these results indicate that it should be possible to run other experiments while waiting on the relaxation similar to embedded experiments on materials [48].

The resolution of the spectra is another factor in the applicability of these experiments, as it is for all pseudo-3D methods. While it is not routinely done, it should be possible to adapt these experiments into pseudo-4D experiments. The 3D experiments would be combined around a common pulse sequence elements such as a CN/NC transfer in the hNCH and hCNH, and the relaxation period is added at an appropriate place before the transfer back to proton. The experiment time to acquire a series of 3Ds is likely to be prohibitively long (which is one reason they are rarely acquired), so a reduced dimensionality style experiment or sparse sampling scheme would likely need to be applied. In that same vein, the resolution of the ^{13}C spectra could probably be improved by labelling the chemical shift of the $^{13}C^{\alpha}$ nucleus or combining the $^{13}C'$ and $^{13}C^{\alpha}$ chemical shift evolution.

Declaration of Competing Interest

The authors declare that they have no known competing financial interests or personal relationships that could have appeared to influence the work reported in this paper.

Acknowledgements

The authors declare no conflicts of interest. We thank Professor Steven P. Brown for helpful discussions. The research leading to these results has received funding from the European Research Council under the European Union's Seventh Framework Programme (FP/2007-2013) / ERC Grant Agreement 639907. J.R.L. also acknowledges funding from BBSRC Grant BB/R010218/1. Jacqueline Tognetti thanks EPSRC for a PhD studentship through the EPSRC Centre for Doctoral Training in Molecular Analytical Science, grant number EP/L015307/1.

Appendix A. Supplementary material

Supplementary data to this article can be found online at https://doi.org/10.1016/j.jmr.2021.107049.

References

[1] J.M. Lamley, J.R. Lewandowski, Relaxation-based magic-angle spinning NMR approaches for studying protein dynamics, EMagRes. 5 (2016) 1423–1434. https://doi.org/10.1002/9780470034590.emrstm1417.
[2] J.M. Lamley, M.J. Lougher, H.J. Sass, M. Rogowski, S. Grzesiek, J.R. Lewandowski, Unraveling the complexity of protein backbone dynamics with combined ^{13}C and ^{15}N solid-state NMR relaxation measurements, Phys. Chem. Chem. Phys. 17 (34) (2015) 21997–22008, https://doi.org/10.1039/C5CP03484A.
[3] P. Schanda, M. Ernst, Studying dynamics by magic-angle spinning solid-state NMR spectroscopy: Principles and applications to biomolecules, Prog. Nucl. Magn. Reson. Spectrosc. 96 (2016) 1–46, https://doi.org/10.1016/j.pnmrs.2016.02.001.
[4] J.R. Lewandowski, Advances in solid-state relaxation methodology for probing site-specific protein dynamics, Acc. Chem. Res. 46 (9) (2013) 2018–2027, https://doi.org/10.1021/ar300334g.
[5] J.M. Lamley, C. Öster, R.A. Stevens, J.R. Lewandowski, Intermolecular Interactions and Protein Dynamics by Solid-State NMR Spectroscopy, Angew. Chemie Int. Ed. 54 (51) (2015) 15374–15378, https://doi.org/10.1002/anie.v54.5110.1002/anie.201509168.
[6] C. Öster, S. Kosol, J.R. Lewandowski, Quantifying Microsecond Exchange in Large Protein Complexes with Accelerated Relaxation Dispersion Experiments in the Solid State, Sci. Rep. 9 (2019) 1–11, https://doi.org/10.1038/s41598-019-47507-8.
[7] D.B. Good, S. Wang, M.E. Ward, J. Struppe, L.S. Brown, J.R. Lewandowski, V. Ladizhansky, Conformational dynamics of a seven transmembrane helical protein Anabaena Sensory Rhodopsin probed by solid-state NMR, J. Am. Chem. Soc. 136 (7) (2014) 2833–2842, https://doi.org/10.1021/ja411633w.
[8] P. Ma, J.D. Haller, J. Zajakala, P. Macek, A.C. Sivertsen, D. Willbold, J. Boisbouvier, P. Schanda, Probing transient conformational states of proteins by solid-state $R_{1\rho}$ relaxation-dispersion NMR spectroscopy, Angew. Chemie - Int. Ed. 53 (17) (2014) 4312–4317, https://doi.org/10.1002/anie.201311275.
[9] J.R. Lewandowski, M.E. Halse, M. Blackledge, L. Emsley, Direct observation of hierarchical protein dynamics, Science (80-.). 348 (2015) 578–581. https://doi.org/10.1126/science.aaa6111.
[10] B. Busi, J.R. Yarava, A. Hofstetter, N. Salvi, D. Cala-De Paepe, J.R. Lewandowski, M. Blackledge, L. Emsley, Probing Protein Dynamics Using Multifield Variable Temperature NMR Relaxation and Molecular Dynamics Simulation, J. Phys. Chem. B. 122 (42) (2018) 9697–9702, https://doi.org/10.1021/acs.jpcb.8b0857810.1021/acs.jpcb.8b08578.s001.
[11] R. Linser, V. Chevelkov, A. Diehl, B. Reif, Sensitivity enhancement using paramagnetic relaxation in MAS solid-state NMR of perdeuterated proteins, J. Magn. Reson. 189 (2) (2007) 209–216, https://doi.org/10.1016/j.jmr.2007.09.007.
[12] N.P. Wickramasinghe, M. Kotecha, A. Samoson, J. Past, Y. Ishii, Sensitivity enhancement in ^{13}C solid-state NMR of protein microcrystals by use of paramagnetic metal ions for optimizing ^{1}H T_1 relaxation, J. Magn. Reson. 184 (2) (2007) 350–356, https://doi.org/10.1016/j.jmr.2006.10.012.
[13] S. Parthasarathy, Y. Nishiyama, Y. Ishii, Sensitivity and resolution enhanced solid-state NMR for paramagnetic systems and biomolecules under very fast magic angle spinning, Acc. Chem. Res. 46 (9) (2013) 2127–2135, https://doi.org/10.1021/ar4000482.
[14] G. Pintacuda, N. Giraud, R. Pierattelli, A. Böckmann, I. Bertini, L. Emsley, Solid-state NMR spectroscopy of a paramagnetic protein: Assignment and study of human dimeric oxidized CuII-ZnII superoxide dismutase (SOD), Angew. Chemie - Int. Ed. 46 (7) (2007) 1079–1082, https://doi.org/10.1002/(ISSN)1521-377310.1002/anie.v46:710.1002/anie.200603093.
[15] C. Öster, S. Kosol, C. Hartlmüller, J.M. Lamley, D. Iuga, A. Oss, M.-L. Org, K. Vanatalu, A. Samoson, T. Madl, J.R. Lewandowski, Characterization of Protein-Protein Interfaces in Large Complexes by Solid-State NMR Solvent Paramagnetic Relaxation Enhancements, J. Am. Chem. Soc. 139 (35) (2017) 12165–12174, https://doi.org/10.1021/jacs.7b0387510.1021/jacs.7b03875.s001.
[16] E. Lescop, T. Kern, B. Brutscher, Guidelines for the use of band-selective radiofrequency pulses in hetero-nuclear NMR: Example of longitudinal-relaxation-enhanced BEST-type ^{1}H–^{15}N correlation experiments, J. Magn. Reson. 203 (1) (2010) 190–198, https://doi.org/10.1016/j.jmr.2009.12.001.
[17] P. Schanda, V. Forge, B. Brutscher, HET-SOFAST NMR for fast detection of structural compactness and heterogeneity along polypeptide chains, Magn. Reson. Chem. 44 (S1) (2006) S177–S184, https://doi.org/10.1002/(ISSN)1097-458X10.1002/mrc.v44:1+10.1002/mrc.1825.
[18] J.M. Lamley, J.R. Lewandowski, Simultaneous acquisition of homonuclear and heteronuclear long-distance contacts with time-shared third spin assisted recoupling, J. Magn. Reson. 218 (2012) 30–34, https://doi.org/10.1016/j.jmr.2012.03.013.
[19] F. Löhr, A. Laguerre, C. Bock, S. Reckel, P.J. Connolly, N. Abdul-Manan, F. Tumulka, R. Abele, J.M. Moore, V. Dötsch, Time-shared experiments for efficient assignment of triple-selectively labeled proteins, J. Magn. Reson. 248 (2014) 81–95, https://doi.org/10.1016/j.jmr.2014.09.014.
[20] T. Gopinath, G. Veglia, 3D DUMAS: Simultaneous acquisition of three-dimensional magic angle spinning solid-state NMR experiments of proteins, J. Magn. Reson. 220 (2012) 79–84, https://doi.org/10.1016/j.jmr.2012.04.006.
[21] K. Sharma, P.K. Madhu, K.R. Mote, A suite of pulse sequences based on multiple sequential acquisitions at one and two radiofrequency channels for solid-state magic-angle spinning NMR studies of proteins, J. Biomol. NMR. 65 (3-4) (2016) 127–141, https://doi.org/10.1007/s10858-016-0043-z.
[22] T. Gopinath, G. Veglia, Orphan spin operators enable the acquisition of multiple 2D and 3D magic angle spinning solid-state NMR spectra, J. Chem. Phys. 138 (18) (2013) 184201, https://doi.org/10.1063/1.4803126.
[23] A. Gallo, W.T. Franks, J.R. Lewandowski, A suite of solid-state NMR experiments to utilize orphaned magnetization for assignment of proteins using parallel high and low gamma detection, J. Magn. Reson. 305 (2019) 219–231, https://doi.org/10.1016/j.jmr.2019.07.006.
[24] J.R. Lewandowski, H.J. Sass, S. Grzesiek, M. Blackledge, L. Emsley, Site-specific measurement of slow motions in proteins, J. Am. Chem. Soc. 133 (42) (2011) 16762–16765, https://doi.org/10.1021/ja206815h.
[25] A.G. Palmer, F. Massi, Characterization of the dynamics of biomacromolecules using rotating-frame spin relaxation NMR spectroscopy, Chem. Rev. 106 (5) (2006) 1700–1719, https://doi.org/10.1021/cr0404287.
[26] N. Giraud, M. Blackledge, M. Goldman, A. Böckmann, A. Lesage, F. Penin, L. Emsley, Quantitative analysis of backbone dynamics in a crystalline protein from nitrogen-15 spin-lattice relaxation, J. Am. Chem. Soc. 127 (51) (2005) 18190–18201, https://doi.org/10.1021/ja055182h10.1021/ja055182h.s001.
[27] J.R. Lewandowski, J. Sein, H.J. Sass, S. Grzesiek, M. Blackledge, L. Emsley, Measurement of site-specific 13C spin-lattice relaxation in a crystalline protein, J. Am. Chem. Soc. 132 (24) (2010) 8252–8254, https://doi.org/10.1021/ja102744b.
[28] W.T. Franks, D.H. Zhou, B.J. Wylie, B.G. Money, D.T. Graesser, H.L. Frericks, G. Sahota, C.M. Rienstra, Magic-angle spinning solid-state NMR spectroscopy of the β1 immunoglobulin binding domain of protein G (GB1): ^{15}N and ^{13}C chemical shift assignments and conformational analysis, J. Am. Chem. Soc. 127 (2005) 12291–12305, https://doi.org/10.1021/ja044497e.
[29] R. Stevens, The Development of Solid-state NMR Methodology to Study the Dynamics of Proteins and Ice, University of Warwick, 2018.
[30] Y.T. van den Hoogen, S.J. Treurniet, H.C.P.F. Roelen, E. de Vroom, G.A. van der Marel, J.H. van Boom, C. Altona, Conformational analysis of the

tetranucleotides m_2^6A–m_2^6A-U-m_2^6A (m_2^6A =N^6-dimethyladenosine) and U-m_2^6A-U-m_2^6A and of the hybrid dA-r(U-A): A one- and two-dimensional NMR study, Eur. J. Biochem. 171 (1-2) (1988) 155–162, https://doi.org/10.1111/ejb.1988.171.issue-1-210.1111/j.1432-1033.1988.tb13771.x.
[31] D.S. Wishart, C.G. Bigam, J. Yao, F. Abildgaard, H.J. Dyson, E. Oldfield, J.L. Markley, B.D. Sykes, ^{1}H, ^{13}C and ^{15}N chemical shift referencing in biomolecular NMR, J. Biomol. NMR. 6 (2) (1995) 135–140.
[32] D. Marion, M. Ikura, R. Tschudin, A.d. Bax, Rapid recording of 2D NMR spectra without phase cycling. Application to the study of hydrogen exchange in proteins, J. Magn. Reson. 85 (2) (1989) 393–399, https://doi.org/10.1016/0022-2364(89)90152-2.
[33] Z. Zhou, R. Kümmerle, X. Qiu, D. Redwine, R. Cong, A. Taha, D. Baugh, B. Winniford, A new decoupling method for accurate quantification of polyethylene copolymer composition and triad sequence distribution with ^{13}C NMR, J. Magn. Reson. 187 (2) (2007) 225–233, https://doi.org/10.1016/j.jmr.2007.05.005.
[34] D.H. Zhou, C.M. Rienstra, High-performance solvent suppression for proton detected solid-state NMR, J. Magn. Reson. 192 (1) (2008) 167–172, https://doi.org/10.1016/j.jmr.2008.01.012.
[35] T. Gopinath, G. Veglia, Dual acquisition magic-angle spinning solid-State NMR-spectroscopy: Simultaneous acquisition of multidimensional spectra of biomacromolecules, Angew. Chemie - Int. Ed. 51 (11) (2012) 2731–2735, https://doi.org/10.1002/anie.201108132.
[36] R. Kurbanov, T. Zinkevich, A. Krushelnitsky, The nuclear magnetic resonance relaxation data analysis in solids: General $R_1/R_{1\rho}$ equations and the model-free approach, J. Chem. Phys. 135 (2011), https://doi.org/10.1063/1.3658383.
[37] A. Grommek, B.H. Meier, M. Ernst, Distance information from proton-driven spin diffusion under MAS, Chem. Phys. Lett. 427 (4-6) (2006) 404–409, https://doi.org/10.1016/j.cplett.2006.07.005.
[38] N. Giraud, M. Blackledge, A. Böckmann, L. Emsley, The influence of nitrogen-15 proton-driven spin diffusion on the measurement of nitrogen-15 longitudinal relaxation times, J. Magn. Reson. 184 (1) (2007) 51–61, https://doi.org/10.1016/j.jmr.2006.09.015.
[39] S. Asami, J.R. Porter, O.F. Lange, B. Reif, Access to Cα backbone dynamics of biological solids by^{13}C T_1 Relaxation and molecular dynamics simulation, J. Am. Chem. Soc. 137 (3) (2015) 1094–1100, https://doi.org/10.1021/ja509367q.
[40] A. Krushelnitsky, T. Bräuniger, D. Reichert, ^{15}N spin diffusion rate in solid-state NMR of totally enriched proteins: The magic angle spinning frequency effect, J. Magn. Reson. 182 (2) (2006) 339–342, https://doi.org/10.1016/j.jmr.2006.06.028.
[41] M.D. Sørensen, A. Meissner, O.W. Sørensen, Spin-state-selective coherence transfer via intermediate states of two-spin coherence in IS spin systems: Application to E.COSY-type measurement of J coupling constants, J. Biomol. NMR. 10 (1997) 181–186, https://doi.org/10.1023/A:1018323913680.
[42] A. Vallet, A. Favier, B. Brutscher, P. Schanda, ssNMRlib: a comprehensive library and tool box for acquisition of solid-state nuclear magnetic resonance experiments on Bruker spectrometers, Magn. Reson. 1 (2) (2020) 331–345, https://doi.org/10.5194/mr-1-331-202010.5194/mr-1-331-2020-supplement.
[43] J. Sein, N. Giraud, M. Blackledge, L. Emsley, The role of ^{15}N CSA and CSA/dipole cross-correlation in (15)N relaxation in solid proteins, J. Magn. Reson. 186 (1) (2007) 26–33, https://doi.org/10.1016/j.jmr.2007.01.010.
[44] V. Chevelkov, A.V. Zhuravleva, Y.i. Xue, B. Reif, N.R. Skrynnikov, Combined analysis of ^{15}N relaxation data from solid- and solution-state NMR spectroscopy, J. Am. Chem. Soc. 129 (42) (2007) 12594–12595, https://doi.org/10.1021/ja073234s10.1021/ja073234s.s001.
[45] L.E. Kay, T.E. Bull, L.K. Nicholson, C. Griesinger, H. Schwalbe, A. Bax, D.A. Torchia, The measurement of heteronuclear transverse relaxation times in ax3 spin systems via polarization-transfer techniques, J. Magn. Reson. 100 (3) (1992) 538–558, https://doi.org/10.1016/0022-2364(92)90058-F.
[46] U. Sternberg, R. Witter, I. Kuprov, J.M. Lamley, A. Oss, J.R. Lewandowski, A. Samoson, ^{1}H line width dependence on MAS speed in solid state NMR – Comparison of experiment and simulation, J. Magn. Reson. 291 (2018) 32–39, https://doi.org/10.1016/j.jmr.2018.04.003.
[47] J.M. Lamley, D. Iuga, C. Öster, H.-J. Sass, M. Rogowski, A. Oss, J. Past, A. Reinhold, S. Grzesiek, A. Samoson, J.R. Lewandowski, Solid-State NMR of a Protein in a Precipitated Complex with a Full-Length Antibody, J. Am. Chem. Soc. 136 (48) (2014) 16800–16806, https://doi.org/10.1021/ja5069992.
[48] S.J. Page, A. Gallo, S.P. Brown, J.R. Lewandowski, J.V. Hanna, W.T. Franks, Simultaneous MQMAS NMR Experiments for Two Half-Integer Quadrupolar Nuclei, J. Magn. Reson. 320 (2020) 106831, https://doi.org/10.1016/j.jmr.2020.106831.

6.1 Supporting Information

Supporting Information for

Accelerating ^{15}N and ^{13}C R_1 and $R_{1\rho}$ relaxation measurements by multiple pathway solid-state NMR experiments

Jacqueline Tognetti[1,2], W. Trent Franks[1,2], Angelo Gallo[2], Józef R. Lewandowski[2*]

[1]Department of Physics, University of Warwick, Coventry CV4 7AL, United Kingdom
[2]Department of Chemistry, University of Warwick, Coventry CV4 7AL, United Kingdom
**Corresponding author: J.R.Lewandowski@warwick.ac.uk*

Table 1. Lengths of spin-locking pulses used for $^{13}C'$ and ^{15}N $R_{1\rho}$ measurements. The lists are the same for individual and all the three variants of staggered acquisition: C'cα, SLIDE and cαC'cα.

^{13}C' (s)	^{15}N (s)
0.002	0.002
0.010	0.010
0.020	0.020
0.030	0.030
0.042	0.042
0.055	0.055
0.075	0.075
0.100	0.100
0.130	0.130
0.170	0.170

Table 2. Relaxation delays for $^{13}C'$ and ^{15}N R_1 measurements used in the individual and staggered acquisitions.

^{13}C' (s)	^{15}N (s)
0.1	0.25
0.2	0.4
0.5	0.8
0.9	1.2
1.4	2
2.3	4
3.6	7
5.9	11
9.5	17
15	28

Table 3. Comparison of ^{13}C' R_1 rates for individual residues of crystalline [U-^{1}H,^{13}C,^{15}N]GB1 measured at 16.4 T and 100 kHz spinning frequency with a nominal sample temperature of 282.1 K. The heavily overlapping peaks were eliminated.

Residue	**Individual**		**Staggered**	
	^{13}C' (10^2 s^{-1})	Error	^{13}C' (10^2 s^{-1})	Error
M01	5.83	0.96	7.50	1.73
Q02	-	-	-	-
Y03	-	-	-	-
K04	-	-	-	-
L05	-	-	-	-
I06	5.52	2.42	4.41	2.93
L07	5.60	1.51	6.72	2.18
N08	19.69	1.79	19.01	2.26
G09	-	-	-	-
K10	9.09	1.46	9.28	1.99
T11	9.33	1.56	9.61	1.78
L12	-	-	-	-
K13	-	-	-	-
G14	-	-	-	-
E15	6.78	0.99	6.14	1.14
T16	4.72	0.79	4.75	0.91
T17	6.93	1.14	6.55	1.30
T18	6.38	0.78	6.79	1.16
E19	6.71	0.61	6.65	0.67
A20	4.71	0.57	4.02	0.77
V21	11.10	2.12	9.90	2.32
D22	-	-	-	-
A23	8.71	0.64	6.88	0.69
A24	6.40	0.64	7.10	0.74
T25	-	-	-	-
A26	5.76	0.60	6.53	0.77
E27	6.37	2.18	5.54	2.97
K28	4.95	1.36	4.13	1.65
V29	7.67	0.77	7.65	1.01
F30	-	-	-	-
K31	7.64	1.02	7.46	1.15
Q32	9.31	1.05	9.37	1.24
Y33	9.32	2.00	8.31	2.06
A34	7.46	0.56	7.21	0.70
N35	7.89	0.80	6.78	0.87
D36	13.93	1.36	13.60	1.59
N37	3.41	2.18	4.50	3.36
G38	7.96	1.90	6.27	2.20
V39	12.53	1.21	11.97	1.63
D40	11.00	0.84	10.55	1.07
G41	9.43	3.35	10.78	5.35
E42	6.30	0.71	6.75	0.99
W43	5.34	0.94	5.64	1.09
T44	6.25	2.64	8.21	3.50
Y45	3.95	1.05	4.25	1.10
D46	-	-	-	-
D47	8.18	1.72	6.74	1.59
A48	7.68	0.96	7.39	1.26
T49	6.59	3.07	6.26	3.57
K50	5.97	1.96	5.20	2.65
T51	4.83	0.93	6.13	1.26
F52	2.86	1.77	3.70	1.77
T53	6.89	1.23	7.49	1.53
V54	7.56	1.31	8.18	1.79
T55	6.56	0.40	6.44	0.48
E56	-	-	-	-

Table 4. Comparison of ^{15}N R_1 rates for crystalline [U-^{1}H,^{13}C,^{15}N]GB1 measured at 16.4 T and 100 kHz spinning frequency with a nominal sample temperature of 282.1 K. The heavily overlapping peaks were eliminated.

	Individual		**Staggered**	
	^{15}N (10^2 s^{-1})	Error	^{15}N (10^2 s^{-1})	Error
Q02	7.67	1.44	7.47	0.97
Y03	2.98	0.96	2.97	0.72
K04	-	-	-	-
L05	-	-	-	-
I06	1.67	0.88	1.40	0.87
L07	-	-	-	-
N08	2.98	0.70	2.96	0.66
G09	3.76	1.05	3.32	0.85
K10	7.47	2.57	5.73	1.77
T11	9.25	1.20	8.10	0.80
L12	10.79	2.34	9.75	2.06
K13	4.19	1.38	3.66	0.91
G14	4.71	1.53	3.57	1.03
E15	2.22	1.01	2.98	0.78
T16	4.23	0.87	3.32	0.74
T17	-	-	-	-
T18	7.17	1.51	5.77	0.98
E19	10.91	1.32	9.88	0.91
A20	4.74	1.38	4.70	0.91
V21	-	-	-	-
D22	-	-	-	-
A23	-	-	-	-
A24	4.42	0.75	4.46	0.63
T25	-	-	-	-
A26	1.97	0.68	2.11	0.57
E27	-	-	-	-
K28	3.22	1.93	3.13	1.56
V29	3.00	0.77	2.98	0.61
F30	2.96	0.56	3.02	0.54
K31	1.51	0.93	1.99	0.68
Q32	3.13	1.19	3.12	0.97
Y33	2.21	0.98	1.85	0.72
A34	-	-	-	-
N35	3.21	0.75	2.38	0.79
D36	2.40	0.83	3.07	0.84
N37	-	-	-	-
G38	-	-	-	-
V39	4.82	0.97	4.49	0.73
D40	15.20	1.76	14.43	1.47
G41	-	-	-	-
E42	-	-	-	-
W43	3.55	0.98	3.41	0.65
T44	1.72	1.05	0.73	0.79
Y45	1.30	0.84	1.41	0.62
D46	3.10	1.07	2.38	0.92
D47	4.40	1.38	3.71	1.01
A48	-	-	-	-
T49	5.31	1.01	5.47	0.88
K50	3.86	1.84	3.78	1.28
T51	2.14	0.89	1.87	0.63
F52	1.45	0.83	1.29	0.65
T53	1.24	0.92	1.64	0.69
V54	1.10	0.58	1.25	0.52
T55	2.16	0.75	1.40	0.59
E56	4.18	1.04	4.36	0.76

Table 5. Comparison of $^{13}C'$ $R_{1\rho}$ rates for crystalline [U-^{1}H,^{13}C,^{15}N]GB1 measured at 16.4 T and 100 kHz spinning frequency with a nominal sample temperature of 282.1 K. The heavily overlapping peaks were eliminated.

	Individual experiment		**C'cα**		**SLIDE**		**cαC'cα**	
	$^{13}C'$ (s^{-1})	Error	$^{13}C'$ (s^{-1})	Error	$^{13}C'$ (s^{-1})	Error	$^{13}C'$ (s^{-1})	Error
M01	3.81	0.69	4.53	0.68	4.28	0.66	6.11	1.34
Q02	-	-	-	-	-	-	-	-
Y03	-	-	-	-	-	-	-	-
K04	-	-	-	-	-	-	-	-
L05	-	-	-	-	-	-	-	-
I06	-	-	-	-	-	-	-	-
L07	5.93	1.69	4.56	1.42	4.88	1.86	5.54	2.66
N08	3.75	0.49	3.77	0.55	3.50	0.53	5.63	1.03
G09	-	-	-	-	-	-	-	-
K10	6.38	1.03	5.21	0.91	4.72	1.11	4.50	1.58
T11	6.19	1.11	7.22	1.18	6.97	1.22	5.87	3.00
L12	-	-	-	-	-	-	-	-
K13	-	-	-	-	-	-	-	-
G14	4.51	3.56	5.77	3.15	3.34	3.78	-	-
E15	5.06	0.86	4.96	0.84	4.54	0.83	5.62	1.42
T16	5.76	0.88	4.92	0.77	5.84	0.85	4.95	1.61
T17	5.51	0.70	5.45	0.91	5.37	0.67	5.22	1.29
T18	3.39	0.62	3.82	0.67	4.01	0.68	3.25	1.23
E19	6.66	0.47	6.56	0.49	6.61	0.47	7.11	0.80
A20	8.13	0.72	7.54	0.73	8.47	0.75	8.91	1.08
V21	4.24	1.18	5.01	1.16	4.60	1.26	4.34	1.66
D22	-	-	-	-	-	-	-	-
A23	4.45	0.43	4.11	0.38	4.14	0.43	4.22	0.55
A24	3.76	0.44	3.96	0.50	3.48	0.48	4.02	0.64
T25	2.91	2.22	3.53	1.82	3.25	2.31	-	-
A26	5.23	0.45	4.73	0.45	4.90	0.44	5.46	0.62
E27	3.06	1.51	4.02	1.37	2.53	1.27	3.05	2.29
K28	2.83	0.92	2.22	0.91	3.23	0.93	2.49	1.26
V29	3.34	0.41	3.39	0.40	3.70	0.43	3.62	0.61
F30	5.23	1.41	4.78	2.00	6.66	1.48	3.55	4.06
K31	4.67	0.92	4.28	1.13	4.74	0.88	3.39	1.34
Q32	3.76	0.51	4.11	0.52	3.66	0.50	4.37	0.73
Y33	5.24	0.85	4.81	0.99	3.18	0.98	5.60	1.57
A34	3.05	0.34	2.98	0.32	2.91	0.32	3.41	0.49
N35	2.77	0.36	2.21	0.46	2.91	0.34	2.70	0.51
D36	3.63	0.49	3.66	0.47	3.72	0.46	3.68	0.70
N37	-	-	-	-	-	-	-	-
G38	5.12	1.29	3.98	0.99	3.95	1.17	4.28	1.91
V39	3.93	0.50	3.67	0.52	3.58	0.52	4.00	0.77
D40	4.09	0.47	3.56	0.51	3.87	0.45	4.94	0.81
G41	2.56	1.46	3.23	1.34	3.37	1.48	2.50	4.61
E42	5.79	0.62	5.35	0.62	6.39	0.59	5.38	1.05
W43	5.51	0.75	5.90	0.76	6.18	0.71	5.47	1.20
T44	6.27	2.51	5.28	2.19	5.23	2.30	12.55	6.00
Y45	2.63	0.92	3.98	1.22	4.37	0.98	5.41	2.03
D46	-	-	-	-	-	-	-	-
D47	5.14	1.18	5.39	1.14	5.43	1.04	5.56	3.06
A48	4.39	0.44	3.84	0.43	4.36	0.44	4.61	0.65
T49	2.98	1.34	3.12	1.27	3.32	1.37	3.23	2.50
K50	3.27	1.38	3.37	1.43	3.38	1.46	3.32	2.79
T51	4.09	0.74	4.33	0.70	3.75	0.73	2.76	1.34
F52	5.99	1.43	5.57	1.94	4.56	1.80	5.99	4.71
T53	8.28	1.17	7.05	1.16	7.04	1.20	9.99	4.95
V54	3.16	0.65	3.88	0.62	3.61	0.66	4.19	1.19
T55	2.15	0.25	2.68	0.24	2.16	0.25	3.98	0.50
E56	13.30	3.26	11.16	2.29	9.53	2.12	13.74	3.42

Table 5. Comparison of ^{15}N $R_{1\rho}$ rates for crystalline [U-^{1}H,^{13}C,^{15}N]GB1 measured at 16.4 T and 100 kHz spinning frequency with a nominal sample temperature of 282.1 K. The heavily overlapping peaks were eliminated.

	Individual experiment		**C'cα**		**SLIDE**		**cαC'cα**	
	^{15}N (s^{-1})	Error	^{15}N (s^{-1})	Error	^{15}N (s^{-1})	Error	^{15}N (s^{-1})	Error
Q02	3.31	0.28	2.91	0.32	3.21	0.35	3.62	0.50
Y03	7.86	0.60	8.58	0.94	8.95	1.03	8.85	1.36
K04	-	-	-	-	-	-	-	-
L05	-	-	-	-	-	-	-	-
I06	11.54	1.11	12.71	1.35	12.50	1.51	13.02	2.20
L07	-	-	-	-	-	-	-	-
N08	7.41	0.45	7.53	0.37	7.36	0.41	8.23	0.56
G09	7.14	0.46	8.01	1.02	7.52	0.62	8.22	1.35
K10	7.18	0.91	7.80	1.25	6.41	1.20	6.73	2.07
T11	10.04	0.53	9.95	0.56	10.03	0.56	10.86	0.89
L12	5.76	0.48	5.66	0.50	5.47	0.55	5.93	0.76
K13	9.32	0.88	8.84	1.05	9.44	1.20	11.00	1.72
G14	11.54	0.95	10.47	1.02	10.03	1.03	12.03	1.63
E15	7.66	0.69	7.48	0.65	7.59	0.68	7.43	0.95
T16	9.92	0.81	10.61	0.60	9.92	0.60	11.27	1.25
T17	-	-	-	-	-	-	-	-
T18	6.36	0.38	6.18	0.37	6.66	0.39	6.72	0.62
E19	3.98	0.22	4.00	0.26	3.96	0.27	4.22	0.40
A20	10.18	0.68	10.40	0.80	10.33	0.84	11.19	1.39
V21	-	-	-	-	-	-	-	-
D22	2.73	0.21	2.66	0.25	2.54	0.28	2.91	0.38
A23	-	-	-	-	-	-	-	-
A24	3.35	0.28	3.75	0.33	3.57	0.35	4.08	0.52
T25	-	-	-	-	-	-	-	-
A26	2.25	0.25	2.51	0.28	2.91	0.31	2.67	0.43
E27	-	-	-	-	-	-	-	-
K28	1.49	0.53	1.16	0.50	1.57	0.63	1.86	0.80
V29	3.40	0.29	3.17	0.26	2.92	0.29	3.57	0.44
F30	7.41	0.68	7.47	0.61	7.02	0.59	7.89	0.93
K31	6.31	0.87	6.71	0.85	6.55	0.79	6.38	1.17
Q32	4.53	0.67	4.42	0.58	4.40	0.59	5.27	0.89
Y33	6.83	0.83	6.78	0.60	6.33	0.68	6.43	0.85
A34	-	-	-	-	-	-	-	-
N35	4.39	0.21	4.06	0.33	4.08	0.36	4.57	0.50
D36	3.90	0.86	4.15	0.87	4.20	0.94	4.56	1.41
N37	-	-	-	-	-	-	-	-
G38	-	-	-	-	-	-	-	-
V39	6.95	0.80	7.70	0.51	6.75	0.53	7.71	0.79
D40	3.72	0.33	4.01	0.34	4.11	0.34	4.12	0.48
G41	-	-	-	-	-	-	-	-
E42	-	-	-	-	-	-	-	-
W43	8.49	0.62	8.14	0.65	8.71	0.72	8.29	0.92
T44	7.62	0.49	7.58	0.60	6.82	0.60	6.65	0.92
Y45	9.24	0.61	9.94	0.68	9.90	0.66	11.09	1.14
D46	2.04	0.40	2.10	0.32	1.89	0.33	2.15	0.43
D47	7.16	0.62	7.90	0.81	8.29	0.89	7.86	1.19
A48	-	-	-	-	-	-	-	-
T49	2.01	0.21	2.01	0.26	1.61	0.29	2.14	0.39
K50	5.79	0.95	6.57	1.07	5.79	1.03	7.36	1.62
T51	1.36	0.21	1.46	0.23	1.52	0.24	1.63	0.37
F52	6.81	0.63	6.49	0.55	6.37	0.57	7.14	0.90
T53	5.33	0.36	5.48	0.40	5.51	0.43	6.21	0.64
V54	12.23	0.92	11.90	0.83	11.43	0.83	12.16	1.22
T55	5.78	0.50	5.75	0.36	5.47	0.38	6.07	0.53
E56	2.89	0.24	2.94	0.29	3.04	0.32	3.39	0.42

Chapter 7

Slice and Dice: Nested Spin-lattice Relaxation Measurements

Slice and Dice: Nested Spin-lattice Relaxation Measurements

W. Trent Franks[a,b]†, Jacqueline Tognetti[a,b]†, and Józef R. Lewandowski[a]*

[a] Dr. W.T. Franks, J. Tognetti, Prof. J.R. Lewandowski
Department of Chemistry
University of Warwick
Coventry CV4 7AL
E-mail: J.R.Lewandowski@warwick.ac.uk

[b] Dr. W.T. Franks, J. Tognetti
Department of Physics
University of Warwick
Coventry CV4 7AL

Supporting information for this article is given via a link at the end of the document.((Please delete this text if not appropriate))

Abstract: Spin-lattice relaxation rate (R_1) measurements are commonly used to characterize protein dynamics. However, the time needed to collect the data can be quite long due to long relaxation times of the low-gamma nuclei, especially in the solid state. We present a method to collect backbone heavy atom relaxation data by nesting the collection of datasets in the solid state. This method results in a factor of 2 to 2.5 times faster data acquisition for backbone R_1 relaxation data for the ^{13}C and ^{15}N sites of proteins.

Introduction

One of the strengths of Nuclear Magnetic Resonance (NMR) is that it can probe molecular motions under near physiological conditions in which the only perturbation is labelling with NMR-active isotopes. NMR relaxation measurements are commonly employed to probe time scales and amplitudes of molecular motions at atomic resolution.[1] In the solid state in the absence of the overall tumbling the time scale window that can be observed is expanded compared to solution and measurements could be performed in even very large systems. For example, local dynamics could be studied in large protein complexes that are amenable to structural characterization only via cryo-EM. However, since each individual relaxation rate samples only limited range of frequencies, multiple measurements are typically required to reasonably constrain the motions. To increase the range of sampled frequencies and improve the description of dynamics measurements are performed at different magnetic field, different temperatures and for different nuclei[2]. This contributes to relaxation measurements being generally time-consuming experiments.

Longitudinal relaxation rates (R_1)[3] report on motions with correlation times in the order of ps-ns. In the solid state, backbone ^{13}C and ^{15}N nuclei are typically characterized by long T_1 times in the order of tens of seconds. It is common to measure the relaxation in biological systems using pseudo-3D experiments[3-4][5] in which site resolution is achieved from a 2D correlation spectrum, and the relaxation is encoded in the third, pseudo-dimension. The delays in this third pseudo-dimension are dictated by the length of T_1s, which renders the experiments for probing backbone relaxation very long.

There have been several approaches to speed up the direct collection of R_1 relaxation data, usually by partitioning the signal so that only one scan is needed. Single scan methods to measure T_1 were first demonstrated by Kaptein *et al.*[6] and later adapted using magnetic resonance imaging techniques (MRI)[7]. These techniques need very sensitive samples with detection on ^{1}H or on hyperpolarized nuclei[8] such as ^{13}C or ^{15}N. The high sensitivity is required due to signal splitting, alongside with good chemical shift resolution for site resolution, and powerful gradients which are all uncommon in biological NMR, and especially so for MAS experiments. Other approaches focus on speeding up acquisition or improving the efficiency of data acquisition by acquiring several experiments at once (Panacea[9], DUMAS[10]), utilizing orphaned polarization[11], encoding multiple pathways into the same experiment[12], using multiple detectors[13], and by interleaving experiments into the recovery delay of another[14].

We recently introduced experiments to collect protein backbone ^{13}C' and amide ^{15}N relaxation data with a single excitation and sequential acquisitions[15]. Our previous work presented simultaneous cross polarization (SIM-CP)[16] and staggered acquisitions to encode carbon and nitrogen relaxation experiments using a shared time period[16]. The ^{13}C' and ^{15}N R_1 rates are collected in the time it would normally take for the ^{15}N R_1 experiment.

Still, the vast majority of instrument time is spent waiting for the longest time points of the relaxation curve. There can be up to a ~15 s delay between the acquisition for the ^{13}C' pathway and the acquisition for the ^{15}N pathway. Taken to the logical extreme, one nucleus could be prepared and allowed to relax, but during its relaxation time a series of experiments could be run on a separate pathway that does not involve the original nucleus. Our previous work demonstrates that the rates measured using staggered acquisition reproduce the rates from standard experiments[15]. Since this is the case, we concluded that the water suppression, ^{13}C-^{13}C COSY transfer, and ^{13}C-^{1}H inverse cross polarization (CP) do not detectably perturb the spin dynamics on the stored ^{15}N polarization. Since there was no measurable difference within error with simultaneous excitations and one intermediate acquisition, perhaps the same will hold for multiple embedded excitations and acquisitions.

To constrain the motions of the protein, the relaxation should be measured on the amide ^{15}N, carbonyl ^{13}C', alpha carbon ^{13}C$^\alpha$ and, if possible, the sidechain aliphatic carbons ^{13}C^{ali}. The experiment time could be optimized by including the spin-lattice relaxation measurements on ^{13}C$^\alpha$ and ^{13}C' with ^{15}N R_1s in an experiment we refer to as Slice & Dice. The magnetization transfer pathway for each nucleus ^{15}N, ^{13}C' and ^{13}C$^\alpha$ is illustrated in Figure 1a. The individual experiments are sliced into separate periods for excitation (square) and acquisition (triangle), as in Figure 1b. The excitation portion of the experiment has an initial CP, the chemical shift evolution and a storage pulse (Fig. S1). With the use of a standard CP where polarization is transferred to one type of nuclei, instead of a SIM-CP (where polarization is transferred to two types of nuclei), the excitation portion is treated separately for all the nuclei during the slice & dice construction. The acquisition portion of the experiment re-excites the stored polarization and then transfers it to the expected detection nucleus. The division of the various experiments into different blocks (of squares and triangles) allows us to assemble them in the most convenient way to fit into the relaxation experiments as described below.

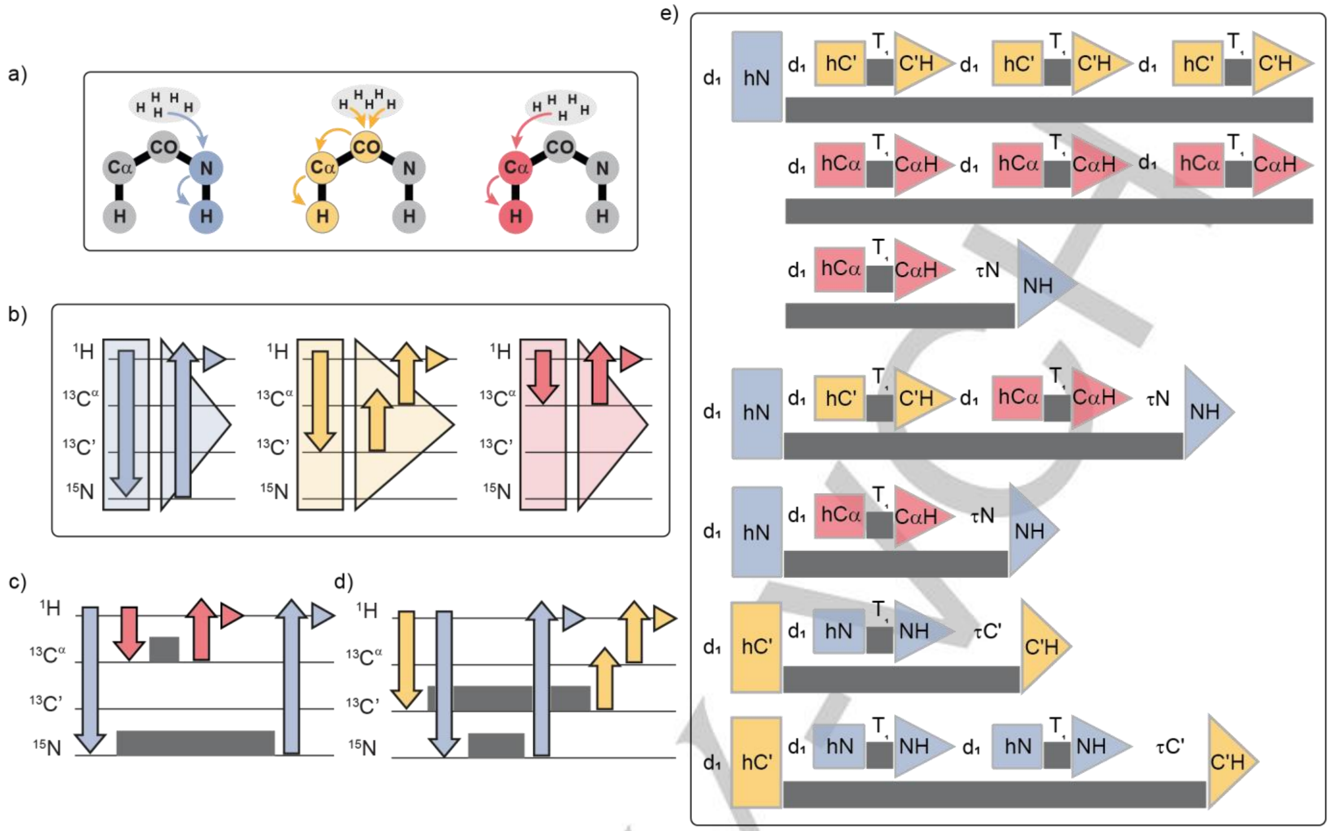

Figure 1. Schematic representation of the Slice & Dice implementation with a) step-by-step magnetization transfer on the protein backbone. The nucleus involved in the R_1 measurement is highlighted with a different colour for ^{15}N (blue), ^{13}C' (yellow), ^{13}C$^{\alpha}$ (red), this colour coding is employed throughout the figure. b) Slicing of the individual experiments in separate periods for excitation (square) and acquisition (triangle) which includes the back-transfer to proton and acquisition. Arrows display magnetization transfer and small triangles portray the acquisition period. c) Representation of magnetization pathway when ^{15}N acts as the "outer" experiment and d) when ^{15}N is the "inner" experiment. Grey squares display T_1 periods and associated pulses. e) Example of the Slice & Dice experiment ordering where coloured squares illustrate the preparation times as indicated, and triangles represent the back-transfer to proton and acquisition following the scheme in b).

In order to embed the experiments, we will only consider placing whole "inner" experiments into the relaxation delay of an "outer" experiment (Figure 1). Generally, the ^{15}N experiment requires the longest maximum time, and the aliphatic carbons the shortest, so the ^{15}N experiment will be made to be the first "outer" experiment, and the two ^{13}C experiments will be the first "inner" experiments (Figure 1c). The nitrogen relaxation is the "outer" experiment for as long as the carbon "inner" experiments will fit into its relaxation delay. The "inner" and "outer" experiments are then exchanged when the long relaxation times of ^{13}C are suitable to accommodate the short relaxation times of ^{15}N that are now the "inner" experiment (as in Figure 1d).

In order to efficiently fit the experiments into one another, the order of the relaxation delays can be changed. It is usually possible to find a solution in which all or most of the desired relaxation times embed into one another nicely by hand, but can be a time-consuming puzzle, so a python program was written to facilitate the creation of the experiments (see Data availability). The program will embed the experiments taking into account for the "AQ" time which includes recovery delay, excitation and evolution, 2* saturation and acquisition, and the "wait" time which ensures a minimum time between acquisitions.

The result of the ordering is an experiment similar to the one found in Figure 1e. There are 8 separate ^{13}C experiments during the first ^{15}N relaxation measurement, and then 2 and 1 in the relaxation delay of the next two ^{15}N experiments. Then there are two ^{13}C' "outer" experiments with 1 and 2 ^{15}N experiments embedded respectively. The provided python program is used to estimate the timings for these experiments. To compare the experiment times, the time is estimated on the relaxation delay list without accounting for second chemical shift dimensions or for the repetitions needed for the phase cycle, then assuming that each experiment requires the same number of scans in total. For example, for crystalline GB1, considering an "AQ" time of 2.6 s, a "wait" time of 1.5 s, and the three delay lists in Table S1 the python pulse program calculated that acquiring one transient for all these datasets in the traditional way would take 157.1 s for the ^{15}N dataset, 62.7 s for the ^{13}C$^{\alpha}$, and 101.2 s for the ^{13}C', or 321.0 s total, while it only takes 181.3 s for the embedded experiment. With the same delay list per nucleus between the usual implementation and Slice and Dice, and involving 16 transients and 64 indirect rows, the standard measurements would be 3 days and ~8 hours (~41 hours for ^{15}N, ~14 hours for ^{13}C$^{\alpha}$ and ~25 hours for ^{13}C'), while the experimental time for Slice and Dice was 2 days and ~2 hours.

Three sets of spin-lattice relaxation measurements for ^{15}N, ^{13}C' and ^{13}C$^{\alpha}$ are then acquired in approximately half the time necessary to collect the full complement of standard R_1s, and if compared to the sole ^{15}N standard experiment it takes only 8% more of the time. Alternatively, a standard ^{13}C$^{\alpha}$ and a SIM-CP N+C'[15] experiment can be acquired separately. In this case, the Slice & Dice implementation takes ~20% less time to collect. Further, the SIM-CP experiments suffer from ~10% lower sensitivity while the interleaved experiments experience no loss since the Slice & Dice employs a standard CP for all of the ^{1}H-X/Y transfer (Fig. S2). It was found to be necessary to add a short "MISSISSIPPI" saturation period at the end of the excitation periods to ensure that the initial ^{1}H polarization is consistent amongst all possible combinations of experiments and relaxation times.

To test our experiments we used a fully protonated uniformly [^{13}C,^{15}N] enriched crystalline GB1 sample prepared as described previously[17]. In solid-state NMR the presence of spin diffusion alters the R_1 rates, losing their site-specific nature due to averaging of nearby sites. In uniformly [^{1}H,^{13}C,^{15}N] labelled samples at MAS > 20 kHz it is possible to obtain site specific rates on ^{15}N[18], while spinning rates > 60 kHz are required for ^{13}C' R_1s[2a, 3]. All our experiments were carried out on a 700 MHz ^{1}H Larmor frequency and a spinning frequency of 100 kHz. 100 kHz MAS guarantees truncation of proton driven spin diffusion PDSD on ^{13}C$^\alpha$ of protonated uniformly labelled sample[19], which allows for the interpretation of R_1 measurements at these sites. At lower spinning frequencies custom labelling schemes are required to minimize the relaxation rates averaging effects of the spin diffusion[20]. Further, the fast MAS preserves the site-specificity bearing an improved ^{1}H detected spectra resolution. The R_1 measurements acquired on ^{15}N, ^{13}C' and ^{13}C$^\alpha$ with the single interleaved experiment are here compared with the rates acquired with the following separate acquisition: ^{15}N (Fig. 2a), ^{13}C' (Fig. 2b), and ^{13}C$^\alpha$ (Fig. 2c), where the whole assignment can be found in SI (Fig. S3 (^{13}C', ^{15}N) and S4 (^{13}C$^\alpha$)). The rates are the same within measurement error to the standard implementation.

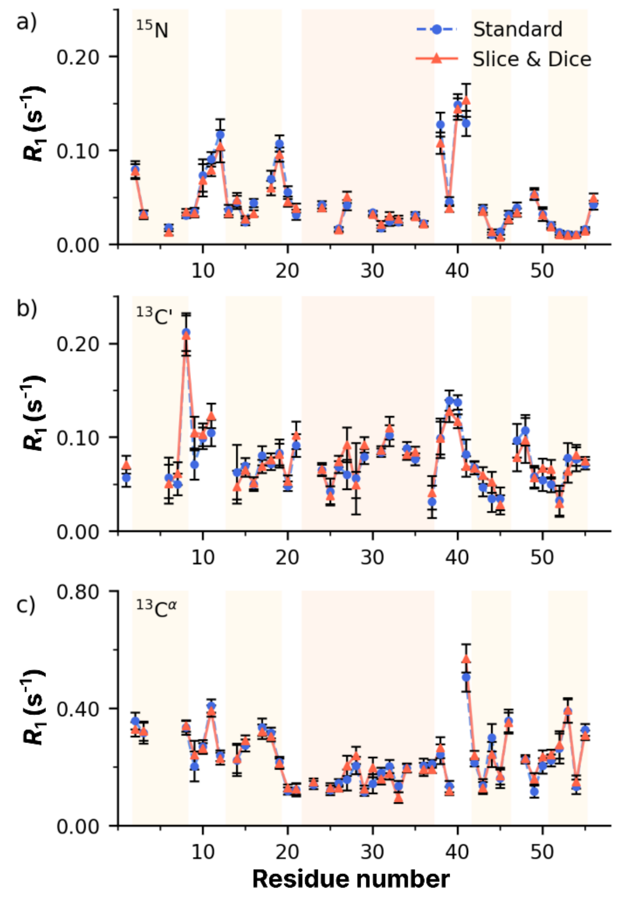

Figure 2. A comparison of the R_1 rates for a) ^{15}N, b) ^{13}C', c) ^{13}C$^\alpha$ obtained from the separated single-acquisition experiment (full-blue circle) and Slice & Dice (full-red triangle) as a function of the residue number. Errors bars represent two standard deviations within the correspondent rate. For the severely overlapping peaks, values are not included

The ^{13}C$^\alpha$ measurement was set up to accommodate the acquisition of the aliphatic ^{13}C, indeed the carbon dimension is folded at ~43 ppm to divide the ^{13}C$^\alpha$ resonances from the rest of the aliphatic carbons (Fig. S4, 5). The complete ^{13}C^{ali} indirect dimension is incidentally acquired during the collection of the ^{13}C$^\alpha$ measurements obtaining a well resolved sidechain ^{1}H detected spectrum which may be feasible for relaxation measurements. However, 100 kHz MAS is still often not sufficient to average out spin diffusion on ^{13}C^{ali} on an uniformly [^{1}H,^{13}C,^{15}N] labelled sample[19] and alternate ^{13}C-labelling should be applied to minimise the effect of spin diffusion. For completeness, the comparisons between standard and Slice & Dice aliphatic ^{13}C, ^{13}C$^\beta$ to ^{13}C$^\varepsilon$, spin-lattice relaxation rates are reported in Figure S6.

One of the challenges for these experiments is that the sampling of the indirect dimensions is linked to one another. The spectral width needed for the aliphatic ^{13}C, or even the ^{13}C$^\alpha$, is two to four times that needed for the C' or ^{15}N, depending on how the spectrum is folded. This discrepancy creates some relatively difficult decisions with respect to the sampling of the aliphatic fingerprint spectrum. In this sample there is a convenient place for folding the spectrum, but still the indirect ^{13}C$^\alpha$ dimension is only sampled to about half the digital resolution of the other two spectra. This causes the resolution to be worse in the more crowded spectrum, which is not an ideal situation. This issue might be addressed by doubling the number of ^{13}C$^\alpha$ acquisitions, where the spectra would probably require more preprocessing.

The method used here to split and rearrange the experiments should be valid under different experimental conditions. For example, in triply labelled [^{2}H, ^{13}C, ^{15}N] and back-exchanged samples at slower spinning, the amide proton may be used exclusively as the read-out nucleus since the CP is efficient and fairly predictable amongst the three backbone nuclei: the amide, alpha carbon and carbonyl carbon. In this case, the COSY transfer in the C' experiment would be removed in favor of a simple CP back to the amide proton. For site specific R_1 measurements the aliphatic carbons could be made accessible at 50/60 kHz MAS through a combination of alternate ^{13}C labelling and extensive deuteration[20], and at >80 kHz with alternate ^{13}C labelling[19].

In summary, we demonstrate a strategy to more thoroughly utilize the instrument time for the collection of longitudinal relaxation experiments. We presented an approach to interleave the collection of R_1 datasets for three sets of data ^{15}N, ^{13}C' and ^{13}C$^\alpha$ with no loss in sensitivity, and a decrease in the data collection time of 2 to 2.5 times that of the standard experiments. Further development of interleaved relaxation measurements could be the application to solution-state NMR or the creation of a higher dimensional experiments to improve the resolution in solid-state. Potentially it could be possible to obtain a 3D spectrum for the ^{13}C. Heavily overlapping peaks on these resonances could then be potentially deconvoluted obtaining an even more complete picture of dynamics, especially considering the application of the Slice & Dice on large proteins and complexes.

Acknowledgements

The authors declare no conflicts of interest. We thank Professor Steven P. Brown and Professor Nikolaus Loening for helpful discussions. The research leading to these results has received funding from the European Research Council under the European Union's Seventh Framework Programme (FP/2007-2013) / ERC Grant Agreement 639907. J.R.L. also acknowledges funding from BBSRC Grant BB/R010218/1. Jacqueline Tognetti thanks EPSRC for a PhD studentship through the EPSRC Centre for Doctoral Training in Molecular Analytical Science, grant number EP/L015307/1.

Data availibility

The raw data presented in this manuscript, pulse program and python program for calculating nested lists can be accessed at: https://zenodo.org/record/5965023?token=eyJhbGciOiJIUzUxMiIsImV4cCI6MTY1MDU4MTk5OSwiaWF0IjoxNjQ3OTQzODM5fQ.eyJkYXRhIjp7InJlY2lkIjo1OTY1MDIzfSwiaWQiOjIxNDkyLCJybmQiOiIzOGVhOTdhOCJ9.0oXX9EY7N-TlJ_x_0rg66nSQLjFeMAKgZyoz25wZ5fkFyZM4HgVxKYGDhyMI57vbIMGQQHvcafEFaWSp1YnWdg#.YjmixTWny3A

(upon acceptance this will be modified to an open access record with a unique DOI; the above private anonymous link will not reveal the identity of the reviewers to the authors)

Keywords: magic angle spinning • NMR spectroscopy • NMR relaxation • nested experiment

[1] a) P. Schanda, M. Ernst, *Prog. Nucl. Magn. Reson. Spectrosc.* **2016**, *96*, 1-46; b) J. M. Lamley, J. R. Lewandowski, *Emagres* **2007**, 1423-1434.
[2] a) J. M. Lamley, M. J. Lougher, H. J. Sass, M. Rogowski, S. Grzesiek, J. R. Lewandowski, *Phys. Chem. Chem. Phys.* **2015**, *17*, 21997-22008; b) B. Busi, J. R. Yarava, A. Hofstetter, N. Salvi, D. Cala-De Paepe, J. R. Lewandowski, M. Blackledge, L. Emsley, *J. Phys. Chem. B* **2018**, *122*, 9697-9702; c) J. R. Lewandowski, M. E. Halse, M. Blackledge, L. Emsley, *Science* **2015**, *348*.
[3] J. R. Lewandowski, J. Sein, H. J. Sass, S. Grzesiek, M. Blackledge, L. Emsley, *J. Am. Chem. Soc.* **2010**, *132*, 8252-8254.
[4] L. Kai, D. Torchia, A. Bax, *Biochemistry* **1989**, *28*, 8972.
[5] a) C. Oster, S. Kosol, J. R. Lewandowski, *Sci. Rep.* **2019**, *9*, 11082; b) J. M. Lamley, C. Oster, R. A. Stevens, J. R. Lewandowski, *Angew. Chem. Int. Ed. Engl.* **2015**, *127*, 15594-15598; c) D. B. Good, S. Wang, M. E. Ward, J. Struppe, L. S. Brown, J. R. Lewandowski, V. Ladizhansky, *J. Am. Chem. Soc.* **2014**, *136*, 2833-2842.
[6] R. Kaptein, K. Dijkstra, C. Tarr, *J. Magn. Reson.* **1976**, *24*, 295-300.
[7] a) R. Deichmann, A. Haase, *J. Magn. Reson.* **1992**, *96*, 608-612; b) R. Deichmann, D. Hahn, A. Haase, *Magn. Reson. Med.* **1999**, *42*, 206-209; c) A. Haase, *Magn. Reson. Med.* **1990**, *13*, 77-89.
[8] I. J. Day, J. C. Mitchell, M. J. Snowden, A. L. Davis, *J. Magn. Reson.* **2007**, *187*, 216-224.
[9] E. Kupce, R. Freeman, *J. Magn. Reson.* **2010**, *206*, 147-153.
[10] T. Gopinath, G. Veglia, *J. Magn. Reson.* **2012**, *220*, 79-84.
[11] T. Gopinath, G. Veglia, *J. Chem. Phys.* **2013**, *138*, 184201.
[12] D. P. Frueh, H. Arthanari, G. Wagner, *J. Biomol. NMR* **2005**, *33*, 187-196.
[13] a) T. Gopinath, D. K. Weber, G. Veglia, *J. Biomol. NMR* **2020**, *74*, 267-285; b) A. Gallo, W. T. Franks, J. R. Lewandowski, *J. Magn. Reson.* **2019**, *305*, 219-231; c) K. Sharma, P. K. Madhu, K. R. Mote, *J. Biomol. NMR* **2016**, *65*, 127-141.
[14] S. J. Page, A. Gallo, S. P. Brown, J. R. Lewandowski, J. V. Hanna, W. T. Franks, *J. Magn. Reson.* **2020**, *320*, 106831.
[15] J. Tognetti, W. Trent Franks, A. Gallo, J. R. Lewandowski, *J. Magn. Reson.* **2021**, *331*, 107049.
[16] T. Gopinath, G. Veglia, *Angew. Chem., Int. Ed. Engl.* **2012**, *51*, 2731-2735.
[17] W. T. Franks, D. H. Zhou, B. J. Wylie, B. G. Money, D. T. Graesser, H. L. Frericks, G. Sahota, C. M. Rienstra, *J. Am. Chem. Soc.* **2005**, *127*, 12291-12305.
[18] a) N. Giraud, M. Blackledge, A. Bockmann, L. Emsley, *J. Magn. Reson.* **2007**, *184*, 51-61; b) A. Krushelnitsky, T. Brauniger, D. Reichert, *J. Magn. Reson.* **2006**, *182*, 339-342.
[19] R. A. Stevens, PhD thesis, University of Warwick **2018**.
[20] S. Asami, J. R. Porter, O. F. Lange, B. Reif, *J. Am. Chem. Soc.* **2015**, *137*, 1094-1100.

Entry for the Table of Contents

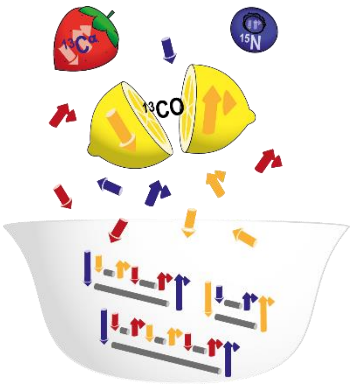

Slice & Dice experiment accelerates measurements of spin-lattice relaxation rates for characterizing protein dynamics by nesting ^{13}C and ^{15}N experiments. With this approach the measurements can be performed more than two times faster.

7.1 Supporting Information

Supporting Information for

Slice and Dice: Nested Spin-lattice Relaxation Measurements

W. Trent Franks[1,2†], Jacqueline Tognetti[1,2†], and Józef R. Lewandowski[1*]

1. *Department of Chemistry, University of Warwick, Coventry CV4 7AL, United Kingdom*
2. *Department of Physics, University of Warwick, Coventry CV4 7AL, United Kingdom*

Experimental methods

The T2Q mutant of GB1 was prepared with uniformly [^{1}H,^{13}C,^{15}N] isotope enrichment as described previously[1] and doped with 4,4-dimethyl-4-silapentane-1-sulfonic acid (DSS) as an internal standard. Approximately 0.5 mg of hydrated microcrystalline protein was packed into a 0.7 mm solid-state NMR rotor by centrifugation.

The experiments were carried out on a Bruker a 0.7 mm HCND ultrafast MAS probe in triple resonance (HCN) mode at 700.13 ^{1}H Larmor Frequency with a Bruker Avance III spectrometer. The sample was spinning at 100 kHz +/- 3 Hz and was at a nominal temperature of 281.2 K (based on external calibration, calculated by the difference between the water and DSS peaks[2] under a gas flow of 400 L/h. The ^{1}H RF carrier was placed at the center of the water resonance at ~4.5 ppm, while the ^{15}N was centered at 120 ppm. The ^{13}C carrier was placed at 55 ppm for the alpha (^{13}C$^{\alpha}$) and aliphatic (^{13}C^{ali}) carbons and at 175 ppm for the carbonyl carbons (^{13}C'). The carbon carrier frequency was moved within the experiment using pre-determined constants to change the frequency. Each ^{1}H FID was acquired for 30 ms, with a spectral width of 35 ppm with 16 coadded transients. ^{13}C^{ali}, ^{13}C' and ^{15}N dimensions of the Slice and Dice and the standard ^{13}C$^{\alpha}$ experiment were acquired with 64 rows each. The ^{13}C^{ali} dimension was acquired with a dwell of 175 μs, with a spectral width of 32 ppm, for a total of 5.6 ms in the indirect dimension. Both ^{13}C' and ^{15}N dimensions were acquired with a dwell of 300 μs for a total of 9.6 ms in the indirect dimension, and a spectral width of 19 ppm for ^{13}C' and 47 ppm for ^{15}N. For the ^{13}C' standard measurement 72 rows were acquired with a dwell of 300 μs for a total of 10.8 ms in the indirect dimension. The ^{15}N standard measurement was acquired with 84 rows in the indirect dimension with a dwell of 300 μs for a total of 12.6 ms in the indirect dimension. The States-TPPI method was employed for quadrature detection in the indirect dimension[3]. The recovery delay was 1.5 s for all the experiments and the wait time was 1.5 s.

The nutation frequencies were calibrated for ^{1}H at 2 μs (ν_1 = 125 kHz), ^{13}C at 2.5 μs (ν_1 = 100 kHz) and ^{15}N at 4.15 μs (ν_1 = 60 kHz). Heteronuclear ^{1}H decoupling (~10 kHz WALTZ-64[4]) was applied during ^{13}C and ^{15}N t_1 evolution and during the COSY-based transfer. ^{13}C heteronuclear decoupling (~10 kHz WALTZ-64) was applied during the acquisition of both ^{13}C experiments, while ^{15}N heteronuclear decoupling (~10 kHz WALTZ-64) was used only for the HN acquisition. The MISSISSIPPI[5] solvent suppression scheme was applied with a spinlock field of ~50 kHz for four 10 ms intervals after the excitation and chemical shift encoding period (*i.e.* immediately after storing the polarization along the *z*-axis) and for four 20 ms intervals immediately before transfer back to the ^{1}H for detection for each individual R_1 experiment.

Cross-polarization (CP) was used for the initial excitation of ^{13}C and ^{15}N and the transfer back to ^{1}H for acquisition. For all the experiments the average ^{1}H field was chosen at ~130 kHz with a linear 15% ramp (85%-100%, from ~121.5 to 139.5 kHz) and a zero-quantum (ZQ) match condition transfer was used on ^{13}C and ^{15}N channel. Each ^{13}C and ^{15}N frequency was irradiated at a field of ~30 kHz and the carrier placed on the appropriate resonance. The contact times were optimized individually for the ^{1}H-X/Y CP. The CP contact times were 1.2 ms, 2.1 ms and 2 ms for ^{13}C^{ali}, ^{13}C' and ^{15}N respectively, while they were 150 μs for the one-bond ^{13}C^{ali}-^{1}H transfer and 500 μs for ^{15}N-^{1}H CP. Gaussian Q3 cascade pulses were used for the selective ^{13}C inversion where a 320 μs pulse gives a bandwidth of 10.5 kHz (~60 ppm) and 760 μs gives a bandwidth of 5.3 kHz (~30 ppm) for ^{13}C' and ^{13}C$^{\alpha}$ respectively. For the selective ^{13}C'-^{13}C$^{\alpha}$ coherence transfer, the J-coupling delay was 4.25 ms when ^{13}C' is along the transverse plane and 3 ms when ^{13}C$^{\alpha}$ is transverse.

The program used for arranging the experiments in the Slice and Dice experiments of the R_1 was created in Python 3.7. The minimum and maximum relaxation times and the desired number of points for each sub-experiment can be entered manually or spaced automatically where the Fibonacci sequence is the basis for the spacing between time points. The pulse sequences, datasets, lists, compound pulse lists, and pulse shapes can be found online at Warwick archive (WRAP *Link*). The relaxation delays used in the presented experiments are given in Table S1.

To allow for direct comparison of the relaxation rates, the same number of rows in the indirect dimension were considered for all spectra. All spectra were processed in Bruker Topspin 3.6.1 with -40 Hz LB in the direct dimension and Lorentz to gauss line broadening with -20 Hz and an offset of 0.1 in the indirect dimensions. Peak assignment and integration were performed using CARA version 1.9.1.7. The integrated intensities of each well-resolved peak were normalized and fit to a single exponential to find the relaxation rate. All relaxation rates are reported at the 95% confidence level from 2000 steps of Monte Carlo error analysis[6].

Table S1. Delay lists for ^{15}N, $^{13}C'$ and $^{13}C^{\alpha}$ and R_1 measurements used in the standard and Slice & Dice experiments. Highlighted in grey the times used for the analysis which correspond to the initial part of the relaxation slope until the ~60% decay of the signal.

^{15}N (s)		$^{13}C'$ (s)		$^{13}C^{ali}$ (s)
Standard	Slice & Dice	Standard	Slice & Dice	Standard/Slice & Dice
0.25	0.01	0.10	0.01	0.01
0.40	0.07	0.20	0.07	0.03
0.80	0.15	0.50	0.13	0.05
1.20	0.22	0.90	0.20	0.08
2.00	0.37	1.40	0.33	0.13
4.00	0.60	2.30	0.50	0.21
7.00	1.00	3.60	0.90	0.34
11.00	1.50	5.90	1.40	0.60
17.00	2.50	9.50	2.30	0.90
28.00	4.10	15.00	3.60	1.50
45.00	6.60	25.00	5.90	2.40
	11.00		9.50	3.80
	17.00		15.00	6.20
	28.00		25.00	10.00
	45.00			

Further in-depth analysis of the Slice & Dice python script

The input parameters in are the "AQ" time, a "Wait" time, the preferred ordering, and the 3 relaxation delay lists, or instructions on how to make the lists. The "AQ" time must be exactly or slightly longer than the time needed to collect one transient without a relaxation delay. The AQ is calculated by adding each part of the experiment, minus any relaxation period. For example, if we take the recovery delay as 1.5 s, each water suppression time is 80 ms and 40 ms (120 ms total), the direct acquisition time is 30 ms, and the transfers and indirect chemical shift evolution times are a maximum of 50 ms, we find a total of 1.8 s for each transient. The "Wait" time specifies the minimum amount of time between acquisitions for the purposes of limiting the probe duty factor. The program will stop after the first solution is found to (mostly) preserve the order of the delay lists. There are thus options to group the experiments together in different ways at the beginning of the calculation, *i.e.* grouping the smallest ^{13}C relaxation times together by alternating the $^{13}C^{ali}$ and $^{13}C'$ experiments, or grouping by the same type of experiment ($^{13}C^{ali}$ and $^{13}C'$ start separated). Finally, the delay schedules may be specified explicitly or automatically generated using a Fibonacci spacing with a minimum and maximum values and the number of points. Fibonacci spacing closely matches previously used delay schedules and is useful for when there is a large dynamic range in the relaxation rates in one measurement, such as in the $^{13}C^{ali}$ experiment. The ^{15}N list is initially arranged in reverse chronological order (largest time to smallest) and the ^{13}C experiments arranged chronologically. On the first pass, the program will fit as many ^{13}C experiments into the longest ^{15}N relaxation times as time allows. Once the ^{15}N delays can no longer accommodate the ^{13}C experiments, the inner and outer experiments are swapped, and the ^{15}N are fit inside the remaining ^{13}C delays. If a solution is not found on the first pass, the order of the relaxation times is varied until a solution is found. The order of the lists is varied using bubble sorts as follows: ^{15}N alone, then ^{15}N and $^{13}C'$ together, then ^{15}N and $^{13}C^{ali}$ together, and finally ^{15}N, $^{13}C'$and $^{13}C^{ali}$ altogether. If there are no solutions the lowest relaxation time of each list is removed and the search continues until a solution is found, or until there are only four items in the lists. If there are still no solutions, the best fit is reported. The output from the program prints the arrays and lists needed to modify the Bruker pulse program ("region", "Inner", "Outer", and the Actual Timings: "CA", "CO", "N"). An estimate is produced for the time required to collect 1 transient of the standard and embedded experiments to gauge the efficiency improvements. A "T_1" array is also produced that shows the estimated wait time between the final "Inner" loop acquisition and the "Outer" loop acquisition, where large values in the T_1 array may indicate inefficient packing. Changing either the "AQ" or "Wait" time slightly, or by adjusting the time scheduling slightly, may result in a more efficient use of time.

Table S2. Comparison of ^{15}N, ^{13}C' and ^{13}C$^{\alpha}$ R_1 fits for individual residues of [U-^{1}H,^{13}C,^{15}N]GB1 crystal at 16.4 T and 100 kHz MAS with a nominal temperature of 282.1 K. The heavily overlapping peaks were eliminated. For each residue the white background denotes the rates acquired the traditional experiment, while the grey background indicates the Slice & Dice.

Residue	**^{15}N**		**^{13}C'**		**^{13}C$^{\alpha}$**	
	R_1 (10^2 s^{-1})	Error	R_1 (10^2 s^{-1})	Error	R_1 (10^1 s^{-1})	Error
M01	-	-	5.68	0.98	-	-
	-	-	7.06	0.96	-	-
Q02	7.97	0.87	-	-	3.57	0.29
	7.75	0.78	-	-	3.29	0.24
Y03	3.17	0.49	-	-	3.17	0.36
	3.20	0.36	-	-	3.22	0.32
K04	-	-	-	-	-	-
	-	-	-	-	-	-
L05	-	-	-	-	-	-
	-	-	-	-	-	-
I06	1.76	0.33	5.69	2.16	-	-
	1.30	0.34	5.03	2.07	-	-
L07	-	-	4.98	1.13	-	-
	-	-	6.11	1.20	-	-
N08	3.07	0.30	21.20	2.01	3.35	0.24
	3.43	0.34	20.85	2.14	3.40	0.20
G09	3.45	0.46	7.05	1.59	2.02	0.52
	3.34	0.45	10.48	1.69	2.41	0.48
K10	7.33	1.72	9.89	1.13	2.69	0.24
	6.81	1.73	10.28	1.20	2.64	0.17
T11	9.04	0.77	10.47	1.40	4.09	0.22
	7.93	0.69	12.29	1.33	3.91	0.20
L12	11.69	1.66	-	-	2.39	0.18
	10.44	1.71	-	-	2.28	0.21
K13	3.66	0.53	-	-	-	-
	3.34	0.44	-	-	-	-
G14	4.43	0.70	6.26	2.90	2.23	0.53
	4.74	0.74	4.69	1.73	2.30	0.50
E15	2.38	0.34	6.94	0.84	2.74	0.21
	2.65	0.37	6.49	0.68	2.90	0.18
T16	4.39	0.43	4.99	0.73	-	-
	3.26	0.35	5.11	0.66	-	-
T17	-	-	8.01	1.02	3.36	0.29
	-	-	6.89	0.72	3.21	0.24
T18	6.94	0.93	7.18	0.69	3.17	0.18
	5.97	0.77	7.62	0.67	3.04	0.17
E19	10.73	0.87	8.29	1.49	2.17	0.19
	9.55	0.75	8.15	1.16	2.12	0.17
A20	5.53	0.67	4.79	0.54	1.19	0.13
	4.53	0.54	5.31	0.62	1.30	0.12
V21	3.15	0.55	9.14	1.22	1.22	0.22
	3.85	0.46	10.21	1.49	1.25	0.19
D22	-	-	5.24	0.35	-	-
	-	-	5.69	0.79	-	-
A23	-	-	8.27	0.67	1.39	0.14
	-	-	7.85	0.60	1.49	0.13
A24	4.21	0.36	6.48	0.63	-	-
	3.87	0.36	6.60	0.67	-	-
T25	-	-	4.24	1.37	1.20	0.16
	-	-	3.77	1.02	1.30	0.16
A26	1.63	0.21	6.85	0.65	1.46	0.12
	1.53	0.23	7.43	0.59	1.28	0.12
E27	4.17	0.53	6.03	1.57	1.57	0.35
	5.01	0.62	9.19	1.83	2.04	0.35
K28	-	-	5.61	3.79	2.05	0.29
	-	-	4.91	1.38	2.40	0.30
V29	-	-	7.93	0.79	1.15	0.13
	-	-	9.22	0.83	1.25	0.12
F30	3.36	0.22	14.81	3.56	1.44	0.33
	3.20	0.29	9.50	2.56	1.99	0.33
K31	1.72	0.29	8.37	0.46	1.79	0.19
	2.11	0.37	8.61	0.44	1.60	0.19
Q32	2.43	0.47	10.20	1.11	2.02	0.22
	3.02	0.42	10.96	1.20	1.78	0.21
Y33	2.38	0.34	-	-	1.35	0.19
	2.65	0.39	-	-	0.96	0.18

A34	-	-	8.81	0.71	1.97	0.15
	-	-	8.18	0.58	1.96	0.14
N35	3.11	0.30	7.68	0.64	-	-
	2.94	0.27	8.39	0.60	-	-
D36	2.21	0.29	-	-	2.04	0.26
	2.16	0.33	-	-	1.92	0.22
N37	-	-	3.12	1.70	2.11	0.14
	-	-	4.09	1.76	1.92	0.13
G38	12.75	1.29	9.88	2.10	2.44	0.34
	10.79	1.15	9.92	1.74	2.67	0.36
V39	4.55	0.48	13.92	1.10	1.35	0.19
	3.85	0.39	12.79	1.18	1.19	0.15
D40	14.84	1.17	13.72	0.78	-	-
	14.39	1.16	11.71	0.71	-	-
G41	12.88	1.35	8.18	1.59	5.07	0.50
	15.34	1.73	6.89	1.09	5.71	0.47
E42	-	-	6.76	0.68	2.16	0.13
	-	-	6.73	0.67	2.40	0.16
W43	3.78	0.42	4.65	0.92	1.36	0.23
	3.52	0.38	5.94	0.92	1.29	0.21
T44	0.99	0.30	3.45	1.41	3.00	0.47
	1.33	0.30	5.21	1.09	2.43	0.43
Y45	1.32	0.29	3.46	1.21	1.61	0.32
	0.79	0.25	2.79	1.01	1.69	0.29
D46	3.12	0.45	-	-	3.57	0.39
	2.67	0.43	-	-	3.51	0.35
D47	3.89	0.55	9.63	1.76	-	-
	3.39	0.44	7.87	1.48	-	-
A48	-	-	10.75	1.64	2.24	0.12
	-	-	9.69	2.39	2.30	0.11
T49	5.26	0.53	5.80	1.16	1.16	0.20
	5.39	0.59	5.66	1.13	1.60	0.20
K50	3.21	0.76	5.45	1.19	2.04	0.26
	3.12	0.64	6.71	1.01	2.35	0.23
T51	2.06	0.30	4.96	0.81	2.23	0.21
	1.84	0.27	6.60	1.01	2.41	0.19
F52	1.25	0.25	3.27	1.61	2.64	0.52
	1.01	0.24	2.91	1.36	2.77	0.47
T53	1.06	0.28	7.81	1.60	3.91	0.40
	0.93	0.25	6.41	1.23	3.93	0.42
V54	1.03	0.19	7.65	1.27	1.33	0.24
	1.00	0.18	8.07	1.10	1.49	0.22
T55	1.61	0.25	7.09	0.50	3.27	0.21
	1.43	0.24	7.48	0.46	3.08	0.16
E56	4.18	0.49	-	-	-	-
	4.90	0.54	-	-	-	-

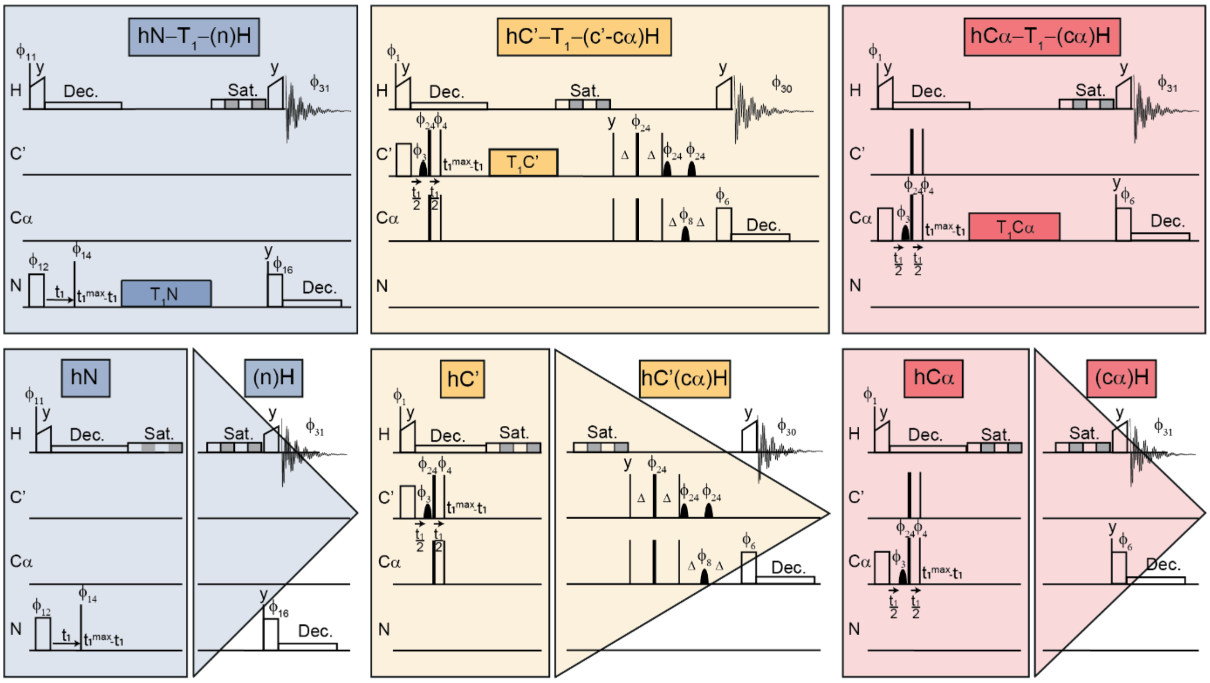

Figure S1. Pulse sequence of the individual ^{15}N (blue), ^{13}C' (yellow) and ^{13}C$^{\alpha}$ (red) R_1 measurements for the Slice & Dice experiment. Below each experiment is sliced into portions for excitation (square) and acquisition (triangle). Narrow and broad black lines represent 90˚ and 180˚ hard pulses, respectively. Rounded pulses represent 180° selective shaped pulses. When not shown, the phase of the pulses is x. The phase cycling for both the experiments is as follow.
hNH$_N$ experiment: φ_{11}= {x*2, -x*2}, φ_{12}= {x*4, -x*4}, φ_{14}= {y, -y}, φ_{16}= {x*8, -x*8} and acquisition φ_{31}= {y, -y, -y, y, -y, y, y, -y, -y, y, y, -y, y, y, -y, y, -y, -y, y}. States-TPPI is employed on φ_{14}.
hCαHα and hC'CαHα experiment: φ_1= {x*4, -x*4}, φ_3= {x*2, y*2}, φ_4= {y, -y}, φ_6= {x*8, -x*8}, φ_8= {x*16, y*16}, φ_{24}= {x, -x}. The acquisition is φ_{31}= {y, -y, -y, y, -y, y, y, -y, -y, y, y, -y, y, y, -y, y, -y, -y, y} for hCαHα, and φ_{30}= {y, -y, -y, y, -y, y, y, -y, -y, y, y, -y, y, -y, y, -y, -y, y, -y, y, y, -y, y, -y, -y, y, y, -y, -y, y, -y, y, y, -y} for hC'CαHα. States-TPPI is employed on φ_4.

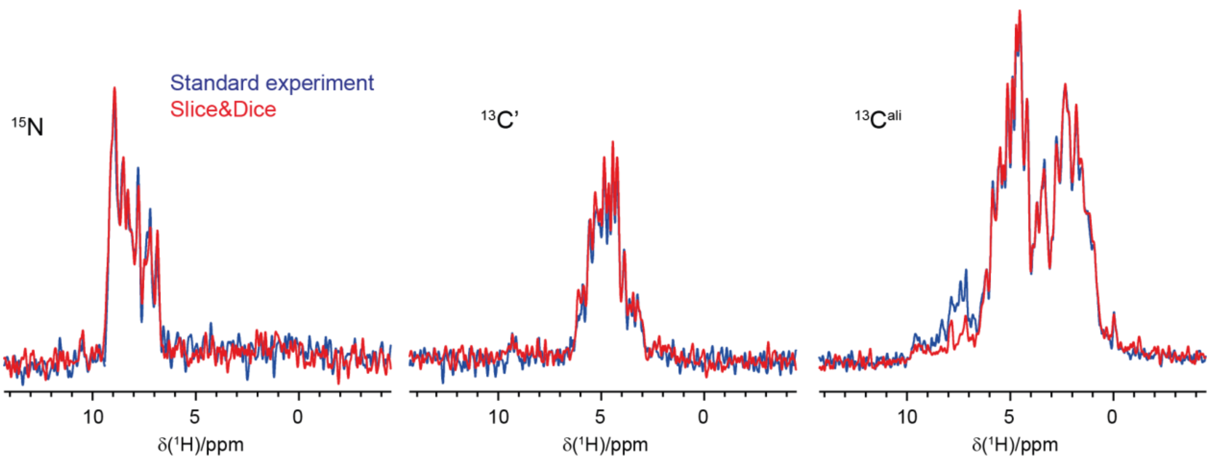

Figure S2. Sensitivity comparison of ^{1}H 1D integrated spectrum intensity on ^{15}N, ^{13}C' and ^{13}C^{ali} for the R_1 individual and the Slice & Dice experiment. Both implement a standard CP for all of the ^{1}H-X/Y transfer. The experiments were acquired with 32 coadded transients.

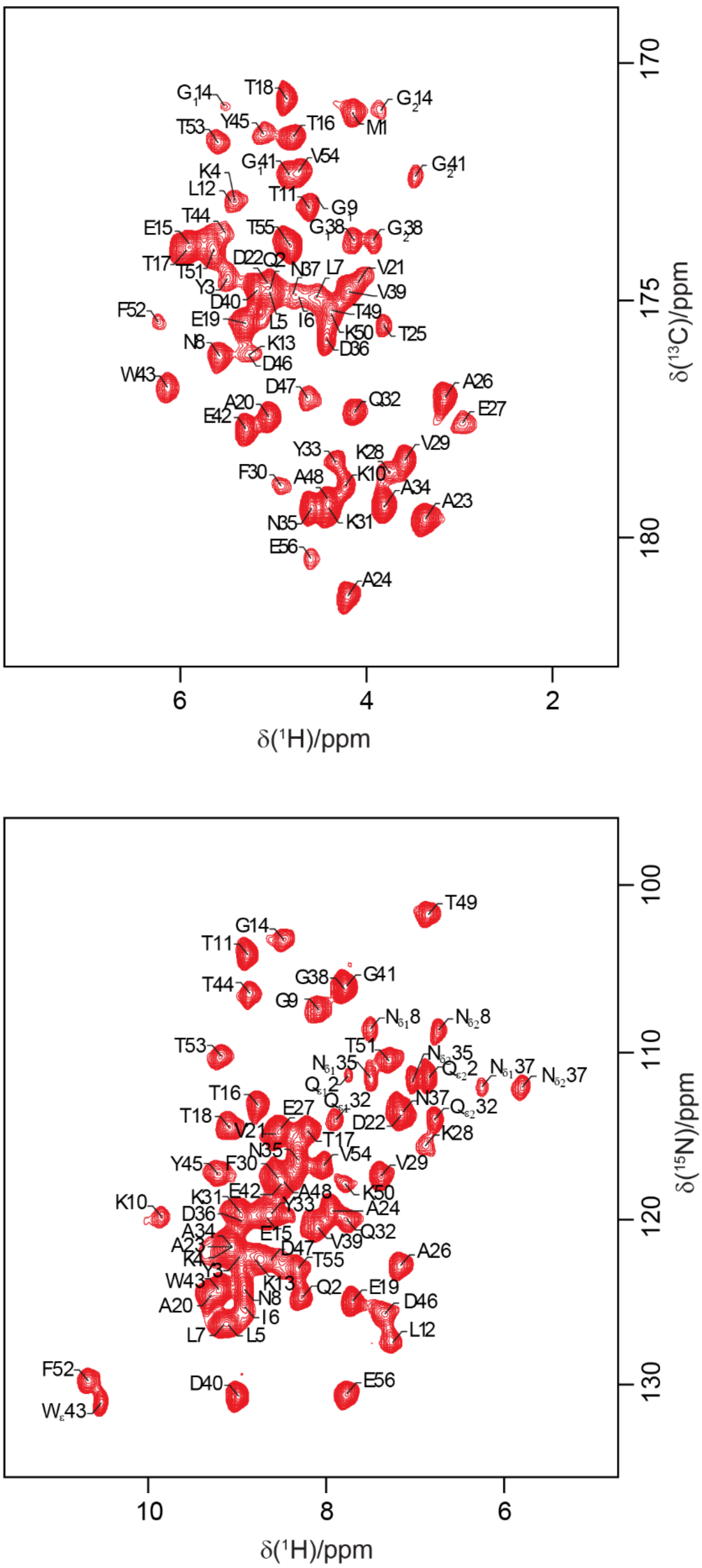

Figure S3. 2D spectra for crystalline [U-^{13}C,^{15}N]GB1 obtained at 100 kHz spinning using the Slice & Dice experiment with assignments of ^{13}C' (up) and ^{15}N (down) resonances.

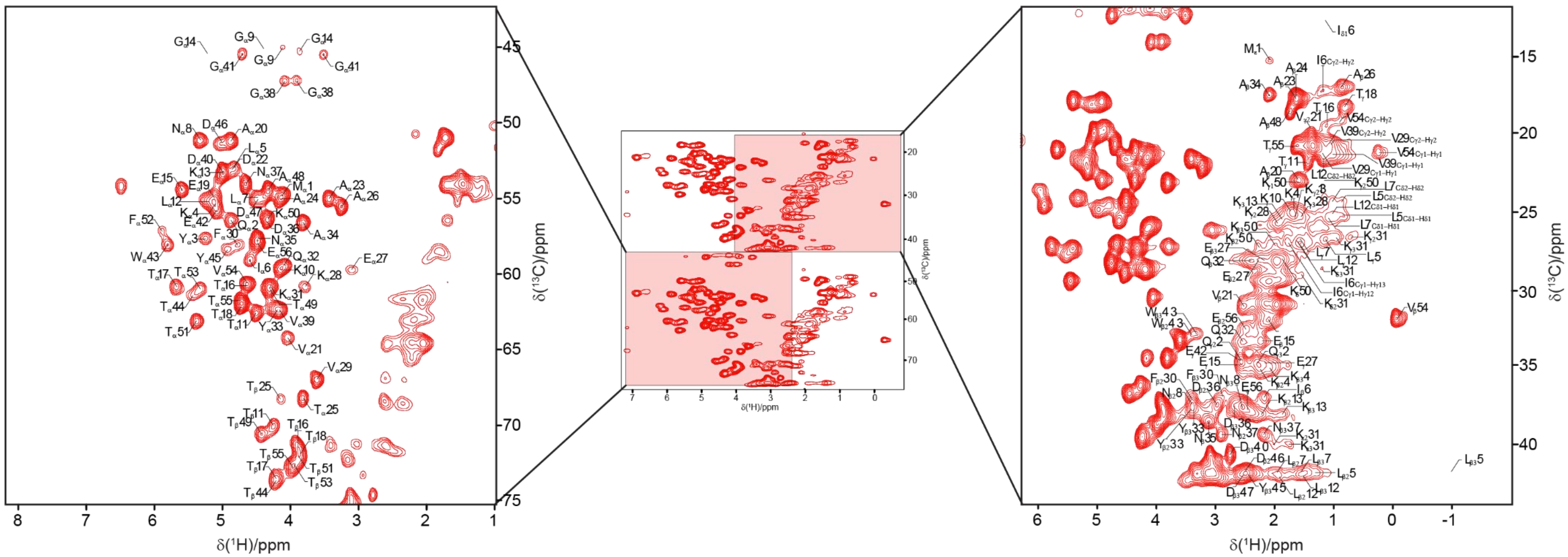

Figure S4a. 2D spectra for crystalline [U-^{13}C,^{15}N]GB1 obtained at 100 kHz spinning using the Slice & Dice experiment with assignments of the aliphatic ^{13}C. The spectrum is acquired folded and here is presented unfolded with a zoom on the α-region on the left, and of the rest of the $^{13}C^{ali}$ on the right, in which only assignments for non-overlapping peaks are shown for the spectrum. The contours for the aliphatic region are drawn lower than the $^{13}C^{\alpha}$ region to highlight the number of resonances present.

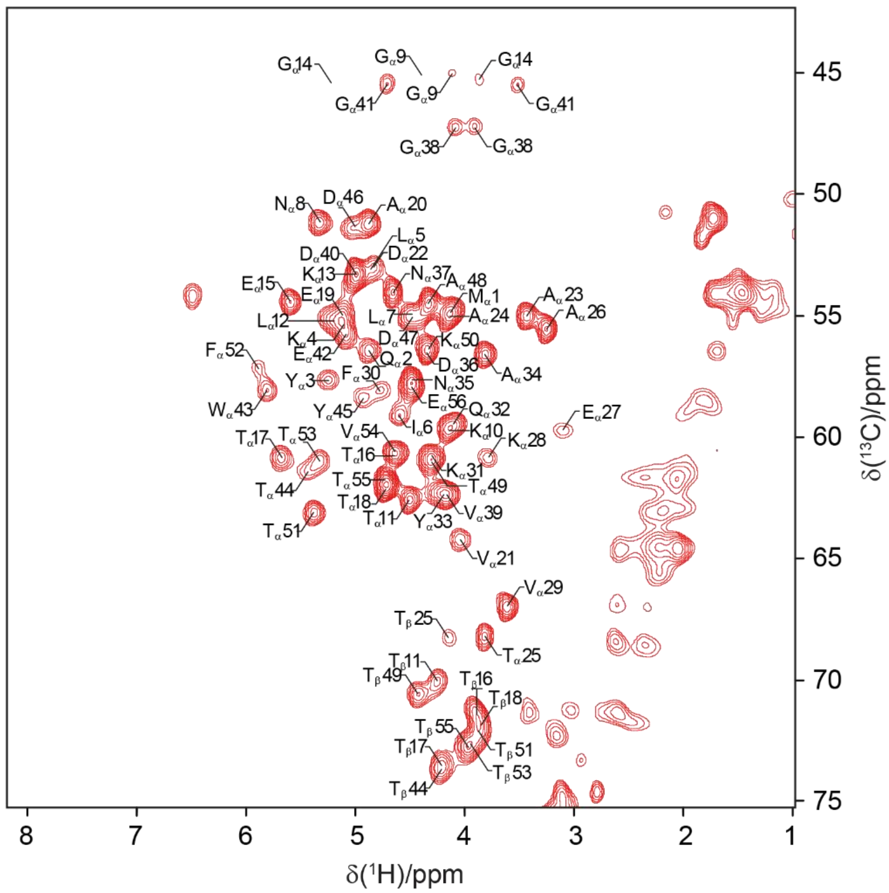

Figure S4b. Zoom of the 2D spectrum for the $^{13}C^{\alpha}$-region for crystalline [U-^{13}C,^{15}N]GB1 obtained at 100 kHz spinning using the Slice & Dice experiment (left spectrum in **Fig.S4a**).

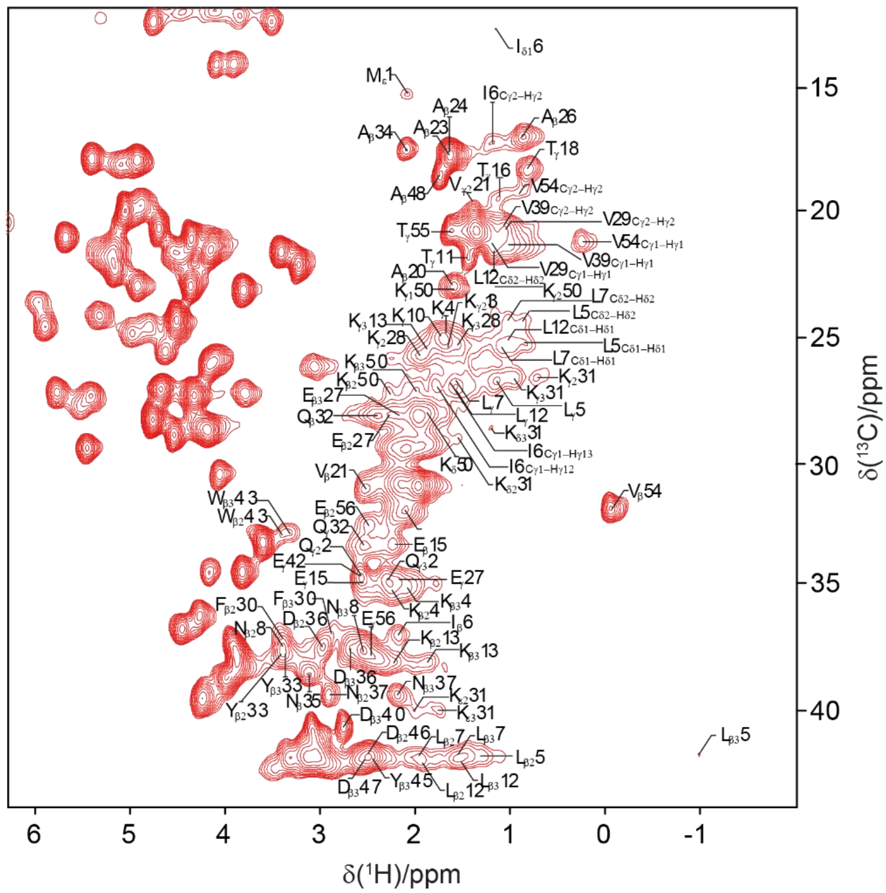

Figure S4c. Zoom of the 2D spectrum for the aliphatic carbon region for crystalline [U-^{13}C,^{15}N]GB1 obtained at 100 kHz spinning using the Slice & Dice experiment (right spectrum in **Fig.S4a)**.

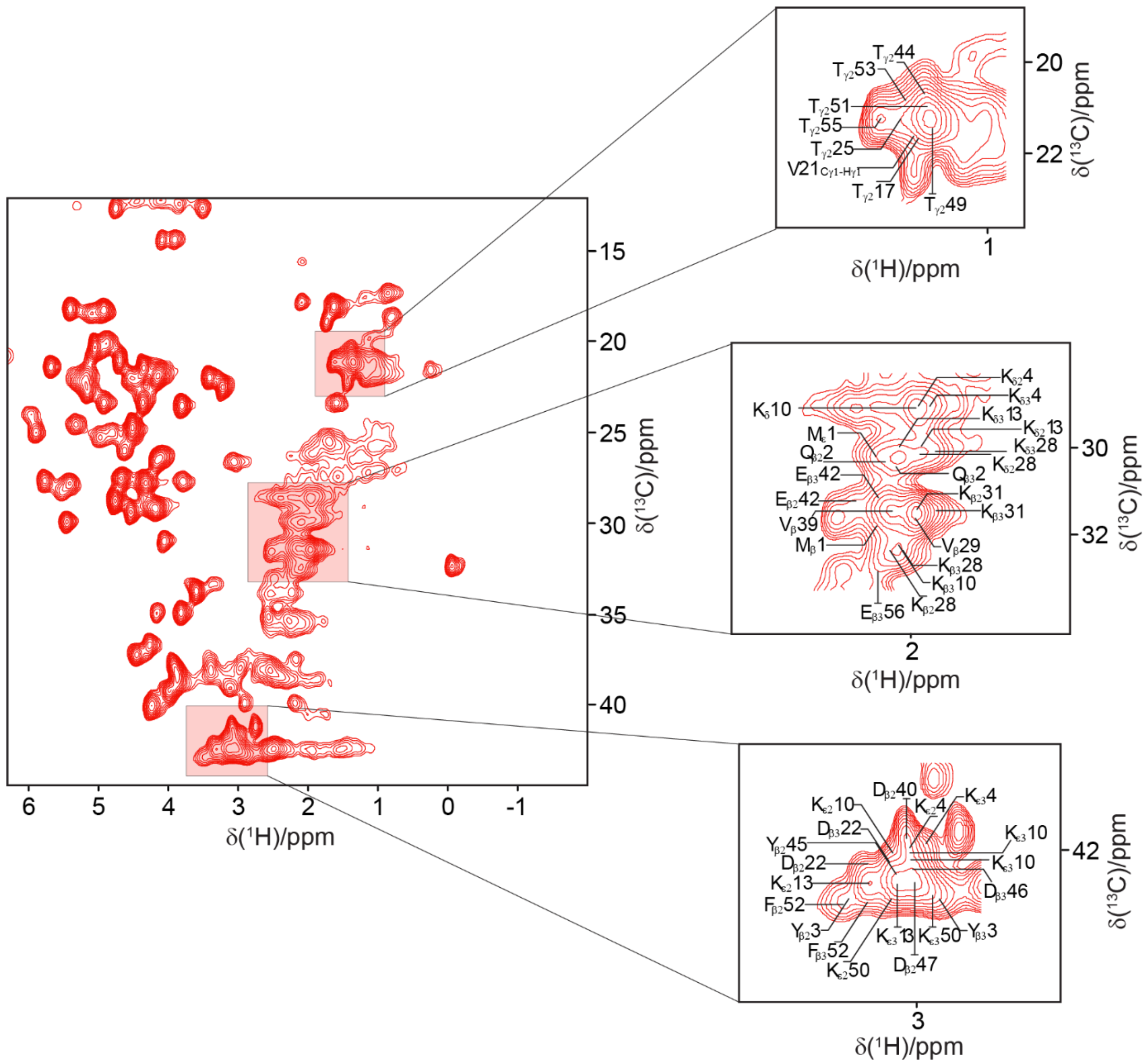

Figure S5. Expansion of the 2D spectrum for the aliphatic carbon region for crystalline [U-^{13}C,^{15}N]GB1 obtained at 100 kHz spinning using the Slice & Dice experiment with highlighted the overlapping resonances.

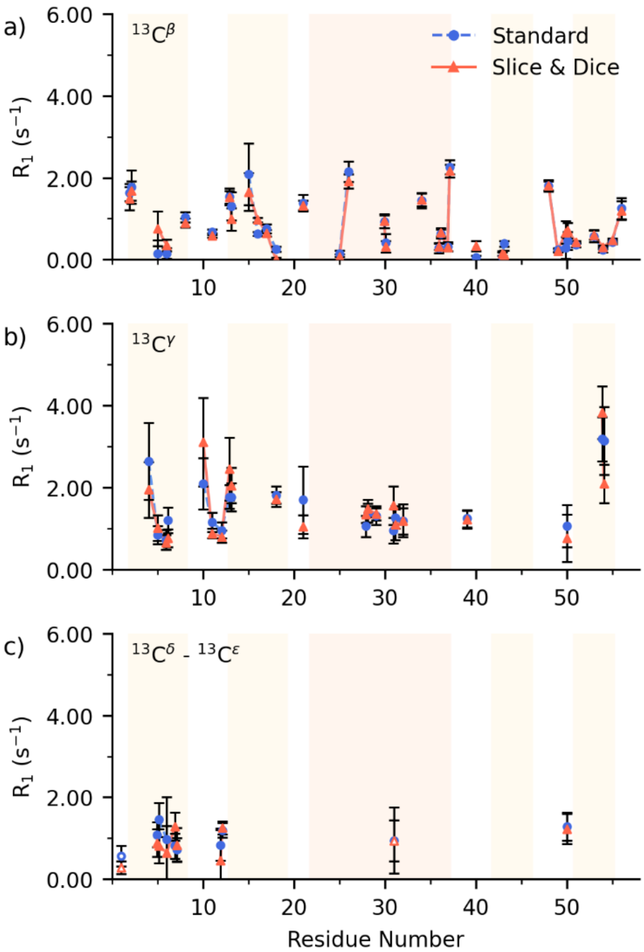

Figure S6. A comparison of the R_1 rates for a) ^{15}N, b) ^{13}C', c) ^{13}C$^{\alpha}$ obtained from the separated single-acquisition experiment (full-blue circle) and Slice & Dice (full-red triangle) as a function of the residue number. In c) ^{13}C$^{\delta}$ are indicated as described above and ^{13}C$^{\varepsilon}$ are indicated with empty-blue circle for standard acquisition and red-empty triangles for Slice & Dice. Errors bars represent two standard deviations within the correspondent rate. For the severely overlapping peaks, values are not included.

References

[1] W. T. Franks, D. H. Zhou, B. J. Wylie, B. G. Money, D. T. Graesser, H. L. Frericks, G. Sahota, C. M. Rienstra, *J. Am. Chem. Soc.* **2005**, *127*, 12291-12305.

[2] D. S. Wishart, C. G. Bigam, J. Yao, F. Abildgaard, H. J. Dyson, E. Oldfield, J. L. Markley, B. D. Sykes, *J. Biomol. NMR* **1995**, *6*, 135-140.

[3] D. Marion, M. Ikura, R. Tschudin, A. Bax, *J. Magn. Reson.* **1989**, *85*, 393-399.

[4] Z. Zhou, R. Kummerle, X. Qiu, D. Redwine, R. Cong, A. Taha, D. Baugh, B. Winniford, *J. Magn. Reson.* **2007**, *187*, 225-233.

[5] D. H. Zhou, C. M. Rienstra, *J. Magn. Reson.* **2008**, *192*, 167-172.

[6] R. Kurbanov, T. Zinkevich, A. Krushelnitsky, *J. Chem. Phys.* **2011**, *135*, 184104.

Chapter 8

Summary and Outlook

Chapter 5 showed how the implementation of ^{1}H homonuclear decoupling at fast MAS (60 kHz) could further improve linewidth, reflected in the resolution and sensitivity of the spectrum. The chapter showed how at 500 MHz with supercycled windowed PMLG ^{1}H homonuclear decoupling on a rigid solid such as glycine, it is possible to achieve a better resolution of the CH_2 group than in a one pulse MAS spectrum acquired at a 1 GHz spectrometer. Furthermore, the application of proton homonuclear decoupling can be useful even at the higher field spectrometer, being able to reach a baseline resolution in glycine at a nutation frequency of ≈100 kHz, which is manageable for probe and rigid solid. Good sensitivity and resolution can be achieved with a proton nutation frequency of 50 kHz, which could open the application of this method even to biological samples, avoiding overheating and consequently degradation of the sample itself. In previous cited work it was seen that good proton resolution was obtained using a windowed DUMBO variance, eDUMBO-PLUS, on a 1 GHz spectrometer[71] for a ^{1}H nutation frequency of ≈170 kHz and by Leskes *et al.*[70] at ^{1}H $\nu_1 = 254$ kHz (DUMBO, 65 kHz MAS at 14.1 T). As well the use of PMLG for a ^{1}H ν_1 125 kHz at faster MAS of 80 kHz,[66] and at 65 kHz MAS for higher nutation frequencies of 216 kHz[70] allowed to record improved ^{1}H detected spectra.

We showed how the enhancement of resolution was enabled by using a windowed sequence in a CRAMPS experiment, and these same conditions were then implemented to improve the sensitivity in a 2D CP-Refocused INEPT experiment. Specifically, ^{15}N-^{1}H heteronuclear correlation is particularly important for spectral assignment for structure and dynamics determination. Indeed, contrary to ^{14}N, an $I = 1$[114] nucleus subject to quadrupolar induced shifts, and anisotropic contributions due to scaled-down second-order quadrupolar interaction, the isotope ^{15}N is spin-1/2. Therefore, even with very low natural abundance (0.4%), ^{15}N NMR can directly access chemical shift information without interference from the quadrupolar effect. We demonstrated how the technique can be applied to a natural abundance sample at 60 kHz MAS in a ^{1}H detected experiment, where the limited quantity of material inside the rotor makes the detection of low γ and natural abundance nuclei, as ^{15}N, particularly challenging. It could be advantageous for pharmaceuticals, where isotope labelling is not of common practice due to its high cost. Even in labelled samples, such as biological macromolecules, the use of this scheme could be useful for improving the INEPT transfer of relatively rigid biomolecules such as GB1. However, the application to biological samples still requires further optimization. The application of ^{1}H homonuclear decoupling during the INEPT transfer ensures that the transfer occours through-bond and could represent a good alternative with respect to CRAMPS acquisition. Firstly, CRAMPS limits the total acquisition time of the spectrum and, while in solids of rigid molecules this is not a huge problem because the signal decays quite rapidly, it can become an issue in biological samples, which have, typically, a longer FID. Secondly, having ^{1}H homonuclear decoupling in acquisition will induce scaling in the spectrum, which can be a further issue that can impact the reliability of the assignment, especially for large macromolecules.

We demonstrated that, even if the conditions for the ^{1}H homonuclear decoupling at fast MAS are clearly different with respect to the classic PMLG implementation, it is possible to have a straightforward optimization recipe to follow for the set-up at 60 kHz MAS. Furthermore, we place our approach in a literature context, showing that for nutation frequency of ≈100 kHz and less, the PMLG conditions follow a similar pattern with the ones seen in various works at fast MAS (> 40 kHz).[56,66,70] The ideal PMLG conditions, such as total angle rotation and chemical shift scaling factor, are shifted, and the Ψ parameter, which is ratio between the MAS rotor period and the decoupling scheme cycle time, follows the trend seen in the literature[66,70] with a value of ≈0.57. Noting the high amount of decoupling parameters, a simple equation for indicating the decoupling efficiency was provided: it considers the increased resolution after scaling, giving essentially an idea of the averaging of the dipolar coupling.

In chapter 6 and 7, the focus is on the improvement of experimental time in both R_1 and $R_{1\rho}$ relaxation measurements. In our approach, we discard as little magnetization as possible per excitation by taking advantage of the magnetization that is normally not used in a relaxation experiment on one nucleus. For example, during a ^{15}N relaxation measurement the polarization from ^{1}H$^{\alpha}$ would not be used. We showed how it is possible to obtain relaxation rates from time-optimized experiments, by direct comparison with data acquired in the traditional way, at 100 kHz MAS on uniformly labelled [^{1}H, ^{13}C, ^{15}N] crystalline GB1 on a 700 MHz spectrometer. One of the advantages that 100 kHz MAS brings is the possibility to have sufficient resolution on the proton channel to acquire on the alpha proton, ^{1}H$^\alpha$, leaving two completely different magnetization pathways for ^{15}N (^{1}H-^{15}N-^{1}HN) and carbonyl, ^{13}CO, (^{1}H-^{13}CO-^{13}C$^\alpha$-^{1}H$^\alpha$). However, at lower spinning frequencies, the samples are usually either deuterated, or alternatively labelled, and the lower resolution on the alpha protons does not allow the same pathway for the carbon experiment. Future work will involve making the technique accessible to lower spinning frequencies, and possibly in the solution-state where, unfortunately, the INEPT transfer, in contrast to CP, could become detrimental for the coherence transfer. We presented a $R_{1\rho}$ experiment which takes advantage of only one recycle delay for two nuclei, and, even with a small reduction in sensitivity (≈10 %) due to the simultaneous CP on both ^{13}CO and ^{15}N, and sequential acquisition on ^{1}H, the advantage that this method brings is still very good. Other than the original implementation of ^{1}H-^{13}CO-^{13}C$^\alpha$-^{1}H$^\alpha$, we give two alternatives, one where the magnetization transfer in SIM-CP is pool specific from proton to ^{13}C$^\alpha$, followed by a specific ^{13}C$^\alpha$-^{13}CO J-coupling transfer, in a ^{1}H$^\alpha$ -^{13}C$^\alpha$ -^{13}CO-^{13}C$^\alpha$-^{1}H$^\alpha$ pathway. We obtained the best time performance by SimultaneousLy Increasing and DEcreasing (SLIDE) the spinlock pulses in a time-shared chemical shift evolution, demonstrating that possible introduction of T_1 relaxation is not an issue due to the different order of magnitude and because the intensity change is $< 2\%$. However, if the T_1s were shorter, the use of constant time periods for the spinlock block will negate any T_1 interference. A concern for $R_{1\rho}$, which limits the aspect of time combination, is that the spin-lock pulses must be separated on the two channels to avoid interaction between the two as with CP, so in this case the magnetization on one of the nuclei is stored to be retrieved later, while on the other channel the measurement is taking place.

This feature is not a concern for the R_1 experiments where the relaxation delays can overlap. Firstly, using SIM-CP and time-shared, and during the long waiting time on one nucleus, the other experiment can be completed in the meantime. Essentially, we showed it is possible to obtain the R_1 experiment on ^{13}CO for free for a small payment of SNR due to SIM-CP. The comparison with relaxation data acquired with the standard implementation showed that pulsing during the relaxation measurement on the different channel does not disrupt the rates of the sequential acquisition experiment. Furthermore, it was possible to take advantage of the long waiting time of ^{15}N, ^{13}CO and ^{13}C$^\alpha$ to embed and nest magnetization on multiple nuclei with no sensitivity losses, since the nested experiments have their own specific magnetization transfer. We showed that it is possible to obtain at 100 kHz MAS a well resolved 2D-spectra for the aliphatic carbon region. However, due to unaveraged spin diffusion even at 100 kHz MAS, the detection of these measurements needs a high degree of deuterium labelling, which could require adaptation of the pulse sequence. A natural evolution of this kind of experiment is to increase the dimensionality of the spectra to potentially allow the deconvolution of heavily overlapping peaks to obtain a more complete picture of dynamics, as for example on the ^{13}C dimension.

Bibliography

[1] P. C. Vioglio, M. R. Chierotti and R. Gobetto, Pharmaceutical aspects of salt and cocrystal forms of APIs and characterization challenges, *Adv. Drug Deliv. Rev.*, 2017, **117**, 86–110.

[2] M. Li, W. Xu and Y. Su, Solid-state NMR spectroscopy in pharmaceutical sciences, *Trends Anal. Chem.*, 2021, **135**, 116152.

[3] V. Jirasko, A. Lends, N. A. Lakomek, M. L. Fogeron, M. E. Weber, A. A. Malär, S. Penzel, R. Bartenschlager, B. H. Meier and A. Böckmann, Dimer Organization of Membrane-Associated NS5A of Hepatitis C Virus as Determined by Highly Sensitive ^{1}H-Detected Solid-State NMR, *Angew. Chem.*, 2021, **133**, 5399–5407.

[4] P. Schanda and M. Ernst, Studying Dynamics by Magic-Angle Spinning Solid-State NMR Spectroscopy: Principles and Applications to Biomolecules, *Prog. Nucl. Magn. Reson. Spectrosc.*, 2016, **96**, 1–46.

[5] D. B. Good, S. Wang, M. E. Ward, J. Struppe, L. S. Brown, J. R. Lewandowski and V. Ladizhansky, Conformational dynamics of a seven transmembrane helical protein Anabaena Sensory Rhodopsin probed by solid-state NMR, *J. Am. Chem. Soc.*, 2014, **136**, 2833–42.

[6] J. M. Lamley, C. Oster, R. A. Stevens and J. R. Lewandowski, Intermolecular Interactions and Protein Dynamics by Solid-State NMR Spectroscopy, *Angew. Chem.*, 2015, **127**, 15594–15598.

[7] F. Bloch and W. W. P. M. Hansen, W., Packard, M. The nuclear induction experiment, *Phys. Rev.*, 1946, **70**, 474–485.

[8] E. M. Purcell, H. C. Torrey and R. V. Pound, Resonance absorption by nuclear magnetic moments in a solid, *Phys. Rev.*, 1946, **69**, 37.

[9] J. R. Lewandowski, M. E. Halse, M. Blackledge and L. Emsley, Direct observation of hierarchical protein dynamics, *Science*, **348**, 578–581.

[10] Z. Zhang, A. Oss, M. L. Org, A. Samoson, M. Li, H. Tan, Y. Su and J. Yang, Selectively enhanced ^{1}H–^{1}H correlations in proton-detected solid-state NMR under ultrafast MAS conditions, *J. Phys. Chem. Lett.*, 2020, **11**, 8077–8083.

[11] K. Maruyoshi, D. Iuga, A. E. Watts, C. E. Hughes, K. D. M. Harris and S. P. Brown, Assessing the detection limit of a minority solid-state form of a pharmaceutical by ^{1}H double-quantum magic-angle spinning nuclear magnetic resonance spectroscopy, *J. Pharm. Sci.*, 2017, **106**, 3372–3377.

[12] P. Hodgkinson, High-resolution ^{1}H NMR spectroscopy of solids, *Annu. Rep. NMR Spectrosc.*, 2011, **72**, 185–223.

[13] K. R. Mote, V. Agarwal and P. K. Madhu, Five decades of homonuclear dipolar decoupling in solid-state NMR: Status and outlook, *Prog. Nucl. Magn. Reson. Spectrosc.*, 2016, **97**, 1–39.

[14] S. R. Hartmann and E. L. Hahn, Nuclear double resonance in the rotating frame, *Phys. Rev.*, 1962, **128**, 2042.

[15] B. Elena, A. Lesage, S. Steuernagel, A. Bockmann and L. Emsley, Proton to Carbon-13 INEPT in Solid-State NMR Spectroscopy, *J. Am. Chem. Soc.*, 2005, **127**, 17296–17302.

[16] C. A. Fyfe, K. C. Wong-Moon, Y. Huang and H. Grondey, INEPT experiments in solid-state NMR, journal = J. Am. Chem. Soc., volume = 117, number = 41, pages = 10397-10398, ISSN = 0002-7863, year = 1995, type = Journal Article.

[17] P. K. Madhu, X. Zhao and M. H. Levitt, High-resolution ^{1}H NMR in the solid state using symmetry-based pulse sequences, *Chem. Phys. Lett.*, 2001, **346**, 142–148.

[18] P. K. Madhu, High-resolution solid-state NMR spectroscopy of protons with homonuclear dipolar decoupling schemes under magic-angle spinning, *Solid State Nucl. Magn. Reson.*, 2009, **35**, 2–11.

[19] D. Sakellariou, A. Lesage, P. Hodgkinson and L. Emsley, Homonuclear dipolar decoupling in solid-state NMR using continuous phase modulation, *Chem. Phys. Lett.*, 2000, 253–260.

[20] E. Vinogradov, P. K. Madhu and S. Vega, Strategies for high-resolution proton spectroscopy in solid-state NMR, *New Techniques in Solid-State NMR*, 2005, 33–90.

[21] M. Lee and W. I. Goldburg, Nuclear-Magnetic-Resonance Line Narrowing by a Rotating rf Field, *Phys. Rev.*, 1965, **140**, A1261–A1271.

[22] M. H. Levitt, A. C. Kolbert., A. Bielecki and D. J. Ruben, High-resolution ^{1}H NMR in solids with frequency-switched multiple-pulse sequences, *Solid State Nucl. Magn. Reson.*, 1993, **2**, 151–163.

[23] D. P. Burum, M. Linder and R. R. Ernst, Low-power multipulse line narrowing in solid-state NMR, *J. Magn. Reson.*, 1981, **44**, 173–188.

[24] K. Takegoshi and C. A. McDowell, A "Magic Echo" Pulse Sequence For The High-Resolution NMR Spectrum Of Abundant Spins In Solids, *Chem. Phys. Lett.*, 1985, **316**, year.

[25] F. M. Paruzzo and L. Emsley, High-resolution ^{1}H NMR of powdered solids by homonuclear dipolar decoupling, *J. Magn. Reson.*, 2019, **309**, 106598.

[26] M. Mehring and J. S. Waugh, Magic-angle NMR experiments in solids, *Phys. Rev. B*, 1972, **5**, 3459.

[27] J. S. Waugh, L. M. Huber and U. Haeberlen, Approach to high-resolution NMR in solids, *Phys. Rev. Lett.*, 1968, **20**, 180.

[28] B. C. Gerstein, R. G. Pembleton, R. C. Wilson and L. M. Ryan, High resolution NMR in randomly oriented solids with homonuclear dipolar broadening: combined multiple pulse NMR and magic angle spinning, *J. Phys. Chem.*, 1977, **66**, 361–362.

[29] M. Hohwy, P. V. Bower, H. J. Jakobsen and N. C. Nielsen, A high-order and broadband CRAMPS experiment using z-rotational decoupling, *Chem. Phys. Lett.*, 1997, **273**, 297–303.

[30] R. A. Venters, C. C. Huang, B. T. Farmer, R. Trolard, L. D. Spicer and C. A. Fierke, High-level ^{2}H/^{13}C/^{15}N labeling of proteins for NMR studies, *J. Biomol. NMR*, 1995, **5**, 339–344.

[31] M. Kainosho, T. Torizawa, Y. Iwashita, T. Terauchi, A. Mei Ono and P. Güntert, Optimal isotope labelling for NMR protein structure determinations, *Nature*, 2006, **440**, 52–57.

[32] V. Chevelkov, K. Rehbein, A. Diehl and B. Reif, Ultrahigh resolution in proton solid-state NMR spectroscopy at high levels of deuteration, *Angew. Chem., Int. Ed. Engl.*, 2006, **45**, 3878–3881.

[33] B. Reif, Deuteration for High-Resolution Detection of Protons in Protein Magic Angle Spinning (MAS) Solid-State NMR, *Chem. Rev.*, 2021.

[34] Y. Kofuku, T. Ueda, J. Okude, Y. Shiraishi, K. Kondo, T. Mizumura, S. Suzuki and I. Shimada, Functional dynamics of deuterated β2-adrenergic receptor in lipid bilayers revealed by NMR spectroscopy, *Angew. Chem.*, 2014, **126**, 13594–13597.

[35] D. Nietlispach, R. T. Clowes, R. W. Broadhurst, Y. Ito, J. Keeler, M. Kelly, J. Ashurst, H. Oschkinat, P. J. Domaille and E. D. Laue, An approach to the structure determination of larger proteins using triple resonance NMR experiments in conjunction with random fractional deuteration, *J. Am. Chem. Soc.*, 1996, **118**, 407–415.

[36] D. H. Zhou, D. T. Graesser, W. T. Franks and C. M. Rienstra, Sensitivity and resolution in proton solid-state NMR at intermediate deuteration levels: quantitative linewidth characterization and applications to correlation spectroscopy, *J. Magn. Reson.*, 2006, **178**, 297–307.

[37] N. Giraud, M. Blackledge, A. Bockmann and L. Emsley, The influence of nitrogen-15 proton-driven spin diffusion on the measurement of nitrogen-15 longitudinal relaxation times, *J. Magn. Reson.*, 2007, **184**, 51–61.

[38] A. Krushelnitsky, T. Brauniger and D. Reichert, ^{15}N spin diffusion rate in solid-state NMR of totally enriched proteins: the magic angle spinning frequency effect, *J. Magn. Reson.*, 2006, **182**, 339–42.

[39] J. R. Lewandowski, J. Sein, H. J. Sass, S. Grzesiek, M. Blackledge and L. Emsley, Measurement of site-specific ^{13}C spin-lattice relaxation in a crystalline protein, *J. Am. Chem. Soc.*, 2010, **132**, 8252–8254.

[40] J. R. Lewandowski, H. J. Sass, S. Grzesiek, M. Blackledge and L. Emsley, Site-specific measurement of slow motions in proteins, *J. Am. Chem. Soc.*, 2011, **133**, 16762–5.

[41] J. M. Lamley, M. J. Lougher, H. J. Sass, M. Rogowski, S. Grzesiek and J. R. Lewandowski, Unraveling the complexity of protein backbone dynamics

with combined ^{13}C and ^{15}N solid-state NMR relaxation measurements, *Phys. Chem. Chem. Phys.*, 2015, **17**, 21997–2008.

[42] R. A. Stevens, *The Development of Solid-state NMR Methodology to Study the Dynamics of Proteins and Ice*, University of Warwick, PhD Thesis, 2018.

[43] I. Schnell, S. P. Brown, H. Y. Low, H. Ishida and H. W. Spiess, An investigation of hydrogen bonding in benzoxazine dimers by fast magic-angle spinning and double-quantum ^{1}H NMR spectroscopy, *J. Am. Chem. Soc.*, 1998, **120**, 11784–11795.

[44] S. P. Brown and H. W. Spiess, Advanced solid-state NMR methods for the elucidation of structure and dynamics of molecular, macromolecular, and supramolecular systems, *Chem. Rev.*, 2001, **101**, 4125–4156.

[45] J. Struppe, C. M. Quinn, M. Lu, M. Wang, G. Hou, X. Lu, J. Kraus, L. B. Andreas, J. Stanek and D. Lalli, Expanding the horizons for structural analysis of fully protonated protein assemblies by NMR spectroscopy at MAS frequencies above 100 kHz, *Solid State Nucl. Magn. Reson.*, 2017, **87**, 117–125.

[46] L. Lecoq, M. Schledorn, S. Wang, S. Smith-Penzel, A. A. Malär, M. Callon, M. Nassal, B. H. Meier and A. Böckmann, 100 kHz MAS proton-detected NMR spectroscopy of hepatitis B virus capsids, *Front. Mol. Biosci.*, 2019, 58.

[47] E. Nimerovsky, K. T. Movellan, X. C. Zhang, M. C. Forster, E. Najbauer, K. Xue, R. Dervişoğlu, K. Giller, C. Griesinger and S. Becker, Proton detected solid-state NMR of membrane proteins at 28 Tesla (1.2 GHz) and 100 kHz magic-angle spinning, *Biomolecules*, 2021, **11**, 752.

[48] J. Struppe, C. M. Quinn, S. Sarkar, A. M. Gronenborn and T. Polenova, Ultrafast ^{1}H MAS NMR crystallography for natural abundance pharmaceutical compounds, *Mol. Pharm.*, 2019, **17**, 674–682.

[49] S. P. Brown, Applications of high-resolution ^{1}H solid-state NMR, *Solid State Nucl. Magn. Reson.*, 2012, **41**, 1–27.

[50] V. Agarwal, S. Penzel, K. Szekely, R. Cadalbert, E. Testori, A. Oss, J. Past, A. Samoson, M. Ernst and A. Böckmann, De novo 3D structure determination from sub-milligram protein samples by solid-state 100 kHz MAS NMR spectroscopy, *Angew. Chem., Int. Ed. Engl.*, 2014, **53**, 12253–12256.

[51] Y. Nishiyama, Fast magic-angle sample spinning solid-state NMR at 60–100 kHz for natural abundance samples, *Solid State Nucl. Magn. Reson.*, 2016, **78**, 24–36.

[52] Y. Nishiyama, T. Kobayashi, M. Malon, D. Singappuli-Arachchige, I. I. Slowing and M. Pruski, Studies of minute quantities of natural abundance molecules using 2D heteronuclear correlation spectroscopy under 100 kHz MAS, *Solid State Nucl. Magn. Reson.*, 2015, **66**, 56–61.

[53] Y. Ishii, J. P. Yesinowski and R. Tycko, Sensitivity enhancement in solid-state ^{13}C NMR of synthetic polymers and biopolymers by 1H NMR detection with high-speed magic angle spinning, *J. Am. Chem. Soc.*, 2001, **123**, 2921–2922.

[54] D. H. Zhou, G. Shah, C. Mullen, D. Sandoz and C. M. Rienstra, Proton-detected solid-state NMR spectroscopy of natural-abundance peptide and protein pharmaceuticals, *Angew. Chem. Int. Ed. Engl.*, 2009, **48**, 1253–6.

[55] S. M. Althaus, K. Mao, J. A. Stringer, T. Kobayashi and M. Pruski, Indirectly detected heteronuclear correlation solid-state NMR spectroscopy of naturally abundant ^{15}N nuclei, *Solid State Nucl. Magn. Reson.*, 2014, **57-58**, 17–21.

[56] K. Mao and M. Pruski, Directly and indirectly detected through-bond heteronuclear correlation solid-state NMR spectroscopy under fast MAS, *J. Magn. Reson.*, 2009, **201**, 165–74.

[57] C. Guzmán-Afonso, Y. Hong, H. Colaux, H. Iijima, A. Saitow, T. Fukumura, Y. Aoyama, S. Motoki, T. Oikawa, T. Yamazaki, K. Yonekura and Y. Nishiyama, Understanding hydrogen-bonding structures of molecular crystals via electron and NMR nanocrystallography, *Nat. Commun.*, 2019, **10**, 3537.

[58] E. K. Paulson, C. R. Morcombe, V. Gaponenko, B. Dancheck, R. A. Byrd and K. W. Zilm, Sensitive high resolution inverse detection NMR spectroscopy of proteins in the solid state, *J. Am. Chem. Soc.*, 2003, **125**, 15831–15836.

[59] D. H. Zhou, G. Shah, M. Cormos, C. Mullen, D. Sandoz and C. M. Rienstra, Proton-detected solid-state NMR spectroscopy of fully protonated proteins at 40 kHz magic-angle spinning, *J. Am. Chem. Soc.*, 2007, **129**, 11791–11801.

[60] G. P. Holland, B. R. Cherry, J. E. Jenkins and J. L. Yarger, Proton-detected heteronuclear single quantum correlation NMR spectroscopy in rigid solids with ultra-fast MAS, *J. Magn. Reson.*, 2010, **202**, 64–71.

[61] V. E. Zorin, S. P. Brown and P. Hodgkinson, Origins of linewidth in ^{1}H magic-angle spinning NMR, *J. Chem. Phys.*, 2006, **125**, 144508.

[62] D. Cala-De Paepe, J. Stanek, K. Jaudzems, K. Tars, L. B. Andreas and G. Pintacuda, Is protein deuteration beneficial for proton detected solid-state NMR at and above 100 kHz magic-angle spinning?, *Solid State Nucl. Magn. Reson.*, 2017, **87**, 126–136.

[63] M. Schledorn, A. A. Malär, A. Torosyan, S. Penzel, D. Klose, A. Oss, M. L. Org, S. Wang, L. Lecoq and R. Cadalbert, Protein NMR spectroscopy at 150 kHz magic-angle spinning continues to improve resolution and mass sensitivity, *Chembiochem*, 2020, **21**, 2540–2548.

[64] A. A. Malär, S. Smith-Penzel, G. M. Camenisch, T. Wiegand, A. Samoson, A. Böckmann, M. Ernst and B. H. Meier, Quantifying proton NMR coherent linewidth in proteins under fast MAS conditions: a second moment approach, *Phys. Chem. Chem. Phys.*, 2019, **21**, 18850–18865.

[65] C. Coelho, J. Rocha, P. K. Madhu and L. Mafra, Practical aspects of Lee–Goldburg based CRAMPS techniques for high-resolution ^{1}H NMR spectroscopy in solids: Implementation and applications, *J. Magn. Reson.*, 2008, **194**, 264–282.

[66] Y. Nishiyama, X. Lu, J. Trebosc, O. Lafon, Z. Gan, P. K. Madhu and J. P. Amoureux, Practical choice of (1)H-(1)H decoupling schemes in through-bond (1)H-X HMQC experiments at ultra-fast MAS, *J. Magn. Reson.*, 2012, **214**, 151–8.

[67] J. P. Amoureux, B. Hu and J. Trébosc, Enhanced resolution in proton solid-state NMR with very-fast MAS experiments, *J. Magn. Reson.*, 2008, **193**, 305–307.

[68] J. P. Amoureux, B. Hu, J. Trébosc, Q. Wang, O. Lafon and F. Deng, Homonuclear dipolar decoupling schemes for fast MAS, *Solid State Nucl. Magn. Reson.*, 2009, **35**, 19–24.

[69] Z. Gan, P. K. Madhu, J. P. Amoureux, J. Trébosc and O. Lafon, A tunable homonuclear dipolar decoupling scheme for high-resolution proton NMR of solids from slow to fast magic-angle spinning, *Chem. Phys. Lett.*, 2011, **503**, 167–170.

[70] M. Leskes, S. Steuernagel, D. Schneider, P. K. Madhu and S. Vega, Homonuclear dipolar decoupling at magic-angle spinning frequencies up to 65kHz in solid-state nuclear magnetic resonance, *Chem. Phys. Lett.*, 2008, **466**, 95–99.

[71] E. Salager, J. N. Dumez, R. S. Stein, S. Steuernagel, A. Lesage, B. Elena-Herrmann and L. Emsley, Homonuclear dipolar decoupling with very large scaling factors for high-resolution ultrafast magic angle spinning 1H solid-state NMR spectroscopy, *Chem. Phys. Lett.*, 2010, **498**, 214–220.

[72] E. Salager, R. S. Stein, S. Steuernagel, A. Lesage, B. Elena and L. Emsley, Enhanced sensitivity in high-resolution 1H solid-state NMR spectroscopy with DUMBO dipolar decoupling under ultra-fast MAS, *Chem. Phys. Lett.*, 2009, **469**, 336–341.

[73] M. Leskes, P. K. Madhu and S. Vega, Why does PMLG proton decoupling work at 65kHz MAS?, *J. Magn. Reson.*, 2009, **199**, 208–13.

[74] J. M. Lamley and J. R. Lewandowski, Relaxation-based magic-angle spinning NMR approaches for studying protein dynamics, *Emagres*.

[75] D. Marion, D. F. Gauto, I. Ayala, K. Giandoreggio-Barranco and P. Schanda, Microsecond protein dynamics from combined Bloch-McConnell and near-rotary-resonance $R_1\rho$ relaxation-dispersion MAS NMR, *ChemPhysChem*, 2019, **20**, 276–284.

[76] J. R. Lewandowski, Advances in Solid-State Relaxation Methodology for Probing Site-Specific Protein Dynamics, *Acc. Chem. Res.*, 2013, **46**, year.

[77] N. Giraud, M. Blackledge, M. Goldman, A. Bockmann, A. Lesage, F. Penin and L. Emsley, Quantitative analysis of backbone dynamics in a crystalline protein from nitrogen-15 spin-lattice relaxation, *J. Am. Chem. Soc.*, 2005, **127**, 18190–18201.

[78] V. Chevelkov, A. Diehl and B. Reif, Measurement of ^{15}N-T_1 relaxation rates in a perdeuterated protein by magic angle spinning solid-state nuclear magnetic resonance spectroscopy, *J. Phys. Chem.*, 2008, **128**, 02B603.

[79] A. G. Palmer and F. Massi, Characterization of the dynamics of biomacromolecules using rotating-frame spin relaxation NMR spectroscopy, *Chem. Rev.*, 2006, **106**, 1700–1719.

[80] A. Krushelnitsky, D. Gauto, D. C. Rodriguez Camargo, P. Schanda and K. Saalwächter, Microsecond motions probed by near-rotary-resonance $R_{1\rho}$ ^{15}N MAS NMR experiments: the model case of protein overall-rocking in crystals, *J. Biomol. NMR*, 2018, **71**, 53–67.

[81] P. Ma, J. D. Haller, J. Zajakala, P. Macek, A. C. Sivertsen, D. Willbold, J. Boisbouvier and P. Schanda, Probing transient conformational states of proteins by solid-state R(1rho) relaxation-dispersion NMR spectroscopy, *Angew. Chem. Int. Ed. Engl.*, 2014, **53**, 4312–7.

[82] B. Busi, J. R. Yarava, A. Hofstetter, N. Salvi, D. Cala-De Paepe, J. R. Lewandowski, M. Blackledge and L. Emsley, Probing protein dynamics using multifield variable temperature NMR relaxation and molecular dynamics simulation, *J. Phys. Chem. B*, 2018, **122**, 9697–9702.

[83] B. Busi, J. R. Yarava, A. Bertarello, F. Freymond, W. Adamski, D. Maurin, M. Hiller, H. Oschkinat, M. Blackledge and L. Emsley, Similarities and differences among protein dynamics studied by variable temperature nuclear magnetic resonance relaxation, *J. Phys. Chem. B*, 2021, **125**, 2212–2221.

[84] R. Linser, V. Chevelkov, A. Diehl and B. Reif, Sensitivity enhancement using paramagnetic relaxation in MAS solid-state NMR of perdeuterated proteins, *J. Magn. Reson.*, 2007, **189**, 209–216.

[85] N. P. Wickramasinghe, M. Kotecha, A. Samoson, J. Past and Y. Ishii, Sensitivity enhancement in ^{13}C solid-state NMR of protein microcrystals by use of paramagnetic metal ions for optimizing ^{1}H T_1 relaxation, *J. Magn. Reson.*, 2007, **184**, 350–356.

[86] S. Parthasarathy, Y. Nishiyama and Y. Ishii, Sensitivity and resolution enhanced solid-state NMR for paramagnetic systems and biomolecules under very fast magic angle spinning, *Acc. Chem. Res.*, 2013, **46**, 2127–2135.

[87] G. Pintacuda, N. Giraud, R. Pierattelli, A. Böckmann, I. Bertini and L. Emsley, Solid-state NMR spectroscopy of a paramagnetic protein: assignment and study of human dimeric oxidized CuII–ZnII superoxide dismutase (SOD), *Angew. Chem.*, 2007, **119**, 1097–1100.

[88] X. Lu, Y. Tsutsumi, C. Huang, W. Xu, S. R. Byrn, A. C. Templeton, A. V. Buevich, J. P. Amoureux and Y. Su, Molecular packing of pharmaceuticals analyzed with paramagnetic relaxation enhancement and ultrafast magic angle pinning NMR, *Phys. Chem. Chem. Phys.*, 2020, **22**, 13160–13170.

[89] C. Oster, S. Kosol and J. R. Lewandowski, Quantifying microsecond exchange in large protein complexes with accelerated relaxation dispersion experiments in the solid state, *Sci. Rep.*, 2019, **9**, 11082.

[90] C. Oster, S. Kosol, C. Hartlmuller, J. M. Lamley, D. Iuga, A. Oss, M. L. Org, K. Vanatalu, A. Samoson and T. Madl, Characterization of protein–protein interfaces in large complexes by solid-state NMR solvent paramagnetic relaxation enhancements, *J. Am. Chem. Soc.*, 2017, **139**, 12165–12174.

[91] M. J. Knight, I. C. Felli, R. Pierattelli, L. Emsley and G. Pintacuda, Magic angle spinning NMR of paramagnetic proteins, *Acc. Chem. Res.*, 2013, **46**, 2108–2116.

[92] T. Gopinath and G. Veglia, Dual acquisition magic-angle spinning solid-state NMR-spectroscopy: simultaneous acquisition of multidimensional spectra of biomacromolecules, *Angew. Chem. Int. Ed. Engl.*, 2012, **51**, 2731–5.

[93] F. Lohr, A. Laguerre, C. Bock, S. Reckel, P. J. Connolly, N. Abdul-Manan, F. Tumulka, R. Abele, J. M. Moore and V. Dotsch, Time-shared experiments for efficient assignment of triple-selectively labeled proteins, *J. Magn. Reson.*, 2014, **248**, 81–95.

[94] J. M. Lamley and J. R. Lewandowski, Simultaneous acquisition of homonuclear and heteronuclear long-distance contacts with time-shared third spin assisted recoupling, *J. Magn. Reson.*, 2012, **218**, 30–4.

[95] T. Gopinath and G. Veglia, 3D DUMAS: simultaneous acquisition of three-dimensional magic angle spinning solid-state NMR experiments of proteins, *J. Magn. Reson.*, 2012, **220**, 79–84.

[96] K. Sharma, P. K. Madhu and K. R. Mote, A suite of pulse sequences based on multiple sequential acquisitions at one and two radiofrequency channels for solid-state magic-angle spinning NMR studies of proteins, *J. Biomol. NMR*, 2016, **65**, 127–141.

[97] T. Gopinath and G. Veglia, Orphan spin operators enable the acquisition of multiple 2D and 3D magic angle spinning solid-state NMR spectra, *J. Chem. Phys.*, 2013, **138**, 184201.

[98] T. Gopinath, D. K. Weber and G. Veglia, Multi-receiver solid-state NMR using polarization optimized experiments (POE) at ultrafast magic angle spinning, *J. Biomol. NMR*, 2020, **74**, 267–285.

[99] A. Gallo, W. T. Franks and J. R. Lewandowski, A suite of solid-state NMR experiments to utilize orphaned magnetization for assignment of proteins using parallel high and low gamma detection, *J. Magn. Reson.*, 2019, **305**, 219–231.

[100] M. H. Levitt, *Spin dynamics: basics of nuclear magnetic resonance*, John Wiley Sons, 2013.

[101] J. Keeler, *Understanding NMR spectroscopy*, John Wiley Sons, 2011.

[102] M. J. Duer, *Introduction to solid-state NMR spectroscopy*, Oxford, UK, 2004.

[103] J. Cavanagh, W. J. Fairbrother, A. G. Palmer III and N. J. Skelton, *Protein NMR spectroscopy: principles and practice*, Academic press, 1996.

[104] A. E. McDermott and T. Polenova, *Solid state NMR studies of biopolymers*, John Wiley Sons, 2012.

[105] M. H. Levitt, Why do spinning sidebands have the same phase?, *J. Magn. Reson. (1969)*, 1989, **82**, 427–433.

[106] G. Lipari and A. Szabo, Model-free approach to the interpretation of nuclear magnetic resonance relaxation in macromolecules. 1. Theory and range of validity, *J. Am. Chem. Soc.*, 1982, **104**, 4546–4559.

[107] G. M. Clore, A. Szabo, A. Bax, L. E. Kay, P. C. Driscoll and A. M. Gronenborn, Deviations from the simple two-parameter model-free approach to the interpretation of nitrogen-15 nuclear magnetic relaxation of proteins, *J. Am. Chem. Soc.*, 1990, **112**, 4989–4991.

[108] V. Chevelkov, U. Fink and B. Reif, Quantitative analysis of backbone motion in proteins using MAS solid-state NMR spectroscopy, *J. Biomol. NMR*, 2009, **45**, 197–206.

[109] T. Zinkevich, V. Chevelkov, B. Reif, K. Saalwächter and A. Krushelnitsky, Internal protein dynamics on ps to s timescales as studied by multi-frequency ^{15}HN solid-state NMR relaxation, *J. Biomol. NMR*, 2013, **57**, 219–235.

[110] B. Alonso and D. Massiot, Multi-scale NMR characterisation of mesostructured materials using $^{1}H \rightarrow {}^{13}C$ through-bond polarisation transfer, fast MAS, and ^{1}H spin diffusion, *J. Magn. Reson.*, 2003, **163**, 347–352.

[111] G. METz, X. Wu and S. O. Smith, Ramped-amplitude cross polarization in magic-angle-spinning NMR, *J. Magn. Reson. A*, 1994, **110**, 219–227.

[112] L. Kai, D. Torchia and A. Bax, Backbone dynamics of proteins as studied by ^{15}N inverse detected heteronuclear NMR spectroscopy: application to staphyloccal nuclase, *Biochemistry*, 1989, **28**, 8972.

[113] D. A. Torchia, The measurement of proton-enhanced carbon-13 T_1 values by a method which suppresses artifacts, *J. Magn. Reson. (1969)*, 1978, **30**, 613–616.

[114] A. S. Tatton, T. N. Pham, F. G. Vogt, D. Iuga, A. J. Edwards and S. P. Brown, Probing intermolecular interactions and nitrogen protonation in pharmaceuticals by novel 15 N-edited and 2D ^{14}N-^{1}H solid-state NMR, *Crystengcomm*, 2012, **14**, 2654–2659.